



**This electronic thesis or dissertation has been
downloaded from Explore Bristol Research,
<http://research-information.bristol.ac.uk>**

Author:

Humphries, Rachel E

Title:

Cholinergic modulation of CA3 synaptic transmission and integration

General rights

Access to the thesis is subject to the Creative Commons Attribution - NonCommercial-No Derivatives 4.0 International Public License. A copy of this may be found at <https://creativecommons.org/licenses/by-nc-nd/4.0/legalcode>. This license sets out your rights and the restrictions that apply to your access to the thesis so it is important you read this before proceeding.

Take down policy

Some pages of this thesis may have been removed for copyright restrictions prior to having it been deposited in Explore Bristol Research. However, if you have discovered material within the thesis that you consider to be unlawful e.g. breaches of copyright (either yours or that of a third party) or any other law, including but not limited to those relating to patent, trademark, confidentiality, data protection, obscenity, defamation, libel, then please contact collections-metadata@bristol.ac.uk and include the following information in your message:

- Your contact details
- Bibliographic details for the item, including a URL
- An outline nature of the complaint

Your claim will be investigated and, where appropriate, the item in question will be removed from public view as soon as possible.



Cholinergic modulation of CA3 synaptic transmission and integration

Rachel Emma Humphries

A dissertation submitted to the University of Bristol in accordance with the requirements for award of the degree of Doctor of Philosophy in the Faculty of Life Sciences.

School of Physiology, Pharmacology and Neuroscience

March 2022

Word count: 35465

Abstract

Hippocampal CA3 is a region of the brain essential for memory processing. Neuromodulators, such as acetylcholine and noradrenaline, are released into the hippocampus during particular behavioural states and are suggested to modulate hippocampal circuitry to enable the encoding of memories during novel and salient experiences.

In this thesis, I used a combination of biophysical neuron modelling, *ex vivo* whole-cell patch clamp and optogenetic techniques to assess the impact of acetylcholine on synaptic transmission and dendritic integration in CA3 pyramidal neurons.

NMDA-mediated nonlinear integration was investigated in a biophysical multi-compartment model of a CA3 pyramidal neuron. Increasing the number of stimulated synaptic inputs within individual dendritic branches generated nonlinear increases in the dendritic response amplitude, with lower thresholds for nonlinearity in the distal SLM dendrites, due to increased dendritic input resistance. Simulation of acetylcholine, via inhibition of specific potassium channels, reduced the threshold for NMDA-mediated nonlinear synaptic integration to a greater extent in the proximal SR dendrites compared to the SLM dendrites.

In *ex vivo* hippocampal slices, bath application of a cholinergic agonist reduced CA3-CA3 recurrent transmission, via a pre-synaptic mechanism, and increased CA3 neuron excitability. On the other hand, noradrenaline had no impact on CA3 recurrent transmission or on neuron excitability. In contrast, optogenetic stimulation of cholinergic fibres in the CA3 region did not affect this recurrent transmission or synaptic transmission from perforant path stimulation. Endogenous acetylcholine did however reduce inhibitory inputs to CA3 pyramidal neurons, suggesting a disinhibitory action, with the primary impact of increasing CA3 excitability.

Overall, the ability of acetylcholine to increase CA3 neuron excitability and reduce the threshold of dendritic nonlinearity indicates potential mechanisms for cholinergic facilitation of synaptic plasticity and memory encoding within the CA3 network.

Acknowledgements

This PhD could not have been completed without the support and guidance of a considerable number of people. I'd first and foremost like to thank my supervisors, Jack Mellor and Cian O'Donnell, for being incredibly supportive and encouraging throughout all the ups and downs of my PhD.

I would like to thank all past and present members of the Mellor and O'Donnell labs for helpful discussions and general office chats over the years. I owe special thanks to Sarah Stuart and Jon Palacios for all the support and teaching involving the mobile home-cage (even if it didn't make it into this thesis) as well as to Matt Udakis, Travis Bacon and Simon Griesius for endless help with patching that included moving and re-building my rig and generally helping to troubleshoot all the problems. I would also like to thank members of the Bashir lab where I spent time doing a rotation project, particularly Zaf Bashir as well as Paul Banks for being an excellent *ex vivo* patch clamp teacher. I also owe thanks to all members of the Ashby lab for their useful discussions and advice during lab meetings.

Additionally, I would like to thank my progression panel, Paul Chadderton and Conor Houghton, for providing extra support and advice (and yoga), as well as the Neural Dynamics directors, students, and community. I also thank the Wellcome Trust for funding this PhD and providing my very generous stipend.

Finally, I'd like to thank all the friends and family that have continuously supported me throughout this journey (and given me breaks from science), with a special mention to Bristol housemates (Sonam, Alex, Lea and Joe), Heather, "Guildford Girlies", Nikita, Andrew, and of course my wonderfully supportive Mum and Dad.

COVID-19 Statement

Parts of the work in this thesis were impacted by the COVID-19 pandemic. Particularly, lab experiments were required to stop, which led to an extended break in performing any *ex vivo* electrophysiology. On return to the lab, it then took additional time to get experiments running smoothly and efficiently again. Overall, the focus of the thesis shifted more onto the modelling and fewer electrophysiology experiments were performed as originally planned.

Author's declaration

I declare that the work in this dissertation was carried out in accordance with the requirements of the University's Regulations and Code of Practice for Research Degree Programmes and that it has not been submitted for any other academic award. Except where indicated by specific reference in the text, the work is the candidate's own work. Work done in collaboration with, or with the assistance of, others, is indicated as such. Any views expressed in the dissertation are those of the author.

SIGNED:

DATE:

Table of contents

CHAPTER 1	INTRODUCTION	1
1.1	HIPPOCAMPAL/CA3 CIRCUITY AND FUNCTION	1
1.1.1	<i>Learning and memory</i>	1
1.1.2	<i>Synaptic transmission and plasticity</i>	2
1.1.3	<i>Hippocampal/CA3 circuitry</i>	3
1.1.4	<i>CA3 network and pattern completion</i>	7
1.1.5	<i>Interneuron function within CA3</i>	9
1.1.6	<i>Role of CA3 region in learning and memory</i>	9
1.1.7	<i>Plasticity mechanisms in CA3</i>	10
1.1.8	<i>Place cells in CA3</i>	11
1.2	DENDRITIC INTEGRATION	13
1.2.1	<i>Dendritic integration in CA3 neurons</i>	14
1.2.2	<i>Plateau potentials in the hippocampus</i>	15
1.2.3	<i>Dendritic integration and plasticity</i>	15
1.3	NEUROMODULATION IN THE HIPPOCAMPUS	17
1.3.1	<i>Acetylcholine in learning and memory</i>	17
1.3.2	<i>Acetylcholine in the hippocampus</i>	17
1.3.3	<i>Cholinergic modulation of CA3 network</i>	21
1.3.4	<i>Cholinergic modulation of dendritic integration and plasticity</i>	22
1.3.5	<i>Noradrenaline in the hippocampus</i>	23
1.3.6	<i>Noradrenaline in learning and memory</i>	24
1.3.7	<i>Noradrenergic modulation of CA3 network</i>	25
1.4	AIMS AND HYPOTHESES	27
CHAPTER 2	CHOLINERGIC MODULATION OF DENDRITIC INTEGRATION IN A RECONSTRUCTED CA3 NEURON MODEL.....	29
2.1	INTRODUCTION	29
2.2	METHODS	32
2.2.1	<i>Software</i>	32
2.2.2	<i>Two-compartment model</i>	32
2.2.3	<i>Channel conductance optimisation</i>	33
2.2.4	<i>Reconstructed CA3 neuron model</i>	34
2.2.5	<i>AMPA and NMDAR mechanisms</i>	36
2.2.6	<i>NMDA spike generation</i>	37
2.2.7	<i>Analysis of nonlinear output</i>	37
2.2.8	<i>Cholinergic and potassium channel modulation</i>	38

2.2.9	<i>Statistical analysis.....</i>	38
2.3	RESULTS.....	39
2.3.1	<i>Cholinergic modulation of NMDA spikes in a two-compartment model</i>	39
2.3.2	<i>Heterogeneity of nonlinear dendritic integration in a reconstructed CA3 neuron model</i>	47
2.3.3	<i>Cholinergic modulation of nonlinear integration in a reconstructed CA3 neuron model</i>	54
2.3.4	<i>Effect of potassium channel inhibition on NMDA-mediated nonlinearity in the reconstructed neuron model.....</i>	63
2.3.5	<i>Results comparison with a physiological range of potassium conductances.....</i>	67
2.4	DISCUSSION	70
2.4.1	<i>Functional implications</i>	72
2.4.2	<i>Limitations / improvements.....</i>	73
2.4.3	<i>Future work.....</i>	74
2.4.4	<i>Conclusion.....</i>	75
CHAPTER 3	NEUROMODULATION OF CA3 SYNAPTIC TRANSMISSION EX VIVO.....	77
3.1	INTRODUCTION	77
3.2	METHODS	79
3.2.1	<i>Mouse lines</i>	79
3.2.2	<i>Preparation of brain slices</i>	79
3.2.3	<i>Electrophysiology.....</i>	79
3.2.4	<i>Electrical stimulation protocol</i>	81
3.2.5	<i>Dendritic integration stimulation protocol</i>	82
3.2.6	<i>Drug wash on</i>	82
3.2.7	<i>Statistical analysis.....</i>	82
3.2.8	<i>Optogenetic stimulation</i>	82
3.2.9	<i>Synaptic transmission analysis.....</i>	83
3.2.10	<i>Dendritic integration analysis.....</i>	84
3.3	RESULTS.....	86
3.3.1	<i>Cholinergic modulation of CA3 recurrent synaptic transmission</i>	86
3.3.2	<i>Noradrenergic modulation of CA3 recurrent synaptic transmission.....</i>	89
3.3.3	<i>Comparison between cholinergic and noradrenergic effect on CA3 synaptic transmission.....</i>	91
3.3.4	<i>Effect of endogenous acetylcholine release on CA3 excitatory synaptic inputs.....</i>	92
3.3.5	<i>Effect of endogenous acetylcholine release on CA3 inhibitory synaptic inputs</i>	100
3.3.6	<i>Preliminary experiments to study dendritic integration in CA3 neurons</i>	104

3.4	Discussion	109
3.4.1	<i>Limitations / improvements</i>	112
3.4.2	<i>Functional implications</i>	113
3.4.3	<i>Future studies</i>	113
CHAPTER 4	GENERAL DISCUSSION	115
APPENDIX A	121
APPENDIX B	129
REFERENCES	133

List of Figures

FIGURE 1-1: ENTORHINAL – HIPPOCAMPAL CIRCUITRY.	3
FIGURE 1-2: INPUTS TO DENDRITIC REGIONS OF A CA3 PYRAMIDAL NEURON.....	4
FIGURE 1-3: FEEDFORWARD AND FEEDBACK INHIBITION WITHIN CA3.....	5
FIGURE 1-4 INHIBITORY INPUTS TO CA3 PYRAMIDAL NEURONS.	6
FIGURE 1-5: STRUCTURAL AND FUNCTIONAL HETEROGENEITY ALONG CA3 PROXIMODISTAL AXIS.....	7
FIGURE 1-6 CIRCUITRY IMPORTANT FOR ENCODING AND RETRIEVAL.....	8
FIGURE 1-7 DENDRITIC SPIKES AND NONLINEAR INTEGRATION.	14
FIGURE 1-8 DISTRIBUTION OF MUSCARINIC RECEPTORS WITHIN CA3 CIRCUITRY.....	20
FIGURE 1-9 EFFECT OF ACETYLCHOLINE ON CA3 CIRCUITRY.	21
FIGURE 1-10 NORADRENERGIC MODULATION OF CA3 CIRCUITRY.	25
FIGURE 2-1: TWO-COMPARTMENT NEURON MODEL STRUCTURE	33
FIGURE 2-2: OPTIMISATION PROCESS.	34
FIGURE 2-3: MEASURES TAKEN FROM NONLINEAR INPUT-OUTPUT CURVE.....	38
FIGURE 2-4: EXAMPLE EPSPs RECORDED IN THE TWO-COMPARTMENT MODEL FROM DENDRITIC (LEFT) AND SOMATIC (RIGHT) COMPARTMENTS WITHOUT (UPPER) AND WITH (MIDDLE) ACETYLCHOLINE.....	39
FIGURE 2-5: NONLINEAR CURVES RECORDED IN THE TWO-COMPARTMENT MODEL FROM DENDRITE (LEFT) AND SOMA (RIGHT) FOR DIFFERENT POTASSIUM CHANNEL BLOCKS.	41
FIGURE 2-6: ACETYLCHOLINE REDUCED THE SYNAPTIC WEIGHT NEEDED TO REACH THE MAXIMUM SLOPE OF NONLINEARITY.....	42
FIGURE 2-7: MEMBRANE POTENTIAL AND INPUT RESISTANCE INCREASES CAUSED BY POTASSIUM CHANNEL INHIBITION CORRELATED WITH REDUCTIONS IN SYNAPTIC WEIGHT THRESHOLD AND NONLINEAR SLOPE	43
FIGURE 2-8: ACETYLCHOLINE MODULATED VOLTAGE- AND CALCIUM-DEPENDENT POTASSIUM CONDUCTANCE ACTIVATION CURVES.	44
FIGURE 2-9: A-TYPE POTASSIUM CHANNEL VOLTAGE-DEPENDENT STEADY-STATE KINETICS.	44
FIGURE 2-10: KA CHANNEL SUPPRESSION CAUSED A LARGE INCREASE IN AMPLITUDE AT THE MAXIMUM NONLINEAR SLOPE.....	45
FIGURE 2-11: ACETYLCHOLINE CAUSED A REDUCTION IN THE VOLTAGE AMPLITUDE AT THE MAXIMUM NONLINEAR SLOPE.....	46
FIGURE 2-12: CHANGE IN NONLINEAR SLOPE AS A FUNCTION OF THE CHANGE IN SYNAPTIC WEIGHT REQUIRED TO REACH THE SLOPE.	47
FIGURE 2-13: COMPARISON OF MODEL SIMULATIONS WITH EXPERIMENTAL DATA FROM MAKARA AND MAGEE (2013).....	48
FIGURE 2-14: VOLTAGE TRACE EXAMPLES FROM SYNAPTIC STIMULATION IN DIFFERENT DENDRITES IN THE SR AND SLM RECORDED IN THE DENDRITE AND SOMA..	49
FIGURE 2-15: DENDRITE DIAMETER AND POSITION IN TREE EFFECT ON DENDRITIC INPUT RESISTANCE.	50
FIGURE 2-16: HETEROGENEOUS NONLINEAR INTEGRATION THROUGHOUT THE DENDRITIC TREE.	51

FIGURE 2-17: A REDUCED DENDRITE DIAMETER IS ASSOCIATED WITH A HIGHER SLOPE OF NONLINEARITY AND A LOWER NUMBER OF SYNAPSES AT THE NONLINEAR THRESHOLD.	52
FIGURE 2-18: DENDRITIC INPUT RESISTANCE EXPLAINS NMDA SPIKE THRESHOLD DIFFERENCES ACROSS DENDRITIC TREE.....	52
FIGURE 2-19: VARIATION IN THE SLOPE OF NONLINEARITY ACROSS DENDRITIC BRANCHES.	53
FIGURE 2-20: MAXIMUM SLOPE OF NONLINEARITY CALCULATED FROM NORMALISED AMPLITUDES.	54
FIGURE 2-21: EPSP EXAMPLE TRACES FROM SYNAPTIC STIMULATION WITH CHOLINERGIC MODULATION IN DIFFERENT DENDRITES IN THE SR AND SLM.	55
FIGURE 2-22: EXTENT OF CHOLINERGIC MODULATION ACROSS ALL DENDRITES.....	56
FIGURE 2-23: IMPACT OF DENDRITE INITIAL INPUT RESISTANCE ON CHOLINERGIC EFFECT.	56
FIGURE 2-24: PROXIMAL SR DENDRITES WITH A LOW RESTING INPUT RESISTANCE REACH A SIGNIFICANTLY LOWER MAXIMUM NMDA VOLTAGE PEAK.....	57
FIGURE 2-25: CHANGE IN DENDRITIC RESTING INPUT RESISTANCE WITH ACETYLCHOLINE EXPLAINED THE EXTENT OF REDUCTION IN SYNAPSE NUMBER AT THE MAXIMUM SLOPE OF NONLINEARITY IN THE MAJORITY OF DENDRITES.	58
FIGURE 2-26: CHANGE IN MAXIMUM SLOPE OF NONLINEARITY WITH ACETYLCHOLINE ON DIFFERENT DENDRITE BRANCHES.....	59
FIGURE 2-27: COMPARISONS BETWEEN THE DISTAL DENDRITE GROUPS IN WHICH ACETYLCHOLINE CAUSED OPPOSING EFFECTS ON THE SLOPE OF NONLINEARITY.....	60
FIGURE 2-28: AVERAGED EPSP NMDA-COMPONENT TRACES BEFORE AND AFTER THE LARGEST JUMP IN AMPLITUDE (MAXIMUM NONLINEAR SLOPE) IN THE DISTAL DENDRITES WITH HIGH (LEFT) AND LOWER (RIGHT) INPUT RESISTANCE.	61
FIGURE 2-29: THE COMBINATION OF A HIGH KA PEAK CONDUCTANCE WITH A LOWER INPUT RESISTANCE IN THE DISTAL DENDRITES COULD EXPLAIN THE ACETYLCHOLINE-MEDIATED INCREASE IN THE NONLINEAR SLOPE.	63
FIGURE 2-30: CHANGE IN RESTING MEMBRANE POTENTIAL AND INPUT RESISTANCE IN DENDRITES UPON BLOCKING POTASSIUM CHANNELS.	64
FIGURE 2-31: CHANGE IN NMDA SPIKE THRESHOLD AND MAXIMUM SLOPE OF NONLINEARITY IN DENDRITES UPON BLOCKING POTASSIUM CHANNELS.	65
FIGURE 2-32: BIMODAL DISTRIBUTION OF SR DENDRITE NMDA SPIKE THRESHOLDS EXPLAINED BY DENDRITE DIAMETER.....	66
FIGURE 2-33: RELATIONSHIP BETWEEN CHANGE IN NMDA SPIKE THRESHOLD AND CHANGE IN MEMBRANE POTENTIAL (LEFT) AND DENDRITIC INPUT RESISTANCE (RIGHT).....	66
FIGURE 2-34: CHANGE IN NMDA SPIKE HALF-WIDTH AND AMPLITUDE IN DENDRITES UPON BLOCKING POTASSIUM CHANNELS.....	67
FIGURE 2-35: EFFECT OF TESTING A REALISTIC RANGE OF POTASSIUM CONDUCTANCES ON NMDA SPIKE PROPERTIES.	69
FIGURE 3-1: EXAMPLE CURRENT RECORDING WITH 200 MS VOLTAGE STEP WITH MEASUREMENTS TAKEN FOR CALCULATING SERIES AND INPUT RESISTANCE.	80
FIGURE 3-2: STIMULATING ELECTRODE POSITIONS IN HIPPOCAMPAL BRAIN SLICE.	81
FIGURE 3-3: CALCULATION OF PAIRED PULSE RATIO.....	83

FIGURE 3-4: CALCULATION OF EPSC 20-80% RISE TIME.	84
FIGURE 3-5: STIMULATION PROTOCOL AND MEASUREMENTS TAKEN FOR DENDRITIC INTEGRATION EXPERIMENTS. ..	85
FIGURE 3-6: 5 μ M CARBACHOL REDUCED CA3 RECURRENT EXCITATORY POST-SYNAPTIC CURRENT AMPLITUDE.	86
FIGURE 3-7: EFFECT OF CARBACHOL ON EPSC AMPLITUDE AND PAIRED PULSE RATIO.....	87
FIGURE 3-8: EFFECT OF CARBACHOL ON CA3 CELL EXCITABILITY.....	88
FIGURE 3-9: EFFECT ON EPSC AMPLITUDE WITH INCREASING CARBACHOL CONCENTRATIONS.....	88
FIGURE 3-10: IMPACT OF 20 μ M NORADRENALINE ON CA3 RECURRENT EXCITATORY TRANSMISSION.	89
FIGURE 3-11: EFFECT OF NORADRENALINE ON EPSC AMPLITUDE AND PAIRED PULSE RATIO	90
FIGURE 3-12: EFFECT OF NORADRENALINE ON RESTING MEMBRANE POTENTIAL AND INPUT RESISTANCE.	90
FIGURE 3-13: COMPARISON BETWEEN EFFECT OF CARBACHOL AND NORADRENALINE ON CA3 SYNAPTIC TRANSMISSION AND PYRAMIDAL CELL EXCITABILITY.....	91
FIGURE 3-14: OPTOGENETIC ACTIVATION OF NICOTINIC RECEPTORS ON OLM INTERNEURONS.....	92
FIGURE 3-15: APPLICATION OF DCG-IV REDUCED PERFORANT PATH BUT NOT RECURRENT EPSC AMPLITUDES.....	93
FIGURE 3-16: EFFECT OF OPTOGENETIC ACETYLCHOLINE RELEASE ON RECURRENT EPSC AMPLITUDES IN CA3 PYRAMIDAL NEURONS	94
FIGURE 3-17: EFFECT OF OPTOGENETIC ACETYLCHOLINE RELEASE ON PERFORANT PATH EPSC AMPLITUDES IN CA3 PYRAMIDAL NEURONS	95
FIGURE 3-18: COMPARISON BETWEEN BASELINE RECURRENT AND PERFORANT PATH EPSC PROPERTIES	96
FIGURE 3-19: AVERAGE CHANGE IN EPSC AMPLITUDE AND PAIRED PULSE RATIO WITH OPTOGENETIC ACETYLCHOLINE RELEASE.....	97
FIGURE 3-20: RELATIONSHIPS BETWEEN THE CHANGE IN EPSC WITH OPTOGENETIC ACTIVATION AND THE CHANGE IN PPR, RISE TIME AND MOUSE AGE	98
FIGURE 3-21: EFFECT OF ANIMAL AND GENDER ON THE CHANGE IN EPSC AMPLITUDE.	99
FIGURE 3-22: RELATIONSHIP BETWEEN CHANGE IN RECURRENT AND PERFORANT PATH EPSC AMPLITUDE WITH ENDOGENOUS ACETYLCHOLINE RELEASE.	100
FIGURE 3-23: CHANGE IN EPSC AMPLITUDES WITH ENDOGENOUS ACETYLCHOLINE RELEASE IN RELATION TO CHANGE IN SERIES RESISTANCE OVER EXPERIMENT.	100
FIGURE 3-24: EFFECT OF LIGHT-EVOKED ENDOGENOUS ACETYLCHOLINE RELEASE ON IPSCs RECORDED IN CA3 PYRAMIDAL NEURONS.	102
FIGURE 3-25: IMPACT OF CHANGE IN PAIRED PULSE RATIO, RISE TIME AND MOUSE AGE ON THE CHANGE IN IPSC AMPLITUDE WITH ENDOGENOUS ACETYLCHOLINE RELEASE.	103
FIGURE 3-26: EFFECT OF ANIMAL AND GENDER ON THE CHANGE IN IPSC AMPLITUDE.	103
FIGURE 3-27: EXAMPLE DATA FROM DENDRITIC INTEGRATION EXPERIMENT STIMULATING RECURRENT INPUTS.....	104
FIGURE 3-28: EXAMPLE DATA FROM DENDRITIC INTEGRATION EXPERIMENT STIMULATING PERFORANT PATH INPUTS.	105
FIGURE 3-29: COMPARISON OF BASELINE PROPERTIES BETWEEN RECURRENT- AND PERFORANT PATH-EVOKED RESPONSES.....	106

FIGURE 3-30: EFFECT OF ACETYLCHOLINE ON SUBTHRESHOLD RISING SLOPE AND COMPOUND EPSP DECAY	107
FIGURE 3-31: EFFECT OF ACETYLCHOLINE ON DENDRITIC INTEGRATION PROPERTIES IN RECURRENT AND PERFORANT PATH-EVOKED RESPONSES.	108
FIGURE 4-1: PRIOR AND UPDATED IMPACT OF ACETYLCHOLINE ON CA3 CIRCUITRY.....	117

List of Tables

TABLE 1: ION CHANNEL MAXIMAL CONDUCTANCE VALUES FOR THE TWO-COMPARTMENT AND RECONSTRUCTED MODELS.....	36
TABLE 2: MODEL AND SYNAPSE PARAMETERS.....	37
TABLE 3: PEAK CONDUCTANCE OPTIMISATION OUTPUTS FOR EACH POTASSIUM CONDUCTANCE.	68

Chapter 1 Introduction

1.1 Hippocampal/CA3 circuitry and function

1.1.1 Learning and memory

The ability to form and retrieve memories is essential for functioning in everyday life. Conditions such as dementia, in which memory is impaired, can severely affect a person's independence and quality of life. It's important for us to understand the biological mechanisms that underpin learning and memory so that we can understand how it is affected in disease and develop appropriate therapeutic interventions.

There are several types of memory as well as different stages of memory processing. Each type and stage occur via different mechanisms and in different regions throughout the brain. Memory can be categorised as either declarative or non-declarative (Squire and Zola-Morgan, 2015). Declarative memory is the main type processed by the hippocampus (Eichenbaum, 1999) and includes remembering facts and events (Tulving, 1972). On the other hand, non-declarative, or implicit, memory (Schacter, 1987) includes motor memory of learned skills and habits and is thought to be processed by the cerebellum, striatum, neocortex and the limbic system. Memory can also be classified by its different timespans. For example, short term memories last for seconds to minutes, whereas long term memories can be stored and recalled for years. Furthermore, the different stages of memory processing, as well as the different timespans (Norris, 2017), occur via distinct mechanisms in the brain. Encoding is the initial learning stage where a new memory is formed; consolidation of the memory enables long-term memory storage; memory retrieval allows the stored memory to be accessed at a later time.

The discovery of the hippocampus' role in memory processing arose with the case of patient H.M. (Scoville and Milner, 1957). Removal of the patient's medial temporal lobe, in the hope of curing their epilepsy, led to anterograde amnesia meaning the patient was incapable of forming new memories. They also suffered from temporally graded retrograde amnesia, in which they couldn't remember events one to two years before the surgery. However, their longer-term memory as well as non-declarative memory was intact. This suggested that the hippocampal region was important for the formation and initial storage of declarative memories but not required for the retrieval of consolidated long-term or non-declarative memories. This was the initial case study that led to further investigations into the hippocampus' involvement in memory processing.

As well as memory processing, another key function associated with the hippocampus is spatial processing and navigation. A novel cell type was discovered in the rat hippocampus in 1971 that provided evidence for the importance of the hippocampus in spatial processing and navigation (O'Keefe and Dostrovsky, 1971). These cells, termed place cells, expressed location-specific firing fields when animals moved around an arena, suggesting the hippocampus may convey a spatial map of an environment and possibly encode the "place" component of a memory. In fact, more recently, a direct link between place cells and spatial memory has been shown (Robinson et al., 2020). Specifically activating place cells encoding a reward area in a different location caused the mice to lick for the reward in this new location, suggesting that the mice' memory of the reward zone location was influenced through the manipulation of place cells.

1.1.2 Synaptic transmission and plasticity

Synapses allow neurons to communicate and form circuits. Neurotransmitters released from the pre-synapse bind to receptors on the post-synapse and either excite or inhibit the post-synaptic neuron. Excitatory synapses are mediated by glutamate signalling (Biscoe and Straughan, 1966; Nadler et al., 1976) and when an action potential arrives at the pre-synapse, glutamate is released into the synaptic cleft and binds to α -amino-3-hydroxy-5-methyl-4-isoxazolepropionic acid (AMPA) and N-methyl-D-aspartic acid (NMDA) receptors on the post-synaptic neuron (Traynelis et al., 2010). AMPARs are predominantly permeable to sodium and potassium ions and elicit fast responses in the post-synaptic neuron. On the other hand, NMDARs are permeable to both sodium and calcium and generate a slower rise and decay. NMDARs also contain a magnesium block within the channel and therefore require post-synaptic depolarisation to remove the magnesium block before ions can flow through (Nowak et al., 1984). Inhibitory neurons release the neurotransmitter γ -aminobutyric acid (GABA) (Biscoe and Straughan, 1966) which binds to GABAergic receptors on the post-synaptic neuron (Sigel and Steinmann, 2012). These channels are permeable to chloride ions which hyperpolarize the neuron, reducing the likelihood of the cell firing an action potential.

It is believed that synaptic plasticity is a mechanism as to how memories are encoded and stored within brain circuitry. Synaptic plasticity refers to the strengthening or weakening of synaptic connections between neurons and can have short-term or long-term effects. Long-term potentiation (LTP) is the most associated with memory formation and storage and was first evidenced in the hippocampal region in 1973 (Bliss and Lømo, 1973). Since then, multiple different types and induction protocols have been discovered in different neuron populations throughout the brain and plasticity can occur from pre- or post-synaptic mechanisms. When pre- and post-synaptic neurons are active close in time, the connection between them can strengthen, forming an association, which is thought to represent a learned memory (Hebb, 2005; Caporale and Dan, 2008).

1.1.3 Hippocampal/CA3 circuitry

As explained above, the hippocampus, located in the medial temporal lobe, is known for its importance in learning, memory, and navigation. It is divided into subregions and information transfer is mostly unidirectional via a tri-synaptic loop from the main input region, the entorhinal cortex (EC), to the dentate gyrus, (DG), CA3 and CA1 (Figure 1-1). From CA1, neurons project back to deep layers of the EC via the subiculum. Neurons in the EC also project directly to CA3 and CA1 bypassing the DG via the perforant path. Neurons in the EC also project directly to CA3 and CA1 bypassing the DG via the perforant path.

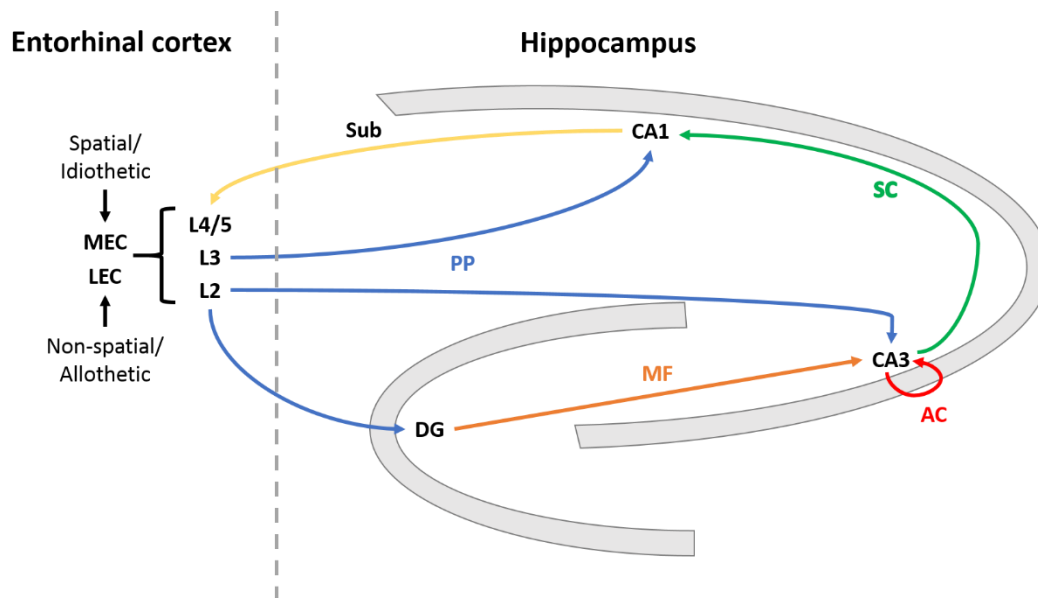


Figure 1-1: Entorhinal – hippocampal circuitry. Arrows represent direction of information transfer. MEC = medial entorhinal cortex, LEC = lateral entorhinal cortex, DG = dentate gyrus, MF = mossy fibres, AC = associational-commissural, SC = Schaffer collaterals, Sub = subiculum, PP = perforant path.

CA3 pyramidal neurons receive glutamatergic inputs from: the dentate gyrus (DG) granule cells via mossy fibres; cells in layer II of the entorhinal cortex (EC) via the perforant path; neighbouring CA3 neurons via recurrent collaterals, exclusive to the CA3 region (Figure 1-1). These inputs are received in segregated regions of the dendritic tree architecture (Figure 1-2). Mossy fibres from DG cells synapse close to the soma in the stratum lucidum (SL) layer where they form complex spines known as thorny excrescences. CA3 recurrent collaterals synapse in the stratum radiatum (SR) and oriens (SO) layers and EC neurons onto the most distal dendrites in the stratum lacunosum-moleculare (SLM).

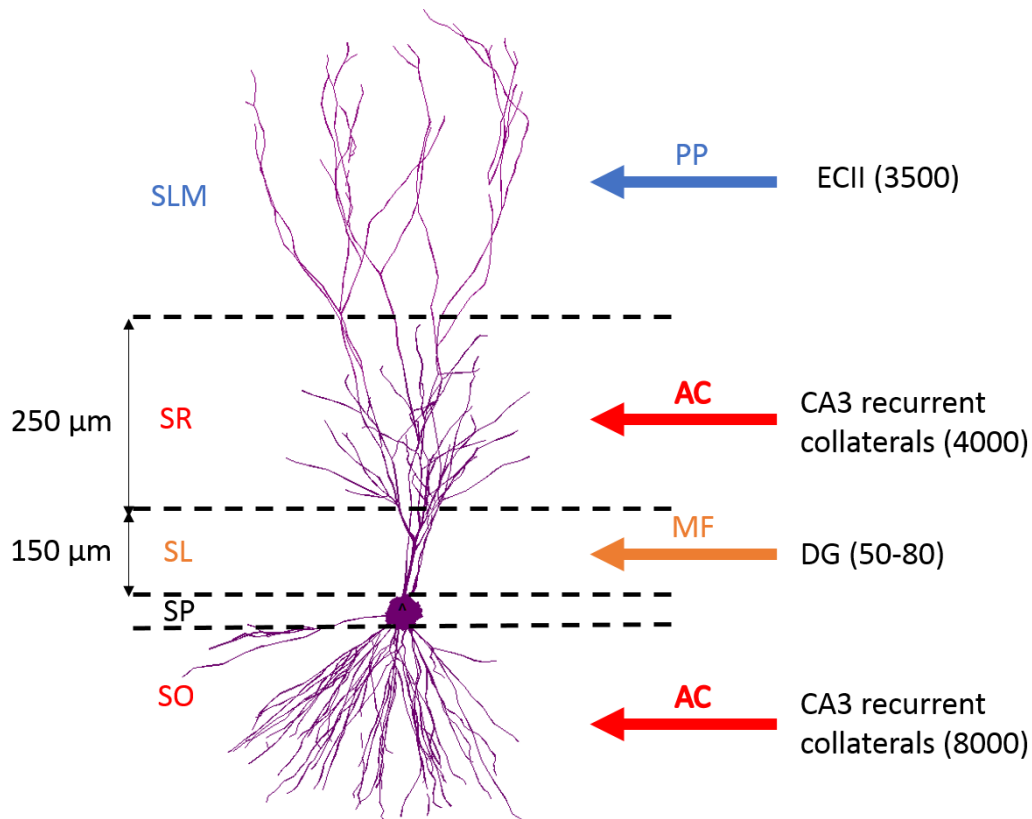
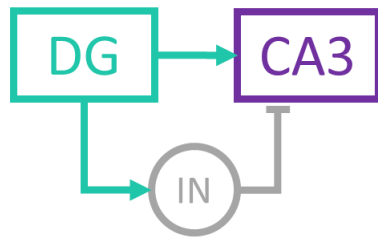


Figure 1-2: Inputs to dendritic regions of a CA3 pyramidal neuron. CA3 neuron reconstructed by and taken from (Hemond et al., 2008). Distances on left represent average size of dendritic regions but this can vary between cells. Numbers in brackets on right represent average synapse numbers from each pathway in rat CA3 (Treves and Rolls, 1992). SLM = stratum lacunosum-moleculare, SR = stratum radiatum, SL = stratum lucidum, SP = stratum pyramidale, SO = stratum oriens, PP = perforant path, AC = associational-commissural, MF = mossy fibres, ECII = entorhinal cortex layer 2, DG = dentate gyrus.

As well as excitatory inputs, CA3 pyramidal neurons also receive inputs from feedforward and feedback GABAergic inhibitory neurons (Figure 1-4). Feedback inhibitory neurons form a local feedback loop with CA3 pyramidal neurons (Figure 1-3) to regulate CA3 firing and prevent overexcitability within the recurrent network (Miles and Wong, 1987; Fortunato et al., 1996). Feedforward inhibition occurs when an interneuron is activated via stimulation of excitatory inputs from other brain regions, such as the dentate gyrus (Figure 1-3), and can reduce the impact of excitatory inputs to CA3 neurons and prevent CA3 neuron firing (Buzsáki, 1984).

Feedforward inhibition



Feedback inhibition



Figure 1-3: Feedforward and feedback inhibition within CA3. Granule cells in the dentate gyrus (DG) have direct excitatory connections (arrowhead) to CA3 pyramidal neurons and indirect projections via interneurons (IN), known as feedforward inhibition (left). CA3 neurons also project to local interneurons which can form a feedback loop, known as feedback inhibition (right).

There are a wide variety of interneuron subtypes in the CA3 region including: parvalbumin-positive (PV+) (Kosaka et al., 1987) and cholecystokinin-positive (CCK+) (Kosaka et al., 1985) basket cells which target the soma and proximal dendrites; PV+ axo-axonic cells that target the axon initial segment as well as interneurons that target the distal dendrites, such as somatostatin-positive (SST+) OLM interneurons (Kosaka et al., 1988; Gulyás et al., 1991, 1993; Miles et al., 1996). Figure 1-4 shows a few of the better studied interneuron types in the CA3 region. It displays where the majority of interneuron cell bodies are located as well as which region they target on the pyramidal neuron, however there is evidence of these cell types also being present in other layers as well as targeting different dendritic regions (Cox et al., 2008; Lasztóczy et al., 2011; Kohus et al., 2016).

As mentioned above, there are feedforward and feedback inhibitory circuits present within CA3. MFs have been shown to innervate four different types of interneurons in the CA3 region, with varying degrees of connectivity and strength (Szabadics and Soltesz, 2009), demonstrating an example of feedforward inhibition. These interneurons include fast-spiking and regular-spiking basket cells (PV+ and CCK+, respectively), as well as dendritically targeting ivy cells and septum-projecting interneurons in the stratum lucidum (Szabadics and Soltesz, 2009). As these interneuron types target CA3 dendrites as well as the perisomatic region, MF feedforward inhibition could be involved in preventing back-propagating action potentials or LTP occurring in the apical dendrites (Szabadics and Soltesz, 2009). Feedforward inhibition from the PP has not been well studied in the CA3 region.

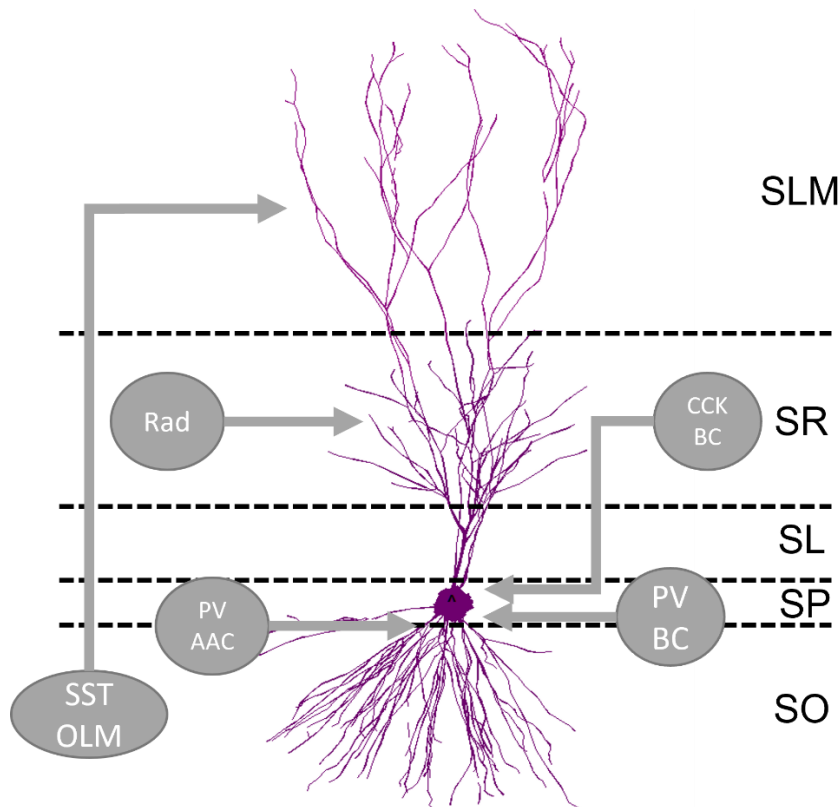


Figure 1-4 Inhibitory inputs to CA3 pyramidal neurons. CA3 neuron reconstructed by and taken from (Hemond et al., 2008). SST OLM = somatostatin oriens lacunosum-moleculare; PV AAC = parvalbumin-positive axo-axonic cells; Rad = radiatum interneuron; CCK BC = cholecystokinin-positive basket cell; PV BC = parvalbumin-positive basket cell.

Explained above is the general connectivity within the CA3 region; however, there are variations in these inputs along the proximodistal axis of CA3 (Figure 1-5). For example, MF input becomes weaker and EC input becomes stronger closer to CA2/1 region (Sun et al., 2017) and the CA3 region (CA3c) within the blades of the DG does not receive direct EC input. Furthermore, the most apparent recurrent activity is within mid CA3 (CA3b) (Sun et al., 2017). Recent evidence also shows there is a CA3 pyramidal neuron population without thorny excrescences that receives less MF input and exhibit different firing patterns *in vivo* under anaesthesia (Hunt et al., 2018). Inhibitory inputs are also different along the CA3 axis (Sun et al., 2017) with feedback inhibition getting progressively stronger towards CA3a and the inhibition/excitation ratio at its lowest in CA3b where there is the highest recurrent activity. To add to the complexity, there is a proximodistal bias in projections to CA1 (Witter, 2007). The MEC and distal CA3 project to proximal CA1 whereas the LEC and proximal CA3 project to distal CA1 (Figure 1-5). This proximodistal heterogeneity reflects the functional differences along this axis, explained in the section below.

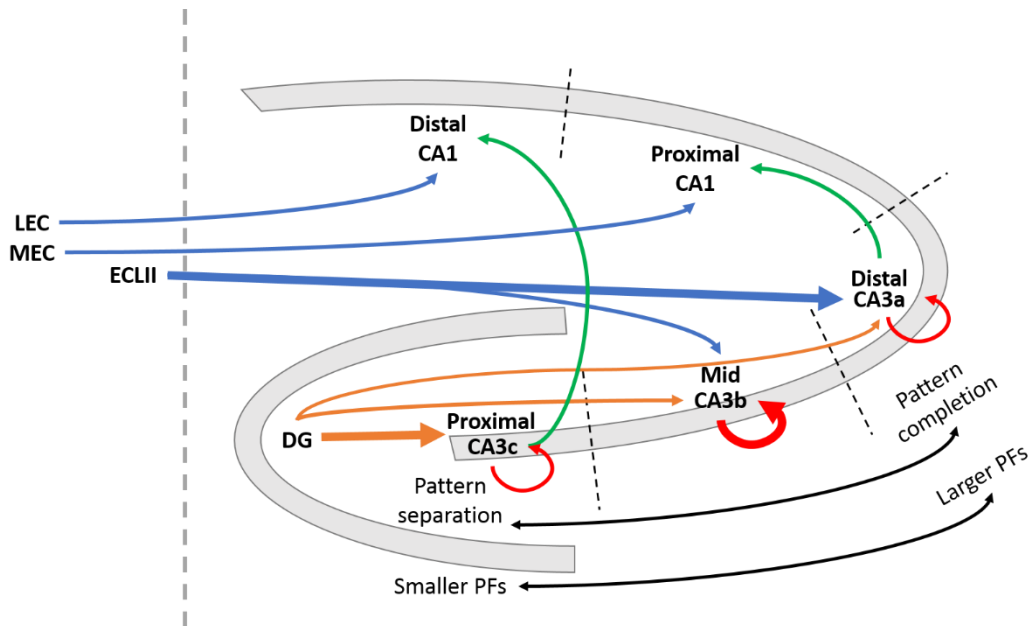


Figure 1-5: Structural and functional heterogeneity along CA3 proximodistal axis. Arrow thickness represents strength of inputs. LEC = lateral entorhinal cortex, MEC = medial entorhinal cortex, ECLII = entorhinal cortex layer 2, DG = dentate gyrus, PFs = place fields.

1.1.4 CA3 network and pattern completion

The CA3 region is specifically relevant for memory processing due to its recurrent circuitry, and this allows it to behave as an attractor network (Hopfield, 1982). The recurrent collaterals produce cell networks within CA3 that are thought to form stable ensembles important for memory storage, retrieval and pattern completion (Guzman et al., 2016). Recently, evidence for the stability and co-activity of CA3 neuron activity *in vivo* has been demonstrated using calcium imaging during animal exploration (Schoenfeld et al., 2021). This co-activity was stable across days and pairs of neurons that were active together maintained their correlated activity providing evidence for stable ensemble activity in the CA3 region.

It has been proposed that CA3 performs pattern completion whereas the DG performs pattern separation (Knierim and Neunuebel, 2016). Pattern completion can be defined as the retrieval of a memory from incomplete information whereas pattern separation is the ability to differentiate between similar, but not identical, information. The recurrent connectivity in the CA3 region is particularly suited to perform pattern completion as a degraded input can reactivate a group of CA3 neurons (or a memory engram) that has previously been formed via synaptic plasticity when the memory was initially established (Hopfield, 1982). This plasticity and therefore the formation of the memory is thought to be driven by MF input whereas the EC input is thought to instigate memory retrieval (Treves and Rolls, 1992) (Figure 1-6). The activity observed in the DG is suited to perform pattern separation as the MF-CA3 synapse

produces very powerful but sparse transmission meaning it could orthogonalize inputs to the CA3 network. There have been multiple studies that provide evidence for the distinct involvement of these two regions in pattern separation and completion (Treves and Rolls, 1992, 1994; O'Reilly and McClelland, 1994; Rolls, 2018, 1996, 2016; Nakazawa et al., 2002; Lee and Kesner, 2004a; Gold and Kesner, 2005; McHugh et al., 2007; Nakashiba et al., 2008; Neunuebel and Knierim, 2014; Posani et al., 2018).

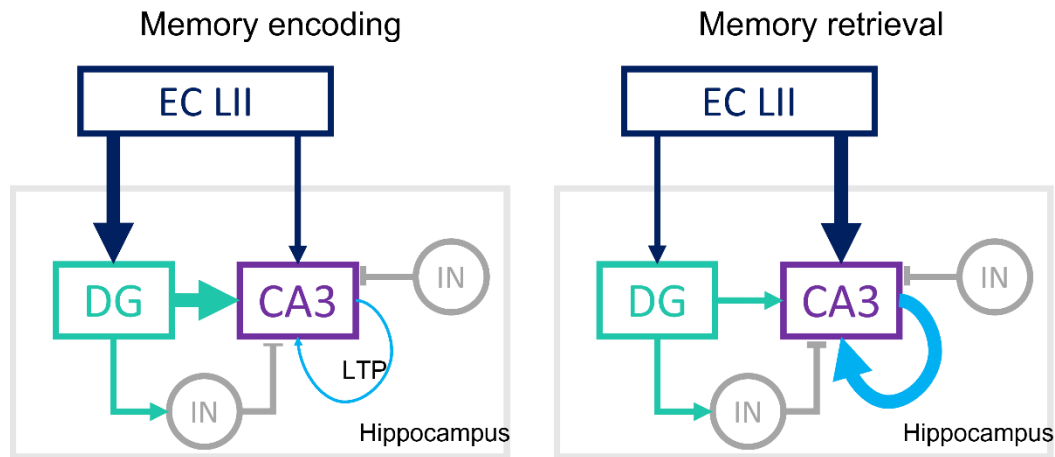


Figure 1-6 Circuitry important for encoding and retrieval. Size of the arrows represents the contribution to the memory processing stage. In the encoding phase, DG inputs to CA3 are promoted. In the retrieval phase, EC input and the recurrent connections are thought to be more important. EC LII = entorhinal cortex layer II; DG = dentate gyrus; IN = inhibitory interneuron. Figure is adapted from Hasselmo, (2006).

As explained in the previous section, there is heterogeneity within the CA3 region with cellular and synaptic properties varying along the proximodistal axis (Figure 1-5). It has been shown that distal CA3 (CA3a) has reduced MF input and higher EC input (Sun et al., 2017; Hunt et al., 2018) compared to proximal CA3 (CA3c) and that the mid CA3 region (CA3b) has the strongest recurrent activity and undergoes the most robust reactivation during retrieval (Sun et al., 2017). The distinct roles of the DG and CA3 in pattern separation and completion are also less distinctive than previously thought. Proximal CA3c has demonstrated evidence of pattern separation, which is not observed in distal CA3 (Marrone et al., 2014; Lee et al., 2015, 2020). In light of these results, the structural heterogeneity in CA3 seems to also reflect functional differences along the axis, with CA3c playing more of a role similar to the DG and mid/distal CA3 being more involved in pattern completion and memory retrieval (Figure 1-5).

The EC-CA3 synapse has been less well studied compared to the MF-CA3 input, but as indicated above it is thought to play a role in reactivating a CA3 ensemble and initiating the retrieval of a memory (Treves and Rolls, 1992) and there is evidence that impairing the EC-CA3 input impairs memory retrieval (Lee and Kesner, 2004b). Both the lateral and medial EC project to the hippocampus to convey distinct inputs. As grid cells with grid-like firing fields are present in the EC, the role of the EC has mostly been studied in terms of its contribution to spatial processing and navigation. Grid cells in the

medial EC have been shown to provide information regarding global cues within the environment and support path integration whereas the lateral EC is thought to offer information about local objects or landmarks (Figure 1-1) (Knierim et al., 2013; Neunuebel et al., 2013; Van Cauter et al., 2013; Kuruvilla and Ainge, 2017; Save and Sargolini, 2017; Tennant et al., 2018).

1.1.5 Interneuron function within CA3

Interneurons within CA3 also have specific functions. They have been shown to be important for pyramidal neuron phase firing coupled to oscillations (Hájos et al., 2004) as well as have a role in the generation of sharp-wave ripples (Viney et al., 2013; Schlingloff et al., 2014; Bazelot et al., 2016; Kohus et al., 2016; Rogers et al., 2021; Noguchi et al., 2022). Perisomatic interneurons exhibit the strongest phase coupling and are therefore thought to modulate the timing of pyramidal neuron firing (Hájos et al., 2004). Sharp-wave ripples are high frequency oscillations (150-250 Hz) that are thought to be initiated in CA3 (Csicsvari et al., 2000; Sasaki et al., 2018), occur during sleep and awake periods of immobility and are thought to be important for memory consolidation and retrieval (Lee and Wilson, 2002; Foster and Wilson, 2006; Diba and Buzsáki, 2007; Girardeau et al., 2009; Karlsson and Frank, 2009; Dupret et al., 2010; Ego-Stengel and Wilson, 2010; Jadhav et al., 2012). These different roles have also been shown to occur by specific interneuron subtypes. For example, PV+ axo-axonic interneurons stop firing during sharp waves and fire strongly around the theta peak (Viney et al., 2013) and a GABAergic input from the medial septum inhibiting these axo-axonic cells is thought to facilitate sharp wave ripples and promote memory consolidation (Viney et al., 2013; Joshi et al., 2017). In addition, CA3 PV+ basket cells have large dendritic arborizations in the SLM, fire preferentially during the same theta phase as pyramidal cells and are phase locked to gamma oscillations (Tukker et al., 2013). Furthermore, as well as certain interneuron subtypes having distinct roles, structural and functional diversity also exists within subtypes. For example, CCK+ interneurons within CA3 have been shown to have differences in dendritic and axonal distributions as well as protein expression and that these different subtypes phase lock to different phases of theta oscillations and undergo different firing rate changes during sharp wave ripples (Lasztóczy et al., 2011). Overall, the vast interneuron population play important roles in learning and memory processing within the hippocampus.

1.1.6 Role of CA3 region in learning and memory

Behavioural studies that have removed the CA3 region or blocked synaptic transmission have highlighted the importance of CA3 in learning and memory. These types of studies have shown CA3 to be important for object-place association tasks (Gilbert and Kesner, 2003), rapid contextual learning (Nakashiba et al., 2008), pattern completion (Nakashiba et al., 2008), spatial memory (Nakazawa et al., 2003), non-spatial recognition memory (Nakamura et al., 2013) and CA1 place cell tuning (Nakazawa et al., 2003; Nakashiba et al., 2008; Davoudi and Foster, 2019). In addition, a study that involved

manipulation of CA3 during memory tasks found it was important for spatial short-term, working and short-term episodic memory, but was not necessary for long-term memory (Song et al., 2018). Furthermore, optogenetic stimulation of CA3 neurons can restore impairments in short-term spatial memory in an Alzheimer's disease mouse model (Yang et al., 2021). These studies support the role of CA3 in memory associated tasks.

Cell bursting activity is thought to be important for establishing a memory as well as for recall (Treves and Rolls, 1992; Kaifosh and Losonczy, 2016). The bursting activity of CA3 neurons has been shown to be heterogeneous between different pyramidal cell types and morphologies as well as along the CA3 proximodistal axis (Hunt et al., 2018; Raus Balind et al., 2019; Ding et al., 2020). In Raus Balind et al., (2019) neurons with a high burst propensity only required proximal synaptic inputs to generate somatic bursts whereas regular spiking neurons required proximal and distal coincident input activity. The burst propensity of CA3 neurons has also been shown to correlate well with the extent of SLM dendritic branching (Ding et al., 2020) and to be greater in neurons without thorny excrescences that don't receive MF input (Hunt et al., 2018). These studies suggest that neurons with a high burst propensity could receive greater numbers of EC inputs which could be responsible for generating the burst activity (Ding et al., 2020). However, the intrinsic firing properties of CA3 neurons have also been shown to undergo plasticity and therefore the burst propensity of a neuron may not be a static property and can change depending on pre- and post-synaptic activity (Raus Balind et al., 2019; Soldado-Magraner et al., 2020). In light of these results, it is thought that CA3 neurons with high burst propensity, that can be initiated with recurrent input alone, are involved in memory engram reactivation, or pattern completion mechanisms as well as initiating sharp wave ripples (Hunt et al., 2018). On the other hand, CA3 neurons with lower burst propensity, that can be initiated with proximal and coincident distal inputs, could be involved in pattern separation (Raus Balind et al., 2019).

1.1.7 Plasticity mechanisms in CA3

As explained previously, LTP is a well-regarded mechanism of memory storage within the brain and therefore has been extensively studied within the hippocampus and CA3 network. At the PP-CA3 synapse, LTP has been demonstrated from both lateral and medial EC inputs (Do et al., 2002). One of the first studies to observe plasticity at the AC-CA3 recurrent synapse induced NMDAR-dependent LTP here with high frequency stimulation of the AC fibres (Zalutsky and Nicoll, 1990). Since then, different kinds of induction protocols that are thought to be more physiologically relevant have been investigated. One of these is known as spike timing-dependent plasticity (STDP) and is induced by activation of the pre- and post-synaptic neuron within a specific temporal window. In most cases, this temporal window of activation is asymmetric, meaning LTP is only induced if the post-synaptic neuron is activated after the pre-synaptic neuron (Debanne et al., 1998; Astori et al., 2010). However, at the AC-CA3 synapse, symmetric STDP has also been demonstrated in which plasticity can be induced with

pre- and post-synaptic spiking that occurs close in time, regardless of the activation order. When this asymmetric STDP rule is used in an auto-associative network model it improves CA3's capacity for memory storage and retrieval (Mishra et al., 2016).

Other mechanisms to induce plasticity that have been discovered in CA3 neurons include associative and heterosynaptic plasticity. Associative plasticity occurs when the coincident activity of different synaptic inputs causes plasticity in one of the pathways. Heterosynaptic plasticity is plasticity that occurs at a synapse that was not activated during the induction protocol. Associative plasticity has been shown to occur at AC-CA3 and PP-CA3 synapses when combined with MF stimulation (McMahon and Barrionuevo, 2002; Kobayashi and Poo, 2004; Hunt et al., 2013). Additionally, paired subthreshold MF activation and AC stimulation can cause timing-dependent plasticity at AC synapses (Brandalise and Gerber, 2014). An example of heterosynaptic plasticity was shown when burst stimulation of MFs generated NMDAR-dependent LTP at PP-CA3 synapses without any PP stimulation (Tsukamoto et al., 2003). When and how these different types of plasticity occur in a behaving animal and during memory processing is important to understand. It is currently hypothesised that plasticity at the CA3 recurrent synapse is important for memory storage and that this encoding could be driven by the MF input, as is demonstrated in these studies.

1.1.8 Place cells in CA3

The presence of place cells within CA3 also implies a function for CA3 in spatial navigation and spatial processing. Place cells have mostly been studied in rodents in hippocampal CA1 but there are several studies that have explored CA3 place cells. They seem to be less prevalent in CA3 compared to CA1 (Mizuseki et al., 2012) and as CA3 and CA1 neurons differ in morphology and synaptic inputs, differences in place cell properties could be expected. Compared to CA1 place fields, CA3 place fields: have greater stability and compactness (Mizuseki et al., 2012), are more coherent population-wise after landmarks are rotated (Lee et al., 2004) and are less affected by novelty in object-in-place recognition tasks (Larkin et al., 2014). CA3 place cells have been shown to be more affected with ageing than CA1 place cells (Wilson et al., 2005) and in line with this, in a rat model of Alzheimer's disease CA3 but not CA1 place cells had significantly reduced spatial fidelity (Galloway et al., 2018). These studies suggest the CA3 region to be of particular consideration in ageing and dementia pathology and therefore highlight the importance of understanding its circuitry and function in memory processing. Place cells have also been compared and recorded over trials and days with 2-photon imaging where it was found that CA3 place cells emerge more gradually and are more stable over trials and days, compared to CA1 place cells (Dong et al., 2021). These studies that demonstrate a high stability of CA3 place fields reinforce the hypothesis for CA3's role in pattern completion and in forming stable memory ensembles. Unsurprisingly, there are also differences in place cell firing along the proximodistal CA3 axis with cells exhibiting smaller and sharper place fields closer to the DG compared to distal CA3 and distal

CA3 place cells being more similar between different environments (Lu et al., 2015) (Figure 1-5). This again supports the idea that distal CA3 is more likely involved in pattern completion in comparison to proximal CA3.

1.2 Dendritic integration

Dendritic trees exhibit diverse and complex structures across different neuron types. The complexity of dendritic branching in combination with different ion channel densities influence how synaptic inputs are processed, integrated, and propagated. To understand how inputs are integrated, it is first important to understand how current flows within dendritic trees. Dendritic activity was initially studied, and is still widely studied, using computational models due to the challenge of recording directly from dendrites. Neuronal cable theory was first developed by Wilfrid Rall in the 1950-60's and underpins our understanding of current flow within dendrites (Rall, 1962a, 1962b, 1967; Rall et al., 1967; Segev et al., 1995). The passive electrical cable properties of dendrites are modelled using three key parameters: axial resistance, membrane capacitance and membrane conductance. As axial resistance increases with length and membrane capacitance increases with membrane area, distal synaptic inputs undergo more filtering as the response propagates to the soma, compared to more proximal inputs (Rall, 1967; Rall et al., 1967; Magee, 2000). As a result of this filtering, inputs from distal synapses would produce a reduced amplitude at the soma compared to more proximal inputs. However, to compensate for this filtering effect it has been shown that CA1 distal dendrites have a higher dendritic EPSP amplitude, driven by a high synaptic conductance, which normalises the amplitude of single EPSPs at the soma regardless of input location within the dendritic tree (Magee and Cook, 2000). Additionally, dendritic filtering increases the time window as to which inputs can overlap and therefore the slower propagation results in greater temporal summation from distal dendrites producing a broader EPSP at the soma (Rall, 1967; Rall et al., 1967; Magee, 2000).

It was initially thought that dendrites were passive components of a neuron and that their role was to receive and relay information from other neurons to the soma. One of the first studies recording from CA1 dendrites (Wong et al., 1979) discovered that dendrites can have active properties and generate “action potentials”, from current injection or synaptic stimulation. This ability of dendrites to generate spikes means that inputs are not always linearly summed and can lead to nonlinear integration of inputs (Polsky et al., 2004) (Figure 1-7B) which in turn can amplify certain inputs, help tune the neuron to receive specific information and facilitate synaptic plasticity (Holthoff et al., 2006). Complex dendritic morphology combined with varying ion channel densities and different synaptic input patterns creates diverse dendritic events in distinct branches. These events can either stay confined to single branches (Golding et al., 2002) or generate larger global events and propagate to the soma (Larkum et al., 2009).

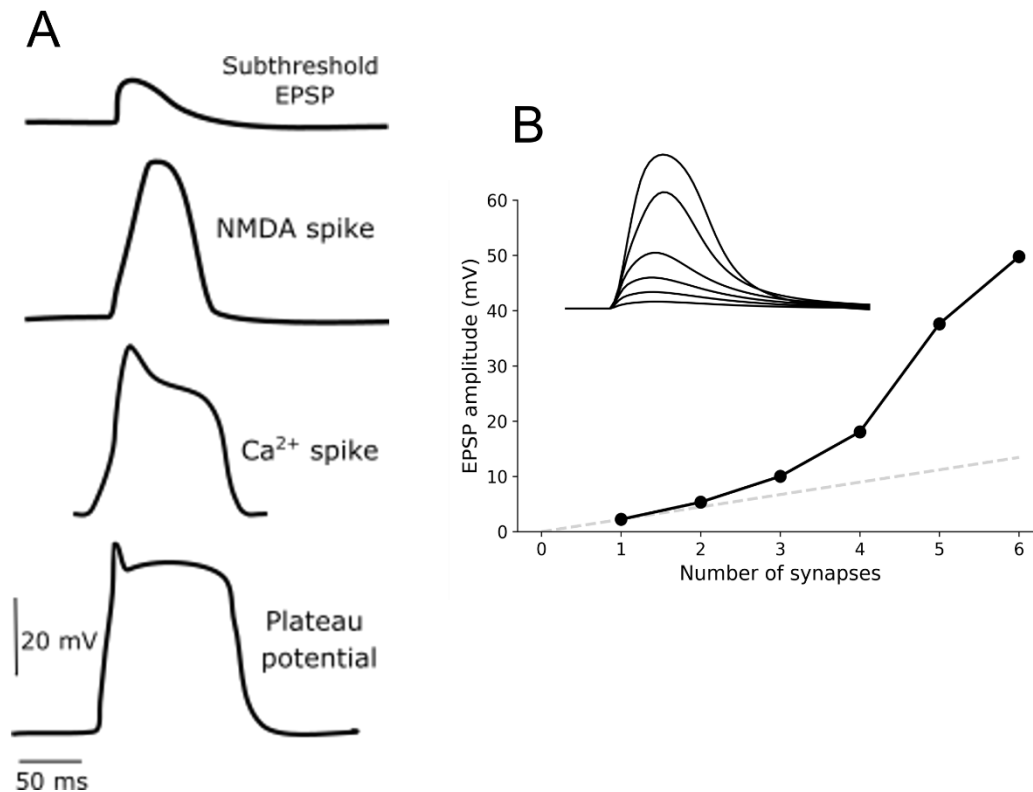


Figure 1-7 Dendritic spikes and nonlinear integration. A = Example waveforms of dendritic spikes. B = Example of supra-linear integration, measured as the peaks in the example traces (inset). Grey dashed line represents linear summation of the inputs. Adapted from Antic et al., (2010).

Local dendritic events that are confined to a single branch are often referred to as dendritic spikes and occur when clustered inputs are stimulated close in time. They have been shown to be mediated by sodium, calcium and/or NMDARs (Figure 1-7A). Sodium spikes are the most similar to an action potential in that they elicit a fast and steep rising and falling phase whereas calcium and NMDA spikes have a slower time course (Figure 1-7A). Dendritic spikes are difficult to record from directly as it requires patching onto dendrites, but they can also be measured using 2-photon calcium imaging to observe calcium fluctuations in the dendrites, signifying a calcium or NMDA driven event. It has been suggested that ~10 clustered inputs or ~20 dispersed inputs along a longer dendrite section is sufficient to generate an NMDA spike (Major et al., 2008).

1.2.1 Dendritic integration in CA3 neurons

As described above, there are three major excitatory inputs to CA3 neurons (Figure 1-2): the dentate gyrus, entorhinal cortex and other CA3 neurons that each synapse onto different regions of the dendritic tree. The extensive branching morphology of CA3 neurons provides a favourable condition for regenerative dendritic activity to occur. The initial evidence for active dendritic properties in CA3 pyramidal neurons was discovered in Kim et al., (2012). They recorded from dendrites and found a high sodium (Na⁺) to potassium (K⁺) conductance density ratio in the distal dendrites that allowed local

sodium spikes to arise upon local activation. Following this, supra-linear integration of synaptic inputs mediated by NMDARs was detected in CA3 basal and apical dendrites (Makara and Magee, 2013). More recently, different forms of dendritic calcium spikes have been studied in CA3 neurons as well as their ability to cause complex bursts at the soma (Brandalise et al., 2016, 2021; Weber et al., 2016; Raus Balind et al., 2019; Magó et al., 2021). Nonlinear integration of inputs have also been suggested to enhance the capacity of the CA3 network to store and retrieve large numbers of memories (Kaifosh and Losonczy, 2016).

1.2.2 Plateau potentials in the hippocampus

As well as single branch integration, previous studies have looked at how inputs sum between branches and between dendritic regions to generate larger global dendritic events, known as plateau potentials (Figure 1-7A). Plateau potentials are long lasting dendritic depolarisations produced from calcium and NMDA spikes. In CA1 neurons, it has been shown that coincident activation of the distal (EC) and proximal (CA3) inputs generates a plateau potential (Golding et al., 2002; Takahashi and Magee, 2009) which underlies the formation of new place fields (Bittner et al., 2015). It was also shown with 2-photon calcium imaging that regenerative dendritic events occur during place cell firing in CA1 (Sheffield et al., 2017) and were most prevalent prior to place cell spiking and during the initial place field traversal. This integration has also been studied in brain slices *ex vivo* in CA3 neurons (Raus Balind et al., 2019).

1.2.3 Dendritic integration and plasticity

Synaptic inputs that activate NMDA or calcium spikes lead to post-synaptic calcium influx which can induce plasticity and therefore these dendritic events could be an important component of memory processing. Dendritic spikes also depolarise sections of dendrite and therefore provide an alternative mechanism for STDP that doesn't require a post-synaptic back-propagating action potential (Golding et al., 2002). NMDA spikes have been shown to be required for associative timing-dependent plasticity in CA3 neurons (Brandalise et al., 2016). Subthreshold activity evoked by mossy fibres can induce plasticity at CA3 recurrent synapses with repetitive pairing of a CA3-CA3 synapse followed by a subthreshold mossy fibre response (Brandalise and Gerber, 2014). These inputs can lead to LTP *ex vivo* and are modulated by NMDAR-mediated current at CA3 recurrent synapses. In a subsequent study, it was shown that these dendritic NMDA spikes were necessary to induce this associative LTP (Brandalise et al., 2016).

The presence of NMDA spikes has also been investigated in *in vivo* experiments. Experiments performed in 1998 were one of the first to show evidence for dendritic spikes *in vivo* in CA1 neurons (Kamondi et al., 1998). Whole cell recordings of pyramidal cells in the somatosensory cortex have shown that whisker stimulation leads to NMDAR-mediated plateau potentials that induce LTP without

somatic spiking, providing evidence for sensory-driven synaptic LTP mediated by dendritic mechanisms (Larkum and Zhu, 2002; Gambino et al., 2014). More recently in CA1, plateau potentials have been shown to induce a type of plasticity known as behavioural time-scale plasticity, which stabilises place fields (Bittner et al., 2017). Detecting dendritic spikes or plateau potentials in CA3 neurons *in vivo* has not yet been achieved but it will be important to understand under what circumstances they are generated, their mechanisms of action and their role in plasticity and memory processing.

1.3 Neuromodulation in the hippocampus

Neuromodulators are released during particular behavioural states, such as during rewarding or novel experiences, and can modulate cell excitability, synaptic transmission and plasticity. The main focus of this thesis is on acetylcholine, but I also investigated noradrenergic modulation of CA3 recurrent circuitry and so noradrenaline is also briefly discussed in this section. Both of these neuromodulators are released during salient experiences (Hervé-Minvielle and Sara, 1995; Vankov et al., 1995; Ma et al., 2020) and it's been suggested that they play a role in uncertainty with acetylcholine signalling expected uncertainty and noradrenaline signalling unexpected uncertainty (Yu and Dayan, 2005).

1.3.1 Acetylcholine in learning and memory

Acetylcholine's importance in learning and memory is well established. It has been shown that blocking muscarinic receptors in the hippocampus impairs memory encoding (Blokland et al., 1992; Rogers and Kesner, 2003; Douchamps et al., 2013; Mitsushima et al., 2013) but doesn't affect memory recall (Ghoneim and Mewaldt, 1977; Rogers and Kesner, 2003, 2004; Douchamps et al., 2013) whereas inhibiting the cholinesterase enzyme and thereby increasing the presence of acetylcholine enhances memory encoding in Alzheimer's patients (Rogers and Friedhoff, 1996; Giacobini, 2000). Furthermore, lesioning cholinergic neurons in the medial septum and thus disrupting the cholinergic input to the hippocampus has been shown to impair object location memory (Cai et al., 2012) and spatial memory (Berger-Sweeney et al., 2001) as well as novel place field formation/remapping (Ikonen et al., 2002). More recently, studies using optogenetics to activate cholinergic neurons *in vivo* have highlighted their importance in spatial representations (Mamad et al., 2015) and memory task performance (Jarzebowski et al., 2021; Zhang et al., 2021).

It is thought that high levels of acetylcholine in CA3 (e.g. during exploration), combined with mossy fibre input, facilitate pattern separation and memory encoding, whereas low levels of acetylcholine (e.g. during slow wave sleep) are important for memory retrieval or consolidation (Hasselmo et al., 1995; Meeter et al., 2004; Hasselmo, 2006; Hummos et al., 2014). Higher levels of acetylcholine suppress the recurrent activity within CA3 (Hasselmo et al., 1995; Vogt and Regehr, 2001; Kremin and Hasselmo, 2007) which is thought to prevent previously stored memories affecting the memory encoding phase. In a spiking network model of CA3, simulation of acetylcholine by increasing cell excitability and reducing AC-CA3 synaptic strength increases the speed at which memory ensembles can form and allows stable overlapping ensembles to be established (Prince et al., 2021).

1.3.2 Acetylcholine in the hippocampus

Acetylcholine is a neuromodulator synthesised from acetyl coenzyme A and by choline acetyltransferase. Acetylcholine is released during novel experiences (Acquas et al., 1996; Miranda et

al., 2000; Giovannini et al., 2001; Caldenhove et al., 2017) such as during learning and active exploration (Ma et al., 2020). The main cholinergic input to the hippocampus is from neurons in the medial septum which project via the fimbria-fornix pathway (Lewis et al., 1967). The fibres terminate in all areas and layers of the hippocampus with the highest density in CA3 on either side of the pyramidal cell layer in the SL and SO (Grybko et al., 2011). It was originally believed that acetylcholine was released into the hippocampus via volume transmission as Umbriaco et al., (1995) found that 93% of cholinergic axons were not directly associated with specific cell contacts and therefore the communication was non-synaptic. However, more recently it was suggested that cholinergic axons in the hippocampus do form synapses with excitatory and inhibitory neurons (Takács et al., 2018). Additionally, acetylcholine release dynamics can vary depending on the task being performed (Teles-Grilo Ruivo et al., 2017). It was demonstrated that during arousal acetylcholine is released tonically whereas during a reward-based memory task, there is additional phasic release (Teles-Grilo Ruivo et al., 2017). These results make the case that acetylcholine can be released into the hippocampus by both volume and synaptic transmission as well as via both phasic and tonic release depending on the specific circumstances (Disney and Higley, 2020).

Cholinergic neurons in the medial septum fire at a relatively low rate (<10 Hz) (Markram and Segal, 1990; Sotty et al., 2003; Simon et al., 2006; Ma et al., 2020) with peak firing rates between 7.5-15 Hz during theta-associated behaviours (Ma et al., 2020). Theta waves are 4-12 Hz oscillations observed in the hippocampal local field potential (LFP) that occur during exploration (Vanderwolf, 1969) and REM sleep (Jouvet, 1969). The glutamatergic and GABAergic projections from the medial septum are thought to initiate and control these hippocampal theta oscillations (Borhegyi et al., 2004; Kaifosh et al., 2013; Fuhrmann et al., 2015) whereas even though cholinergic neuron activity increases during theta, their activity is not phase-coupled to theta oscillations (Zhang et al., 2010). Furthermore, medial septal cholinergic neurons are almost silent during non-theta periods such as slow-wave sleep (Ma et al., 2020). This cholinergic neuron activity correlates with the high levels of acetylcholine measured in the hippocampus during theta-associated behaviours (Zhang et al., 2010; Vandecasteele et al., 2014; Ma et al., 2020). In CA1, the highest levels of acetylcholine release have been observed around the pyramidal layer (Zhang et al., 2010), which reflects the highest density of cholinergic fibres (Aznavour et al., 2002; Grybko et al., 2011). During non-theta-associated behaviours, such as awake rest, the optogenetic activation of cholinergic neurons can suppress sharp-wave ripples (Vandecasteele et al., 2014; Ma et al., 2020) and impair memory processing (Jarzebowski et al., 2021; Zhang et al., 2021). Additionally, optogenetic silencing of cholinergic neurons prevents the termination of slow-wave sleep (Shi et al., 2015).

1.3.2.1 Muscarinic receptors

When released, acetylcholine binds to and activates muscarinic and nicotinic receptors. These receptors are further categorised into subtypes that produce varying effects and are present in different densities on pre- and post-synaptic compartments of different cell types throughout the hippocampus. Muscarinic receptors (mAChRs) are metabotropic receptors coupled to G-proteins (Eglen, 2006). There are five subtypes of muscarinic receptors (M1-M5). M1, M3 and M5 are coupled to Gq proteins whereas M2 and M4 are coupled to Gi/o proteins. Gq protein activates phospholipase C (PLC) which increases inositol trisphosphate (IP₃) and diacylglycerol (DAG) leading to calcium influx and increased neuronal excitability. On the other hand, Gi/o activation inhibits cyclic-adenosine monophosphate (cAMP) production leading to reduced cell activity. Therefore, M1, M3 and M5 activation increase cell excitability whereas M2 and M4 have an inhibitory effect.

M1 receptors are the most prevalent subtype in the hippocampus and are present on the soma and dendrites of CA3 pyramidal neurons (Levey et al., 1995; Dasari and Gullledge, 2011), DG granule cells and MF axons (Martinello et al., 2015) as well as PV-positive interneurons (Yi et al., 2014). As they activate the Gq signalling pathway, this increases the excitability of neurons and can increase the frequency of bursting and lead to persistent firing (Jochems and Yoshida, 2013). M1 activation has been shown to inhibit several potassium channels which also contributes to increased cell excitability. In CA3 neurons, M1 activation reduces the M-type potassium current (K_m) (Sun and Kapur, 2012). In CA1 neurons, M1 activation has also been shown to block the A-type (K_a) (Losonczy et al., 2008), G-protein coupled inward rectifier (GIRK) (Sohn et al., 2007) and small-conductance calcium-activated (SK) potassium currents (Giessel and Sabatini, 2010). Inhibition of the SK current has been shown to increase calcium influx and dendritic excitability and can facilitate LTP (Buchanan et al., 2010; Tigaret et al., 2016, 2018).

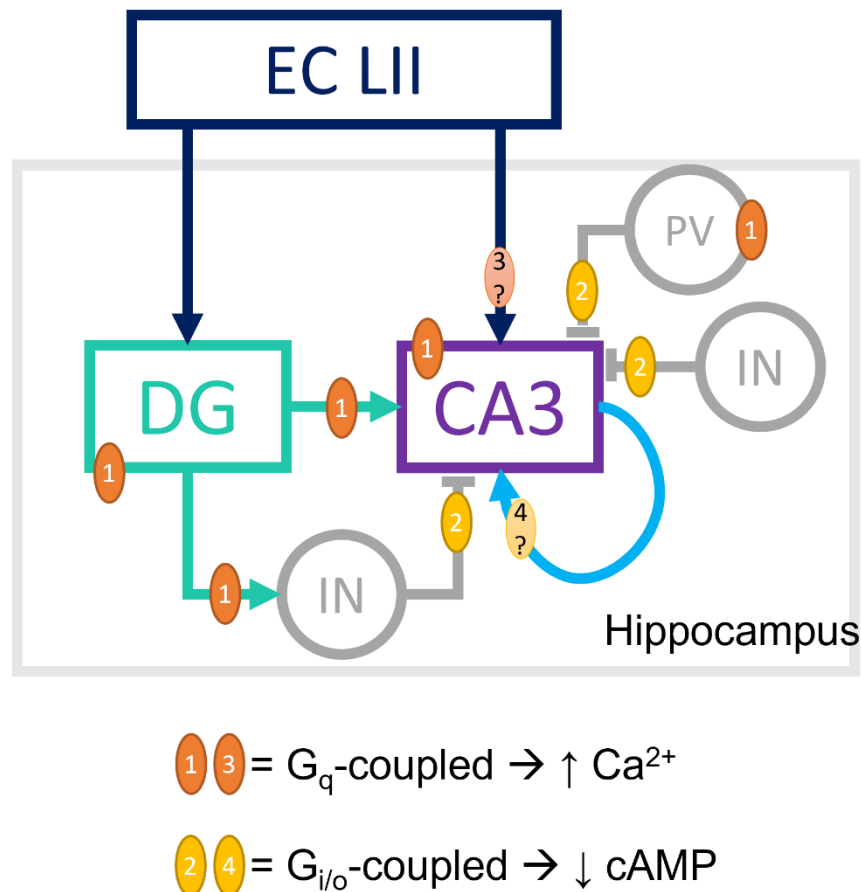


Figure 1-8 Distribution of muscarinic receptors within CA3 circuitry. Numbers correspond to M1-4 receptor subtypes. Orange = receptors coupled to G_q proteins, yellow = receptors coupled to $G_{i/o}$ proteins. M1 receptors are expressed on DG cells and axons, CA3 pyramidal neurons and parvalbumin-positive interneurons. M2 receptors are expressed on interneuron axons. The expression profile of M3 and M4 receptors has not been confirmed within CA3 but are possibly expressed on EC axons and CA3 recurrent axons, respectively. DG = dentate gyrus, IN = interneuron, PV = parvalbumin, EC LII = entorhinal cortex layer 2.

M2 receptors are also expressed in the hippocampus but on interneurons in the SL and PV-positive interneuron axons (Levey et al., 1995; Hájos et al., 1998). M2 muscarinic activation inhibits vesicle release in PV-positive and axo-axonic interneurons thereby reducing inhibitory synaptic currents in CA3 pyramidal neurons (Szabó et al., 2010). M4 receptors are present on CA3 glutamatergic terminals that project to the CA1 region (Dasari and Gullledge, 2011) which again act by inhibiting synaptic release. It is therefore thought that M4 receptors are also the subtype on CA3 recurrent synapses responsible for the reduced excitatory transmission seen when applying a cholinergic agonist, carbachol (Vogt and Regehr, 2001; Kremin and Hasselmo, 2007), however there is no evidence of M4 receptor expression within the CA3 SR layer (Levey et al., 1995). The distribution and action of M3 receptors in the CA3 region is the least well known. Recently it was shown that pre-synaptic M3 receptor activation was responsible for reducing excitatory and feedforward inhibitory transmission in the EC-CA1 pathway (Palacios-Filardo et al., 2021) and therefore this receptor subtype could also modulate EC-CA3 synapses (Kremin and Hasselmo, 2007).

Synaptic transmission can be altered by the presence of neuromodulators. It was suggested that acetylcholine can alter excitatory transmission, and therefore memory processing in CA3 as shown in Figure 1-9 (Hasselmo, 1999, 2006). In support of this theory, it has been demonstrated in electrophysiological experiments in brain slices, that carbachol (a cholinergic agonist) reduces the excitatory synaptic transmission between recurrent CA3-CA3 neurons as well as inputs from the entorhinal cortex (EC) (Kremin and Hasselmo, 2007) (Figure 1-9). However, these results show that different doses of carbachol affect the two pathways differently and therefore suggest the dominant influence on CA3 neurons can shift between EC input and recurrent collateral input. It has also been shown that carbachol increases the net excitatory input from the dentate gyrus (DG) into CA3 by reducing DG-CA3 feedforward inhibition (Prince et al., 2021) (Figure 1-9). These results also complement the proposed mechanism of action of acetylcholine from Hasselmo (1999, 2006) (Figure 1-9), where it was suggested that inputs to the hippocampus are amplified by acetylcholine to promote the incoming information to enable the storage of new memories. In contrast, CA3-CA3 connections are reduced to prevent the retrieval of previously stored memories (Vogt and Regehr, 2001; Kremin and Hasselmo, 2007) (Figure 1-9). The experiments presented here were performed by application of a cholinergic agonist. The effect of endogenous acetylcholine on CA3 synaptic transmission, as can now be performed using optogenetics, has not yet been determined but is one of the aims of this thesis, outlined below.

Acetylcholine can also modulate inhibitory inputs to CA3 pyramidal neurons (Figure 1-9) via pre-synaptic M2 receptor activation in PV-positive interneurons (Szabó et al., 2010). 5 μ M carbachol reduced CA3 inhibitory post-synaptic currents (IPSCs) and short-term depression from PV positive interneurons by approximately 70-75%. It also reduced IPSCs from CCK regular spiking basket cells by ~94%, however this occurred via production of endocannabinoids, as opposed to M2 receptor activation (Szabó et al., 2010). This reduction in inhibitory input upon acetylcholine application could increase CA3 excitability to facilitate plasticity and memory encoding. As explained previously, there are a large variety of interneuron subtypes, known and unknown, within the CA3 region that can be challenging to distinguish between and therefore cholinergic modulation of specific interneuron types could be more complex.

1.3.4 Cholinergic modulation of dendritic integration and plasticity

Acetylcholine has previously been shown to modulate synaptic plasticity within the hippocampus. M1 receptor activation in CA1 neurons can enhance back-propagating action potentials (Tsubokawa and Ross, 1997; Nakamura et al., 2000) and cause an IP3-dependent release of calcium from the endoplasmic reticulum (Nakamura et al., 2000) which, with appropriate synaptic stimulation, can lead to LTP (Fernández De Sevilla and Buño, 2010; Dennis et al., 2016). Cholinergic stimulation at the peak of theta oscillation has also been shown to induce LTP (Huerta and Lisman, 1995). However,

acetylcholine has also been shown to induce depression at SC-CA1 synapses, rather than potentiation, (Brzosko et al., 2017), suggesting the particular dose and plasticity induction protocol are important.

In CA3 neurons, M2 receptors were shown to modulate plasticity differently at different synapses (Zheng et al., 2012). At AC-CA3 synapses, M2 receptor activation supported short-term and long-term potentiation, whereas it had the opposite effect at MF-CA3 synapses, suggesting that activation of M2 receptors can bias plasticity towards a particular synaptic input in CA3 neurons. It is thought that this M2 receptor-induced plasticity used a different mechanism at each synapse. At the AC-CA3 synapse it was thought that M2Rs on nearby interneurons were activated that might reduce GABA release and allow more NMDAR activation on the pyramidal neuron. Alternatively, in MFs, it was thought that M2 activation reduces adenylyl cyclase activity and this prevents MF-CA3 LTP (Zheng et al., 2012).

Acetylcholine blocks several potassium channels via muscarinic receptor activation (K_A (Hoffman and Johnston, 1998; Losonczy et al., 2008), GIRK (Sohn et al., 2007) and SK (Buchanan et al., 2010; Giessel and Sabatini, 2010; Tigaret et al., 2018)), that are known to modulate NMDA spikes (Cai et al., 2004; Makara and Magee, 2013; Malik and Johnston, 2017). Blocking A-type potassium channels (K_A) has been shown to increase the amplitude of dendritic plateau potentials in CA1 neurons whereas blocking SK channels increased their duration (Cai et al., 2004). In addition, blocking GIRK channels has been shown to prolong NMDA spikes in CA3 neurons (Makara and Magee, 2013). However, how acetylcholine affects the generation of NMDA spikes in CA3 neurons has not been explored and therefore is one of the aims of this research. Nevertheless, there are some studies that have looked at the effect of acetylcholine on dendritic integration and plateau potentials in other cell types. Acetylcholine or muscarinic receptor activation has previously been shown to induce and enhance the generation of plateau potentials in retinal ganglion cells (Brombas et al., 2017), CA1 OLM interneurons (Lawrence et al., 2006; Hagger-Vaughan and Storm, 2019), neocortical layer 5 cells (Williams and Fletcher, 2019), subiculum neurons (Kawasaki et al., 1999), supraoptic nucleus neurons (Ghamari-Langroudi and Bourque, 2004) and the layer 5 barrel cortex (Nuñez et al., 2012). Furthermore, optogenetic release of acetylcholine increases dendritic excitability, causes plateau potentials and enhances action potential output without affecting somatic excitability in cortical neurons (Williams and Fletcher, 2019). This effect of acetylcholine facilitating slow dendritic spikes can shift neurons into a bursting mode as well as provide another mechanism for plasticity induction.

1.3.5 Noradrenaline in the hippocampus

Noradrenaline is synthesised from tyrosine in terminal vesicles and is also released into the hippocampus during novelty, as well as emotional experiences (Aston-Jones and Bloom, 1981; Sara et al., 1994; Vankov et al., 1995). Noradrenergic input to the hippocampus comes primarily from the locus coeruleus (LC) and all hippocampal subfields receive noradrenergic input (Walling et al., 2012).

Noradrenaline is also primarily thought to be distributed via volume transmission (Umbriaco et al., 1995) but there has been evidence of synaptic targeting in the CA3 region (Walling et al., 2012). LC neurons fire at approximately 1 Hz (Aston-Jones and Bloom, 1981) and, in contrast to cholinergic neurons, are silent during REM sleep (Takahashi et al., 2010). When experiencing a novel or emotional stimulus, LC neurons switch to burst firing which is the state most linked to learning and memory processing (Aston-Jones and Bloom, 1981; Sara et al., 1994; Vankov et al., 1995).

1.3.5.1 Adrenergic receptors

When released, noradrenaline binds to and activates adrenergic receptors. There are three classes of adrenergic receptors: α_1 , α_2 and β -adrenergic receptors (β -Ars). All types are G-protein coupled receptors with α_1 -receptors activating the Gq signalling cascade, α_2 -receptors activating Gi and β -receptors activating Gs. Gs activation promotes the cAMP signalling pathway to increase cell activity. β -Ars are expressed in CA3 pyramidal neurons (Jurgens et al., 2005; Guo and Li, 2007), DG granule cells (Milner et al., 2000), as well as on PP inputs to DG cells and MF terminals (Lynch and Bliss, 1986). Several types of interneurons also express β -receptors including, including SST-, PV-, CCK-neuropeptide Y-, and calbindin-positive (Cox et al., 2008). The majority of cell types express β_1 -receptors except for CCK interneurons which express β_2 (Cox et al., 2008). There are also α_2 -receptors present predominantly on pre-synaptic terminals in all layers of CA3 pyramidal neurons (Milner et al., 1998) which are thought to inhibit epileptic activity (Jurgens et al., 2007). α_1 -AR activation has been shown to hyperpolarize CA3 neurons and suppress sharp wave ripple generation whereas β_1 -AR activation facilitated sharp wave ripple induction by enhancing LTP (Ul Haq et al., 2012). In CA1, β_1 -AR activation via endogenous noradrenaline release facilitates CA1 neuron spiking (Bacon et al., 2020). As noradrenaline is released during novelty and sharp wave ripples are usually associated with memory consolidation, suppression of sharp wave ripples via α_1 -AR activation would be useful to bias the circuit for memory encoding. Overall, noradrenaline can exhibit various effects in the hippocampus, depending on the brain state and which receptors are activated.

1.3.6 Noradrenaline in learning and memory

As noradrenaline is also released in novel or salient situations (Hervé-Minvielle and Sara, 1995; Vankov et al., 1995), its effect on learning and memory has also been studied. Blocking noradrenergic β -adrenoceptors in the hippocampus and experiments with mutant mice lacking adrenoceptors, have shown to impair memory consolidation (Ji et al., 2003) and retrieval (Murchison et al., 2004). Additionally, stimulating the LC has been shown to enhance spatial memory encoding (Lemon et al., 2009; Hansen and Manahan-Vaughan, 2015) and optogenetic inhibition of the LC impairs fear-related memory as well as disrupts place field formation and stability (Wagatsuma et al., 2017). This was shown by suppressing LC input at the time of encoding which led to more variable place fields in CA3.

1.3.7 Noradrenergic modulation of CA3 network

As noradrenaline has been shown to be important in memory processing, it is reasonable to predict that it would also modulate CA3 circuitry. Noradrenaline has been shown to suppress MF-CA3 feedforward inhibition and therefore increase the net excitation to CA3 neurons (Figure 1-10), but to a lesser extent than acetylcholine (Prince et al., 2021). Noradrenaline could be modulating this feedforward inhibition via activation of α_2 receptors either at MF-interneuron pre-synaptic terminals (Doze et al., 1991) or at interneuron-CA3 pre-synaptic terminals (Milner et al., 1998). Alternatively, β -receptor activation at MFs has been shown to be required for learning-facilitated LTD at this synapse (Hagena and Manahan-Vaughan, 2011) and therefore could also be involved in depressing synaptic transmission. There has been evidence for the DG-CA3 excitatory input increasing and decreasing with noradrenaline application. B-receptor activation has been shown to increase glutamate release from PP-DG (Figure 1-10) and DG-CA3 terminals (Lynch and Bliss, 1986) but more recently it's been shown that noradrenaline has no effect on MF excitatory transmission to CA3 (Prince et al., 2021). It is not yet known how noradrenaline affects CA3-CA3 excitatory synaptic transmission and therefore is one of the aims presented below. As is evident, noradrenergic effects and the different receptor subtypes have been less well studied in CA3 compared to acetylcholine. However, it seems to be producing a similar effect of promoting inputs to CA3 and reducing feedforward inhibition (Figure 1-10), which would support a role in memory encoding, although the mechanisms of action are less understood.

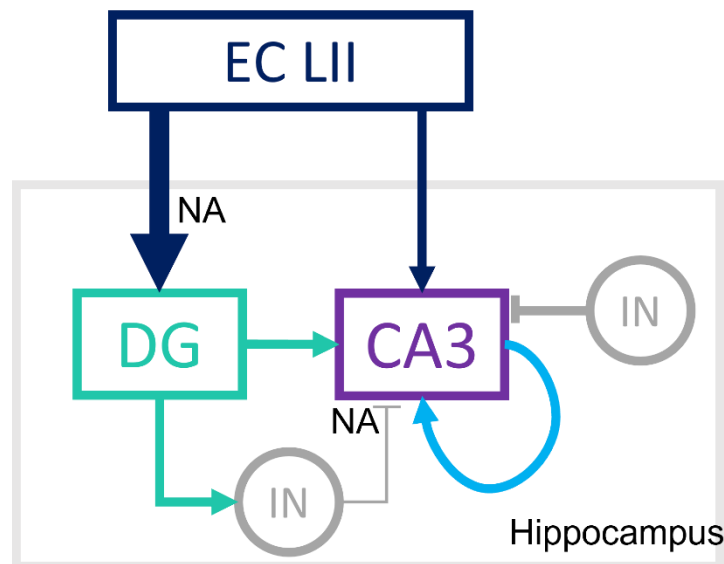


Figure 1-10 Noradrenergic modulation of CA3 circuitry. Changes in synaptic transmission are represented as smaller or larger arrows. Noradrenaline has been shown in *ex vivo* experiments to reduce mossy fibre feedforward inhibition and facilitate EC-DG inputs. NA = noradrenaline. EC LII = entorhinal cortex layer 2, IN = interneuron.

Noradrenaline has also been shown to facilitate LTP within the hippocampus. B-receptor activation has been shown to facilitate NMDAR-dependent LTP at the MF-CA3 synapse (Hopkins and Johnston,

1984, 1988; Huang and Kandel, 1996) via pre- (Huang and Kandel, 1996) and post-synaptic (Haas and Konnerth, 1983) mechanisms. At the PP-DG synapse, β -receptor activation has also been shown to enhance LTP (Bramham et al., 1997) as well as induce a form of heterosynaptic plasticity (Walling and Harley, 2004). There is little evidence of the effect of α -receptors on plasticity in the CA3 region.

1.4 Aims and hypotheses

It's important for us to increase our understanding of how the brain functions in order for us to understand the changes that arise in disease states. In the case of this study, understanding how neuromodulators affect the circuitry involved in learning and memory could help us to understand how these systems are affected in cases of dementia and learning disorders. The overall objective of this thesis is to further our understanding of how acetylcholine modulates synaptic transmission and dendritic integration within the CA3 region of the hippocampus.

The aims of this research are as follows:

1. Compare how acetylcholine and noradrenaline modulate CA3-CA3 recurrent excitatory synaptic transmission.
2. Investigate how endogenous acetylcholine release affects perforant path, recurrent and inhibitory inputs to CA3 neurons.
3. Predict how acetylcholine could modulate dendritic integration/NMDA spikes in a biophysical model of a reconstructed CA3 pyramidal neuron.

Aim 1: Compare how acetylcholine and noradrenaline modulate CA3-CA3 recurrent excitatory synaptic transmission.

I first addressed the question of how two different neuromodulators, released under similar physiological conditions, could affect the recurrent circuitry within the CA3 region. This circuitry is highly important for the formation, short-term storage and retrieval of memories. There is current evidence that carbachol, an acetylcholine agonist, reduces the synaptic transmission in the CA3 recurrent network by activating M2-receptors on the pre-synaptic terminals and reducing glutamatergic release (Vogt and Regehr, 2001; Kremin and Hasselmo, 2007). As acetylcholine is released during novelty or saliency, this mechanism that reduces activity within the recurrent network is thought to prevent memory retrieval in order to promote memory encoding. Noradrenaline is also released during saliency and therefore it could be predicted that it would reduce CA3 recurrent transmission in a similar way to acetylcholine. There is some evidence of $\alpha 2$ -adrenergic receptor expression in the SR on pre-synaptic glutamatergic terminals within CA3 (Milner et al., 1998). Activation of these receptors triggers the Gi signalling cascade and therefore could lead to reduced glutamate release.

Aim 2: Investigate how endogenous acetylcholine release affects perforant path, recurrent and inhibitory inputs to CA3 neurons.

Secondly, I tested the effects of endogenous acetylcholine release on the EC and recurrent inputs to CA3 neurons. As explained above, previous work assessing cholinergic modulation on the CA3 network has mostly been performed using pharmacological interventions. We are now able to take advantage of optogenetic technology to investigate the endogenous release of neuromodulators. For these experiments, mice with channelrhodopsin expressed in medial septal cholinergic neurons were used, in order to precisely stimulate cholinergic fibres in the hippocampus to release acetylcholine. It was predicted that this endogenous release of acetylcholine would have the same effect as has been found in the previous pharmacological studies, but possibly to a lesser extent, as the precise release dynamics of endogenous neuromodulators can produce reduced effects in comparison to bath applying receptor agonists (Rosen et al., 2015; Bacon et al., 2020). Therefore, it was predicted that endogenous acetylcholine release should reduce EC-CA3 and CA3 recurrent glutamatergic transmission (Kremin and Hasselmo, 2007) as well as GABAergic transmission within CA3 (Szabó et al., 2010), through pre-synaptic activation of muscarinic receptors.

Aim 3: Predict how acetylcholine could modulate dendritic integration/NMDA spikes in a biophysical model of a reconstructed CA3 pyramidal neuron.

Finally, I used a biophysically detailed model of a CA3 pyramidal neuron to predict how acetylcholine could modulate dendritic NMDA spike generation. NMDA spikes are important to study because they can alter the output of a neuron as well as induce plasticity (Makara and Magee, 2013; Brandalise et al., 2016; Raus Balind et al., 2019). To simulate the presence of acetylcholine in the model, changes in the conductance of several potassium channels known to be affected by M1 receptor activation were modelled (Hoffman and Johnston, 1998; Sohn et al., 2007; Buchanan et al., 2010; Tigaret et al., 2018). NMDA spikes were generated by including a high NMDA:AMPA ratio in the dendrites, commonly used when investigating NMDA spikes in computational models (Poirazi et al., 2003a; Larkum et al., 2009; Major et al., 2013), and increasing the number of synapses stimulated on a dendritic branch to generate nonlinear integration, signifying an NMDA spike. As M1 receptor activation increases CA3 neuron excitability (Sun and Kapur, 2012), it was predicted that simulated acetylcholine would reduce the threshold for NMDA spike generation. Using a model allowed for analysis of the effect in all dendritic branches within one neuron as well as precise control and manipulation of all parameters.

Chapter 2 Cholinergic modulation of dendritic integration in a reconstructed CA3 neuron model

This chapter is based on the published article:

Humphries, R., Mellor, J., & O'Donnell, C. (2021). Acetylcholine boosts dendritic NMDA spikes in a CA3 pyramidal neuron model. *Neuroscience*.

I produced all the data and Figures in the publication.

2.1 Introduction

As established in the Introduction, the CA3 region is important for memory processing with the recurrent network having particular importance in memory storage (Nakazawa et al., 2003; Nakashiba et al., 2008; Guzman et al., 2016; Song et al., 2018) and synaptic plasticity thought to play a major role in strengthening the recurrent connections to facilitate the storage of a memory (Astori et al., 2010; Brandalise and Gerber, 2014; Mishra et al., 2016). As the mechanisms underlying synaptic plasticity can occur post-synaptically within dendrites, dendritic activity is also thought to play a role in memory storage. Dendritic spikes can locally depolarise dendrites, increase calcium influx and generate somatic spiking all of which can underly plasticity induction. The SR dendrites, which receive inputs from CA3 recurrent collaterals, are specifically implicated in memory storage and plasticity. Distal SLM dendritic activity has been less studied in the CA3 region, and the inputs from the entorhinal cortex received here are thought to possibly signal for retrieval of a memory (Treves and Rolls, 1992). In CA1 neurons, distal dendrite activation has been shown to induce plateau potentials and establish place cell firing (Bittner et al., 2015). The distal region is particularly relevant for investigating regenerative dendritic activity as it has the potential to generate the largest events and dendritic spikes have the ability to enhance propagation to the soma and influence action potential output (Branco and Häusser, 2011).

Acetylcholine also plays an important role in memory encoding (Blokland et al., 1992; Rogers and Kesner, 2003; Douchamps et al., 2013; Mitsushima et al., 2013; Jarzebowski et al., 2021; Prince et al., 2021; Zhang et al., 2021) and plasticity (Fernández De Sevilla and Buño, 2010; Zheng et al., 2012; Dennis et al., 2016). In CA3 pyramidal neurons, acetylcholine activates M1 receptors which depolarises neuron resting membrane potential and input resistance (Sun and Kapur, 2012). This M1 activation inhibits several potassium channels including A-type (K_A), M-type (K_M), SK (K_{Ca}) and GIRK (Kir) (Hoffman and Johnston, 1998; Sohn et al., 2007; Buchanan et al., 2010; Tigaret et al., 2018), several of which are implicated in modulating NMDA spike properties (Cai et al., 2004; Makara and Magee, 2013; Malik and Johnston, 2017). Acetylcholine plays an important role in modifying synaptic communication and one of the ways it could contribute to this is by altering post-synaptic excitability

and influencing dendritic spike generation. Acetylcholine has previously been shown to enhance dendritic excitability and integration in neocortical pyramidal neurons (Williams and Fletcher, 2019).

Dendritic integration properties can vary across the dendritic tree due to differences in morphology, branch thickness as well as the distribution of voltage-gated ion channels (Kim et al., 2012; Makara and Magee, 2013). Synaptic integration and NMDA spikes within CA3 neurons have previously been studied in the SR and SO regions (Makara and Magee, 2013). CA3 SLM dendritic integration has not been studied experimentally, possibly due to technical constraints in recording activity from these thin distal dendrites. In addition, it is not possible experimentally to measure targeted inputs to every dendritic branch within one CA3 neuron.

This chapter addresses Aim 3 investigating how acetylcholine may affect NMDA spike generation in two-compartment and a reconstructed model of a CA3 pyramidal neuron. The simulations specifically focus on synaptic inputs onto the SR and SLM dendrites representing inputs from the recurrent collaterals and the entorhinal cortex, respectively. NMDA spikes have been studied in brain slices in the SR region previously (Makara and Magee, 2013) but it is not known how they could be modulated by the presence of acetylcholine. In other neuron types, acetylcholine has been shown to increase dendritic excitability and facilitate dendritic integration (Williams and Fletcher, 2019).

NMDA spikes were generated by increasing the number of inputs stimulated on a single dendritic branch segment. The resulting nonlinear increases of the NMDA-mediated amplitudes suggested an NMDA spike was initiated. Cholinergic modulation was simulated as the inhibition of several potassium channels that acetylcholine is known to block physiologically (Hoffman and Johnston, 1998; Sohn et al., 2007; Buchanan et al., 2010; Tigaret et al., 2018). The benefits of using a model allowed for assessment of all dendritic branches within one neuron as well as for controlled manipulation of all the parameters. The model was based on physiological parameters where possible, and an optimisation algorithm was employed to ensure accurate relative contributions of the relevant potassium conductances. Comparison of NMDA spike properties between different dendritic branches and regions were initially analysed and then the effect of acetylcholine and potassium channel inhibition on NMDA spike generation was assessed.

It was predicted that NMDA spikes would be more easily generated in the distal SLM dendrites due to thinner dendrites and a higher input resistance, and that acetylcholine would increase dendritic excitability and therefore reduce the threshold synaptic input required for NMDA spike generation. Also, as several potassium channels have previously been implicated in the modulation of NMDA spikes and dendritic integration (Cai et al., 2004; Malik and Johnston, 2017), it was thought that the Ka

and Kca channel in particular would most likely be responsible for the cholinergic modulation of NMDA-mediated nonlinear integration.

2.2 Methods

2.2.1 Software

The simulations detailed in this chapter were performed using NEURON version 7.8 (<https://www.neuron.yale.edu/neuron/>) (Carnevale and Hines, 2006) and Python 3.9.

2.2.2 Two-compartment model

Initial simulations were run on a simple two-compartment model comprised of a somatic and dendritic compartment (Figure 2-1). The soma was $500 \mu\text{m}^2$ and the dendritic section $200 \mu\text{m}$ in length and $1 \mu\text{m}$ in width. The axial resistivity was set at $150 \text{ M}\Omega$ and leak conductance reversal potential at -65 mV . The ion channel mechanisms present in this model were taken from a previous CA3 neuron model (Hemond et al., 2008) and included voltage-gated sodium channels, voltage-gated potassium channels (A-type (Ka), M-type (Km), delayed rectifier (Kdr)), voltage-gated calcium channels (L-type (CaL), N-type (CaN), T-type (CaT)), calcium-activated potassium channels (after-hyperpolarisation (Kahp), large conductance (BK)), and a hyperpolarization-activated current (Ih). Two additional channels, small-conductance calcium-activated (SK/Kca) and inwardly-rectifying (Kir) potassium conductances, both relevant for cholinergic modulation, were also included in the model. These channel mechanisms were obtained from Combe et al., (2018) (Kca) and Yim et al., (2015) (Kir). All equations and parameters describing the ion channel kinetics can be found in Appendix A. Km was only present in the somatic compartment, whereas all other conductances were present in both the soma and dendrite. There was also a calcium extrusion mechanism implemented whereby the calcium concentration (*cai*) within the dendrite decayed according to the following equation:

$$cai' = \frac{2 * (irest - ica)}{F * depth} * (1e4) + \left(\frac{cai0 - cai}{tau} \right)$$

Where *tau* is the decay time constant (100 ms), *depth* is half the dendrite diameter, *irest* is the resting current (0 mA/cm^2), *ica* is the calcium current, *cai0* is the resting calcium concentration ($50\text{e-}6 \text{ mM}$) and *F* is the Faraday constant ($9.649\text{e}4 \text{ C mol}^{-1}$). This mechanism was also included in the original CA3 model from Hemond et al., (2008).

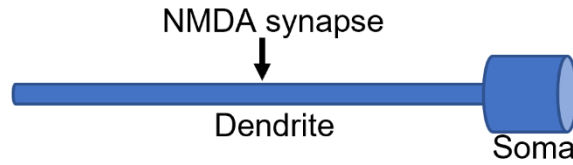


Figure 2-1: Two-compartment neuron model structure. Somatic ($500 \mu\text{m}^2$) and dendritic compartment ($1 \times 200 \mu\text{m}$) with NMDA synapse mechanism on the dendrite.

2.2.3 Channel conductance optimisation

As the contribution of different potassium conductances were to be assessed in the model, an optimisation algorithm was used to ensure the model channel conductances were physiological. The method used was covariance matrix adaptation evolution strategy (CMA-ES) (Hansen, 2016; Jędrzejewski-Szmek et al., 2018) and was implemented using the PyCMA package (<https://github.com/CMA-ES/pycma>). The average change in membrane potential and input resistance when blocking the key potassium channels (K_a , K_m , K_{ca} , K_{ir}) and from M1 receptor activation, were taken from published data (Sun and Kapur, 2012; Makara and Magee, 2013) and used as target values in the optimisation process (Figure 2-2). As these values were taken from two studies with different experimental recording temperatures, the target values for K_m and acetylcholine were reduced to more closely reflect the value that would be expected at a physiological temperature. The peak conductances and the activation curves for these potassium channels were allowed to fluctuate during the optimisation in order to discover an optimal set of parameters for each channel that closely matched with the experimental data (Figure 2-2). The resting membrane potential and input resistance were also included as target values for the optimisation. Figure 2-2 depicts this process as well as displays the target experimental data (right) and the final output data after running the optimisation (left). Table 1 shows the optimised conductance values used in the models. The sodium conductance was set to 0 to prevent action potential generation and back-propagation of action potentials into the dendrites. As there is not one optimal combination of peak conductances, and there could be many possible solutions that reflect the experimental data (Alonso and Marder, 2019), the reconstructed neuron simulations were additionally run on 8 separate models, each with different peak conductances, within a physiologically relevant range. These conductances were chosen using the same optimisation process (Figure 2-2),

while additionally targeting the experimental standard deviation of membrane potential and input resistance changes.

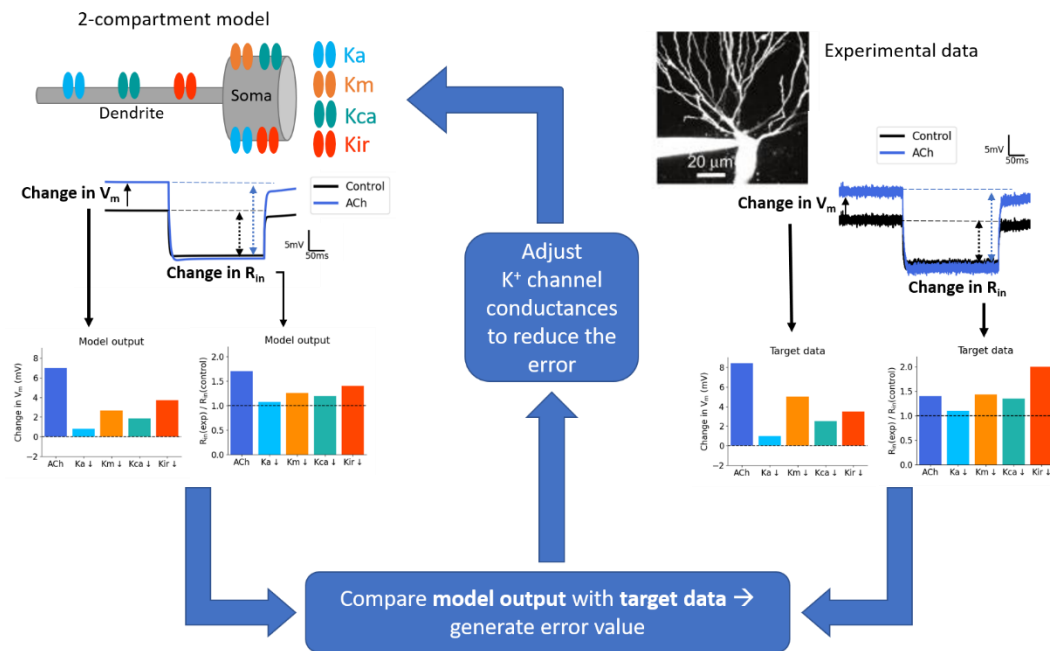


Figure 2-2: Optimisation process. Average membrane potential and input resistance changes from blocking potassium channels were obtained from Makara and Magee (2013) and Sun and Kapur (2012) and used as target values for the optimisation algorithm (right). Potassium conductance mechanisms were added to the two-compartment model and the change in membrane potential and input resistance were measured when blocking these potassium channels to generate the model output values (left). These outputs from the model were then compared with the target data to generate an error value, which contributed to the adjustment of the potassium channel conductances with the aim of finding the minimum error value or the least amount of difference between the model output and the target data (centre). This process was repeated ~1000 times to generate the peak conductance values for the model. Image in top right taken from Makara and Magee (2013).

2.2.4 Reconstructed CA3 neuron model

The reconstructed CA3 neuron model used in this chapter was adapted from a previously published model (Hemond et al., 2008) obtained from ModelDB (<https://senselab.med.yale.edu/ModelDB/>, accession number 101629). The model scripts, ion channel and synaptic mechanisms and neuron geometry used in this chapter are also publicly available on ModelDB (accession number 267298). The morphology was reconstructed from a filled rat pyramidal neuron in the CA3b region from Henze et al., (1996) (Figure 2-14). There were 85 apical dendrite sections, 52 basal dendrite sections, an axon and a soma created from a total of 943 compartments. The apical dendrites were divided into different regions depending on their distance from the soma, with dendritic sections between 150 and 400 μm from the soma being classed as SR dendrites and dendrites >400 μm from the soma as SLM dendrites (Figure 2-14). A range of timesteps between 0.1 and 2 ms were tested, finding a 1 ms timestep as optimal to reduce the simulation run time without compromising the NMDA response dynamics. The

parameters used in this model were similar to the two-compartment model (Table 2), however the potassium channel optimisation was repeated and the peak conductances used for each channel are shown in Table 1. Additionally, the K_a and K_{ir} conductance distributions varied across the dendritic tree corresponding to experimental data (Kim et al., 2012; Degro et al., 2015), which showed a higher density of these channels in the more distal dendrites. The K_{ir} conductance value in Table 1 was multiplied by 2.43, 1.07, 4.79 and 5.25 in the SO, SL, SR and SLM dendrites, respectively (Degro et al., 2015). The K_a conductance was distributed in a distance-dependent manner in apical dendrite sections more than 50 μm from the soma, with the following equation:

$$\text{Adjusted } K_a \text{ } g_{\text{max}} = K_a \text{ } g_{\text{max}} + K_a \text{Slope} * (x_{\text{dist}} - K_a D_t)$$

Where $K_a \text{ } g_{\text{max}}$ was the K_a peak conductance value displayed in Table 1, $K_a \text{Slope}$ was the slope of the K_a increase ($5.5 \times 10^{-5} \text{ Scm}^2/\mu\text{m}$), x_{dist} was the distance of the dendrite from the soma, and $K_a D_t$ was the distance where the conductance started to increase (50 μm). This equation, the $K_a \text{Slope}$ and $K_a D_t$ values were taken from Kim et al., (2012). The final K_a and K_{ir} peak conductances for each stimulated dendrite section are shown in Table 1 below. All other conductances were distributed evenly across the dendritic tree. Furthermore, to account for the lack of dendritic spines in the model, the membrane capacitance was doubled, and the membrane resistance halved.

Table 1: Ion channel maximal conductance values for the two-compartment and reconstructed models. These values were either taken from the model in Hemond et al., (2008) or calculated from the optimisation process. Ka, Km, Kca, Kir leak and Ih peak conductances were generated from the optimisation.

Channel	Peak conductance (S/cm ²)	
	2-compartment model	Reconstructed neuron model
Ka	0.398	5.56×10^{-11}
Km	0.033	0.0011
Kca	0.035	0.0012
Kir	0.0012	3.47×10^{-6}
Leak (gpas)	7.25×10^{-5}	4.4×10^{-10}
Kdr	0.005	4.6×10^{-9}
Na	0.0	0.0
CaT, CaN, CaL	1×10^{-5}	1×10^{-5}
Kc	5×10^{-5}	5×10^{-5}
Kahp	0.0001	0.0001
Ih	0.00001	5.6×10^{-6}

2.2.5 AMPAR and NMDAR mechanisms

Synaptic inputs were simulated as dual-exponential models representing AMPAR and NMDAR activation, with the NMDAR model including a voltage-dependent magnesium block mechanism. NMDA synapses were present in both the two-compartment and reconstructed neuron model whereas AMPA synapses were only included in the reconstructed neuron model. The synapse models and parameters were taken from a previous CA3 modelling study, based on experimental data (Baker et al., 2011; Hyun et al., 2015). Synapse parameters for both models are displayed in Table 2. The peak conductance of synaptic inputs was the same across the SR and SLM dendrites, but the AMPA peak conductance was 0.5x the NMDA peak conductance to enable consistent nonlinear responses in the dendrites. This reduced AMPA:NMDA ratio has previously been used when investigating NMDA spikes in computational models (Poirazi et al., 2003a; Larkum et al., 2009; Major et al., 2013). Synapses were positioned 1 μm apart (Gu et al., 2014; Mendell et al., 2017; Haugland et al., 2020), on dendritic sections at least 20 μm long, and stimulated simultaneously, assuming inputs to a small single branch section would be received from the same pre-synaptic axon. Appendix B contains a table describing the properties of each dendrite section that was stimulated and recorded from.

Table 2: Model and synapse parameters.

	Model parameters	
	2-compartment model	Reconstructed neuron model
Membrane capacitance (soma) ($\mu\text{f}/\text{cm}^2$)	0.7	0.7
Membrane capacitance (dendrites) ($\mu\text{f}/\text{cm}^2$)	1.4	1.4
Axial resistivity (ohm cm)	150	150
	Synapse parameters	
	2-compartment model	Reconstructed neuron model
NMDA rise time constant (ms)	4	5
NMDA decay time constant (ms)	42	16
AMPA rise time constant (ms)	-	0.5
AMPA decay time constant (ms)	-	0.5
NMDA peak conductance (nS)	1	1.17
AMPA peak conductance (nS)	-	0.585

2.2.6 NMDA spike generation

NMDA spikes were generated by increasing synaptic weight (two-compartment model) or the number of synaptic inputs (reconstructed model) stimulated on a dendritic branch section, up to a maximum of 20 synapses (or 20x synaptic weight). Synapses were positioned starting from the centre of the section and extending outwards. Voltages were recorded from the centre of both the somatic and stimulated dendritic compartment. The amplitude of the NMDA-mediated EPSPs were measured and produced a supra-linear relationship between the synaptic input and the resulting amplitude output (Figure 2-3), representing an NMDA spike. To observe the NMDA-mediated responses, simulations with AMPA-only synaptic inputs were subtracted from the NMDA+AMPA voltage traces. This nonlinear relationship was comparable to previously published experimental data from CA3 pyramidal neurons (Makara and Magee, 2013).

2.2.7 Analysis of nonlinear output

To compare the EPSP amplitudes as the stimulus intensity was increased (nonlinear output) between dendrites and conditions, two properties from the nonlinear curves were measured as depicted in Figure 2-3. First, the maximum slope of the curve was calculated, representing how quickly the amplitude was changing in response to inputs; and secondly, the number of inputs required at this maximum slope point. This second measure allowed us to detect a shift in the curve along the x-axis, representing a change in the number of inputs required, or the input threshold required, for generating the nonlinear output.

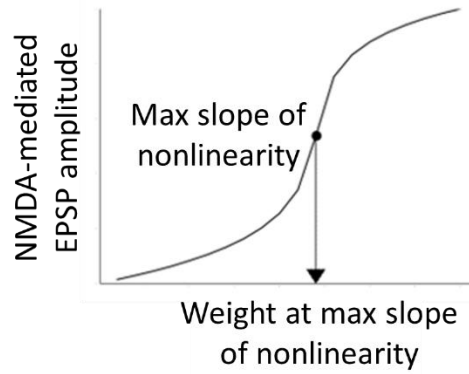


Figure 2-3: Measures taken from nonlinear input-output curve. Max slope of nonlinearity = steepness of the nonlinear slope; Weight at max slope of nonlinearity = synaptic weight or number of synapses (x-axis value) at the maximum slope.

2.2.8 Cholinergic and potassium channel modulation

To model acetylcholine release and M1 receptor activation, several potassium channels (K_a, K_m, K_{ca} and K_{ir}) were modulated to reflect the physiological action of acetylcholine in CA3 pyramidal neurons. The extent of inhibition of each potassium conductance was calculated during the optimisation process to reflect the physiological extent of cholinergic modulation on the membrane potential and input resistance. In light of this, the maximum conductances of each channel were reduced by 50% for K_a, K_m, K_{ca} and 80% for K_{ir}. When assessing the effect of individual potassium channel inhibition, each conductance was set to 0 to reflect pharmacological experiments in which channel blockade was assumed to be 100%.

2.2.9 Statistical analysis

Statistical analysis was performed using Wilcoxon signed-rank and Wilcoxon rank-sum for paired and independent data, respectively. When comparing multiple conditions, Bonferroni correction was applied.

2.3 Results

2.3.1 Cholinergic modulation of NMDA spikes in a two-compartment model

The effect of acetylcholine and blocking potassium channels was first tested in a two-compartment neuron model comprising of a soma and a dendrite (Figure 2-1). An NMDA input, with a peak conductance of 1nS, was simulated on the dendritic compartment and the voltage response recorded in the soma and in the dendrite (Figure 2-4). The weight of the synaptic input was then increased up to 20 and the corresponding voltage traces are depicted in Figure 2-4. Traces with synaptic weights of 2, 10 and 17 are emphasised to allow comparison between the conditions. As would be expected, the somatic voltage responses were substantially reduced compared to responses recorded in the dendrite as the voltage attenuated as it propagated to the soma. The resting membrane potential of this neuron model was determined during the optimisation of the potassium channel conductances and as is shown, it was moderately hyperpolarised at $\sim -80\text{mV}$.

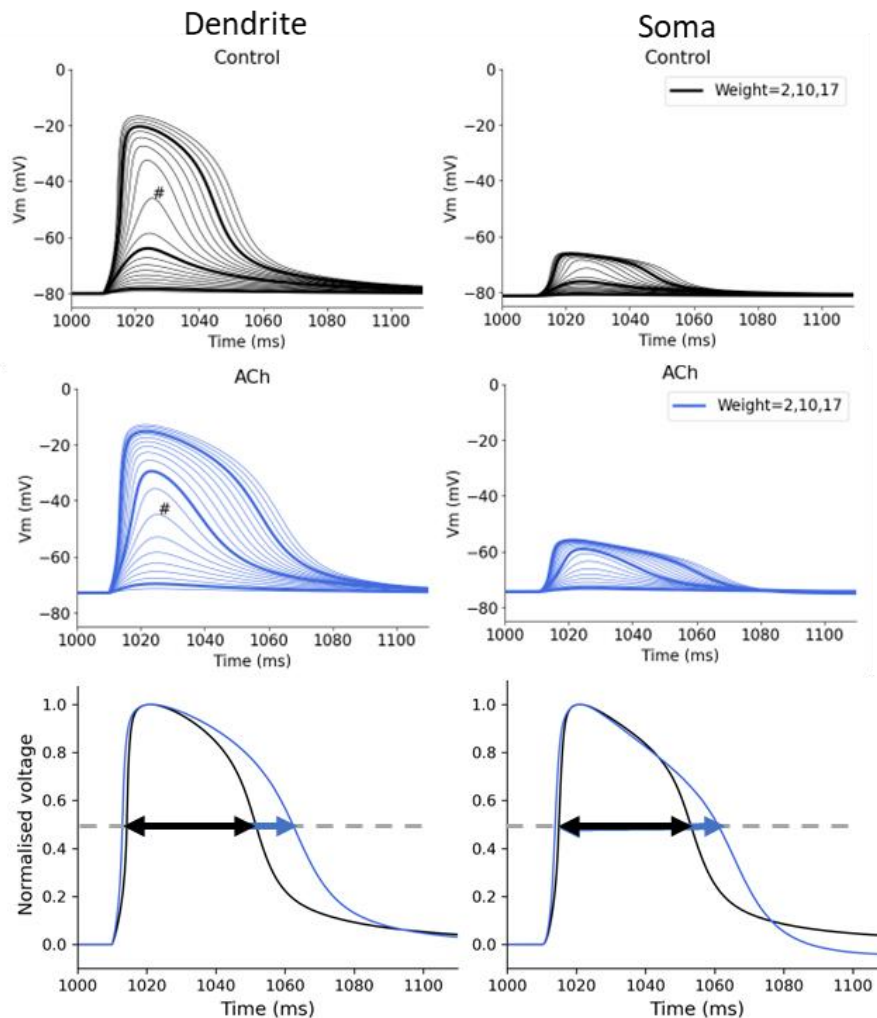


Figure 2-4: Example EPSPs recorded in the two-compartment model from dendritic (left) and somatic (right) compartments without (upper) and with (middle) acetylcholine. Increasing weights of NMDA synaptic inputs from 1 to 20 were stimulated and recorded in the somatic and dendritic compartment. Acetylcholine (blue) was simulated by blocking the four potassium channels (K_a, K_m, K_{ca}, K_{ir}) as explained in the Methods. Emphasised traces = synaptic weight at 2, 10

and 17 for each condition to allow for comparison between plots; # = the trace with the biggest increase in amplitude compared with the next lowest stimulation amplitude, signifying the steepest part of the sigmoidal amplitude curves. Lower panel: Measurement of EPSP half-widths with a 20x synaptic weight in dendrite (left) and soma (right) for control (black) and acetylcholine (blue).

Acetylcholine was simulated by blocking the four potassium channels (K_a, K_m, K_{ca}, K_{ir}) as described in the Methods (Figure 2-4, middle). The most striking difference between the control and acetylcholine traces is the half-width. The half-width (Figure 2-4, lower) of the largest dendritic response was 37.25 ms in the control condition compared to 49.30 ms with cholinergic modulation. Acetylcholine also caused an approximately 7 mV depolarisation in the resting membrane potential and an ~ 70% increase in the resting input resistance, which are comparable to experimental data (Sun and Kapur, 2012). Furthermore, comparing the voltage traces with a synaptic weight of 10 also displayed a large difference with cholinergic modulation. A synaptic weight of 10 gave a dendritic EPSP amplitude of 16.18 mV in the control compared to 43.48 mV with acetylcholine. The amount of synaptic weight required to elicit the largest increase in amplitude, represented by the # in Figure 2-4, was also modulated by acetylcholine. In summary, acetylcholine depolarised the neuron, increased the EPSP half-width, and reduced the amount of synaptic weight needed to reach a certain amplitude.

Next, the EPSP amplitude was evaluated in relation to the synaptic weight to allow interpretation of the input-output curves for each condition (Figure 2-5). The sigmoidal curves represent a supra-linear relationship signifying nonlinear integration caused by an NMDA spike. In this Figure, each of the potassium channels were also blocked individually to assess the contribution of each conductance to the overall effect. As can be seen, the biggest effect occurred with acetylcholine, and is evidenced as a curve shift to the left (Figure 2-5). This means that less synaptic input was required to generate the same response amplitude and therefore the threshold for generating an NMDA spike was reduced. The effects observed are the same in the soma (Figure 2-5, right) and in the dendrite (Figure 2-5, left). In addition, the contribution of each potassium conductance was also assessed, and inhibition of each potassium channel did cause some effect in shifting the curve. Blocking K_m and K_{ca} caused the least amount of shift in the curve, but both acted comparably, and inhibition of K_{ir} caused a slightly larger shift. Inhibition of the K_a channel also shifted the curve slightly, but interestingly, also produced a unique effect of increasing the slope of the curve (Figure 2-5). Overall, acetylcholine produced the largest effect on the input-output relationship, with each potassium conductance contributing slightly, with no single channel in particular dominating the effect, whereas the K_a conductance was the only one that appeared to modulate the slope of the curve.

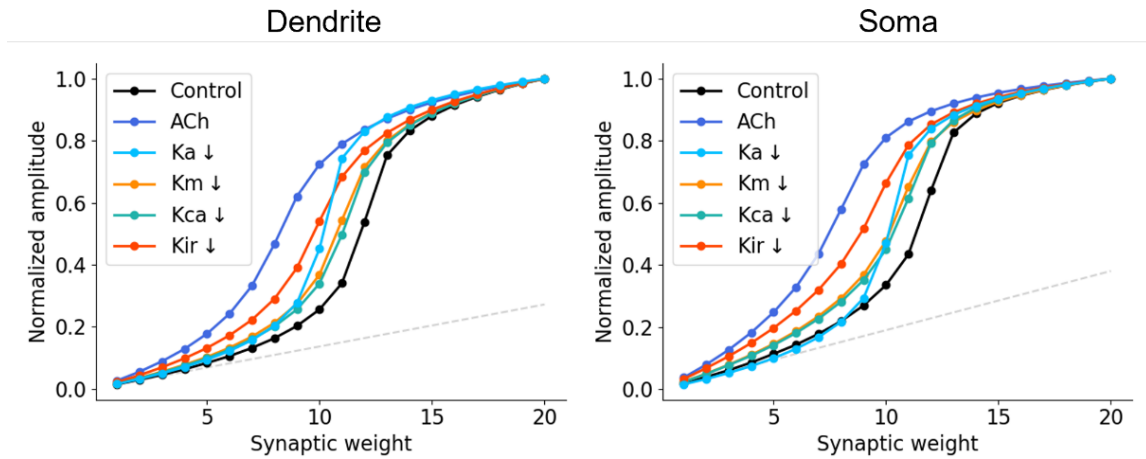


Figure 2-5: Nonlinear curves recorded in the two-compartment model from dendrite (left) and soma (right) for different potassium channel blocks. The normalized EPSP amplitudes for increasing synaptic weight values for each potassium channel block and acetylcholine. The dashed grey line represents a linear relationship for the control condition.

The effect of each potassium conductance block is quantified in Figure 2-6. Again, the results are comparable between the soma and the dendrite. Figure 2-6A shows the synaptic weight required to reach the maximal slope of the nonlinear curve. The larger the reduction compared to the control, the larger the leftward shift in the curve. A synaptic weight of 12 was needed in the control to reach the maximum slope of nonlinearity, compared to a weight of 8 with acetylcholine. Inhibiting the potassium conductances produced a smaller reduction in the synaptic weight required as was also shown in Figure 2-5. Figure 2-6B shows the maximum slope of each condition, quantified as the change in voltage divided by the change in synaptic weight. As was suggested in Figure 2-5, blocking the Ka conductance caused a considerable increase in the maximum slope and remarkably even more so than acetylcholine, whereas the remaining conductances had little impact on the slope.

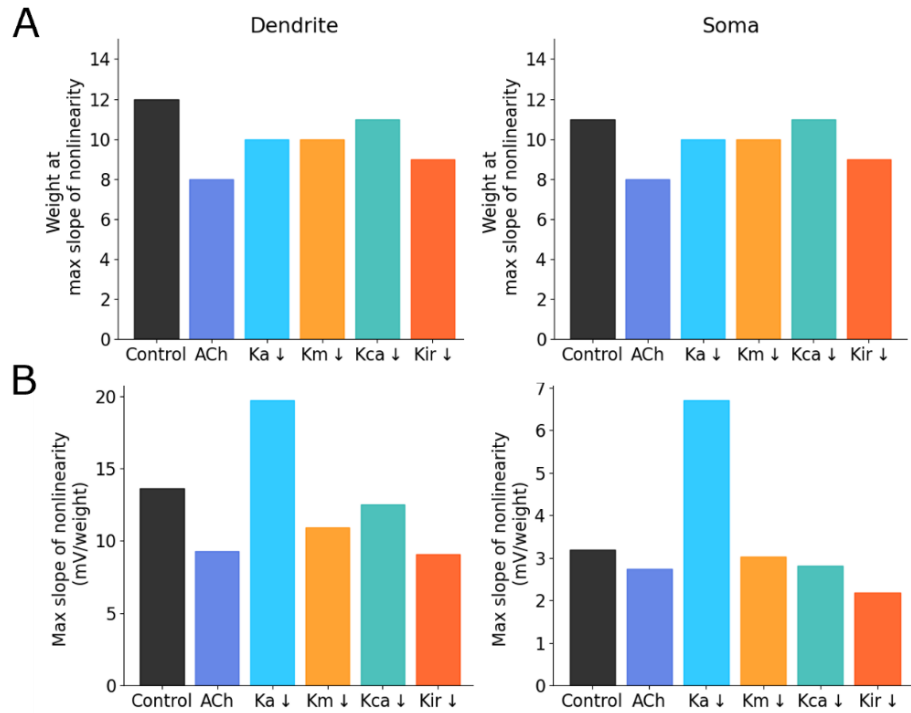


Figure 2-6: Acetylcholine reduced the synaptic weight needed to reach the maximum slope of nonlinearity. (A) Synaptic weight required to reach the maximum slope of nonlinearity and (B) maximum slope of nonlinearity for each potassium channel block and acetylcholine recorded in the dendrite (left) and the soma (right).

To understand the difference in the magnitude of effect from blocking different channels, the change in membrane potential (left) and input resistance (right) were correlated with the change in the slope of nonlinearity (Figure 2-7B) and synaptic weight threshold (Figure 2-7A). In each case, there was a larger reduction in both the slope of nonlinearity and the synaptic input weight at the slope with larger increases in membrane potential and input resistance caused from the potassium channel inhibition. The increase in membrane potential and input resistance explained the reduction in the synaptic weight threshold (Figure 2-7A) more effectively, with R^2 values of 0.760 and 0.820 respectively, compared to the change in the slope (Figure 2-7B). The large increase in the nonlinear slope caused by Ka channel inhibition (Figure 2-7B) did not match the reduction in the slope caused by the other potassium channel blocks.

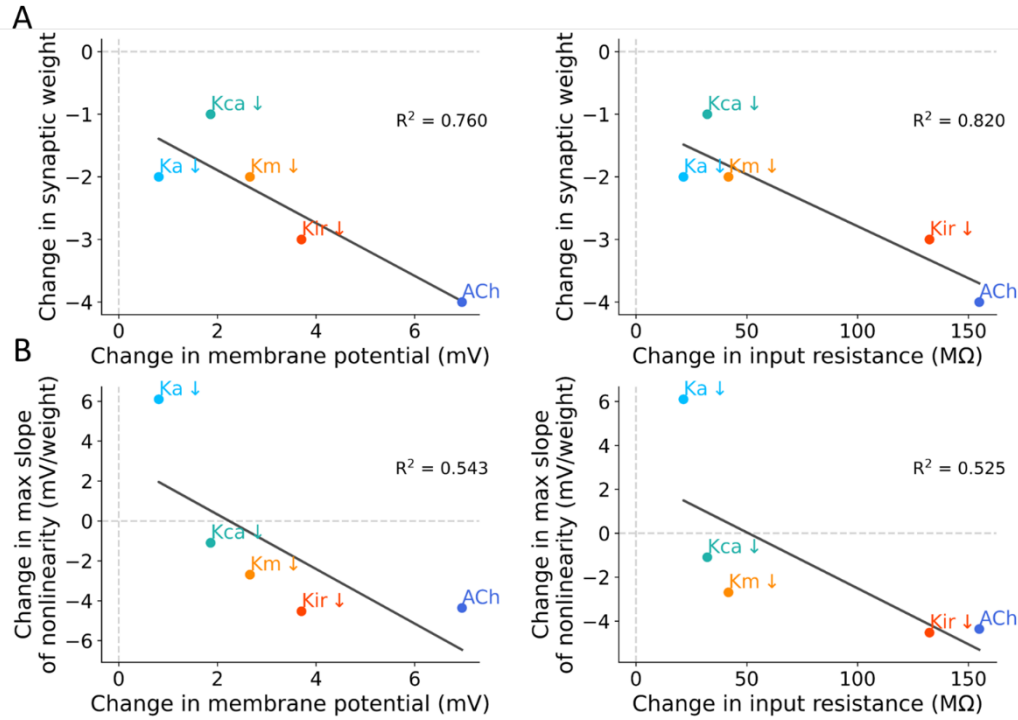


Figure 2-7: Membrane potential and input resistance increases caused by potassium channel inhibition correlated with reductions in synaptic weight threshold and nonlinear slope. (A) Effect of membrane potential (left) and input resistance (right) change on the change in synaptic weight required to reach the maximum slope of nonlinearity. (B) Effect of membrane potential (left) and input resistance (right) change on the change in the slope of nonlinearity. Each point represents measurement from a different channel block or with ACh, as labelled.

To further understand the effect of the different potassium conductance blocks on NMDA nonlinearity, each channels' activation dynamics were assessed. As is shown in Figure 2-8 and Figure 2-9, the channels display various voltage- and calcium-dependent activation profiles. The Km channel becomes more active at increasing membrane potentials (Figure 2-8) and modulates cell excitability. It is only expressed in the soma and plays a role in increasing the threshold of action potential initiation (Shah et al., 2008). Due to Km not being present in the dendritic compartment in the model, it only had a small influence on the dendritic resting membrane potential and input resistance (Figure 2-7). On the other hand, the Kir channel is most active at hyperpolarised potentials (Figure 2-8) with a role in maintaining the membrane potential. As shown here (Figure 2-7), Kir channel inhibition caused the largest increase in membrane potential and input resistance, compared to the other individual potassium channel blocks. Figure 2-8 also shows the activation curve for Kca (right). This channel is regulated by calcium concentration as opposed to voltage and becomes more active with increasing levels of intracellular calcium. Therefore, it is most active at peak voltages and plays a role in dendritic repolarisation (Cai et al., 2004) and action potential after-hyperpolarisation (Sah and McLachlan, 1991, 1992). Consequently, Kca suppression did cause a small increase in resting membrane potential and input resistance but had the least impact on the nonlinear slope and synaptic weight threshold (Figure 2-8).

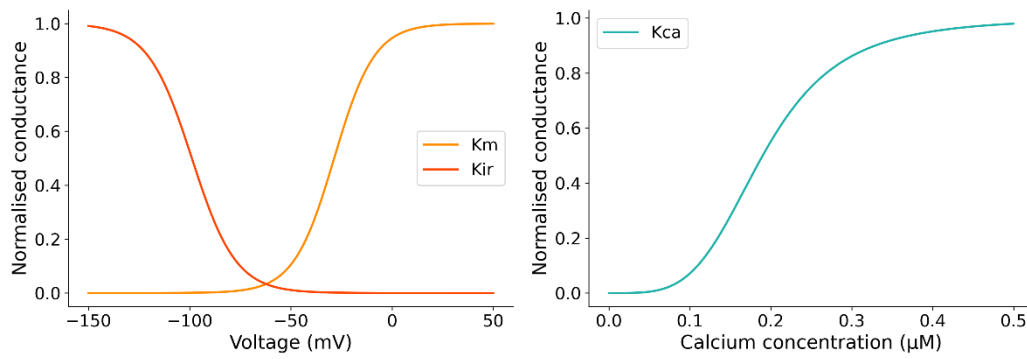


Figure 2-8: Acetylcholine modulated voltage- and calcium-dependent potassium conductance activation curves. Km and Kir activations with respect to voltage (left) and Kca activation with respect to calcium concentration (right).

Ka channel inhibition caused a unique effect of increasing the nonlinear slope (Figure 2-6). Considering its activation and inactivation dynamics can help to explain this effect (Figure 2-9). The inactivation gate is fully open around resting membrane potential but starts to shut upon depolarisation (Figure 2-9A). On the other hand, the activation gate is fully closed around resting membrane potential and begins to open upon depolarisation. Figure 2-9B shows the Ka current-voltage relationship, displaying increasing current until it reaches a peak at -27.4 mV. At voltages above this the current drops, even though the activation gate is open, because the inactivation gate is closing, deeming the channel inactive.

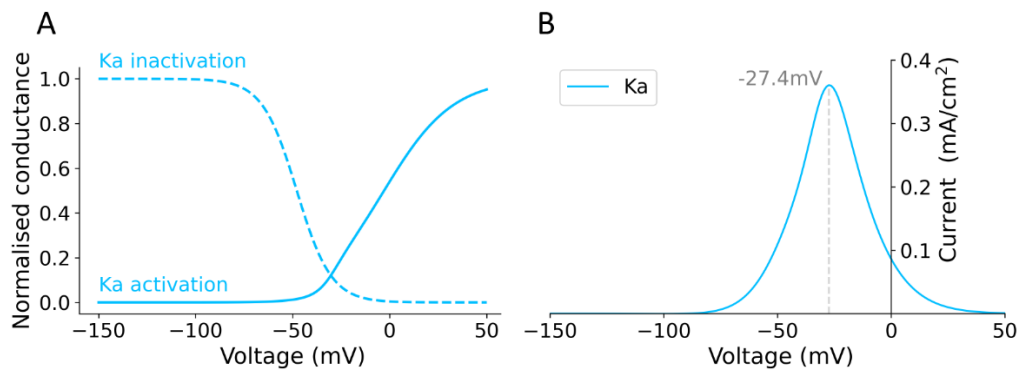


Figure 2-9: A-type potassium channel voltage-dependent steady-state kinetics. (A) Voltage-dependent Ka activation and inactivation gating functions. (B) Ka steady-state current-voltage relationship. Dashed grey line highlights the voltage at which peak current is reached.

Considering these dynamics, unlike the other potassium conductances, the Ka channel has immediate increasing activity upon depolarisation with its conductance peaking at -27.4 mV. To understand how this may impact the NMDA-mediated nonlinear slope, which was characterised as the largest increase in amplitude between consecutive synaptic weights, voltage traces before and after this increase are

shown below (Figure 2-10). The response peak before the large increase (pre-threshold) was -46.0 mV and the response after the largest increase (post-threshold) was -32.4 mV (Figure 2-10A). Therefore, the threshold for NMDA-mediated nonlinearity occurred within this voltage window, which coincides with K_a activity and therefore K_a plays a role in modulating the amplitude of dendritic events that occur within this range. Consequently, K_a channel suppression reduced this restriction on EPSP amplitude allowing the amplitude to increase at voltages when the K_a channel is usually most active (Figure 2-10B). To summarise, the NMDA-mediated nonlinear boost in amplitude that occurred between -46.0 mV and -32.4 mV in the control simulation (Figure 2-10A), coincided with K_a channel activity (Figure 2-9B). When the K_a conductance was suppressed and so no concurrent potassium efflux, the jump in voltage at this threshold was amplified to 19.71 mV (difference between pre- and post-threshold peak) (Figure 2-10B), compared to an amplitude of 13.6 mV in the control (Figure 2-10A).

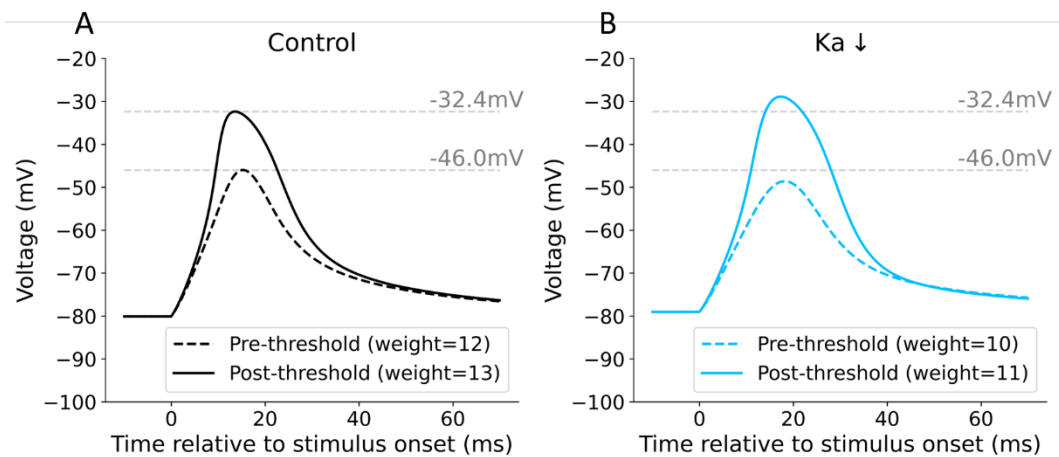


Figure 2-10: K_a channel suppression caused a large increase in amplitude at the maximum nonlinear slope. Voltage traces with pre-threshold and post-threshold synaptic weight representing the largest increases in voltage amplitudes (maximum nonlinear slope). Grey dashed lines highlight the control voltage peaks pre- and post-threshold. (A) Control, (B) K_a inhibition.

As the K_a channel was also partially blocked as part of simulating acetylcholine, it was expected that acetylcholine should also cause an increase in the nonlinear slope. On the contrary, acetylcholine caused a reduction in the slope (Figure 2-7B, Figure 2-11B), even though the K_a channel was partially suppressed. This could be explained by the fact that as acetylcholine increased the resting membrane potential and input resistance and in turn reduced the synaptic weight required to reach the maximum nonlinear slope (Figure 2-7), there is less synaptic weight and therefore less NMDA conductance (Figure 2-11, lower) at the key voltage window to drive a large increase in the amplitude.

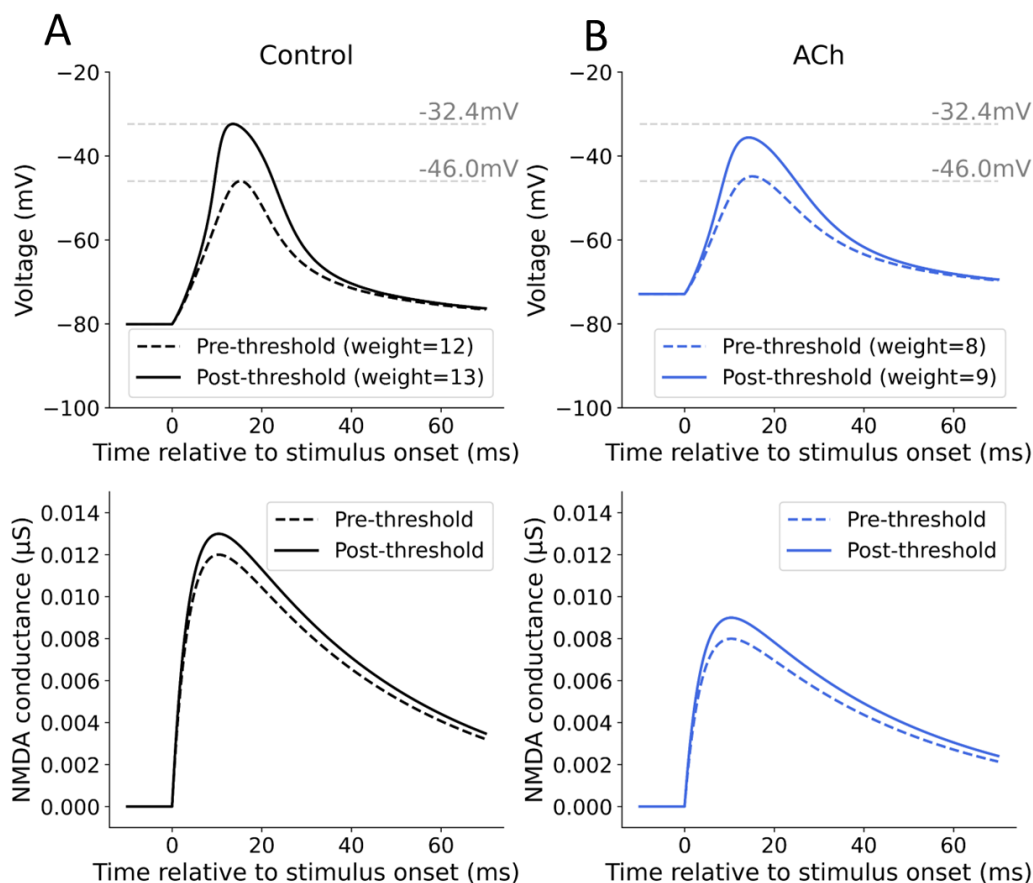


Figure 2-11: Acetylcholine caused a reduction in the voltage amplitude at the maximum nonlinear slope. Upper: Voltage traces with pre-threshold and post-threshold synaptic weight representing the largest increases in voltage amplitudes (maximum nonlinear slope). Grey dashed lines highlight the control voltage peaks pre- and post-threshold. Lower: NMDA conductance at pre- and post-threshold weights. (A) Control, (B) Acetylcholine.

Additionally, Kir inhibition reduced the synaptic weight threshold less than acetylcholine but had a very similar impact on the nonlinear slope (Figure 2-12). Therefore, at the key voltage window, even though there was less NMDA conductance with acetylcholine, the partial suppression of Ka allowed the nonlinear slope to reduce to a lesser extent than if it was fully active. Indeed, as is shown in Figure 2-12, there seemed to be a correlation between the change in synaptic weight and the change in the nonlinear slope whereby a greater reduction in the synaptic weight threshold was associated with a greater reduction in the nonlinear slope. This correlation was particularly strong with Kca, Km and Kir blocks, however Ka suppression and acetylcholine modulation did not wholly fit the correlation, due to Ka suppression having a remarkable increase on the response amplitude at the nonlinearity threshold. To summarise, as acetylcholine reduced the synaptic weight threshold more so than Kir suppression, it could have also been expected to reduce the nonlinear slope more so than Kir inhibition (Figure 2-12). Fitting a linear regression model to the Kir, Km and Kca data points in Figure 2-12 predicted acetylcholine to have an additional 42% reduction in the nonlinear slope (from -4.36 to -6.20 mV/weight). However, this reduction was opposed by acetylcholine's partial Ka suppression.

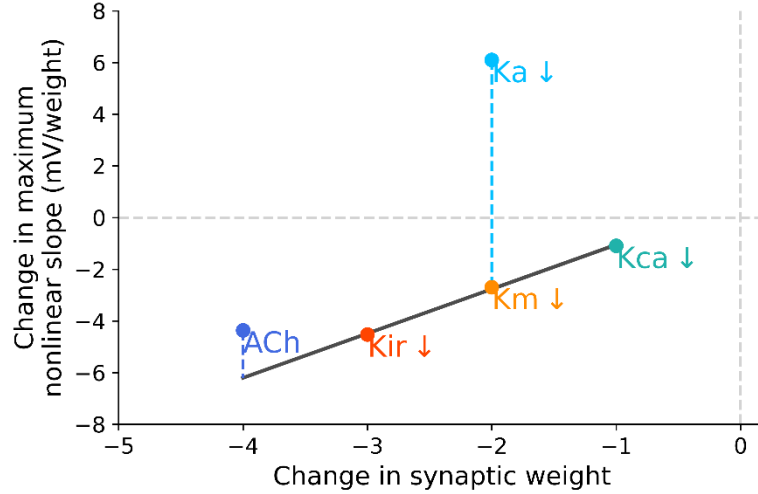


Figure 2-12: Change in nonlinear slope as a function of the change in synaptic weight required to reach the slope. Each point reflects the change in nonlinear slope and the change in synaptic weight required to reach the slope for each of the potassium channel blocks. The line of best fit shown was calculated using Kir, Km and Kca data points.

2.3.2 Heterogeneity of nonlinear dendritic integration in a reconstructed CA3 neuron model

A reconstructed CA3 neuron model was subsequently used to investigate the cholinergic modulation of NMDA spikes across the whole dendritic tree, specifically in CA3 morphology. In this model, an AMPA synaptic input was included in addition to the NMDA input to create a more physiological representation and rather than increasing the synaptic weight, the number of synapses stimulated within a dendritic branch section were increased. The inputs were positioned within a single dendritic branch section, 1 μ m apart and stimulated simultaneously, assuming clustered inputs on one branch are from the same axon or pathway (Sorra and Harris, 1993).

To determine how well the model reflected experimental data on synaptic integration properties in CA3 neurons, Figure 2-13 shows example traces (Figure 2-13A, B) and averaged nonlinear curves (Figure 2-13C, D) comparing data from Makara and Magee (2013) with the model outputs. Makara and Magee (2013) stimulated increasing numbers of synapses via glutamate uncaging in the SO and SR dendrites of CA3 pyramidal neurons. The upper panels in Figure 2-13A and B show voltage traces recorded at the soma with AMPA and NMDA transmission intact. The lower panels compare AMPA-only transmission. Averaged input-output curves for control (black) and AMPA only (grey) input for the experimental data (Figure 2-13C) and the model (Figure 2-13D) are also shown. These plots demonstrate that the experimental and model example traces had similar waveforms and that the divergence between the control and AMPA-only curves (Figure 2-13C, D) occurred at a similar number of inputs (2-3). Therefore, the NMDA-mediated nonlinearity observed in this model accurately reflected experimental data.

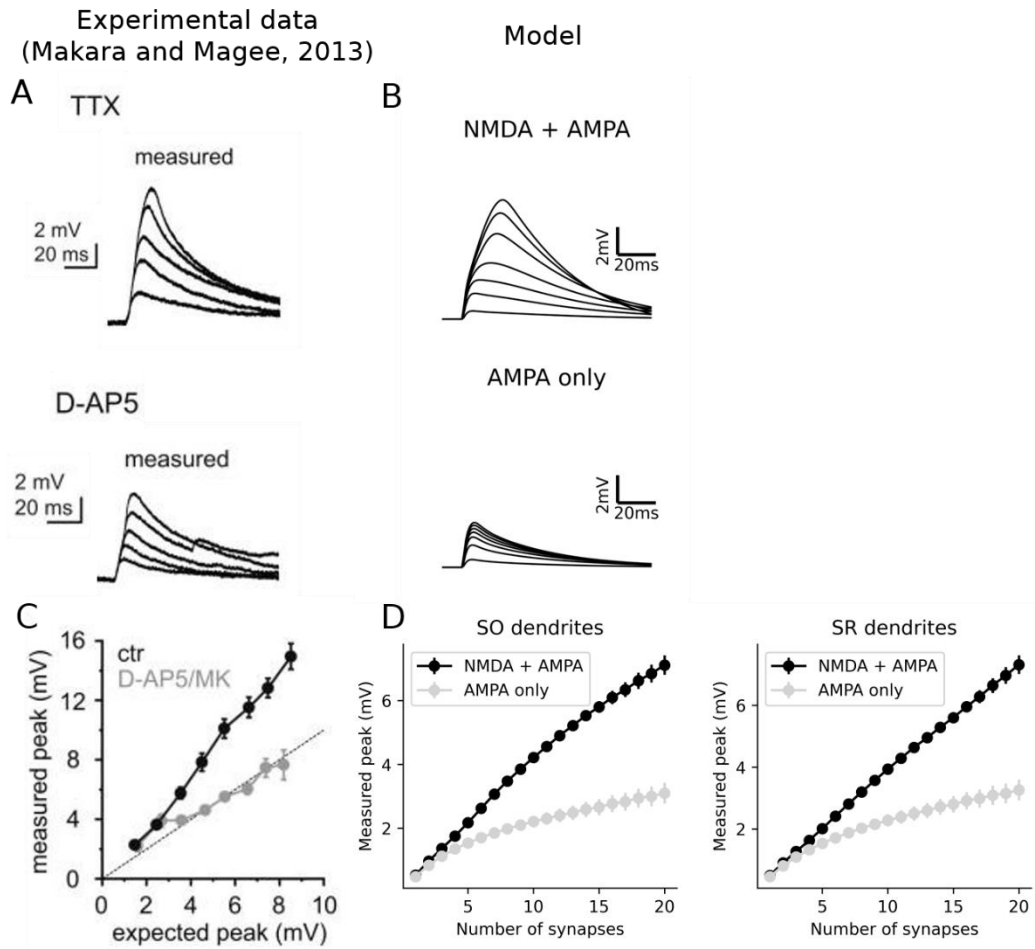


Figure 2-13: Comparison of model simulations with experimental data from Makara and Magee (2013). (A) The experimental figures were taken from Makara and Magee (2013). (A) Example experimental traces (Makara and Magee, 2013: Figure 3B+E) with increasing synapse numbers. The bottom panel represents an AMPA only response, with NMDARs blocked with D-AP5. (B) Example traces from the model, reflective of A. (C) Average expected vs measured peak amplitudes in control and with D-AP5 (Makara and Magee, 2013: Figure 3F). (D) Number of synapses stimulated vs average measured peak amplitudes across stratum oriens (SO) (left) and radiatum (SR) (right) dendrites from the model.

Figure 2-14 shows the reconstructed CA3 neuron morphology as well as example voltage traces from the six dendritic sections highlighted in Figure 2-14A. Figure 2-14B emphasises the variation in responses between dendrites and shows a clear effect of enlarged responses in the dendrite as you move further away from the soma. On the other hand, responses recorded in the soma got smaller the more distal the inputs, due to attenuation of the response (Figure 2-16A). Here, the same weight of synaptic input was used for all dendrites, however it is thought that the synaptic weights of the distal inputs are increased, in order to generate comparable responses between SR and SLM inputs at the soma (Baker et al., 2011; Hyun et al., 2015). Also, in comparison to the two-compartment model, these dendritic voltage traces exhibit two phases reflective of the AMPA and NMDA input components. The initial fast response is mediated by the AMPA component whereas the slower dynamics that display nonlinear increases in amplitude are mediated by the NMDA component.

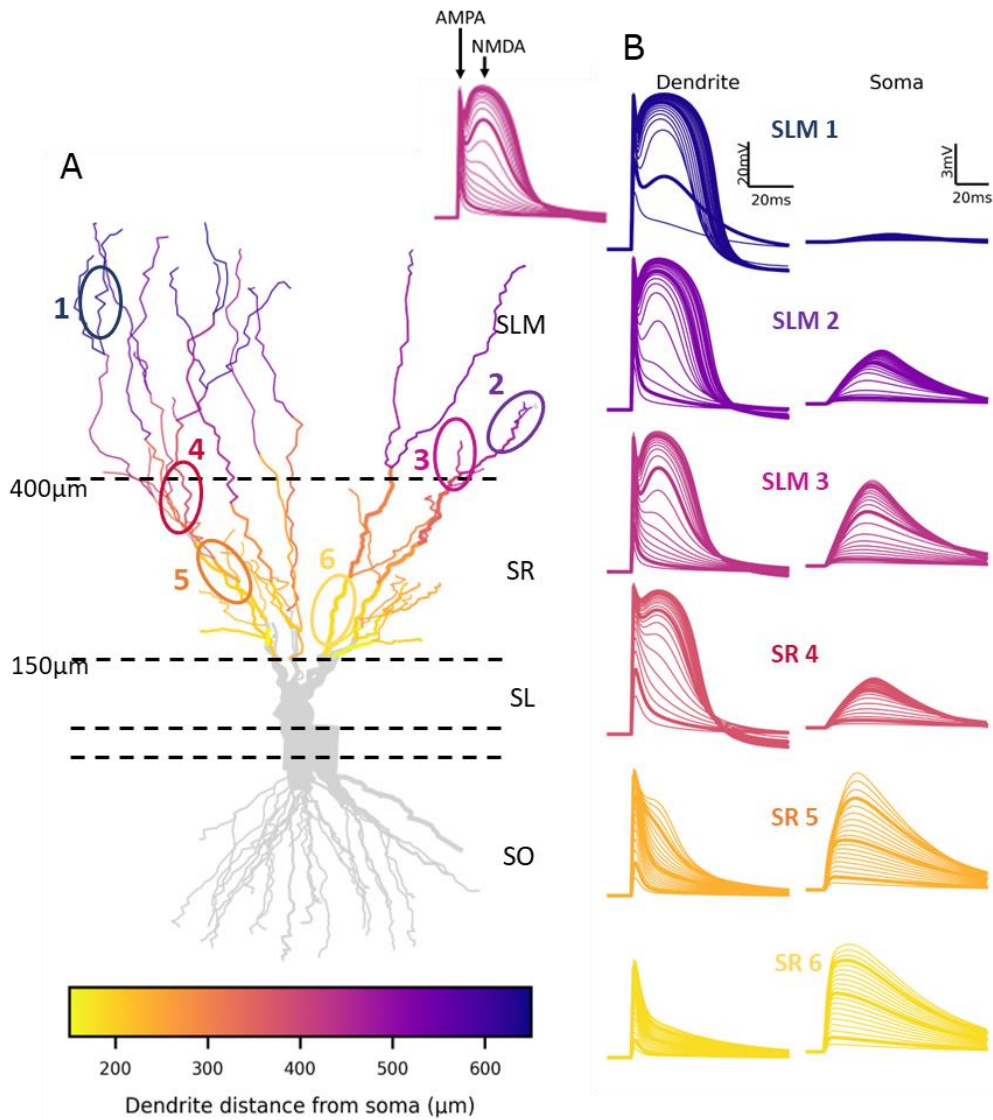


Figure 2-14: Voltage trace examples from synaptic stimulation in different dendrites in the SR and SLM recorded in the dendrite and soma. (A) Reconstructed CA3 pyramidal neuron. Coloured dendrites represent dendrites used in the simulation and the colour corresponds to the distance from the soma. Values on the left reflect the approximate distance from the soma that separates the apical dendritic layers. The six circled dendrite sections represent the voltage trace examples in B. Inset highlights AMPA and NMDA-mediated responses. (B) Voltage trace examples recorded in the dendrite (left) and soma (right) from increasing the number of stimulated synapses from 1 to 20 on the dendritic sections labelled in A. Thicker lines represent 2, 10 and 17 synaptic inputs.

Additionally, looking at the reconstructed neuron morphology in Figure 2-14A, the dendritic section thickness changed across the dendritic tree. Distal dendrites in the SLM region were thinner compared to the more proximal SR dendrites. This difference in dendrite thickness had an influence on the dendritic input resistance measurement, as is shown in Figure 2-15A. As the diameter increased, in dendrites closer to the soma, the dendritic input resistance reduced. However, this relationship was not linear, and the most distal dendrites that had a similar diameter to other SLM dendrites had a significantly greater input resistance (Figure 2-15A). Dendrite position within the tree can also influence the branch input resistance, specifically whether a section is at the end of a branch, known as a terminal

dendrite. Figure 2-15B shows a significant difference ($p < 0.05$) in input resistance between terminal ($1970.20 \pm 197.17 \text{ M}\Omega$) and non-terminal ($1177.75 \pm 181.39 \text{ M}\Omega$) dendrite sections in the SLM region.

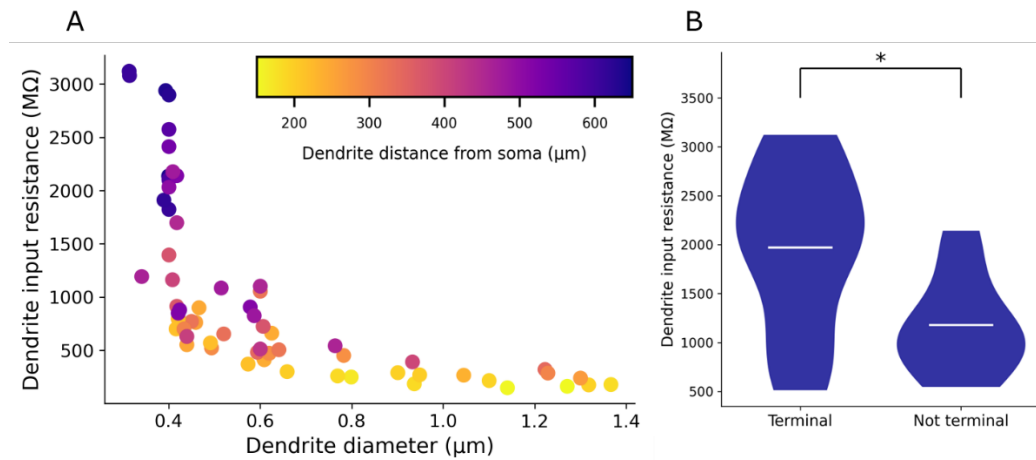


Figure 2-15: Dendrite diameter and position in tree effect on dendritic input resistance. (A) Relationship between dendrite section diameter and the measured section input resistance. Data points are from all coloured dendritic sections in Figure 2-14A. Points are additionally colour-coded according to dendrite distance from the soma. (B) Difference in input resistance between terminal ($n = 18$) and non-terminal ($n = 8$) dendrite sections in the SLM region. * = $p < 0.05$ (Wilcoxon rank sum).

To visualise the nonlinearity of the amplitudes across different dendrites, the amplitude of the NMDA component of each response was measured and plotted against the number of synapses stimulated (Figure 2-16). To isolate the NMDA response and measure the resulting nonlinear increases in amplitude, AMPAR-only stimulations were subtracted from the combined AMPA + NMDA traces shown in Figure 2-14. Figure 2-16B and C reveal the diversity in nonlinearity between different dendritic branches and highlight the prominent proximodistal effect in which the steep nonlinear portion of the curve occurs at lower numbers of synapses in the distal SLM dendrites (Figure 2-16B), compared to the more proximal SR dendrites (Figure 2-16C).

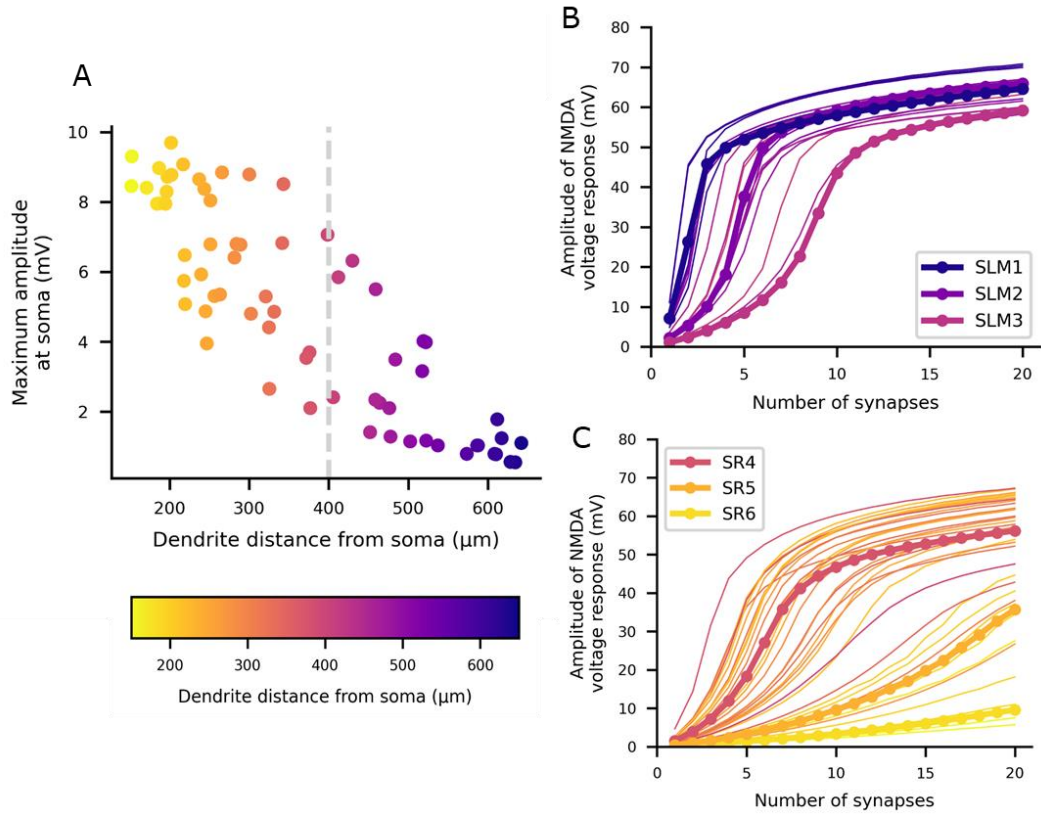


Figure 2-16: Heterogeneous nonlinear integration throughout the dendritic tree. (A) Amplitude measured at the soma in relation to the stimulated dendrite distance from the soma. (B+C) Amplitude of the dendritic NMDA response with increasing numbers of synapses stimulated in the SLM (B) and SR dendrites (C). The labelled data points refer to the highlighted six example dendrites in the previous Figure.

To quantify the nonlinearity threshold across different dendrites, the number of synapses at the maximum slope of the curves in Figure 2-16B and C were plotted on the neuron morphology (Figure 2-18A) and against the dendrite distance from the soma (Figure 2-18B). As anticipated, the nonlinear threshold number of synapses was well correlated with dendrite distance from the soma. To investigate possible explanations for this effect, the nonlinear threshold was correlated to dendritic diameter (Figure 2-17A) and input resistance (Figure 2-18C), as these are both correlated with dendrite distance from the soma (Figure 2-15A). The NMDA spike threshold was well correlated with dendrite diameter, with a higher diameter associated with a higher threshold number of synapses. This relationship was slightly stronger in the SR dendrites ($R^2 = 0.745$) compared to the SLM dendrites ($R^2 = 0.590$). However, dendritic input resistance displayed an even tighter relationship and the R^2 values suggested that the number of synapses required for nonlinearity was likely explained by the dendritic input resistance (Figure 2-18C, SR R^2 : 0.804, SLM R^2 : 0.783). It is also important to note the nonlinear threshold relationships were almost identical at the soma (right) and the dendrite (left) (Figure 2-18B, C).

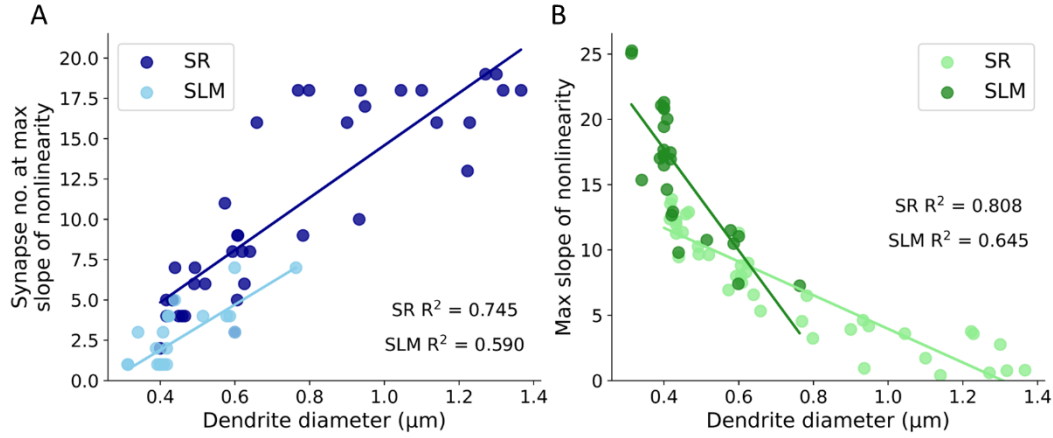


Figure 2-17: A reduced dendrite diameter is associated with a higher slope of nonlinearity and a lower number of synapses at the nonlinear threshold. Dendrite diameter correlated with (A) the number of synapses required to reach the slope of nonlinearity and (B) the maximum slope of nonlinearity. The R^2 values of the linear regressions are displayed on each plot for the SR and SLM dendrites separately.

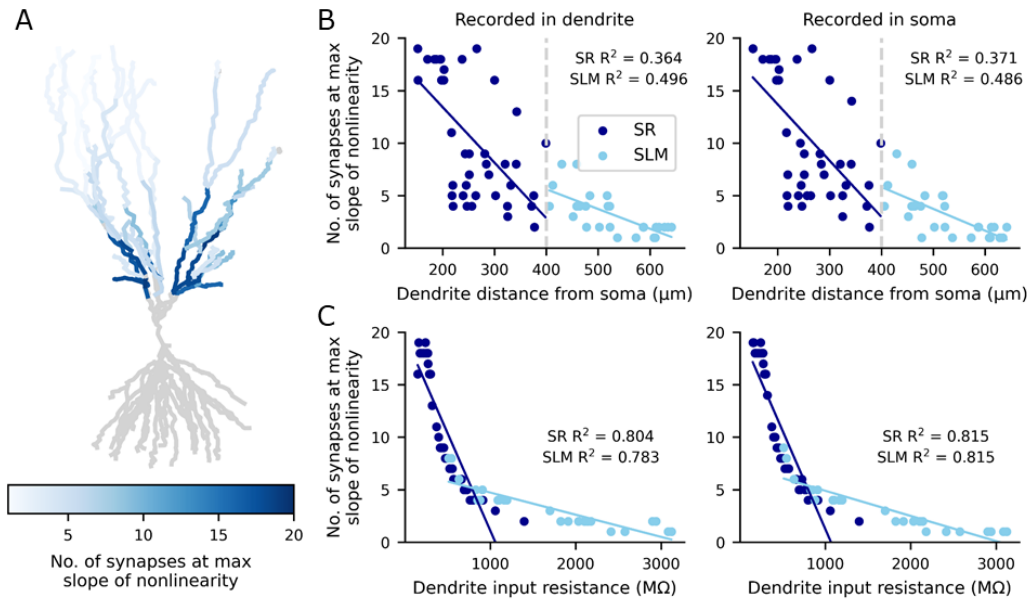


Figure 2-18: Dendritic input resistance explains NMDA spike threshold differences across dendritic tree. (A) Number of synapses required to generate nonlinearity on different dendritic branches. (B+C) Number of synapses required to generate nonlinearity in the dendrite (left) and at the soma (right) with increasing distance from the soma (A) and increasing dendritic input resistance (C). The R^2 values of the linear regressions are displayed on each plot for the SR and SLM dendrites separately.

A less evident impact was the change in the slope of nonlinearity between different dendritic branches (Figure 2-19). From looking at the morphology (Figure 2-19A) and the left plot in Figure 2-19B, there does seem to be a proximodistal effect on the dendritic nonlinear slope in which the further away the dendrite from the soma, the steeper the slope of nonlinearity (SLM $R^2 = 0.403$; SR $R^2 = 0.250$). This difference again could be explained well by dendrite diameter (Figure 2-17B, SLM $R^2 = 0.645$; SR $R^2 = 0.808$) and input resistance (Figure 2-19C, left; SLM $R^2 = 0.597$; SR $R^2 = 0.875$) and in fact here, the

dendrite diameter ($R^2 = 0.645$) explained the slope of nonlinearity slightly better than the input resistance ($R^2 = 0.597$) in the SLM dendrites. Interestingly, the nonlinear slope measured at the soma appeared to have a very different relationship to the dendrite location and input resistance (Figure 2-19B, C, right). However, the maximum slope values at the soma are considerably smaller than in the dendrite as the voltage attenuates with propagation through the dendritic tree and this is causing the relationship shown here. To counteract the attenuation effect of the voltage, the slope was calculated with the amplitudes normalised to the maximum which made it easier to compare the slope between the different dendritic inputs (Figure 2-20).

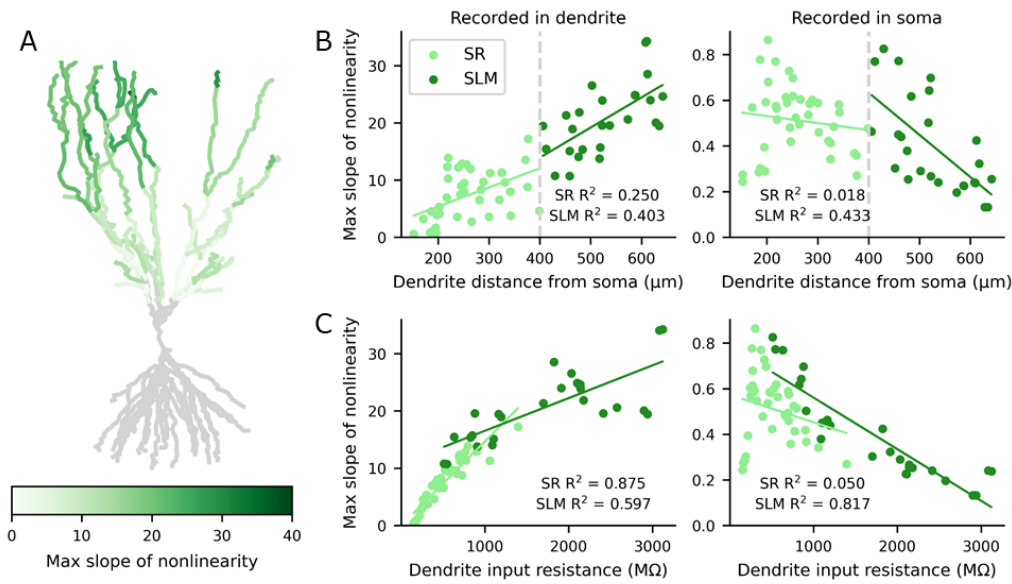


Figure 2-19: Variation in the slope of nonlinearity across dendritic branches. (A) Maximum slope of nonlinearity across different dendritic branches. (B+C) Maximum slope of nonlinearity in the dendrite (left) and at the soma (right) with increasing distance from the soma (B) and increasing dendritic input resistance (C). The R^2 values of the linear regressions are displayed on each plot for the SR and SLM dendrites separately.

By calculating the maximum nonlinearity slope in this way, the relationships are similar between the dendrite and the soma and as before can be explained by the dendritic input resistance (Figure 2-20). Inputs to different dendrites in the SR region did not appear to impact the nonlinear slope measured at the soma ($R^2 = 0.207$), whereas dendrite distance in the SLM region had a much stronger impact ($R^2 = 0.518$, Figure 2-20A, right). This also translated to the impact dendritic input resistance had on the nonlinear slope at the soma (Figure 2-20C, right), with it having a larger effect on the distal SLM dendrites ($R^2 = 0.836$), compared to the SR dendrites ($R^2 = 0.648$).

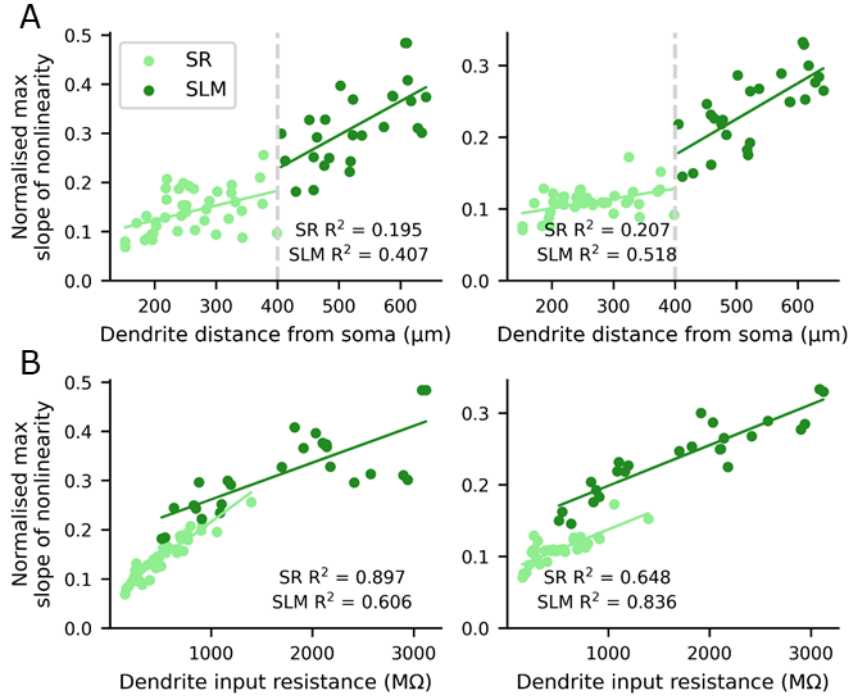


Figure 2-20: Maximum slope of nonlinearity calculated from normalised amplitudes. (A+B) Normalised maximum slope of nonlinearity in the dendrite (left) and at the soma (right) with increasing distance from the soma (A) and increasing dendritic input resistance (B). The R^2 values of the linear regressions are displayed on each plot for the SR and SLM dendrites separately.

2.3.3 Cholinergic modulation of nonlinear integration in a reconstructed CA3 neuron model

The simulations in the two-compartment model predicted that acetylcholine reduced the amount of synaptic input required to generate nonlinearity in the dendrite. The effect of acetylcholine was now tested in the reconstructed neuron model to see if it produced this same effect, as well as to see how dendrites across the whole dendritic tree would respond. Figure 2-21B shows voltage traces of increasing synaptic input on six example dendrites (Figure 2-21A) with and without simulated acetylcholine. The colour coding represents dendrite distance from the soma. The acetylcholine was simulated in the same way as the previous model, by blocking K_a , K_m , K_{ca} and K_{ir} conductances. As would be expected, acetylcholine depolarised the resting membrane potential and increased the EPSP half-width (Figure 2-21B). In Figure 2-21C the amplitude of the NMDA-mediated response is plotted against the number of synapses stimulated and shows that acetylcholine (blue) shifted the curves slightly to the left, indicating less input was needed to reach the same amplitude. The shift in the curve here is less evident than in the two-compartment model.

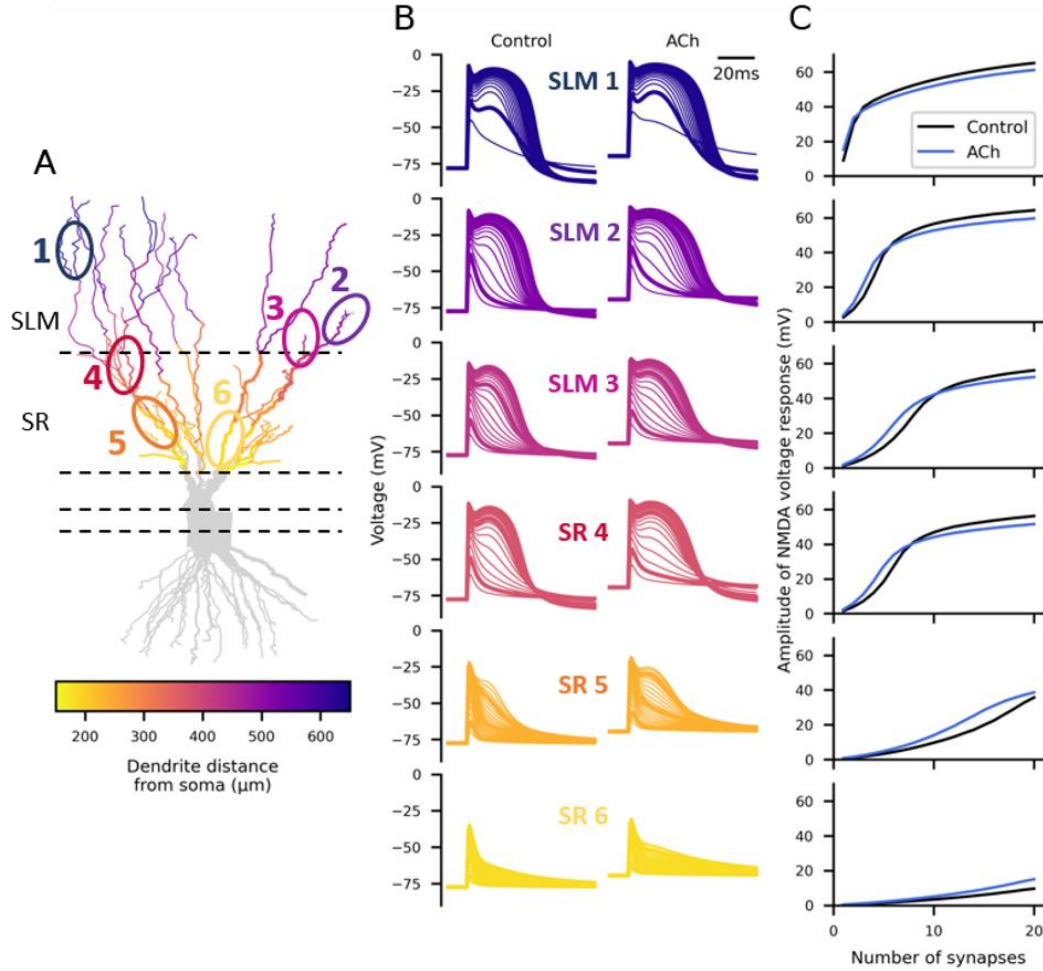


Figure 2-21: EPSP example traces from synaptic stimulation with cholinergic modulation in different dendrites in the SR and SLM. (A) Reconstructed CA3 pyramidal neuron. Coloured dendrites represent dendrites used in the simulation and the colour corresponds to the distance from the soma. The six circled dendrite sections represent the voltage trace examples in B. (B) Voltage trace examples recorded in the dendrite without (left) and with simulated acetylcholine (ACh) (right) on the dendritic sections labelled in A. (C) Amplitude of NMDA-mediated voltage response with increasing synapse number for each of the example dendrites in B, with (blue) and without (black) cholinergic modulation.

Next, the extent of this modulation by acetylcholine was investigated across different dendrites within the dendritic tree (Figure 2-22). Overall, the NMDA spike threshold (Figure 2-22A) in SR dendrites appeared to be modulated to a higher degree compared to dendrites in the SLM region, with acetylcholine causing a larger reduction in the number of inputs required in dendrites closer to the soma. Cholinergic modulation did not seem to affect a large proportion of the SLM dendrite nonlinear thresholds, most likely since the number of synapses needed were very low to begin with. Regarding acetylcholine's effect on the maximum slope of nonlinearity (Figure 2-22B), this seemed to have more of an influence in the SLM dendrites, particularly the most distal dendrites, and minimal impact in the SR dendrites.

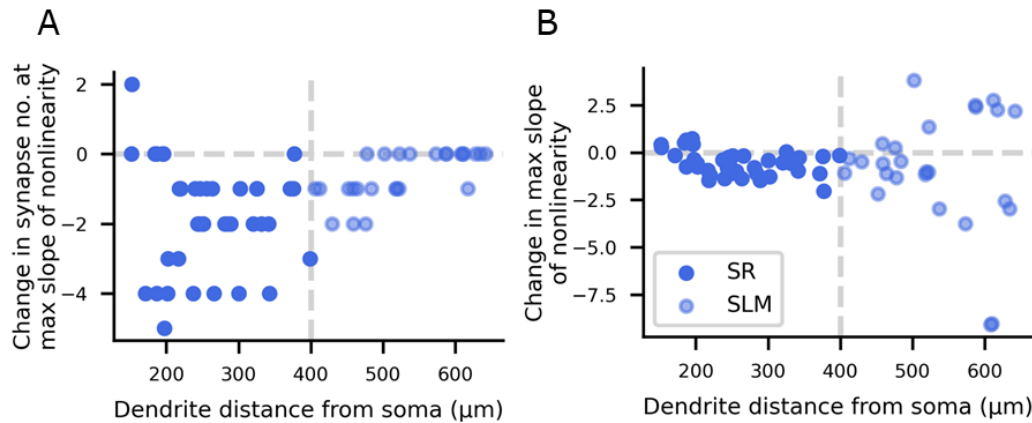


Figure 2-22: Extent of cholinergic modulation across all dendrites. (A) Change in the number of synapses required to reach the maximum slope of nonlinearity with acetylcholine in all dendrites. (B) Change in the maximum slope of nonlinearity with acetylcholine in all dendrites.

To explore whether the resting dendrite input resistance was responsible for the varying cholinergic effects across different dendrites, the change in the number of synapses required to produce nonlinearity with acetylcholine was plotted against the initial dendrite input resistance (Figure 2-23). The change in NMDA spike threshold was well correlated to the input resistance in the SLM dendrites ($R^2 = 0.706$), but less so in the SR dendrites ($R^2 = 0.080$) and therefore, the initial dendrite input resistance did not fully explain the changes seen with acetylcholine.

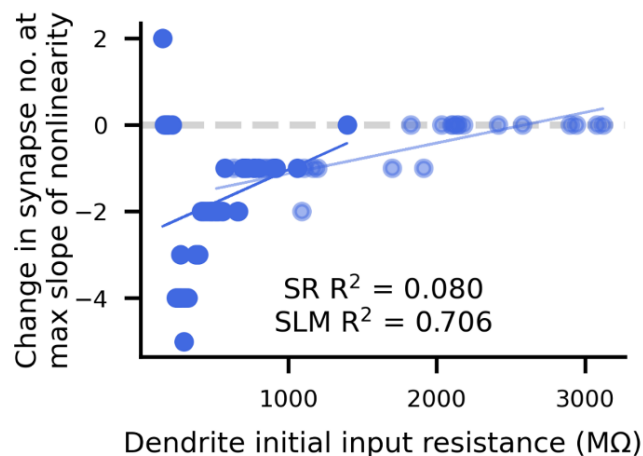


Figure 2-23: Impact of dendrite initial input resistance on cholinergic effect. Change in the number of synapses required to reach nonlinearity in relation to the initial dendritic input resistance. The R^2 values for SR and SLM dendrites are displayed. Light blue = SLM dendrites, dark blue = SR dendrites.

As stated above, in a proportion of SLM dendrites cholinergic modulation did not seem to affect the number of synapses required for nonlinearity. In distal dendrites with a very high initial resting input resistance of more than 2000 MΩ there was no change in the synapse number threshold with cholinergic

modulation as the number of synapses required for nonlinearity was already at 1 and therefore could not be reduced further. Additionally, acetylcholine did not affect the synapse number threshold in a small group of proximal SR dendrites (Figure 2-22A). These dendrites had an initial very low resting input resistance of less than 220 M Ω and in turn a very low slope of nonlinearity in comparison to other SR dendrites. Due to their low initial input resistance, the EPSP NMDA component from stimulated synaptic inputs did not reach a high enough voltage (-67.28 ± 1.75 mV) for a significant NMDA-mediated nonlinear effect (Figure 2-24, Figure 2-21 (SR6 example dendrite)). Cholinergic modulation did increase the peak of the NMDA voltage response (-53.90 ± 2.54 mV) in these dendrites (Figure 2-24, right), but still by not enough to reach the key NMDA voltage window for nonlinearity and therefore did not have an influence on the threshold number of synapses.

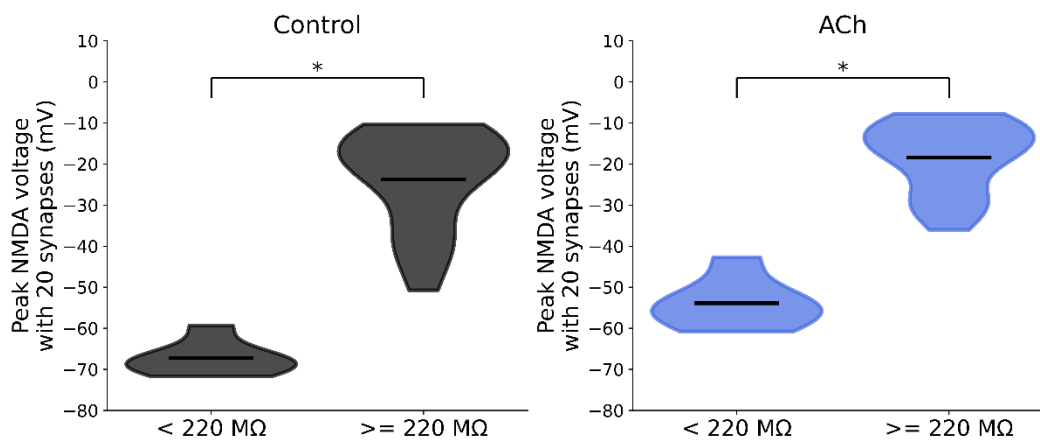


Figure 2-24: Proximal SR dendrites with a low resting input resistance reach a significantly lower maximum NMDA voltage peak. SR dendrites were separated into two groups based on their resting input resistance (< 220 M Ω : n = 6, ≥ 220 M Ω : n = 34) to investigate why the NMDA spike threshold for the low input resistance group was unaffected by acetylcholine. Left: control; Right: Ach. * = $p < 0.05$ (Wilcoxon rank-sum).

Removing these SR dendrites with an initial very low input resistance, as well as the SLM dendrites with an initial synapse number threshold of 1, unveiled a correlation between the change in resting input resistance with acetylcholine and a change in the number of synapses at the maximum nonlinear slope in the remaining dendrites (Figure 2-25A, SR $R^2 = 0.840$, SLM $R^2 = 0.712$). Here, the number of synapses required was reduced to a greater extent in dendrites that had a higher increase in input resistance. This reflects the results in Figure 2-18C whereby the input resistance was highly predictive of the number of synapses at the maximum nonlinear slope. Additionally, the percentage reduction in the number of synapses with acetylcholine was generally within a similar range, between 15 and 35%, regardless of the change in input resistance (Figure 2-25B). Overall, in the majority of dendrites, the acetylcholine-mediated reduction in the absolute number of synapses required to reach the nonlinear threshold could be explained by the relative change in input resistance (Figure 2-25A) and that the percentage change in synapse number was similar across all dendrites (Figure 2-25B).

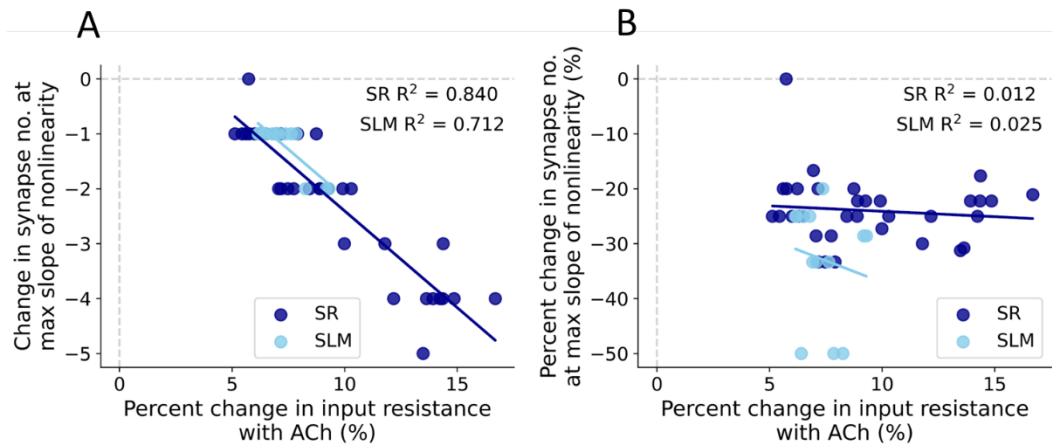


Figure 2-25: Change in dendritic resting input resistance with acetylcholine explained the extent of reduction in synapse number at the maximum slope of nonlinearity in the majority of dendrites. (A) Absolute change in number of synapses required for nonlinearity; (B) Percent change in number of synapses required for nonlinearity. SLM dendrites that had an initial threshold synapse number of 1 and SR dendrites with a resting input resistance of less than 220 M Ω were excluded from these correlations.

As was shown in Figure 2-22B, acetylcholine interestingly had variable effects on the nonlinear slope across the dendritic tree. In the majority of dendrites there was a unified small reduction in the slope with acetylcholine (Figure 2-22B) as was seen and analysed in the two-compartment model (Figure 2-11). However, in SLM dendrites more than 500 μm from the soma with a very high input resistance, above 1800 M Ω , there was high variability in the impact of acetylcholine on the nonlinear slope. Interestingly, acetylcholine reduced the slope in one group of dendrites but increased it in another group (Figure 2-22B). When plotting the change in slope on the neuron morphology, the two groups displaying opposite effects on the nonlinear slope were mostly clustered on two distinct trees (Figure 2-26).

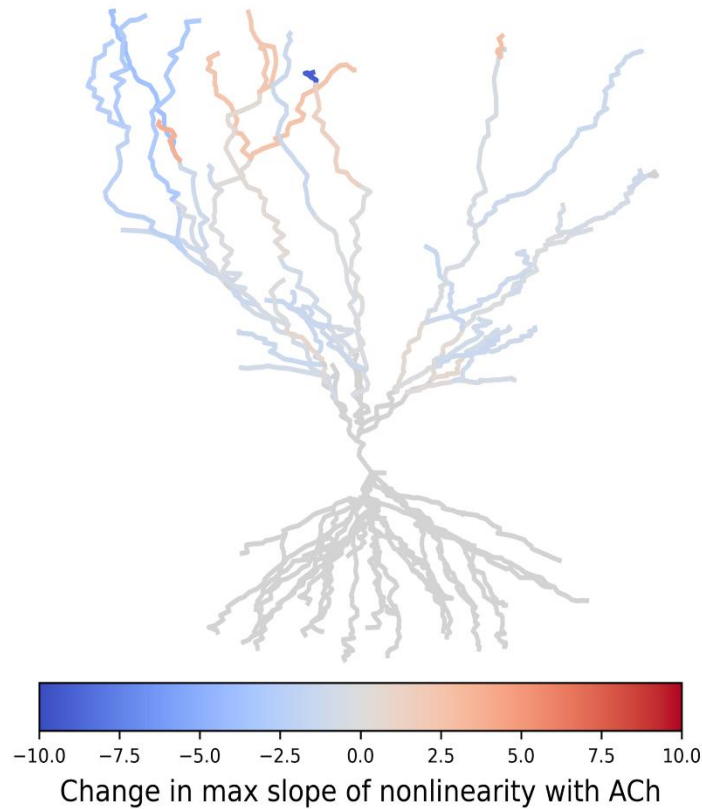


Figure 2-26: Change in maximum slope of nonlinearity with acetylcholine on different dendrite branches. Blue represents a reduction in the maximum slope of nonlinearity whereas red represents an increase.

Figure 2-27 compares different dendritic properties with the acetylcholine-driven change in the nonlinear slope to investigate what could be causing the variability between the contrasting effects in these most distal dendrite sections (Figure 2-27A). All dendrites in both groups were more than 500 μm from the soma (Figure 2-27F) and were nearly all terminal dendrites. There was no difference in dendrite length (Figure 2-27B), diameter (Figure 2-27D), number of compartments (Figure 2-27C), number of branchpoints to the soma (Figure 2-27E) or K_a peak conductance (Figure 2-27H) between the two groups. There was however a significant difference in baseline input resistance (Figure 2-27G), possibly produced from a slight but not significant difference in dendrite diameter (Figure 2-27D). The group of dendrites in which acetylcholine increased the slope had a lower baseline input resistance ($2037.38 \pm 46.73 \text{ M}\Omega$) compared to the surrounding distal dendrites ($2839.00 \pm 116.06 \text{ M}\Omega$) (Figure 2-27G) and consequently a lower baseline nonlinear slope (Figure 2-27I).

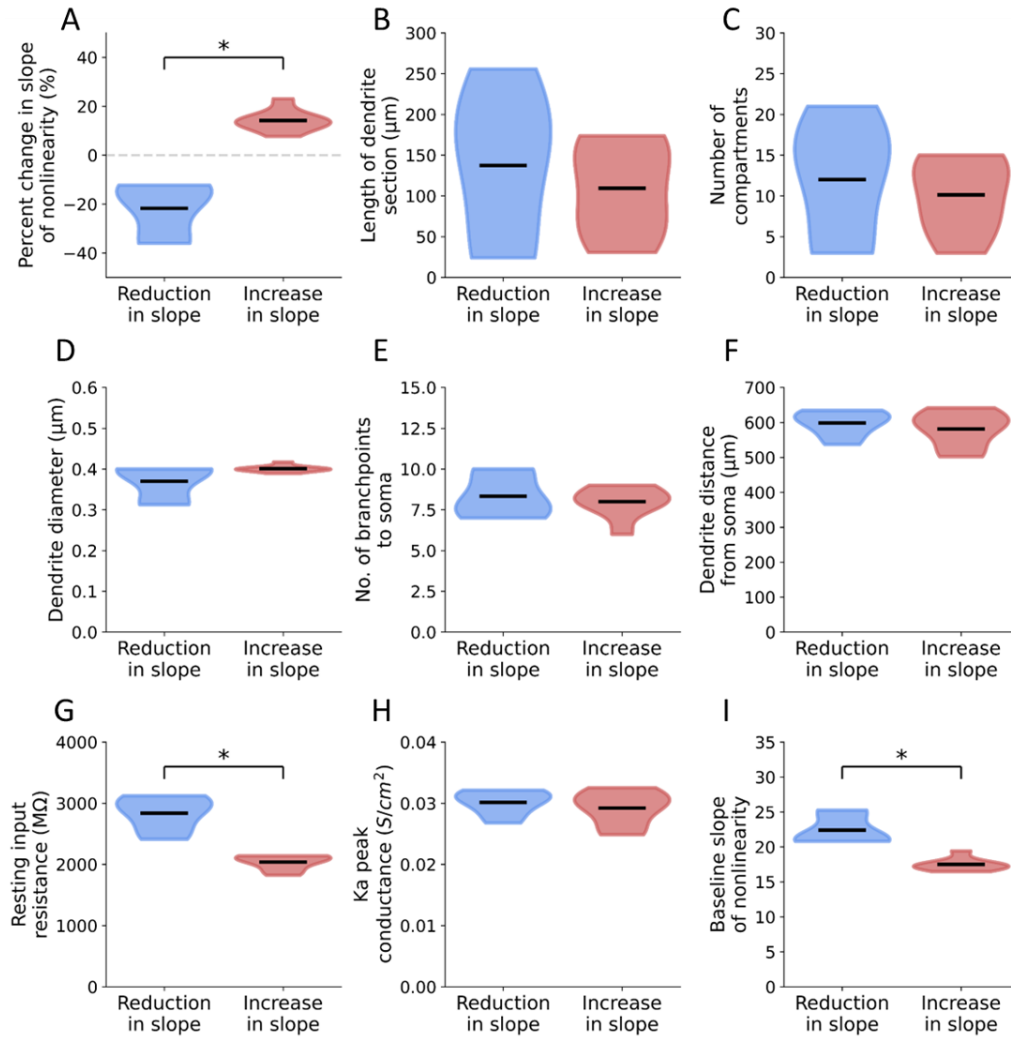


Figure 2-27: Comparisons between the distal dendrite groups in which acetylcholine caused opposing effects on the slope of nonlinearity. (A) Percent change in the slope of nonlinearity. (B) Length of dendrite section. (C) Number of compartments in dendrite section. (D) Dendrite diameter. (E) Number of branchpoints to the soma. (F) Distance of dendrite from the soma. (G) Baseline resting input resistance. (H) Ka peak conductance. (I) Baseline slope of nonlinearity. * = $p < 0.05$ (Wilcoxon rank sum). Reduction in slope group: $n = 6$. Increase in slope group: $n = 7$.

The two-compartment model showed that as the synaptic weight threshold was reduced with acetylcholine there was therefore less NMDA conductance driving the nonlinear increase at the NMDA spike voltage window (Figure 2-11). However, in these distal dendrites in the reconstructed model, cholinergic modulation did not impact the synapse number threshold because it was already at 1 and therefore the NMDA conductance at the threshold was the same in both the control and with acetylcholine. Consequently, there was a different explanation for the reduction in the nonlinear slope in these dendrites as well as an alternative explanation for the contrasting dendrites in which the slope increased. To further investigate these differences in the change in the nonlinear slope, the NMDA-mediated voltage traces, before (pre-threshold) and after (post-threshold) the largest increase in amplitude, were plotted for each group of dendrites from Figure 2-27.

In distal dendrites with an input resistance above 2300 M Ω and an initial synapse threshold of 1, acetylcholine reduced the nonlinear slope (Figure 2-27). The post-threshold NMDA-mediated amplitude was similar in the control and with acetylcholine (Figure 2-28A, control: 33.49 ± 2.12 mV; ACh: 35.36 ± 1.36 mV). However, the pre-threshold NMDA-mediated amplitude was significantly increased with cholinergic modulation (Figure 2-28A, control: 11.09 ± 1.25 mV, ACh: 18 ± 1.75 mV, $p < 0.05$). Therefore, because of the very high input resistance and consequent large response from just one synaptic input in these dendrites, acetylcholine boosted the membrane potential and input resistance so that the initial EPSP reached the NMDA nonlinear voltage window with a single synaptic input. Therefore, the initial EPSP amplitude was already very high with acetylcholine and so the increase in amplitude (nonlinear slope) between the first and second response was reduced (Figure 2-28A).

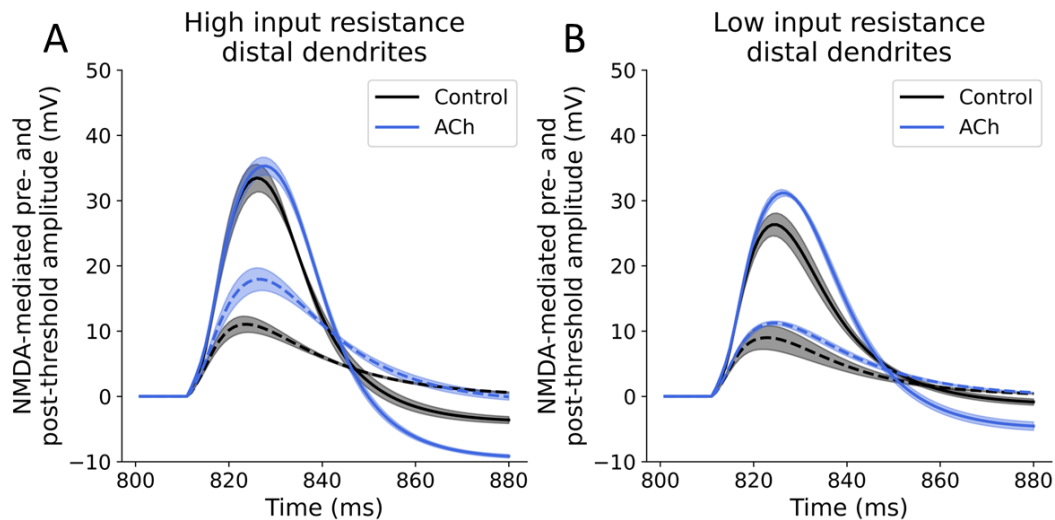


Figure 2-28: Averaged EPSP NMDA-component traces before and after the largest jump in amplitude (maximum nonlinear slope) in the distal dendrites with high (left) and lower (right) input resistance. (A) Averaged traces for the distal dendrites with a high baseline input resistance and reduction in the nonlinear slope with acetylcholine. (B) Averaged traces for the distal dendrites with a lower baseline input resistance and an increase in the nonlinear slope with acetylcholine. Dashed line = pre-threshold. Solid line = post-threshold. The nonlinear slope is the difference in amplitude between the pre- and post-threshold traces.

In comparison, the dendrite group in which acetylcholine increased the nonlinear slope had a significantly lower initial input resistance (Figure 2-27G) and therefore the control pre- and post-threshold amplitudes were lower compared to the higher input resistance dendrites (pre-threshold 9.14 ± 1.82 mV, post-threshold 26.64 ± 1.80 mV, Figure 2-28B). Also, the lower initial input resistance meant that cholinergic modulation did not increase the unitary EPSP amplitude by a large amount (control pre-threshold: 9.14 ± 1.82 mV, ACh pre-threshold: 11.39 ± 0.33 mV, Figure 2-28B). Instead,

the post-threshold amplitude increased significantly with acetylcholine (ACh post-threshold: 31.36 ± 0.59 mV).

The reason this increase occurred can be explained by considering the high K_a conductance in this dendritic region (Figure 2-29A) in conjunction with the lower input resistance at this distance from the soma (Figure 2-29B, Figure 2-29C). As was determined in the two-compartment model, the K_a conductance was the main channel responsible for modulating the slope of nonlinearity. In this reconstructed model, as explained in the Methods (section 2.2.4), the peak conductance of K_a increased with distance from the soma. Therefore, the impact of K_a suppression during cholinergic modulation could be amplified in these distal dendrites that have higher K_a levels. These dendrites in which cholinergic modulation had conflicting effects on were a similar distance from the soma and hence had a similar K_a peak conductance (Figure 2-27H). However, due to their differences in baseline input resistance (Figure 2-27G, Figure 2-29B), the initial unitary EPSP in the group with a slightly lower input resistance did not increase by a large amount with acetylcholine. Alternatively, the post-threshold response with 2 synaptic inputs increased the most with acetylcholine (Figure 2-28B) and this increase occurred within the voltage window that benefitted from partial K_a suppression, to further amplify this nonlinear response. This effect from K_a inhibition is usually obscured, as was seen with the high input resistance dendrites because they already produce a large response with very little input (Figure 2-28A).

Figure 2-29 below summarises the combined effect of high distal K_a conductance (Figure 2-29A), which is similar across these groups of dendrites, with differing baseline input resistances (Figure 2-29B). From calculating the difference between normalised K_a peak conductance and normalised input resistance (Figure 2-29C) between dendrites, it showed that the difference was highest in dendrites that had an acetylcholine-mediated increase in the slope (Figure 2-29D). Therefore, the high K_a peak conductance in distal dendrites in combination with an unusually low input resistance in a group of dendrites, explained the acetylcholine-mediated increase in the nonlinear slope.

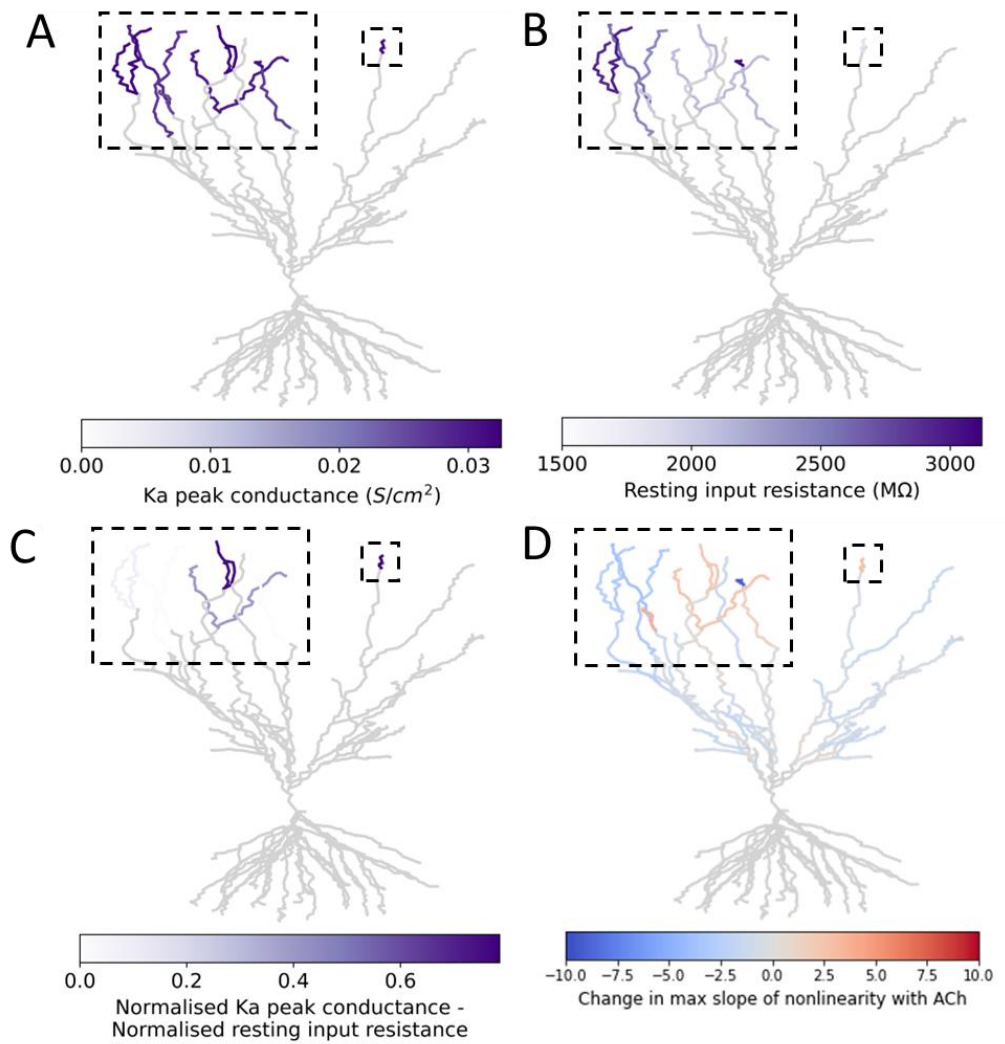


Figure 2-29: The combination of a high Ka peak conductance with a lower input resistance in the distal dendrites could explain the acetylcholine-mediated increase in the nonlinear slope. (A) Ka peak conductance was at a similar amount in all the distal dendrites. (B) Specific dendritic branches have a lower resting input resistance. (C) Overlay of normalised Ka peak conductance with normalised resting input resistance. (D) The increase in the nonlinear slope is more prominent in dendrites with a lower input resistance.

2.3.4 Effect of potassium channel inhibition on NMDA-mediated nonlinearity in the reconstructed neuron model

As in the two-compartment model, the contribution of each potassium conductance to the cholinergic effects was also assessed. Figure 2-30 shows the average change in membrane potential and input resistance across all dendrites in the SR and SLM regions upon simulating acetylcholine as well as blocking each potassium conductance separately. Simulated acetylcholine increased the resting membrane potential the highest amount, by 10.61 ± 0.02 % in SLM and 10.37 ± 0.02 % in SR dendrites, whereas blocking the Ka conductance had the least impact. Blocking the Km conductance had more of

an effect in the proximal SR dendrites as it was only present in the somatic compartment and Kir inhibition had the largest effect on resting membrane potential compared to the other potassium channels. Overall, there was little variability between different dendrites. On the other hand, the change in input resistance was more variable between dendrites. Blocking the Ka conductance produced the greatest increase in input resistance in the SLM dendrites ($10.21 \pm 0.82 \%$), whereas blocking the Km channel had the largest effect in the SR dendrites ($12.66 \pm 1.40 \%$ increase). This again could be explained by the fact that the Km conductance was only present at the soma whereas the Ka conductance was expressed more strongly in the distal dendrites. Blocking the Kca conductance also had a significant effect on the dendritic input resistance but this was less pronounced than the other conductances.

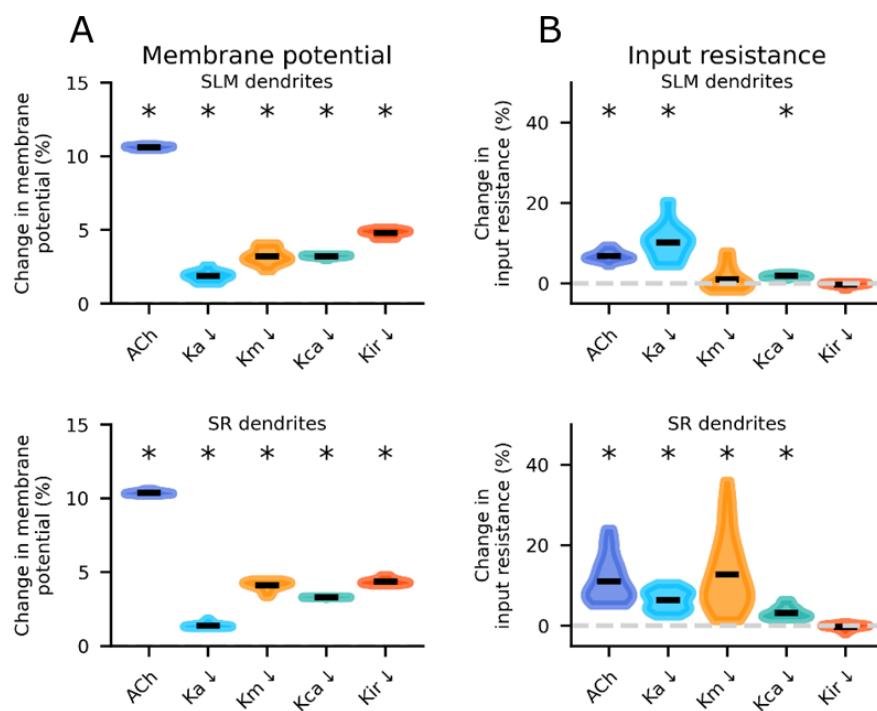


Figure 2-30: Change in resting membrane potential and input resistance in dendrites upon blocking potassium channels. (A) Percent change in membrane potential in SLM (upper) and SR (lower) dendrites. (B) Percent change in dendritic input resistance in SLM (upper) and SR (lower) dendrites. * indicates $p < 0.01$ (Bonferroni adjusted alpha value).

The effect of blocking each potassium channel on the number of synapses required to generate nonlinearity as well as the maximum slope of nonlinearity was also assessed (Figure 2-31). In the SLM dendrites, the number of synapses required to generate nonlinearity was reduced the most with acetylcholine (by $16.43 \pm 3.58 \%$, from 2.50 ± 0.37 to 1.88 ± 0.25) and there was also a significant reduction with Ka inhibition ($9.66 \pm 2.86 \%$). In the SR dendrites, again acetylcholine created the largest reduction in NMDA spike threshold ($20.07 \pm 1.76 \%$, from 10.30 ± 0.92 to 8.50 ± 0.88) and blocking each of the potassium conductances also significantly reduced the threshold, but to a lesser extent. No one particular conductance seemed to be driving the effect seen with acetylcholine. The effect of reducing the threshold was overall higher in the SR dendrites compared to the SLM dendrites most

likely because, as explained previously, the baseline thresholds in the SLM dendrites were already very low. Similar to the two-compartment model, the change in the maximum slope of nonlinearity was mostly impacted by Ka channel inhibition (8.78 ± 2.99 % increase, Figure 2-31B). The Kca conductance also seemed to slightly modulate the nonlinear slope in the SLM dendrites. Interestingly, acetylcholine had little effect on the maximum slope of nonlinearity and in the SLM dendrites caused a small decrease, whereas in the SR dendrites produced a small increase in the slope. Blocking the Ka channel was the only potassium conductance that impacted the slope in the SR dendrites.

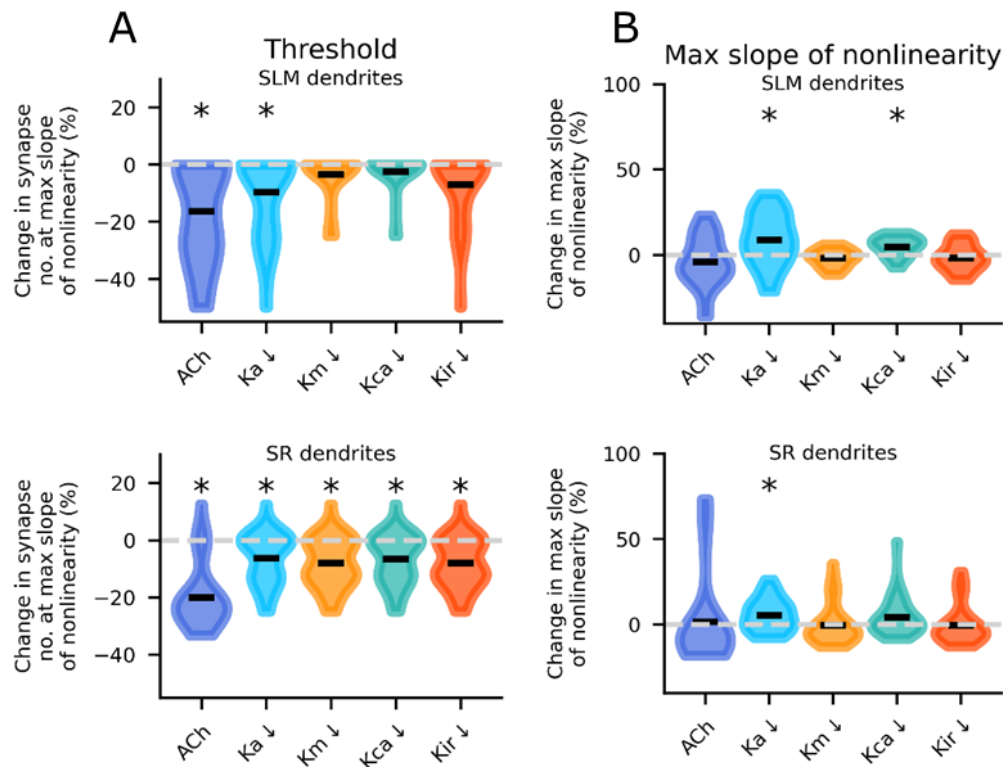


Figure 2-31: Change in NMDA spike threshold and maximum slope of nonlinearity in dendrites upon blocking potassium channels. (A) Percent change in number of synapses at maximum slope of nonlinearity in SLM (upper) and SR (lower) dendrites. (B) Percent change in maximum slope of nonlinearity in SLM (upper) and SR (lower) dendrites. * indicates $p < 0.01$ (Bonferroni adjusted alpha value).

To investigate the bimodal distribution observed in the NMDA spike thresholds in the SR dendrites (Figure 2-31A, lower), the thresholds were plotted against the dendrite diameter size (Figure 2-32A) and whether the stimulated dendrite was a terminal dendrite (Figure 2-32B). Both factors had significant differences between the groups, with the bimodal distribution more apparent with dendrite diameter, suggesting this had more of an impact on the distribution than whether the dendrite was a terminal dendrite. There was a significant difference between the NMDA spike thresholds with a dendrite diameter of more than $0.7 \mu\text{m}$ producing an average threshold of 16.31 ± 0.76 synapses (9 – 19 synapses), compared to a threshold of 6.29 ± 0.61 synapses (2 – 16 synapses) in dendrites less than 0.7

μm in diameter (Figure 2-32A). Along with the results shown in the previous Figure (Figure 2-31A, lower), this suggests that potassium channel inhibition had little effect on the thinner SR dendrites that already had a low threshold and produced a greater threshold reduction in the thicker dendritic sections.

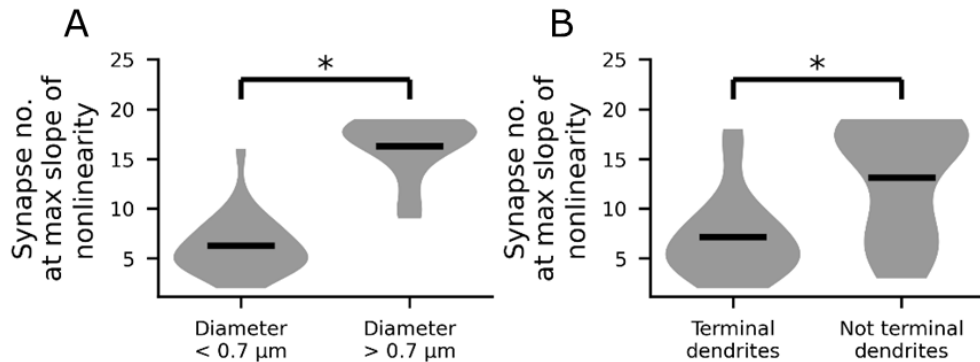


Figure 2-32: Bimodal distribution of SR dendrite NMDA spike thresholds explained by dendrite diameter. (A) Number of synapses at maximum slope of nonlinearity for dendrites greater than and less than $0.7 \mu\text{m}$. (B) Number of synapses at maximum slope of nonlinearity for terminal and non-terminal dendrites. * indicates $p < 0.05$.

As the dendritic input resistance was a good predictor of the number of synapses at maximum nonlinearity (Figure 2-18), it was possible that the change in membrane potential or input resistance from potassium channel inhibition could explain the change in the number of synapses required to generate nonlinearity (Figure 2-33). However, the percent change in the number of synapses required for nonlinearity was not well correlated and could not be explained by the change in membrane potential (Figure 2-33A, $R^2 = 0.147$) or the change in input resistance (Figure 2-33B, $R^2 = 0.004$). This suggested that potassium channel modulation of NMDA spike threshold was not only mediated by increasing the membrane potential and input resistance.

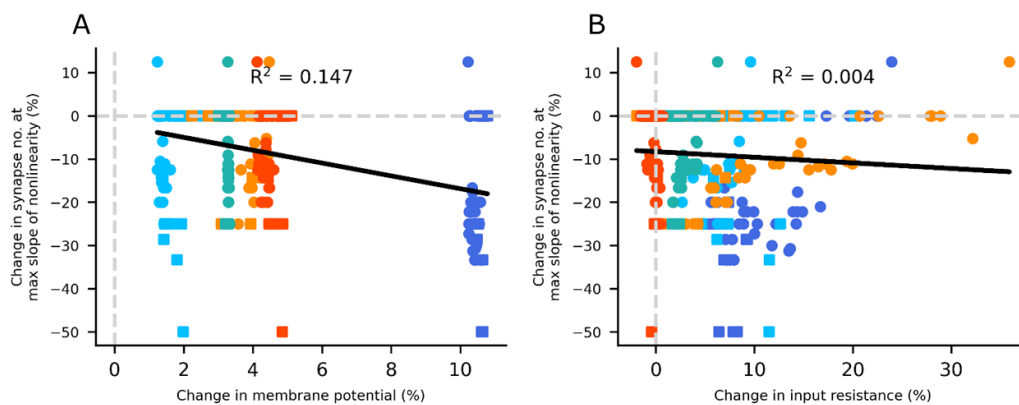


Figure 2-33: Relationship between change in NMDA spike threshold and change in membrane potential (left) and dendritic input resistance (right). (A) Change in the number of synapses required to generate nonlinearity in relation to the change in membrane potential for each potassium channel block. (B) Change in the number of synapses required to generate nonlinearity in relation to the change in input resistance for each potassium channel block. R^2 values from a linear regression are displayed. Dark blue = ACh, light blue = Ka, yellow = Km, green = Kca, orange = Kir.

Considering this and to assess further effects potassium channel inhibition may have on NMDA spike properties, the change in NMDA spike half-width and amplitude were analysed (Figure 2-34). These results suggested that Kca channels strongly modulated the NMDA spike half-width, in both the SR and SLM dendrites (Figure 2-34A), increasing the half-width by $28.19 \pm 2.6\%$ and $64.55 \pm 3.78\%$ respectively. Therefore, inhibition of this particular conductance could be important for increasing the duration of NMDA spikes. Indeed, Kca plays a role in dendritic repolarisation and is most active at high intracellular calcium concentrations (Figure 2-8). Therefore, Kca suppression delayed dendritic repolarisation and increased NMDA spike half-width. NMDA spike amplitude was only impacted by Ka channel inhibition in the SLM dendrites, which caused an $18.23 \pm 7.05\%$ increase in amplitude. Again, this makes sense as Ka was present at higher densities in the distal dendrites and is usually most active during NMDA-mediated nonlinear increases in EPSP amplitude (Figure 2-9). Potassium channel inhibition caused even less alteration in NMDA spike amplitude in the SR dendrites.

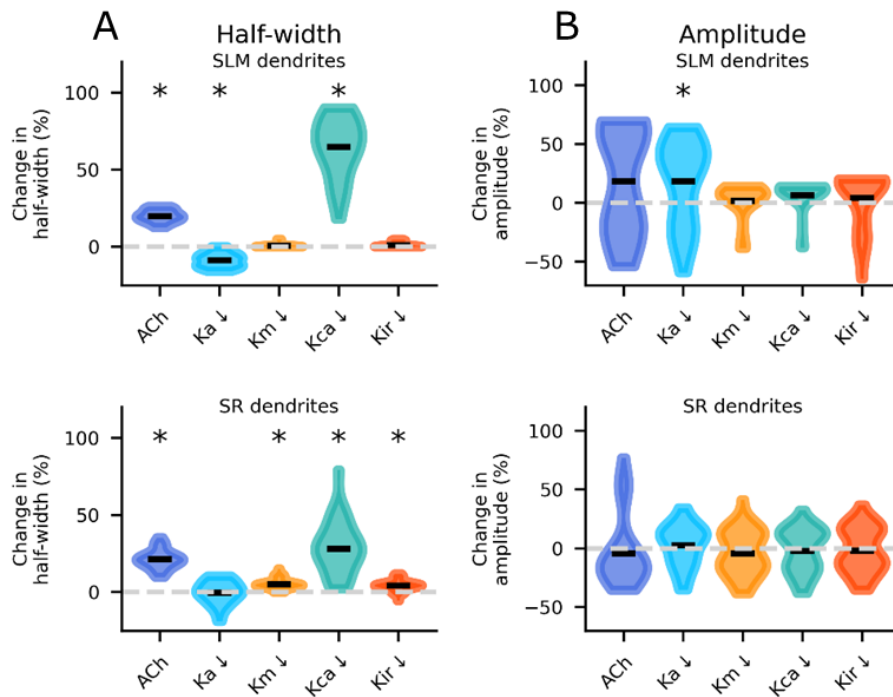


Figure 2-34: Change in NMDA spike half-width and amplitude in dendrites upon blocking potassium channels. (A) Percent change in half-width in SLM (upper) and SR (lower) dendrites. (B) Percent change in NMDA response amplitude in SLM (upper) and SR (lower) dendrites. * indicates $p < 0.01$ (Bonferroni adjusted alpha value).

2.3.5 Results comparison with a physiological range of potassium conductances

To confirm that the changes found in this model could also be applicable to neurons with varying potassium channel conductance configurations, a physiological range of potassium conductances were also modelled. To perform this, the potassium conductance optimisation was run again, to include

standard deviation of the membrane potential and input resistance parameters as well as the average values. This outputted an average and standard deviation for each potassium conductance (Table 3), from which potassium conductances could be randomly drawn from a normal distribution and the simulation repeated with different potassium conductances. The normal distributions were truncated at 0 so no negative conductance values were drawn. The simulation was run 8 times with different potassium conductances configurations on 8 SR and 8 SLM dendrites. The changes were then averaged across these 8 simulations and compared with the data in the previous Figures (Figure 2-35).

Table 3: Peak conductance optimisation outputs for each potassium conductance.

Channel	Peak conductance (S/cm ²)	
	Mean	Standard deviation
Ka	5.56×10^{-11}	9.62×10^{-11}
Km	0.0011	0.0026
Kca	0.0012	0.0010
Kir	3.47×10^{-6}	2.11×10^{-6}

Figure 2-35A shows the mean change in membrane potential averaged across each of the 8 simulations, exhibiting the physiological variability between inhibiting each of the potassium conductances. Figure 2-35B-F display the relationship between the mean data from the previous Figures (Figure 2-30, Figure 2-31, Figure 2-34) and the averaged data across the 8 simulations. Points that fall on the diagonal grey line signify that the average data from the initial simulation is the same as the averaged data from the 8 simulations with varying potassium conductance values. Therefore, the majority of effects observed in the initial simulation were very similar to simulations run with physiologically relevant variability. There were some differences in the NMDA spike threshold and amplitude in SLM dendrites (Figure 2-35C, F) that suggested the additional heterogeneity produced stronger effects. Overall, the data presented here suggested that the qualitative results obtained from the initial simulation were comparable to using a range of potassium conductances and that this additional heterogeneity did not affect the key findings.

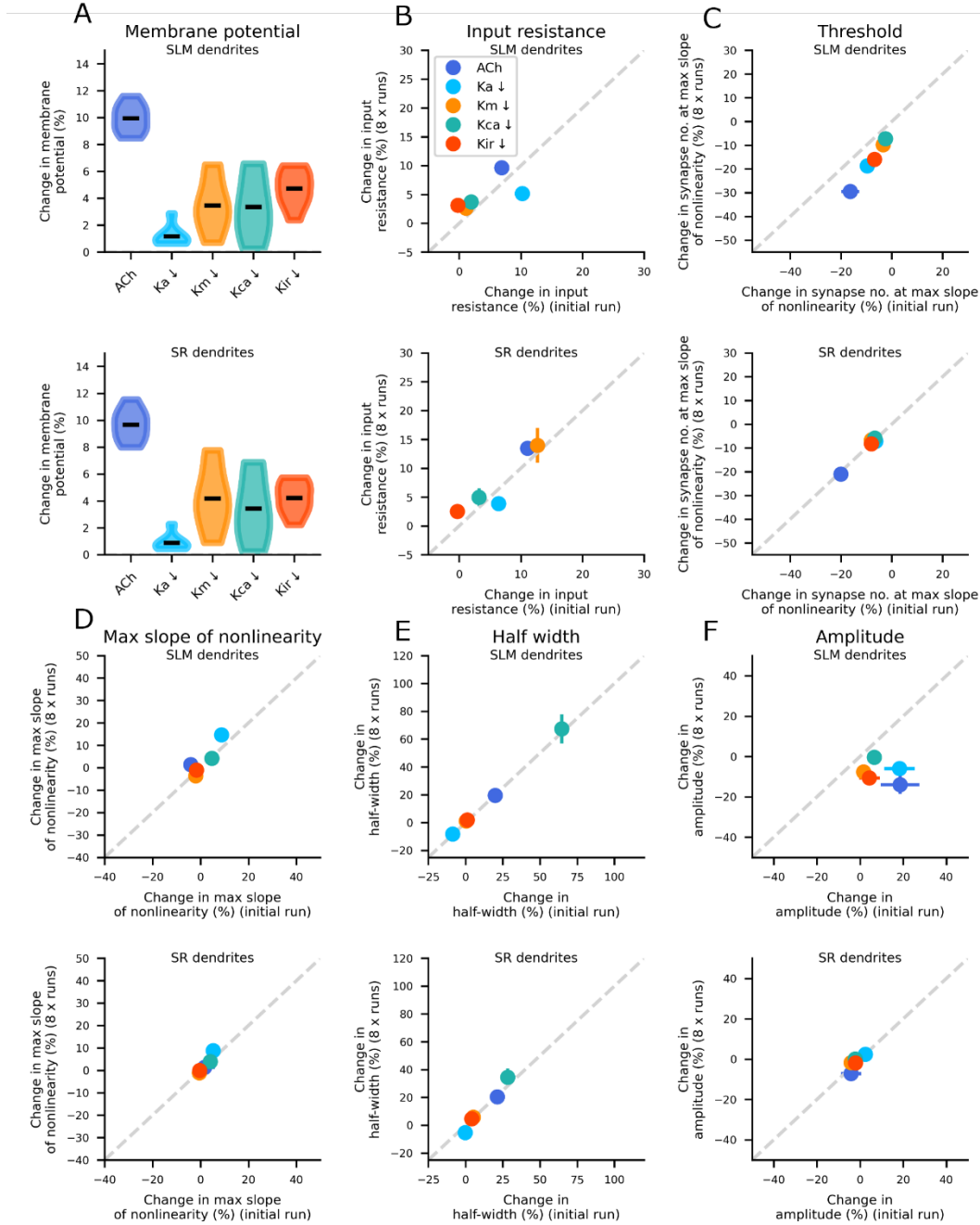


Figure 2-35: Effect of testing a realistic range of potassium conductances on NMDA spike properties. (A) Change in membrane potential when blocking potassium channels, averaged across 8 simulations of different potassium conductances. Scatter plots in B-F are comparing average measurement changes from initial simulation data (Figure 2-30, Figure 2-31, Figure 2-34) (x-axis) to average change from 8 simulations (y-axis). Upper = SLM dendrites, lower = SR dendrites. (B) Dendritic input resistance, (C) Threshold, (D) Maximum slope of nonlinearity, (E) NMDA spike half-width, (F) NMDA spike amplitude.

2.4 Discussion

To summarise, simulating acetylcholine by blocking potassium channels reduced the number of synapses required to generate nonlinearity in a two-compartment and a fully reconstructed CA3 neuron model. Furthermore, dendrite distance from the soma and dendritic input resistance were important factors in determining the dendrite's nonlinearity threshold and there were on average approximately four times less synapses required to generate nonlinearity in the distal SLM dendrites compared to more proximal SR dendrites. Similar observations have been made in CA1 neurons comparing distal and proximal SR dendrites (Weber et al., 2016). Acetylcholine also produced a heterogeneous effect in this reconstructed CA3 neuron model, suggesting that acetylcholine increased the impact of NMDA spikes on particular dendrites as opposed to having a widespread effect across the whole dendritic tree. Additionally, K_A inhibition had the biggest impact on increasing the nonlinearity slope in SLM dendrites and the K_{Ca} channel played the strongest role in modulating the NMDA spike half-width.

In this chapter, simulations were run on both a two-compartment and a reconstructed neuron model. The two-compartment model comprised of a somatic and dendritic compartment to understand the impacts of manipulating channel conductances without the additional complexity of CA3 dendrite branching morphology. On the other hand, the reconstructed neuron model had the ability to additionally assess differences across the dendritic tree, including analysing how different dendritic properties, such as dendritic diameter and input resistance, also influence nonlinear integration. The branching morphology in the reconstructed model also more realistically captured the integration of inputs and encompassed higher dendritic input resistances which in turn facilitated local dendritic events. Additional simulations could also have investigated between-dendrite interactions, which would not be possible in the two-compartment model. One of the disadvantages of using the reconstructed neuron model was the computational power required to run the simulations. This model had 943 compartments and was run on 66 different dendrite sections and therefore took significantly longer to run compared to the two-compartment model.

In general, one of the challenges with creating detailed biophysical neuron models is producing an accurate representation of ion channel conductances, deciding which ones to include and in what quantities and distributions. Matching different neuron model outputs to experimental data helps to validate the model and determine the correct ratios of channel conductances. However, tuning the conductance parameters manually, especially when there are many different conductance mechanisms, is time-consuming and challenging as changing one channel parameter not only impacts that conductance but can additionally affect the behaviour of other conductances on neuron properties. Therefore, to help tune the models, an optimisation algorithm was implemented, aiming to fit the neuron properties to experimental data as closely as possible, to determine an optimal set of peak potassium

conductances. An issue with the optimisation is that there isn't one optimal solution and in fact the optimisation for the two-compartment and reconstructed neuron model produced different optimal channel conductance ratios and activation kinetics. One explanation for this difference between the models is that the reconstructed model also incorporated varying distributions of certain conductances across the dendritic tree. Despite their differing parameters, both models still produced similar overarching results. In addition, physiological variations in conductance levels were introduced in the reconstructed model (section 2.3.5) to test the robustness of the results and again there were no significant differences in the impact of inhibiting the different channels.

Overall, the key findings from both the two-compartment and reconstructed models were similar in which acetylcholine reduced the threshold for nonlinear integration, with the K_a and K_{ca} channels playing specific roles in modulating the slope of nonlinearity and NMDA spike half-width, respectively. The additional simulations run on different dendritic sections in the reconstructed model provided supplementary information on differences in NMDA spike generation and cholinergic impacts across the dendritic tree.

Nonlinear integration in CA3 neurons has been previously studied in *ex vivo* brain slices (Makara and Magee, 2013). In this study, the authors increased the number of synapses stimulated on SR and SO dendritic branches using glutamate uncaging and measured the amplitudes at the soma. The nonlinear increases found in EPSP amplitudes were dependent on NMDAR activation as when the experiments were repeated in the presence of APV there was no nonlinear integration. They also found a bimodal distribution of NMDA spike decay times and that this difference was not dependent on the dendrite distance from the soma but on GIRK channel expression. In this model, there was not a relationship between the K_{ir} conductance expression and NMDA spike half-width and in fact the K_{ca} channel was mostly responsible for modulating NMDA spike half-width, which has been observed previously in CA1 neurons (Cai et al., 2004). The K_{ir} model used here, had a similar current-voltage curve to the GIRK conductance in CA3 neurons, but blocking it did not produce the same effects on the resting input resistance and membrane potential as in Makara and Magee (2013). This was the most appropriate K_{ir} model found at the time of simulations, and it's possible that there could be a better replacement to use which would more accurately represent the results that were found in Makara and Magee (2013). Makara and Magee (2013) also did not find a relationship between NMDA spike properties and dendrite distance from the soma, however a distance-dependent effect has previously been observed in CA3 neurons in relation to dendritic sodium spikes (Kim et al., 2012). They found that dendritic sodium spikes had a reduced initiation threshold with increasing distance from the soma.

The effect of acetylcholine on dendritic integration has previously been studied in other brain regions, such as the somatosensory cortex (Williams and Fletcher, 2019). Here, they used stimulated endogenous

acetylcholine release using optogenetics and found that this increased dendritic excitability and integration and led to long duration plateau potentials that enhanced somatic burst firing. These effects were found to be mediated by activation of R-type calcium channels. Furthermore, in CA1 neurons, carbachol has been shown to enhance sodium spike strength and propagation in dendrites that initially had weaker effects, whereas it did not influence sodium spikes in branches that already produced strong responses (Losonczy et al., 2008). This is in line with the results presented here in that the effect of acetylcholine was greater in the SR region, that initially had a higher threshold for NMDA spike generation compared to the SLM dendrites. This suggests that acetylcholine could selectively facilitate NMDA spikes in the SR region and promote plasticity in the recurrent inputs. The effect of acetylcholine on CA3 somatic excitability has been shown to be dependent on the type of pyramidal neuron (Hunt et al., 2018). Hunt et al., (2018) characterised two types of CA3 pyramidal neuron: athorny bursting and thorny regular-spiking. Acetylcholine increased the firing frequency of regular-spiking neurons and reduced initial firing frequency of bursting neurons. As athorny bursting cells facilitated sharp-wave ripples (SWRs), they were thought to play a role in memory consolidation. In line with acetylcholine's proposed role in memory encoding and not consolidation, the presence of acetylcholine reduced the ability of athorny neurons to generate SWRs, thought to reduce the likelihood of consolidation and bias the network towards a memory encoding state.

Other key results from this study were the effect of the K_a and K_{ca} conductances on the nonlinear maximum slope and on the NMDA spike half-width, respectively. These results support experimental data from CA1 neurons, which showed that downregulation of the A-type potassium channel increased dendritic plateau potential amplitude (Cai et al., 2004) and increased sodium spike strength (Losonczy et al., 2008) and that blocking SK channels increased plateau potential duration (Cai et al., 2004). As was investigated in the results, as K_{ca} is active with high intracellular calcium concentrations and plays a role in dendritic repolarisation, K_{ca} suppression prevented dendritic repolarisation and prolonged the NMDA spike half-width. On the other hand, K_a is most active during the voltage window for NMDA-mediated nonlinear increases in amplitude and therefore K_a suppression enabled larger increases in the nonlinear amplitude.

2.4.1 Functional implications

Dendritic spikes provide a potential mechanism for plasticity induction at synapses. NMDA spikes depolarise dendritic branches and increase local calcium signalling within the dendrite, both of which could facilitate synaptic plasticity. This plasticity could also occur without the need for a backpropagating action potential. In CA3 recurrent synapses, NMDA spikes have been shown to be necessary for inducing a specific type of timing-dependent associative plasticity (Brandalise et al., 2016, 2021). This plasticity is induced from subthreshold mossy-fibre stimulation co-ordinated with NMDA spike initiation in the SR dendrites. The ability of acetylcholine to reduce the threshold of NMDA spike

generation could therefore facilitate CA3 recurrent plasticity and the formation of memory ensembles. Another consequence of dendritic NMDA spikes is that they can induce somatic bursting which could facilitate STDP which has been shown to also be a mechanism of plasticity induction at recurrent synapses (Mishra et al., 2016). The symmetric STDP rule discovered in Mishra et al., (2016) was shown to facilitate the storage of memory ensembles in a model.

NMDA-dependent plateau potentials have been shown to underly place cell formation and plasticity in CA1 neurons (Bittner et al., 2015, 2017) and therefore a similar mechanism is likely at play in CA3 place cells, as there is evidence of plateau potentials can be initiated in CA3 neurons in brain slices (Raus Balind et al., 2019). As place cells can form in novel environments, acetylcholine could also play a role in place cell induction (Fernández de Sevilla et al., 2020; Prince et al., 2021). Indeed, it has been shown that LC noradrenergic input is important for enhancing CA1 excitability and LTP (Liu et al., 2017; Bacon et al., 2020), as well as for place cell formation around reward zones (Kaufman et al., 2020).

2.4.2 Limitations / improvements

Using computational models provides a simplified representation of the concept which can help to understand complex problems, but they can also present limitations. The paradigm here was only tested on one CA3 neuron morphology. As well as morphological variability between CA3 pyramidal neurons there has also been shown to be different classes of CA3 pyramidal neurons with distinct morphological characteristics (Hunt et al., 2018). For example, in Hunt et al., (2018), CA3 pyramidal neurons with thorny excrescences had more basal and apical SR dendrites whereas pyramidal neurons without thorns had a greater proportion of SLM apical dendrites. These differences in dendritic arborizations could mean the distribution in NMDA spike thresholds is different between the two types. Thorny neurons also receive a higher proportion of inputs from recurrent collaterals and mossy fibres; whereas athorny neurons receive a greater number of inputs from the entorhinal cortex, have a higher input resistance, burst propensity and a lower action potential threshold, all of which could also affect dendritic integration properties *in vivo*. Testing a range of potassium conductances in this model provided some heterogeneity that could reflect some of these differences between different pyramidal neurons. However, it would be beneficial to test the results in different morphological reconstructions.

Another constraint is the lack of data on known conductance distributions and densities. Data on K_a , K_{ir} and Na conductance distributions across the dendritic tree (Kim et al., 2012; Degro et al., 2015) were included in the model, but other channel distributions have not been studied in CA3 neurons. The optimisation process included in this work hopefully helped to partially overcome this issue whereby the relevant potassium conductances were best fit to the experimental data and that a range of potassium conductances were tested in order to simulate a heterogeneous CA3 cell population. To address

heterogeneity between cells more accurately, simultaneous measurement of multiple properties within single neurons would need to be achieved (Marder and Taylor, 2011).

Acetylcholine was modelled here by inhibiting several potassium channels that it is known to inhibit via M1 receptor activation (Hoffman and Johnston, 1998; Sohn et al., 2007; Buchanan et al., 2010; Tigaret et al., 2018). However, acetylcholine also has effects on other conductances as well as binds to other muscarinic and nicotinic receptor subtypes and has effects on synaptic transmission and inhibition within the CA3 network. These effects could also influence NMDA spike generation, particularly its influence on calcium signalling by the release of internal calcium stores (Nash et al., 2004) and through activation of R-type calcium channels (Williams and Fletcher, 2019). In addition, acetylcholine can also enhance theta/gamma oscillations (Vandecasteele et al., 2014) which are thought to be important for controlling STDP. Furthermore, acetylcholine has been shown to have different effects on the spiking output of CA3 neurons, with it increasing and decreasing firing frequency in the two different cell classes (Hunt et al., 2018), mentioned previously. Therefore, distinct cell types could also process cholinergic modulation differently, possibly due to different cholinergic receptors or other varying channel expression. Taking these extra effects into consideration would over-complicate the model and so instead, the model focused on acetylcholine's effect on the relevant potassium channels. However, these are additional effects that could be tested to see how they may also affect NMDA spike generation. For example, it's likely that increasing calcium influx would only facilitate NMDA spike generation further and with the Kca channel inhibited could prevent hyperpolarisation and prolong the duration of NMDA spikes. In regard to increasing the firing frequency of thorny CA3 neurons (Hunt et al., 2018), this could in fact be caused by increased NMDA dendritic spike activity, or alternatively could facilitate dendritic spike activity via depolarisation from back-propagating action potentials.

In terms of the synaptic inputs, NMDA inputs modelled here did not include calcium influx. In actual neurons, these additional calcium dynamics could also be important for generating dendritic events and is especially relevant for inducing synaptic plasticity. In particular, the inhibition of Kca channels via M1 receptor activation prevents dendritic repolarisation and increases NMDAR activity facilitating synaptic plasticity (Buchanan et al., 2010).

2.4.3 Future work

The results presented in this chapter are predictions from simulations and therefore would need to be tested experimentally. One of the key predictions is that acetylcholine reduces the amount of synaptic input required to generate NMDA-mediated nonlinearity in CA3 pyramidal neuron dendrites. Specifically, to a greater extent in the SR dendrites compared to the SLM dendrites. To test this experimentally, a similar set-up could be used as in Makara and Magee (2013) where 2-photon glutamate uncaging is used to stimulate increasing numbers of synapses on single CA3 dendrite

branches and nonlinear increases in the EPSP amplitude are measured at the soma. These experiments could first test the prediction that the threshold for nonlinearity is lower in the SLM dendrites compared to the SR dendrites and secondly, could then be repeated in the presence of a cholinergic agonist, or with optogenetic stimulation of cholinergic fibres, to test whether acetylcholine does indeed reduce the threshold for NMDA-mediated nonlinearity.

Plateau potential generation and somatic bursting have also previously been studied in CA3 pyramidal neurons *ex vivo* (Raus Balind et al., 2019) by combined stimulation of proximal and distal inputs. This type of dendritic integration could also be studied in this model by testing how inputs integrate between different dendrites and regions to produce more global widespread events in the dendrites. Acetylcholine could then be simulated in the same way to assess whether it could also affect integration between dendritic branches. Investigating dendritic events *in vivo* during behaviour is more challenging but has been achieved with 2-photon calcium imaging of the dendrites during locomotion to detect dendritic events that occur in CA1 place cells (Sheffield and Dombeck, 2015; Sheffield et al., 2017). Due to its depth in the brain, imaging CA3 neurons *in vivo* is even more challenging, but has recently been achieved in anaesthetised and awake mice (Dong et al., 2021; Schoenfeld et al., 2021). In the future, if it is possible, it would be interesting to also measure dendritic calcium events in CA3 neurons during behaviour, to understand when they occur during learning and memory-related tasks.

This modelling work could also look to incorporate additional effects of acetylcholine or be tested in additional morphologies, as explained in the previous section. Network models of memory formation and ensembles that take into account nonlinear dendritic integration (Kaifosh and Losonczy, 2016) could also help to understand acetylcholine's role in dendritic integration within the CA3 network.

2.4.4 Conclusion

In conclusion, simulating acetylcholine's effect on potassium channels facilitated NMDA spike generation in a reconstructed CA3 neuron model and provides a potential mechanism for the storage of new memories within CA3 recurrent circuitry.

Chapter 3 Neuromodulation of CA3 synaptic transmission *ex vivo*

Figures 3-6 to 3-8 and 3-10 to 3-13 are based on published data in:

Prince LY, Bacon T, Humphries R, Tsaneva-Atanasova K, Clopath C, Mellor JR. Separable actions of acetylcholine and noradrenaline on neuronal ensemble formation in hippocampal CA3 circuits. *PLoS Comput Biol.* 2021 Oct 1;17(10):e1009435.

3.1 Introduction

Neuromodulators are released during particular behavioural states, such as during rewarding or novel experiences, and can modulate cell excitability, synaptic transmission and plasticity. Acetylcholine is released during novel experiences and inhibiting cholinergic receptors or lesioning the cholinergic neuron projection to the hippocampus has been shown to impair memory encoding (Berger-Sweeney et al., 2001; Rogers and Kesner, 2003). Noradrenaline is released into the hippocampus from neurons in the locus coeruleus, which are also active during novelty. Blocking noradrenergic beta-adrenoceptors in the hippocampus, has been shown to impair memory consolidation (Ji et al., 2003) and retrieval (Murchison et al., 2004). Additionally, stimulating the locus coeruleus has been shown to enhance spatial memory encoding (Lemon et al., 2009) and increase the probability of CA1 neuron spiking (Bacon et al., 2020). Therefore, both neuromodulators are associated with novelty and learning, however, one of the proposed differences is that acetylcholine is released during expected uncertainty whereas noradrenaline is released during unexpected uncertainty (Yu and Dayan, 2005).

Acetylcholine has long been proposed to alter synaptic transmission, and memory processing in the hippocampus, as explained in the Introduction (Hasselmo, 1999, 2006). In electrophysiological experiments in brain slices carbachol, a cholinergic agonist, reduces excitatory synaptic transmission between recurrent CA3-CA3 neurons as well as inputs from the entorhinal cortex (EC) (Kremin and Hasselmo, 2007). However, these results also showed that different doses of carbachol affect the two inputs differently and therefore suggest the dominant influence on CA3 neurons can shift between entorhinal and recurrent collateral input. The effect of endogenous acetylcholine on these CA3 synaptic inputs, as can now be performed using optogenetics, has not yet been determined, but may help to determine the effect of a physiological acetylcholine concentration on each of these inputs. It has previously been found that endogenous dopamine affects synaptic transmission in CA1 neurons differently to bath-applied dopamine (Rosen et al., 2015).

As noradrenaline is also released in response to novelty, it is sensible to predict that it would also adapt this CA3 circuitry to promote memory encoding. Noradrenaline has been shown to suppress MF-CA3 feedforward inhibition and therefore increase the net excitation to CA3 neurons, but to a lesser extent

than acetylcholine (Prince et al., 2021). It is not yet known how noradrenaline affects CA3-CA3 excitatory synaptic transmission.

It has not yet been tested how endogenous acetylcholine will affect the synaptic transmission and cell excitability in the CA3 region. To assess the endogenous effect of acetylcholine release, a mouse line with channelrhodopsin-2 (ChR2) expressed in the cholinergic fibres was used for these experiments in order to release acetylcholine from cholinergic axons in the hippocampus via blue light activation. This mouse line has previously been characterised (Hedrick et al., 2016) and used to test the effect of endogenous acetylcholine on different synaptic input pathways in CA1 neurons (Palacios-Filardo et al., 2021).

The aim of the experiments performed here was to compare the action of carbachol and noradrenaline on CA3 recurrent transmission, as well as investigate how endogenous acetylcholine release impacts excitatory and inhibitory inputs to CA3 neurons in *ex vivo* hippocampal slices. It has previously been shown that carbachol reduces CA3-CA3 recurrent transmission (Vogt and Regehr, 2001; Kremin and Hasselmo, 2007) and it was predicted that noradrenaline would also reduce this transmission as it is thought to be released under similar behavioural conditions. Additionally, it was predicted that the optogenetic release of acetylcholine would display similar effects to the application of carbachol, but possibly to a lesser extent, due to variable cholinergic fibre density or acetylcholine release properties. Therefore, acetylcholine would reduce both excitatory and inhibitory inputs to CA3 neurons.

3.2 Methods

3.2.1 Mouse lines

The mice used were either 3–6-week-old wild-type male C57BL/6J mice, supplied by Charles River, or 4–7-week-old ChaT-Cre mice (Chat-IRES-Cre; Stock No. 006410; The Jackson Laboratory) crossed with Ai32 mice (B6.Cg-Gt(ROSA)26Sortm32(CAG-COP4*H134R/EYFP)Hze/J; Stock No. 024109; The Jackson Laboratory) to produce litters expressing heterozygous ChaT-cre and homozygous Ai32. These ChaT-Ai32 mice expressed the light-activated cation channel channelrhodopsin-2 (ChR2) in cre-expressing cholinergic neurons. The expression and activation of ChR2 has previously been validated in this mouse line (Palacios-Filardo et al., 2021).

All animal procedures were performed in accordance with Home Office guidelines as stated in the UK Animals (Scientific Procedures) Act 1986 and EU Directive 2010/63/EU 2010. The protocol was approved by the Animal Welfare and Ethics Review Board at the University of Bristol.

3.2.2 Preparation of brain slices

The mice were culled by cervical dislocation, the brain removed and placed in oxygenated ice-cold sucrose cutting solution (in mM: 252 sucrose, 2.5 KCl, 26 NaHCO₃, 1 CaCl₂, 5 MgCl₂, 1.25 NaH₂PO₄, 10 glucose). Horizontal 400 μ m slices were taken from the hippocampal area using a vibratome (VT1200; Leica) and stored in artificial cerebrospinal fluid (aCSF) (in mM: 119 NaCl, 2.5 KCl, 11 Glucose, 1 NaH₂PO₄, 26.5 NaHCO₃, 1.3 MgSO₄, 2.5 CaCl₂) at 34°C for 30 minutes. The slices were then left to rest at room temperature for a further 30 minutes – 6 hours before being used.

3.2.3 Electrophysiology

Slices were continually perfused with aCSF at a rate of 3–5 ml/min using a peristaltic pump (Watson Marlow 101 U/R) and experiments were performed at 32–38°C. Cells were visualised using infra-red differential interference contrast on an Olympus BX-51W1 microscope. Pipettes were pulled from borosilicate filamented glass capillaries (Harvard Apparatus) using a PC-87 Micropipette puller (Sutter Instrument) to have a resistance of 3 – 7 M Ω at the tip. Whole-cell recordings were made from CA3 pyramidal neurons using caesium (in mM: 130 CsMeSO₄, 4 NaCl, 10 HEPES, 0.5 EGTA, 10 TEA-Cl, 2 Mg-ATP, 0.5 Na-GTP, 1 QX-314) and potassium (in mM: 120 KMeSO₃, 10 HEPES, 0.2 EGTA, 4Mg-ATP, 0.3 Na-GTP, 8 NaCl, 10 KCl) internal solutions for voltage-clamp and current-clamp experiments, respectively. A potassium methanesulfonate internal with the addition of QX-314 (in mM: 120 KMeSO₃, 8 NaCl, 10 HEPES, 4 Mg-ATP, 0.3 Na-GTP, 0.2 EGTA, 10 KCl, 1 QX-314Cl, ~295 mOsm, 7.4 pH) was used in experiments investigating dendritic integration properties. Recordings were collected using a Multiclamp 700A amplifier (Molecular Devices) filtered at 4 kHz and sampled at 10 or 20 kHz, depending on the experiment, using Signal5 acquisition software, and a CED Power 1401

data acquisition board. A 200 ms voltage step enabled input and series resistance to be monitored throughout the voltage clamp experiments (Figure 3-1). The current injected (DC) to maintain the required voltage was also recorded throughout the experiment to monitor the condition of the cell. The series resistance provided information on the quality of the seal and if it exceeded 35 M Ω or changed by >50% the cell was discarded from analysis. The DC was taken as the average current in a 40 ms period before the step and was used as the baseline value for the series and input resistance measurements (Figure 3-1, blue shaded box). The series resistance was calculated as the change in voltage divided by the amplitude of the peak current (I_{peak} , Figure 3-1, Equation 2). The input resistance was measured as the change in voltage divided by the amplitude of the steady state current change (I_{ss} , Figure 3-1, average of orange shaded box, Equation 1).

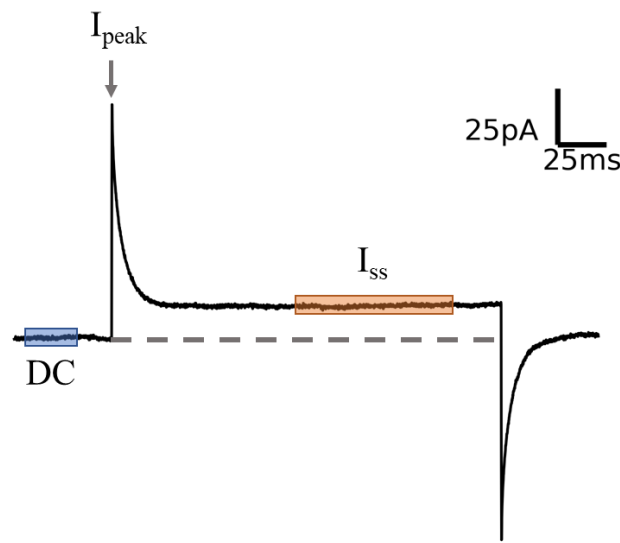


Figure 3-1: Example current recording with 200 ms voltage step with measurements taken for calculating series and input resistance. DC = current injected to maintain voltage, I_{peak} = current peak for series resistance calculation. I_{ss} = steady-state current for input resistance calculation. Shaded boxes indicate approximate averaged area for calculations.

$$R_{in} = \frac{\Delta \text{ voltage}}{|DC - I_{ss}|}$$

Equation 1: Input resistance equation. R_{in} = input resistance, DC = current injected, I_{ss} = steady-state current, Δ voltage = amplitude of voltage step.

$$R_{ser} = \frac{\Delta \text{ voltage}}{|DC - I_{peak}|}$$

Equation 2: Series resistance equation. R_{ser} = series resistance, DC = current injected, I_{peak} = peak current, Δ voltage = amplitude of voltage step.

3.2.4 Electrical stimulation protocol

A bipolar stimulating electrode was positioned in the stratum radiatum (SR) and/or the stratum lacunosum-moleculare (SLM) of CA3 to stimulate the recurrent or perforant path axons, respectively (Figure 3-2), or in the stratum pyramidale (SP) of CA3 for stimulating inhibitory axons. All pathways were stimulated with 2 pulses spaced 50 ms apart (20 Hz), using a Digitimer DS2A stimulator, to measure post-synaptic current (PSC) amplitudes as well as the paired pulse ratio. In experiments where both the recurrent and perforant pathways were stimulated, stimulation was alternated between sweeps at 10 second intervals. To confirm stimulation of the perforant path axons 3 μ M DCG-IV was washed on at the end of experiments if cells were still healthy. DCG-IV is an agonist for mGluR2/3, which is present on perforant path axons, but not on CA3 recurrent collaterals (Neki et al., 1996; Shigemoto et al., 1997), and reduces glutamatergic transmission. All cells were held at the chloride reversal potential of -70 mV during excitatory post-synaptic current (EPSC) recordings and at a more depolarized potential (-40--20 mV) during inhibitory PSC (IPSC) recordings. The chloride reversal potential was determined by measuring the amplitude of IPSCs in the presence of glutamatergic antagonists (20 μ M NBQX (HelloBio), 50 μ M D-APV (HelloBio)) at different holding potentials (from -55 to -80 mV) to find the potential at which no inhibitory current flowed. For IPSC experiments, 20 μ M NBQX (HelloBio) and 50 μ M D-APV (HelloBio) were included in the aCSF solution to block glutamatergic transmission. Inhibitory responses with a rise time of more than 5 ms were excluded from the analysis to isolate faster parvalbumin-positive (PV+) inhibitory inputs (Szabó et al., 2010; Udakis et al., 2020).

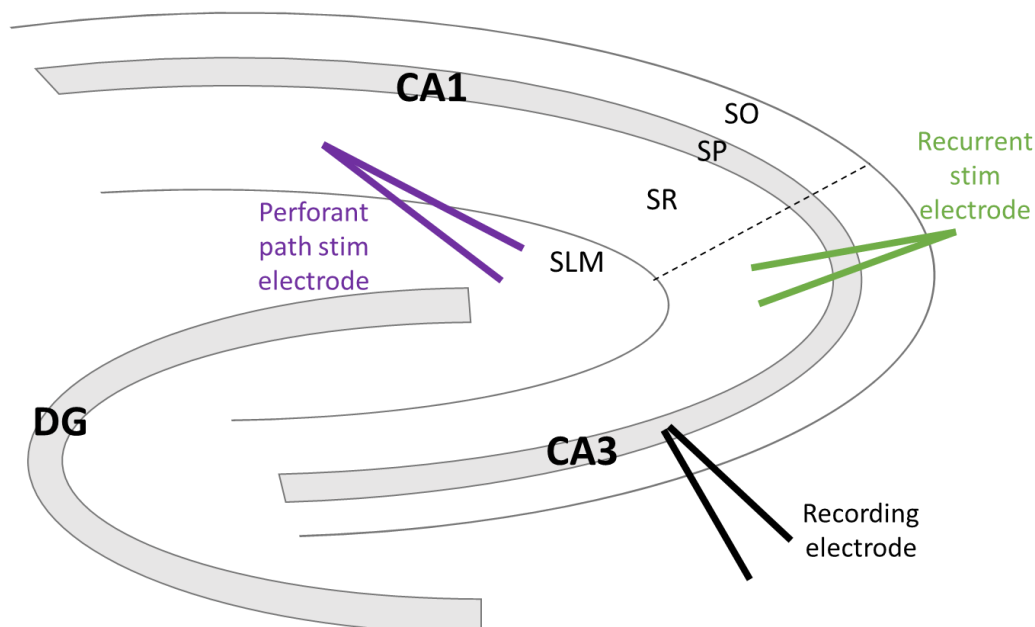


Figure 3-2: Stimulating electrode positions in hippocampal brain slice. Stimulating electrode targeting recurrent collaterals was positioned in the SR layer towards the distal end of CA3. Stimulating electrode targeting the perforant path fibres was positioned near the hippocampal fissure in the SLM layer. Cells were patched in mid CA3 region. Dashed line represents approximate CA3-CA1 boundary.

3.2.5 Dendritic integration stimulation protocol

To test dendritic integration properties, stimulating electrodes were positioned to stimulate the recurrent and perforant path inputs as described above (Figure 3-2). These experiments were performed in current clamp to record excitatory post-synaptic potentials (EPSPs) with a potassium internal (detailed above). The aCSF solution included 1 μ M CGP55845 (HelloBio) and 50 μ M picrotoxin (PTX) (Sigma-Aldrich) to block inhibition. The membrane potential was kept at approximately -70 mV by injecting an appropriate amount of current. The stimulation protocol comprised of a single stimulation, followed by a 400 ms delay and then a burst of 5 stimulations at 100 Hz. The pathway stimulated was alternated between sweeps. The stimulation intensity was manually altered between sweeps to create a range of input intensities (0 - 99V) and assess how increasing numbers of inputs integrated in each pathway.

3.2.6 Drug wash on

After recording a 5-minute stable baseline of PSC amplitudes, carbachol (Sigma-Aldrich) (1, 5 or 10 μ M) or 20 μ M noradrenaline (Sigma-Aldrich) was washed onto the slice, dissolved in aCSF, for 10 minutes. Noradrenaline stock solution was made up on the day of experiment in dH₂O and kept on ice. Carbachol, and other drug (NBQX, DCG-IV, D-APV, CGP55845, PTX), stock solutions were made up in dH₂O and kept at -20°C. The effect on cell excitability and PSC amplitudes was measured between 5-10 minutes of the wash on period. The carbachol and noradrenaline concentrations used were based on similar experiments performed in previous studies (Kremin and Hasselmo, 2007; Bacon et al., 2020; Palacios-Filardo et al., 2021; Prince et al., 2021).

3.2.7 Statistical analysis

An experimental unit was defined as one cell per slice and no more than one cell was recorded per slice. No more than 3 cells were recorded per animal. Paired t-tests or Wilcoxon signed-rank tests were used when analysing the effect of the drugs or optogenetic stimulation. Wilcoxon rank-sum tests were used when comparing between pathways. All values are represented as mean \pm standard error of the mean (SEM). The number of neurons used in each analysis is stated with the data. Data were processed, analysed and presented using Signal5 (CED) and Python 3.8.

3.2.8 Optogenetic stimulation

Blue light from a 470 nm LED (Thorlabs) was flashed onto slices via the 4x or 40x microscope objective. The 4x objective was used when stimulating recurrent and perforant path axons to stimulate a larger area of the slice and ensure activation was targeted at the SR and SLM dendrites where the recurrent and perforant path axons synapse. The 40x objective was used when stimulating inhibitory

axons that synapse close to the soma. The light power was adjusted for each objective to produce an intensity of 7–9 mW/mm². 5 ms light pulses at 2 Hz for 5 minutes were used to release a physiological maximal amount of acetylcholine (Jing et al., 2018; Palacios-Filardo et al., 2021).

3.2.9 Synaptic transmission analysis

All post-synaptic current (PSC) properties were measured from an averaged trace of the 5 minutes before drug application/optogenetic stimulation (baseline) and from minute 5-10 during drug application or the whole 5 minutes during optogenetic stimulation. The time-PSC amplitude plots are an average of 3 or 6 sweeps over 1-minute periods. The membrane potential was measured in the excitability experiments by switching to current clamp before and during drug application. Input resistance was calculated from the 200 ms voltage step, as explained above (Figure 3-1, Equation 1). Paired pulse ratio was measured as the second PSC peak divided by the first PSC peak (Figure 3-3: Calculation of paired pulse ratio. P1 = amplitude of first peak, P2 = amplitude of second peak. PPR = paired pulse ratio.). The rise time of EPSC responses were calculated as the time from 20% to 80% of the peak (Figure 3-4).

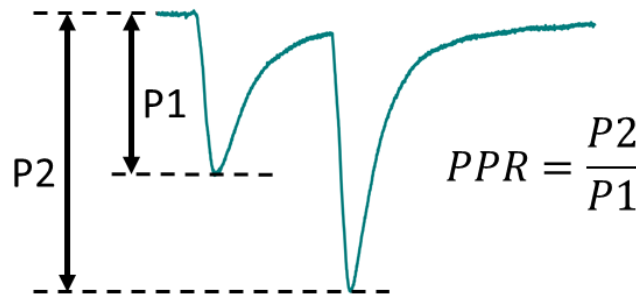


Figure 3-3: Calculation of paired pulse ratio. P1 = amplitude of first peak, P2 = amplitude of second peak. PPR = paired pulse ratio.

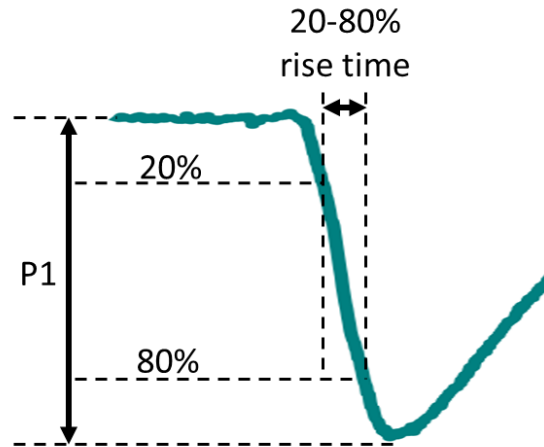


Figure 3-4: Calculation of EPSC 20-80% rise time. P1 = amplitude of peak.

3.2.10 Dendritic integration analysis

To determine the dendritic integration properties, the key measurements taken from each sweep were the subthreshold rising slope of the single EPSP and the area under the curve (AUC) of the decay phase of the compound EPSP (Figure 3-5). The AUC was measured from 50 to 500 ms after the initial compound EPSP pulse. The rising slope represented the stimulation intensity and provided a way to compare measurements across experiments and conditions. The decay AUC represented the output at the soma and the presence of plateau potentials: a long-lasting depolarisation following the compound EPSP. It has previously been shown that these plateaus have a supra-linear relationship between the rising slope and the decay AUC in CA1 neurons (Griesius et al., 2022). To measure this relationship, the raw data was initially smoothed using a Savitzky-Golay filter, a changepoint detection algorithm (Truong et al., 2020) was then employed, followed by a linear regression performed on the data points before and after the changepoint.

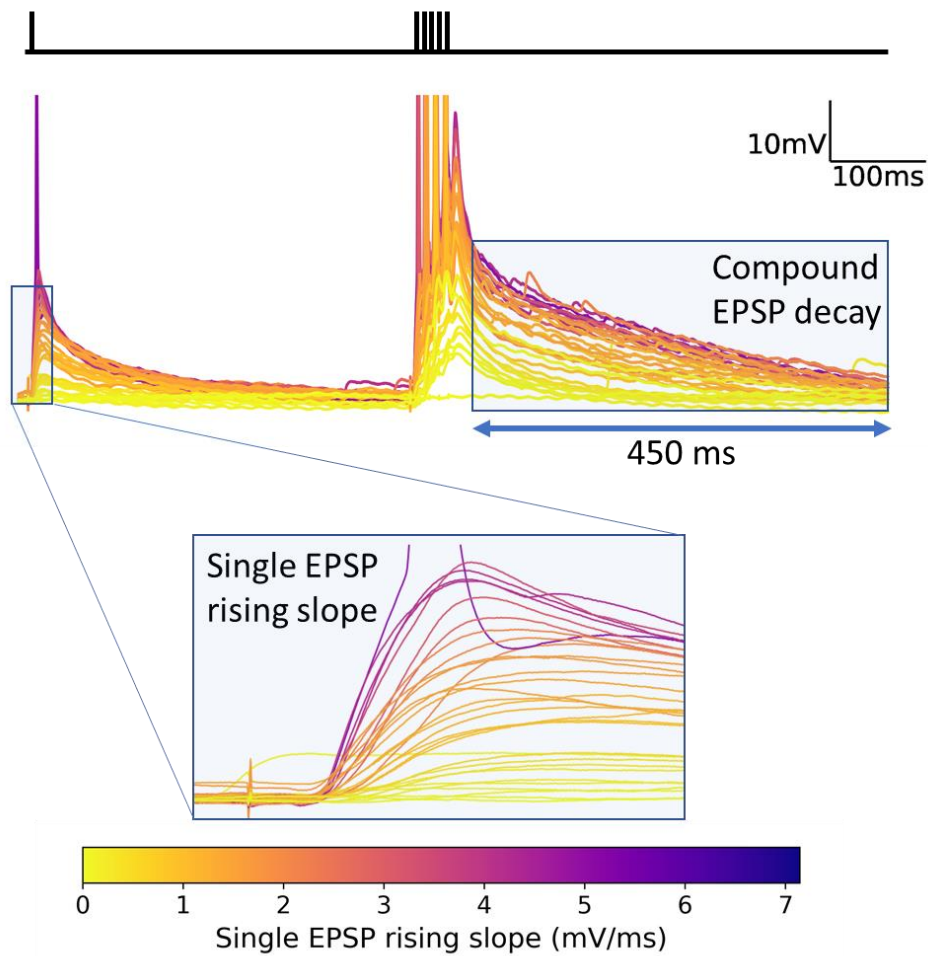


Figure 3-5: Stimulation protocol and measurements taken for dendritic integration experiments. EPSP subthreshold rising slope was measured from the single stimulation. Compound EPSP decay AUC was measured from 50 to 500 ms after the 5x stimulation burst.

3.3 Results

3.3.1 Cholinergic modulation of CA3 recurrent synaptic transmission

The first set of experiments tested how carbachol affects CA3-CA3 recurrent excitatory synaptic transmission and CA3 pyramidal cell excitability in *ex vivo* brain slices. These experiments were performed via electrical stimulation of recurrent axons in the SR region of CA3 and recording excitatory post-synaptic currents (EPSCs), by holding the cell at the experimentally determined chloride reversal potential (-70 mV), before and during perfusion of 5 μ M carbachol. It confirmed that bath applied carbachol significantly reduces the CA3-CA3 recurrent EPSC amplitude by approximately 50%, from 120.38 ± 37.97 pA to 57.03 ± 21.38 pA ($n = 4$ cells from 4 mice, $p < 0.05$) (Figure 3-6, Figure 3-7), as has been shown previously (Vogt and Regehr, 2001; Kremin and Hasselmo, 2007).

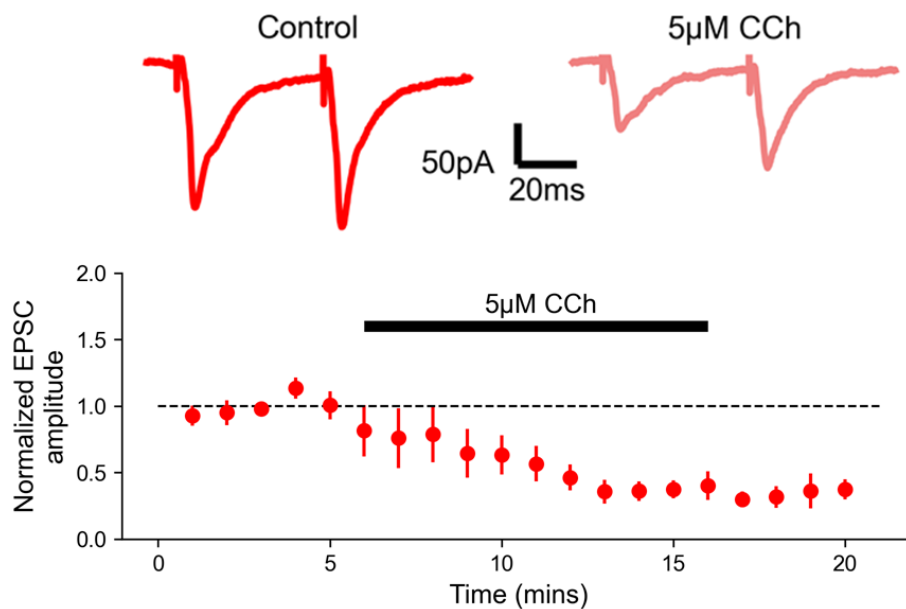


Figure 3-6: 5 μ M carbachol reduced CA3 recurrent excitatory post-synaptic current amplitude. Top left: example trace from one cell averaged over the 5-minute baseline period. Top right: example trace from the same cell averaged over a 5-minute period during carbachol application. Bottom: normalized EPSC amplitude of the first peak over the whole experiment for 4 cells (from 4 mice) averaged in 1-minute bins. Black bar represents the period of carbachol application.

In these experiments there were two stimulations given 50 ms apart (Figure 3-6) which also allowed analysis of the paired pulse ratio (PPR), calculated as the ratio between the first and second EPSC peak. The PPR provides information on the short-term synaptic plasticity. A larger second peak will give a PPR greater than 1 and suggests short-term facilitation, whereas a smaller second peak will give a PPR of less than 1 and proposes short-term depression. A change in the PPR suggests a drug is acting pre-synaptically by changing the transmitter release probability (Dobrunz et al., 1997). The average baseline PPR measured here in CA3-CA3 recurrent transmission was 1.33 ± 0.20 (Figure 3-7), suggesting short-term facilitation. On average, carbachol increased this short-term facilitation to 1.71 ± 0.28 , suggesting

it was acting via pre-synaptic mechanisms, as has also previously been shown in the CA1 region (Auerbach and Segal, 1996; Yun et al., 2000) (Figure 3-7).

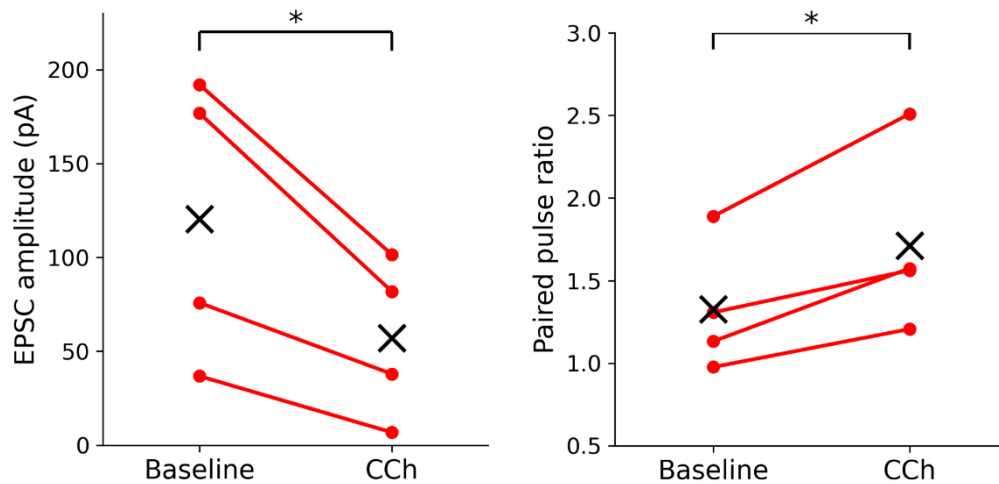


Figure 3-7: Effect of carbachol on EPSC amplitude and paired pulse ratio. Baseline = Average amplitude and paired pulse ratio (PPR) in the 5-minute period before carbachol (CCh) application. CCh = Average amplitude paired pulse ratio (PPR) from 5-minute period during CCh wash on (n = 4 cells from 4 mice). * = $p < 0.05$ (paired t-test). X = mean.

Subsequently, additional experiments were performed to assess carbachol's effect on CA3 pyramidal cell excitability, by measuring the change in resting membrane potential and input resistance, with a potassium-based internal (see Methods), before and during the addition of carbachol (Figure 3-8). The average resting membrane potential increased from -57.98 ± 1.52 mV to -53.16 ± 1.10 mV with carbachol (Figure 3-8), implying it increased CA3 neuron excitability. Input resistance, calculated as the change in current in response to a change in the voltage applied with a 200 ms depolarising voltage step, was averaged over a 5-minute baseline period and a 5-minute period during carbachol perfusion. The effect of carbachol on input resistance was more variable (Figure 3-8) and on average, carbachol slightly increased the input resistance from 114.92 ± 13.07 M Ω to 123.91 ± 10.52 M Ω , but this was not a significant change. These effects of carbachol on membrane potential and input resistance were also in line with results from previous studies (Sun and Kapur, 2012).

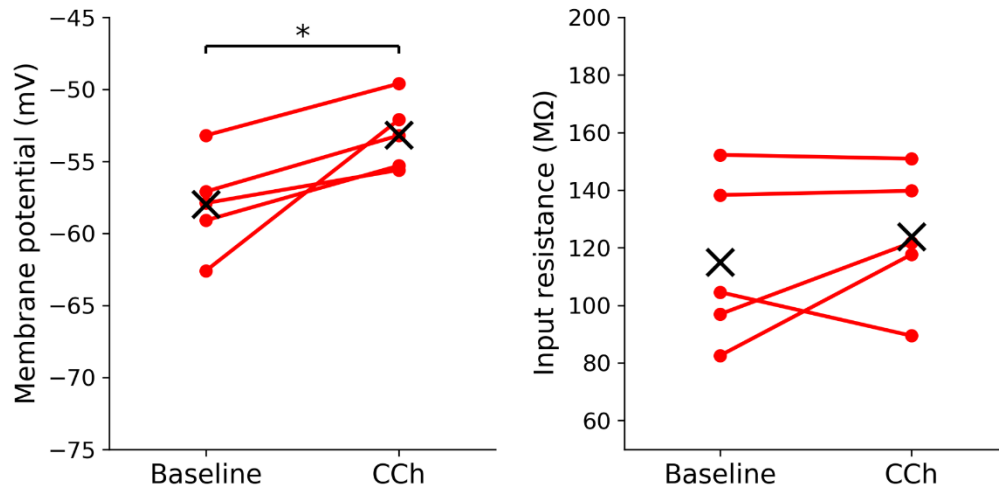


Figure 3-8: Effect of carbachol on CA3 cell excitability. Membrane potential and input resistance measured before (baseline) and after carbachol application (CCh) (n = 5 cells from 3 mice). * = $p < 0.05$ (paired t-test). X = mean.

I next investigated the effect of applying different concentrations of carbachol to produce a dose-response curve (Figure 3-9). On average, 1, 5 and 10 μM carbachol reduced EPSC amplitudes by $30.13 \pm 9.76 \%$ (n = 2 cells from 2 mice), $57.56 \pm 8.20 \%$ (n = 4 cells from 4 mice, $p < 0.05$) and $67.53 \pm 4.63 \%$ (n = 5 cells from 3 mice, $p < 0.05$), respectively (Figure 3-9).

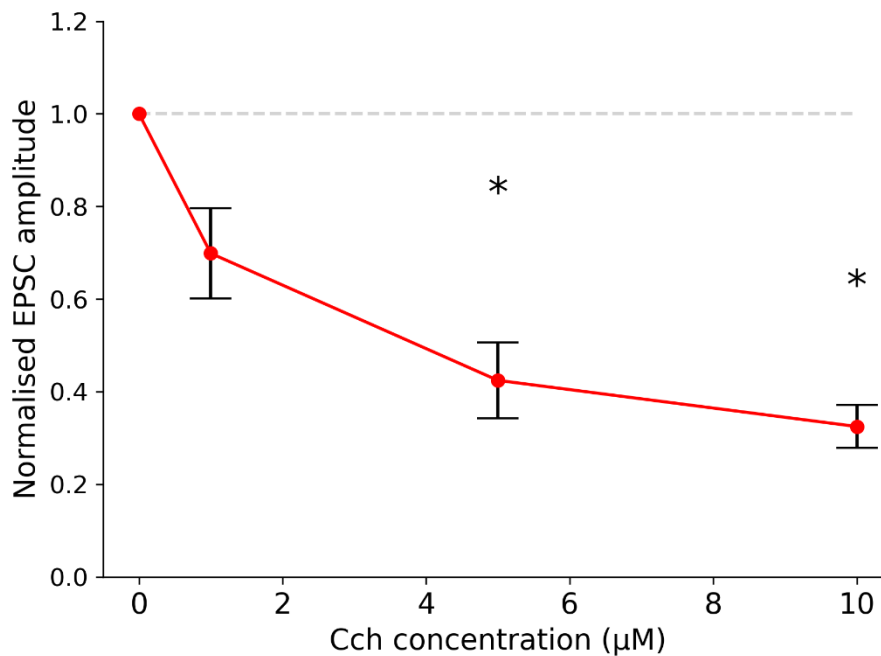


Figure 3-9: Effect on EPSC amplitude with increasing carbachol concentrations. 1 μM : n = 2 cells from 2 mice, 5 μM : n = 4 cells from 4 mice, 10 μM : n = 5 cells from 3 mice. * = $p < 0.05$ (one-sample t-test).

In conclusion, the results presented in this section support previous studies investigating the impact of carbachol on CA3 recurrent transmission (Vogt and Regehr, 2001; Kremin and Hasselmo, 2007) and pyramidal cell excitability (Sun and Kapur, 2012).

3.3.2 Noradrenergic modulation of CA3 recurrent synaptic transmission

I now repeated the experiments described above with noradrenaline, in place of carbachol. Bath applied 20 μ M noradrenaline had little effect on CA3-CA3 EPSC amplitudes ($87.8 \pm 6.2\%$ of baseline with noradrenaline, $n=5$, $p=0.12$) (Figure 3-10, Figure 3-11) or the PPR (Figure 3-11).

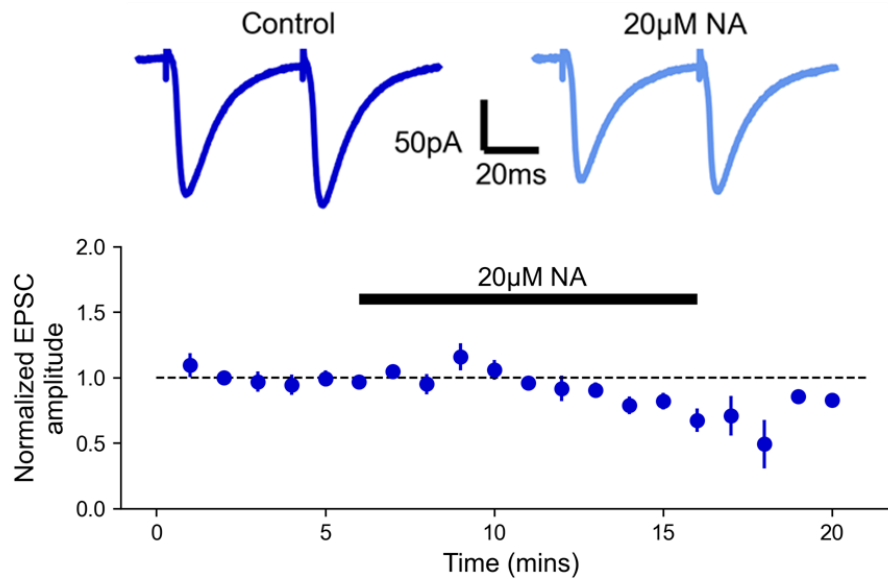


Figure 3-10: Impact of 20 μ M noradrenaline on CA3 recurrent excitatory transmission. Top left: example trace from one cell averaged over the 5-minute baseline period. Top right: example trace from the same cell averaged over a 5-minute period during noradrenaline application. Bottom: normalized EPSC amplitude over the whole experiment for 5 cells (from 3 mice) averaged in 1-minute bins. Black bar represents the period of noradrenaline application.

EPSC amplitudes and PPRs were slightly reduced from 66.73 ± 17.20 pA to 58.45 ± 16.30 pA and 1.25 ± 0.06 to 1.09 ± 0.02 with noradrenaline application, respectively ($n = 5$ cells from 3 mice) (Figure 3-11). Therefore, these results suggest that noradrenaline had little impact on synaptic transmission in the CA3 recurrent network.

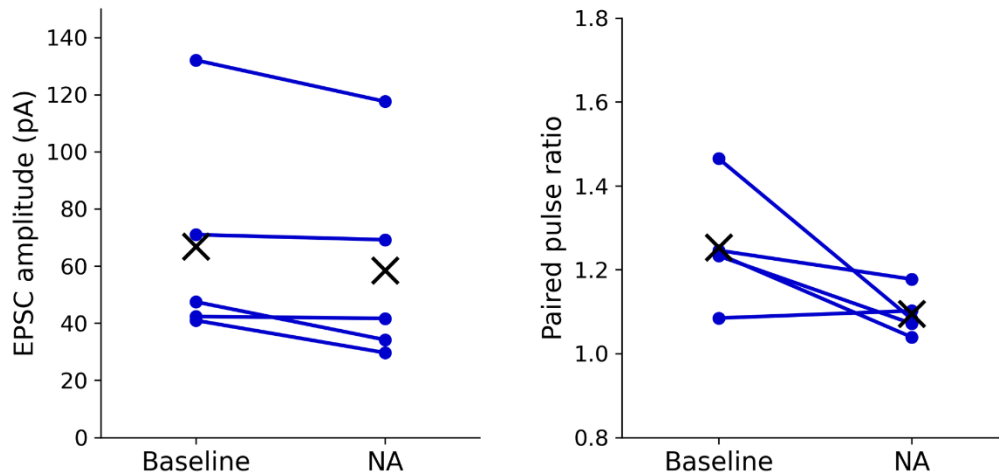


Figure 3-11: Effect of noradrenaline on EPSC amplitude and paired pulse ratio. Baseline = Average amplitude and paired pulse ratio (PPR) in the 5-minute period before noradrenaline (NA) application. NA = Average amplitude paired pulse ratio (PPR) from 5-minute period during NA wash on (n = 5 cells from 3 mice). * = $p < 0.05$ (paired t-test). X = mean.

I next tested the effect of noradrenaline on the resting membrane potential and input resistance (Figure 3-12), as explained in the previous section. Noradrenaline also had minimal impact on resting membrane potential (from -61.90 ± 2.43 mV to -60.19 ± 2.56 mV, n = 7 cells from 4 mice) and input resistance (from 175.52 ± 20.85 M Ω to 167.24 ± 12.84 M Ω , n = 6 cells from 4 mice). Therefore, noradrenaline also seemed to have little influence on CA3 pyramidal neuron excitability as well as on the recurrent synaptic transmission.

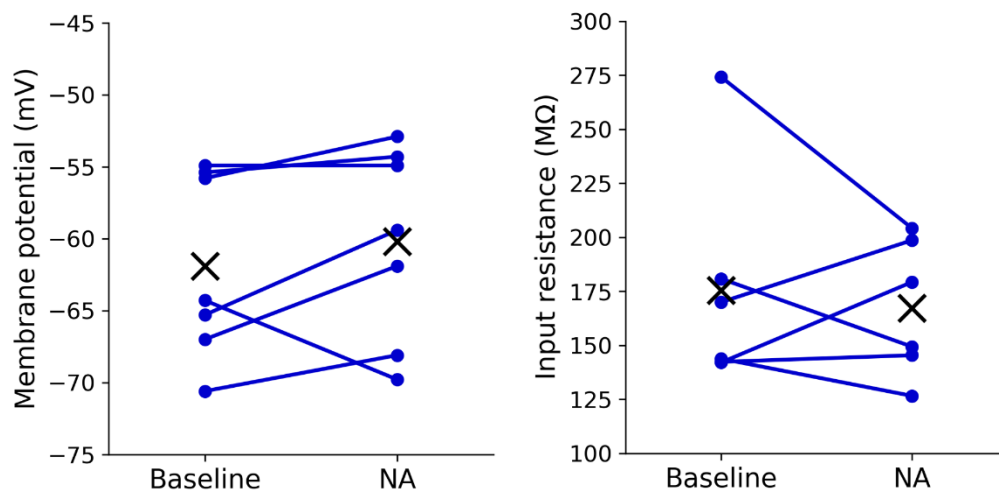


Figure 3-12: Effect of noradrenaline on resting membrane potential and input resistance. Membrane potential (n = 7 cells from 4 mice) and input resistance (n = 6 cells from 4 mice) measured before (baseline) and after noradrenaline application (NA). * = $p < 0.05$ (paired t-test). X = mean.

3.3.3 Comparison between cholinergic and noradrenergic effect on CA3 synaptic transmission

As shown in the previous sections, carbachol and noradrenaline had different impacts on the recurrent EPSC amplitude, paired pulse ratio and CA3 pyramidal cell excitability. Here, I have compared and summarised the effects between both neuromodulators (Figure 3-13). Carbachol reduced the EPSC amplitude ($42.4 \pm 8.2\%$ of baseline, $n = 4$ cells from 4 mice, $p < 0.05$), whereas noradrenaline had little effect on synaptic transmission ($87.8 \pm 6.2\%$ of baseline, $n = 5$ cells from 3 mice). Carbachol increased the paired pulse ratio (by 0.39 ± 0.09 , $n = 4$, $p < 0.05$), whereas with noradrenaline there was also minimal change (reduced PPR by 0.16 ± 0.07 , $n = 5$ cells from 3 mice). Carbachol also increased cell excitability by depolarising the resting membrane potential (by 4.8 ± 1.5 mV, $n = 5$ cells from 3 mice, $p < 0.05$) and slightly increasing the input resistance (by 9.0 ± 9.2 M Ω , $n = 5$ cells from 3 mice, $p = 0.24$), although the input resistance change was not significant here. Noradrenaline, on the other hand, did not significantly change the resting membrane potential (1.7 ± 1.4 mV increase, $n = 7$ cells from 4 mice, $p = 0.28$) or the cell's input resistance (8.3 ± 16.3 M Ω decrease, $n = 6$ cells from 4 mice, $p = 0.63$). In conclusion, these results demonstrated that acetylcholine, but not noradrenaline, modulated CA3-CA3 recurrent circuitry and CA3 pyramidal neuron excitability.

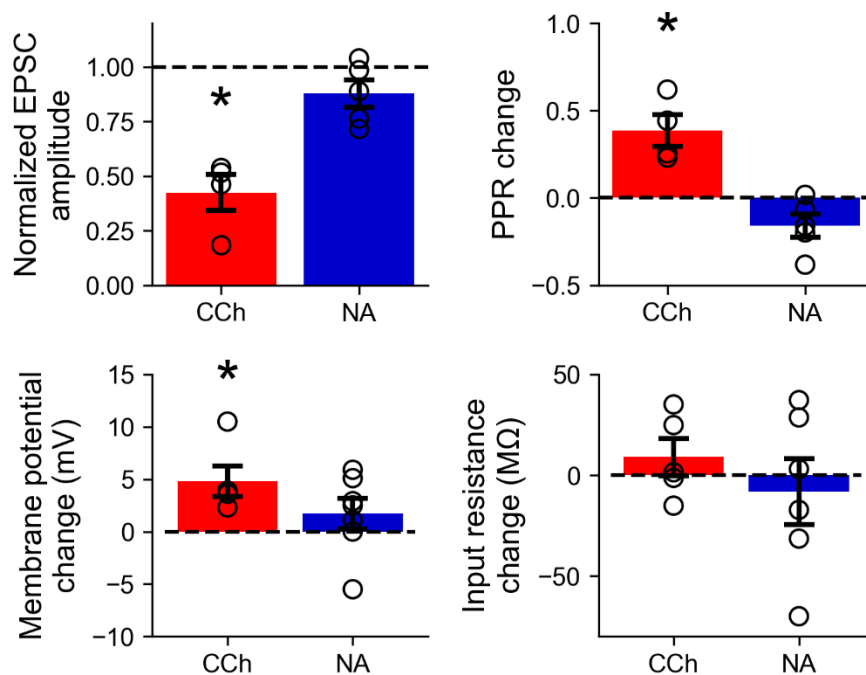


Figure 3-13: Comparison between effect of carbachol and noradrenaline on CA3 synaptic transmission and pyramidal cell excitability. Upper left: normalized average EPSC amplitude with carbachol ($n = 4$ cells, 4 mice) and noradrenaline ($n = 5$ cells, 3 mice). Upper right: change in paired pulse ratio with carbachol ($n = 4$ cells, 4 mice) and noradrenaline ($n = 5$ cells, 3 mice). Lower left: change in membrane potential with carbachol ($n = 5$ cells, 3 mice) and noradrenaline ($n = 7$ cells, 4 mice). Lower right: Change in input resistance with carbachol ($n = 5$ cells, 3 mice) and noradrenaline ($n = 7$ cells, 4 mice). All data represented as mean \pm SEM. CCh = carbachol. NA = noradrenaline. * = $p < 0.05$ (paired t-test).

3.3.4 Effect of endogenous acetylcholine release on CA3 excitatory synaptic inputs

Next, I tested the effect of endogenous acetylcholine release on CA3 excitatory inputs from the recurrent and perforant path. Here, ChAT-Cre x Ai32 mice were used that expressed channelrhodopsin-2 in cholinergic neurons (see Methods). To evoke acetylcholine release, a blue LED was flashed onto the slice, as explained in the Methods, to release acetylcholine from the channelrhodopsin-expressing cholinergic axons in the hippocampus. As a positive control, I initially tested activation of nicotinic receptors on oriens-lacunosum moleculare (OLM) interneurons via blue light stimulation (Figure 3-14). I identified OLM interneurons by their cell body shape and location in the CA1 stratum oriens. A fast nicotinic response and a slower, potentially muscarinic, response was recorded in a couple of CA1 OLM interneurons (Figure 3-14). The response was reduced by $82.22 \pm 6.87 \%$ (from 67.67 ± 0.36 pA to 12.05 ± 4.71 pA) with the addition of nicotinic (50 μ M mecamylamine) and muscarinic (25 μ M atropine) receptor antagonists, confirming that the light-evoked response was driven by cholinergic activation. Hippocampal acetylcholine release upon blue light stimulation has also previously been confirmed in the CA1 region in this mouse line (Palacios-Filardo et al., 2021).

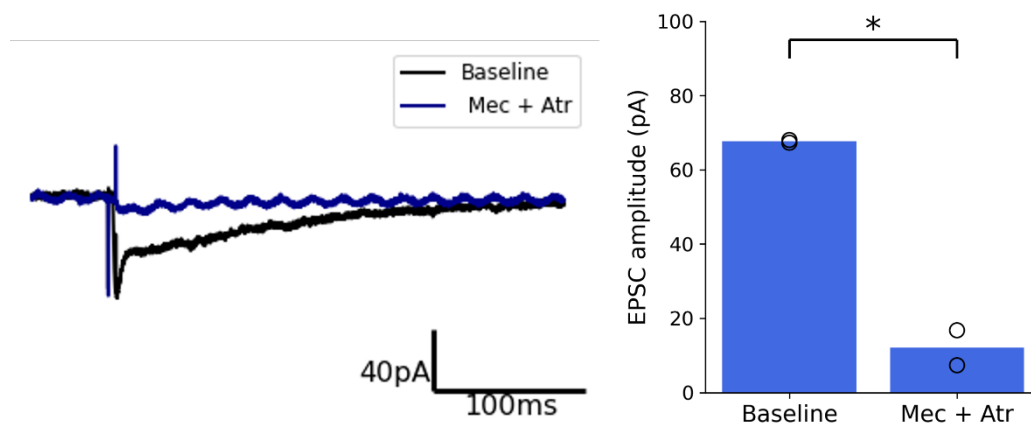


Figure 3-14: Optogenetic activation of nicotinic receptors on OLM interneurons. Left: Example traces from an OLM interneuron with one 5 ms pulse of light stimulation (baseline) and with nicotinic and muscarinic receptor antagonists (Mec + Atr). Artifacts represent time of light stimulation. Mec = mecamylamine, Atr = atropine. Right: Average EPSC amplitude with light stimulation and with cholinergic antagonists (n = 2 cells, 2 mice). * = $p < 0.05$.

As I introduced perforant path stimulation in these next experiments, I applied DCG-IV, if cells were still viable, at the end of experiments to confirm stimulation of the perforant path (Figure 3-15). DCG-IV is an agonist for mGluR2/3, which is present on perforant path axons, but not on CA3 recurrent collaterals (Neki et al., 1996; Shigemoto et al., 1997), and reduces glutamatergic transmission. Figure 3-15 shows that 3 μ M DCG-IV reduced the perforant path EPSC amplitude by approximately $45.26 \pm 10.70 \%$ (n = 3 cells from 2 mice), whereas it did not affect transmission in the recurrent network ($17.67 \pm 10.29 \%$ increase, n = 3 cells from 2 mice).

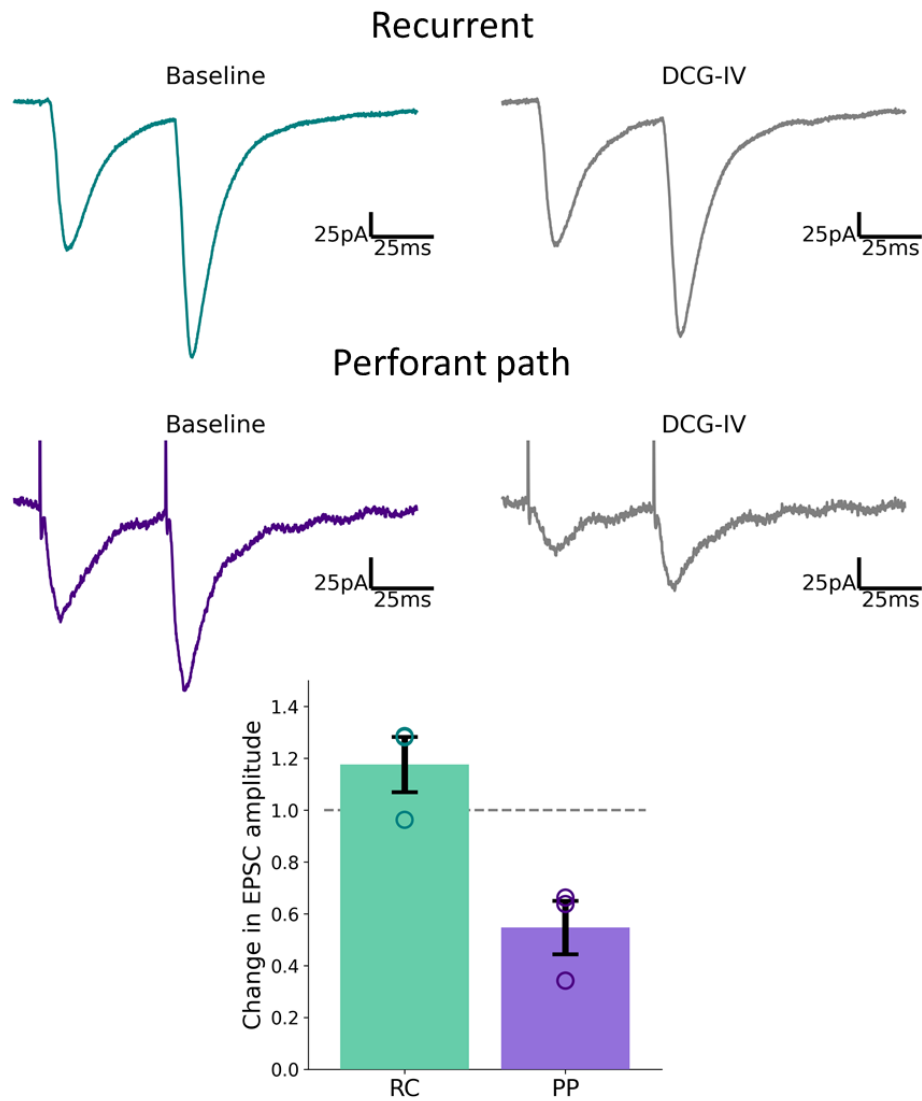


Figure 3-15: Application of DCG-IV reduced perforant path but not recurrent EPSC amplitudes. Example traces from recurrent (upper) and perforant path (lower) stimulation before and after DCG-IV application. Bar plot: average change in EPSC amplitude with DCG-IV in each pathway (n = 3 cells, 2 mice).

I now tested the effect of endogenous acetylcholine release on the recurrent- (Figure 3-16) and perforant path-evoked EPSCs (Figure 3-17). Figure 3-16 shows averaged EPSC traces from stimulating CA3 recurrent axons from an example recording before (Baseline) and during 5 minutes of optogenetic activation (Opto ACh). The lower panel is the normalised EPSC amplitude over time averaged across 14 neurons. As is shown in this Figure, light-evoked acetylcholine release had little influence on EPSC amplitude.

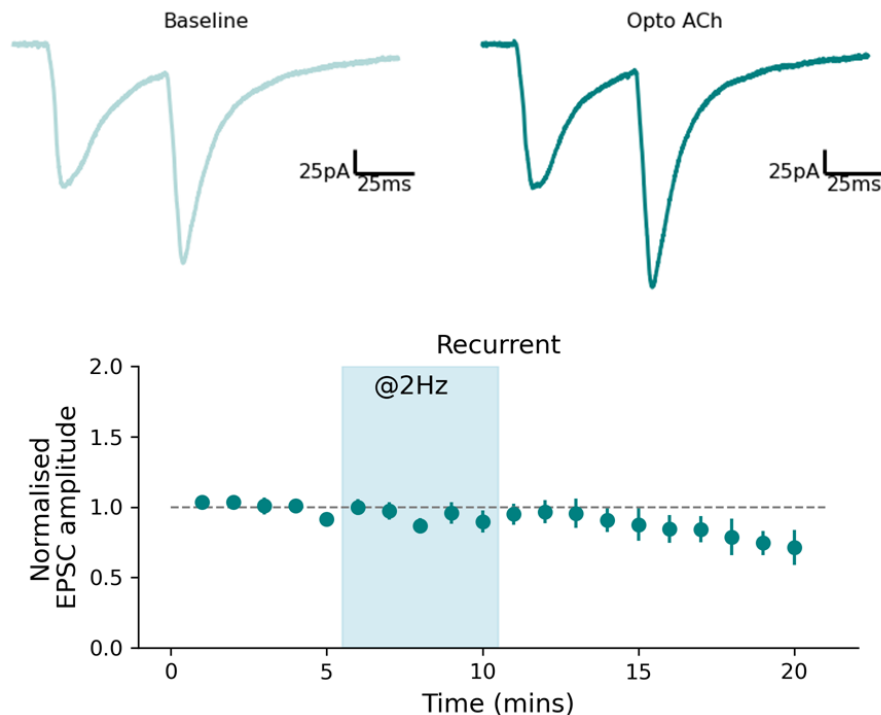


Figure 3-16: Effect of optogenetic acetylcholine release on recurrent EPSC amplitudes in CA3 pyramidal neurons. Upper: example traces from one cell averaged across the 5-minute baseline period (left) and 5-minutes of optogenetic activation (right). Lower: Averaged data from 14 cells (from 8 mice) in over a 20-minute period. @2Hz blue shaded section is when the blue LED was flashed at 2 Hz for 5 minutes.

I also investigated the effect of endogenous acetylcholine release on perforant path EPSCs. As explained in the Methods, the recurrent and perforant path axons were stimulated alternately within one recording so that the two inputs could be compared within a single neuron. Figure 3-17 shows example traces from perforant path stimulation before and during endogenous acetylcholine release as well as averaged EPSC amplitudes over the course of an experiment ($n = 12$ cells from 8 mice). It was slightly more challenging to stimulate the perforant path inputs and I could not always generate a response, hence the fewer number of cells. There was also more variability in the perforant path-evoked responses possibly due to smaller EPSC amplitudes (Figure 3-18). There was also little effect of acetylcholine on the perforant path EPSCs observed here (Figure 3-17).

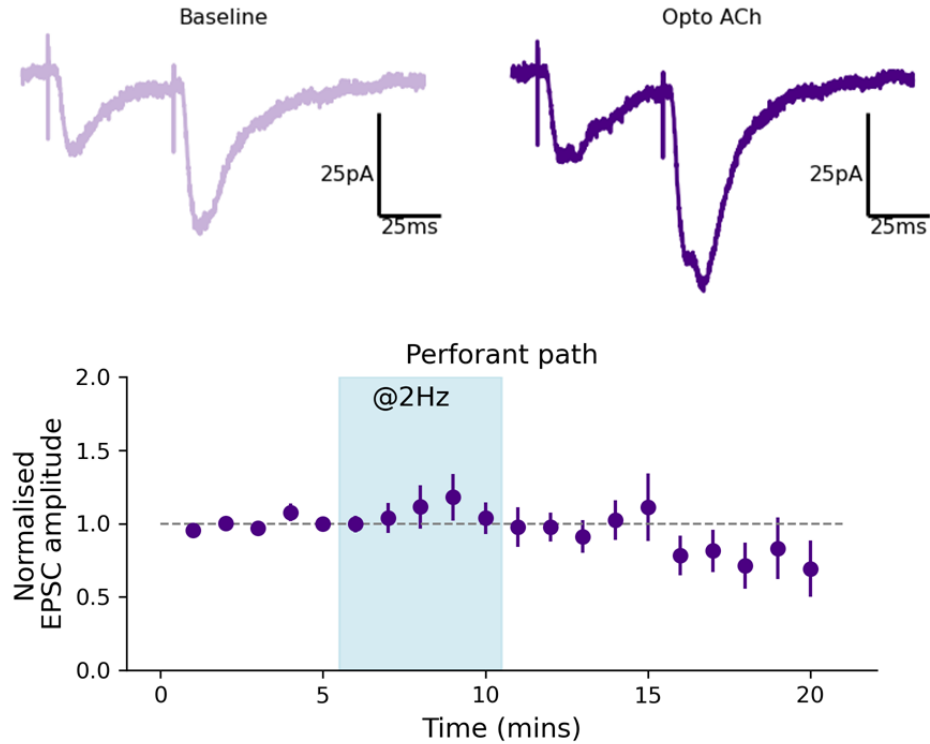


Figure 3-17: Effect of optogenetic acetylcholine release on perforant path EPSC amplitudes in CA3 pyramidal neurons. Upper: example traces from one cell averaged across the 5-minute baseline period (left) and 5-minutes of optogenetic activation (right). Lower: Averaged data from 12 cells (from 8 mice) over a 20-minute period. @2Hz blue shaded section is when the blue LED was flashed at 2 Hz for 5 minutes.

The average EPSC baseline amplitudes were 93.25 ± 11.82 pA ($n = 14$ cells from 8 mice) for the recurrent pathway and 48.18 ± 10.98 pA ($n = 12$ cells from 8 mice) for the perforant path (Figure 3-18). The perforant path EPSCs were significantly smaller (Wilcoxon rank-sum, $p < 0.05$) compared to the recurrent inputs, which was to be expected as neurons receive perforant path inputs to the distal dendrites and therefore the response attenuates as it propagates to the soma. In addition, the baseline paired pulse ratios were significantly different with 1.39 ± 0.08 in recurrent EPSCs and 2.20 ± 0.16 in perforant path EPSCs ($p < 0.05$) (Figure 3-18). There was also a significant difference in the rise times between the perforant path (2.88 ± 0.32 ms) and recurrent evoked EPSCs (1.86 ± 0.14 ms) with a slower rise time in the perforant path responses (Figure 3-18) also due to propagation of the response from distal rather than more proximal dendrites.

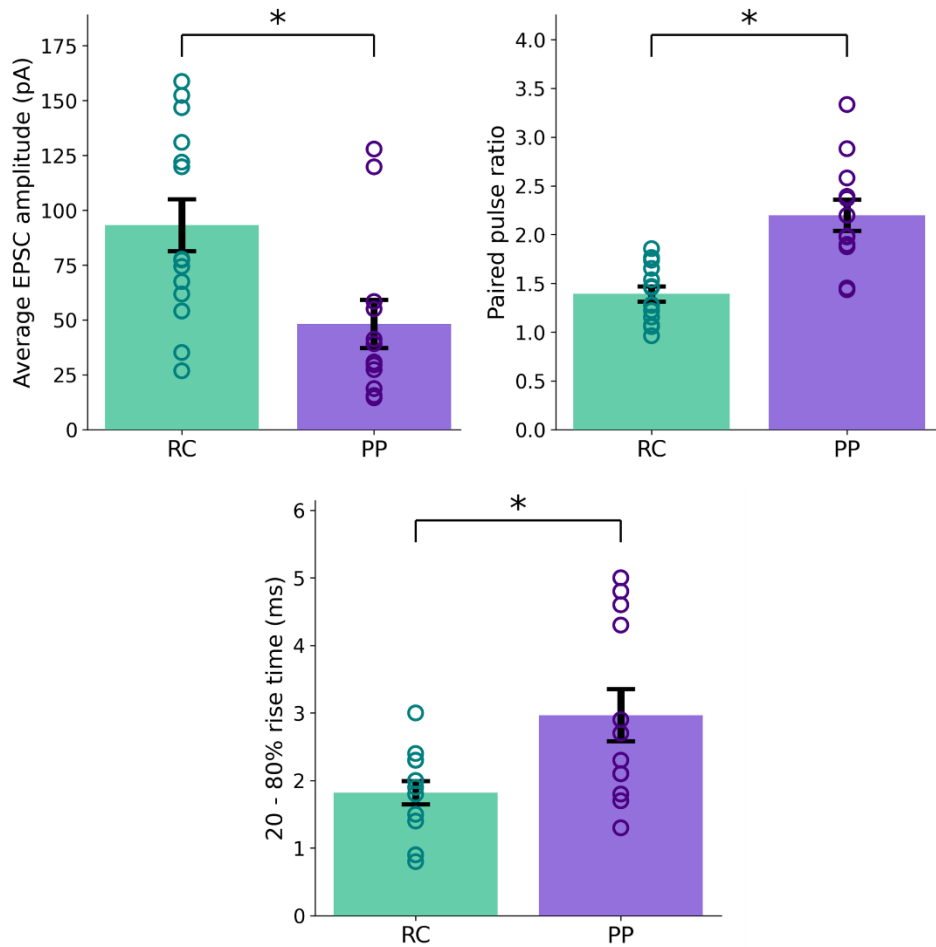


Figure 3-18: Comparison between baseline recurrent and perforant path EPSC properties. Average EPSC amplitude, paired pulse ratio and 20 – 80% rise time comparison between responses recorded from recurrent (RC) (n = 14 cells from 8 mice) and perforant path (PP) (n = 12 cells from 8 mice) stimulation. * = $p < 0.05$ (Wilcoxon rank-sum).

I have next compared the effect of acetylcholine on both the recurrent and perforant path EPSC properties (Figure 3-19). The change in recurrent EPSC amplitude with acetylcholine release was slightly reduced on average by 6.27 ± 5.68 % (n = 14 cells from 8 mice), whereas the perforant path EPSC amplitude was slightly increased by 12.19 ± 9.15 % (n = 12 cells from 8 mice), however neither change was significant. In relation to the short-term plasticity, on average there was little effect of acetylcholine on the recurrent PPR (2.48 ± 3.73 % reduction, n = 14 cells from 8 mice) and a small reduction in the perforant path PPR (by 10.13 ± 4.64 %, n = 12 cells from 8 mice). Overall, optogenetic activation of the cholinergic neurons did not significantly affect the EPSC amplitudes or PPRs recorded from either recurrent or perforant path inputs (Figure 3-19).

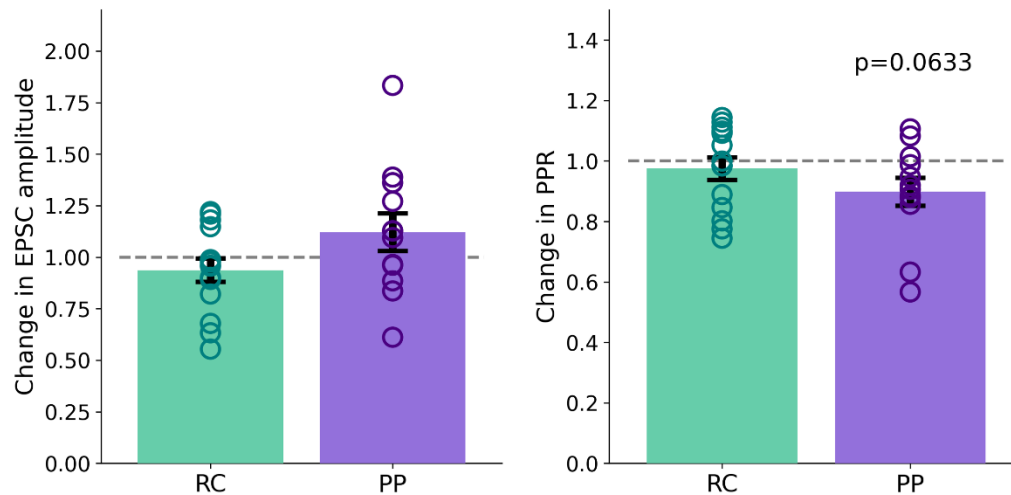


Figure 3-19: Average change in EPSC amplitude and paired pulse ratio with optogenetic acetylcholine release. Left: Change in EPSC amplitude with optogenetic activation. EPSC amplitude is calculated from averaged traces in each cell 5 minutes before and 5 minutes during optogenetic stimulation. Right: Change in paired pulse ratio (PPR). PPR is calculated as the ratio between the first and second EPSC peak. RC = recurrent collateral input; PP = perforant path.

As the effect of endogenous acetylcholine on synaptic transmission was quite variable in both pathways, I tested whether there were other factors that could be contributing to the variability of the effect. Figure 3-20 shows relationships between the change in EPSC amplitude with the change in the paired pulse ratio (Figure 3-20A), the baseline rise time (Figure 3-20B) and the age of the mouse (Figure 3-20C). Differences in the EPSC rise times could suggest contaminated inputs, whereas mouse age could be related to the health of cells or channelrhodopsin expression. However, the response rise time and mouse age were not significantly correlated with the change in EPSC amplitude in either pathway. There was a significant correlation between the change in PPR and the change in EPSC amplitude with perforant path stimulation (Figure 3-20A, right; R-value = -0.813, $p = 0.0013$) but not with recurrent stimulation (Figure 3-20A, left; R-value = -0.42, $p = 0.135$). Both pathways demonstrated a negative correlation, whereby a larger reduction in the EPSC amplitude was associated with an increased PPR.

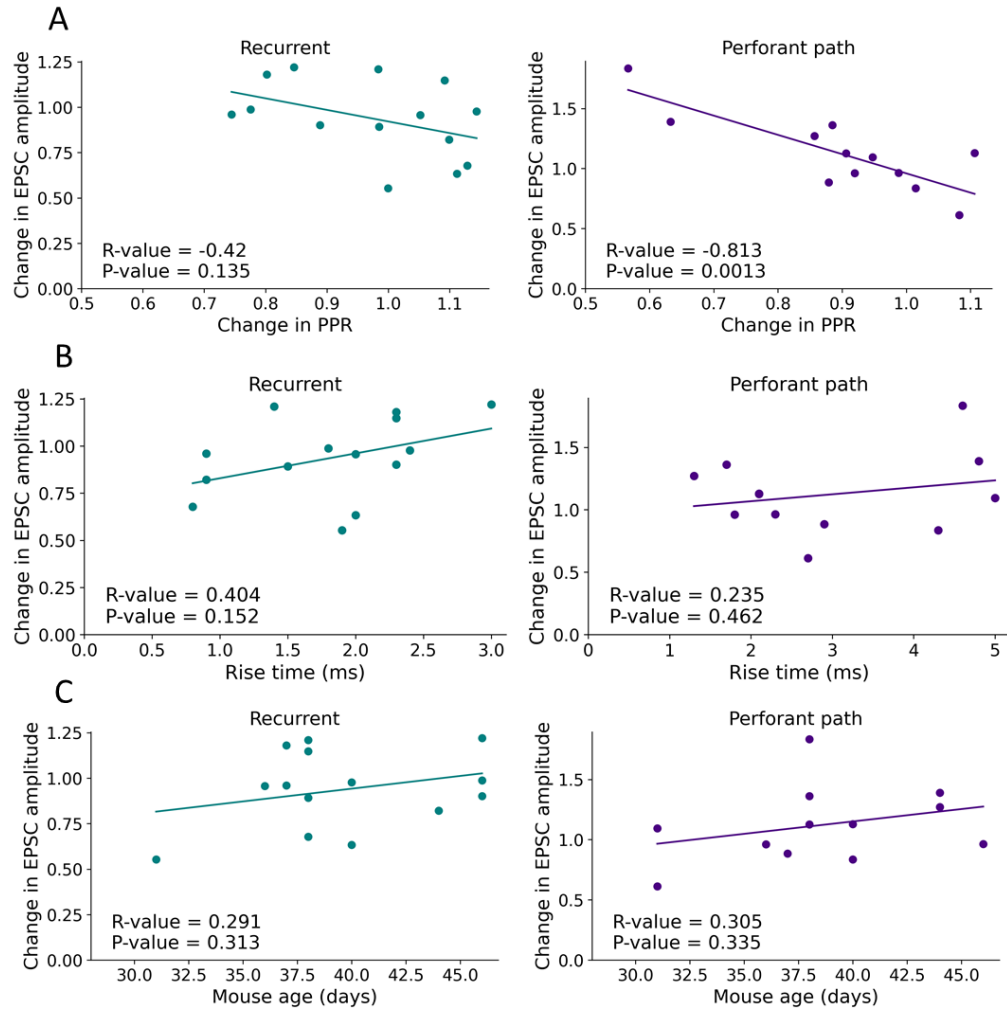


Figure 3-20: Relationships between the change in EPSC with optogenetic activation and the change in PPR, rise time and mouse age. Left: Recurrent EPSCs, right: Perforant path EPSCs. All plots are comparing to the change in EPSC amplitude (y-axis). (A) Change in paired pulse ratio. (B) Baseline rise time. (C) Mouse age. R-value = correlation coefficient.

Additionally, I considered the effect of animal and gender on the change in EPSC amplitude to check there were no major differences between cells recorded from certain animals (Figure 3-21). There were no significant differences in the change in EPSC amplitudes between different animals (Figure 3-21A) or between male or female mice for both stimulation inputs (Figure 3-21B).

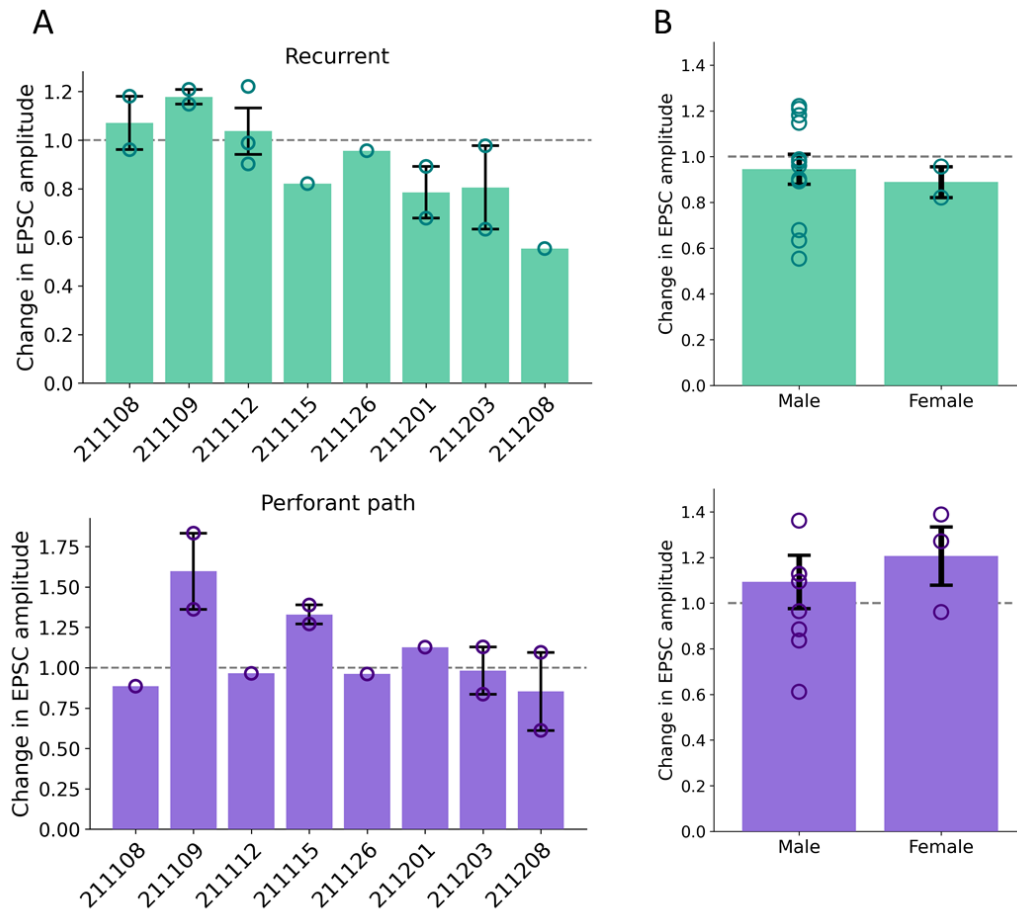


Figure 3-21: Effect of animal and gender on the change in EPSC amplitude. Upper = recurrent EPSCs, lower = perforant path EPSCs. (A) x-axis = date of experiment as a reference to animal used. (B) Effect of mouse gender on change in EPSC amplitude. Recurrent EPSC: 12 cells from 6 male mice, 2 cells from 2 female mice. Perforant path EPSCs: 9 cells from 6 male mice, 3 cells from 2 female mice.

There were 9 cells in total in which I was able to record both recurrent and perforant path evoked EPSCs. Figure 3-22 shows the relationship between the change in EPSC amplitude with acetylcholine in each pathway. There was a positive correlation between the change in EPSC amplitudes (R -value = 0.604), suggesting that acetylcholine produced a similar effect in each neuron, independent of the input pathway, and therefore that the main variability was between slice recordings. In fact, there was a negative correlation between the percentage change in series resistance and the change in RC and PP EPSC amplitudes (Figure 3-23), suggesting the quality of the seal was the main cause of variability between cells.

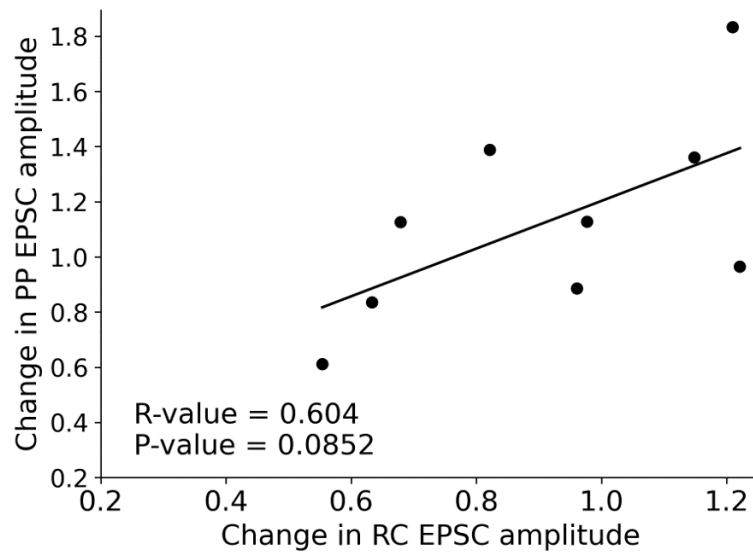


Figure 3-22: Relationship between change in recurrent and perforant path EPSC amplitude with endogenous acetylcholine release. Change in RC and PP amplitudes recorded from the same cell. R-value = correlation coefficient (n = 9 cells, 7 mice). RC = recurrent inputs, PP = perforant path inputs.

To summarise, on average endogenous acetylcholine had minimal effect on recurrent and perforant path stimulated inputs to CA3 pyramidal neurons. The effect was variable between neurons, but this variability was not related to EPSC rise times, mouse age, or animal differences.

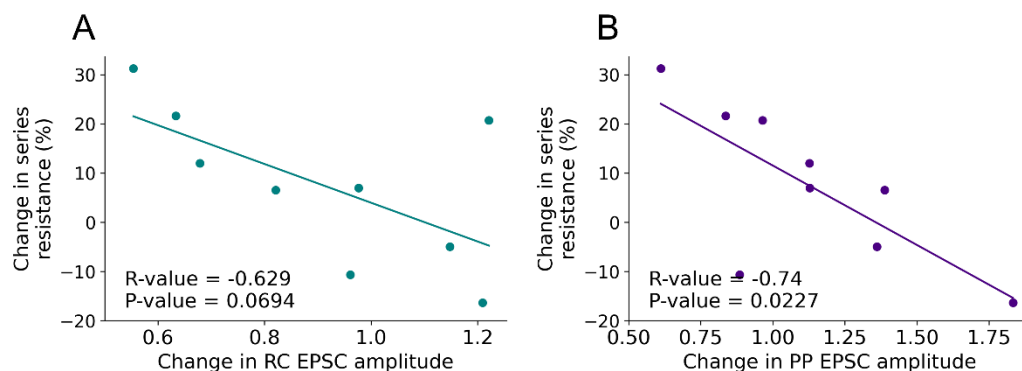


Figure 3-23: Change in EPSC amplitudes with endogenous acetylcholine release in relation to change in series resistance over experiment. Change in series resistance, measured from averaged 5-minute time periods before and after optogenetic release, related to RC (A) and PP (B) EPSC change in amplitudes. R-value = correlation coefficient (n = 9 cells, 7 mice). RC = recurrent inputs, PP = perforant path inputs.

3.3.5 Effect of endogenous acetylcholine release on CA3 inhibitory synaptic inputs

To investigate the effect of endogenous acetylcholine release on inhibitory inputs to CA3 neurons, a stimulating electrode was positioned in the pyramidal cell layer of CA3 to stimulate basket cell axons. The same stimulation protocol was given as in the previous section, with two pulses spaced 50 ms apart. The optogenetic stimulation was also performed in the same way; after a 5-minute period of recording

baseline inhibitory post-synaptic current (IPSC) amplitudes, the blue LED was flashed at 2 Hz for 5 minutes. Baseline IPSCs recorded had an average amplitude of 94.89 ± 13.47 pA, a paired pulse ratio of 0.56 ± 0.074 and a 20 – 80% rise time of 1.75 ± 0.36 ms ($n = 13$ cells from 8 mice), as would be expected for inhibitory post-synaptic currents in CA3 (Szabó et al., 2010). Figure 3-24A displays averaged traces from an example cell during a baseline period and during optogenetic acetylcholine release. The change in IPSC amplitude is also averaged over time for 13 cells in Figure 3-24B and shows a small reduction in IPSC amplitude during optogenetic stimulation. On average, the IPSC amplitude was reduced by 13.98 ± 4.99 % ($p < 0.05$, $n = 13$ cells from 8 mice) and the paired pulse ratio increased from 0.56 ± 0.074 to 0.62 ± 0.08 with optogenetic acetylcholine release (Figure 3-24C, D).

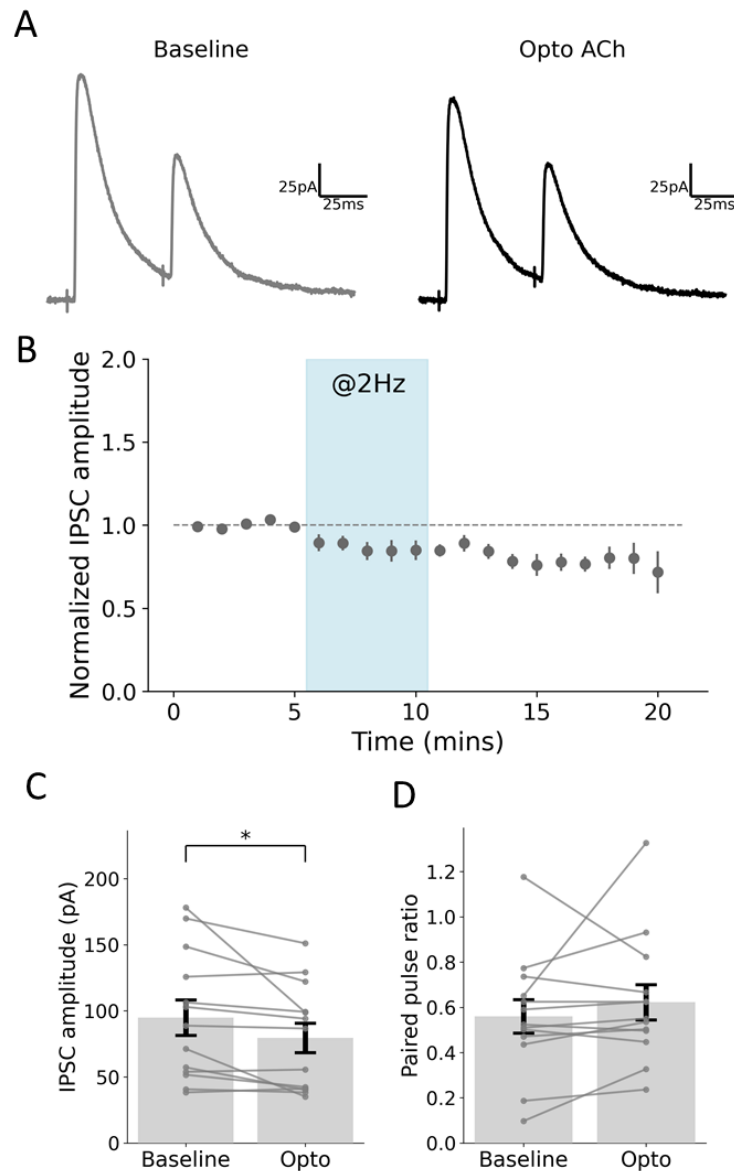


Figure 3-24: Effect of light-evoked endogenous acetylcholine release on IPSCs recorded in CA3 pyramidal neurons. (A) Example averaged traces from one neuron before and during optogenetic stimulation. (B) Averaged IPSC amplitudes over time. (C) Change in IPSC amplitude. (D) Change in PPR. (n = 13 cells, 8 mice). Paired t-test. * = $p < 0.05$.

As with the excitatory inputs, I also investigated the relationship between the change in IPSC amplitude and potential factors that could be influencing the change in IPSC amplitude (Figure 3-25). No correlation was found between the change in PPR (Figure 3-25A), IPSC rise time (Figure 3-25B) or mouse age (Figure 3-25C).

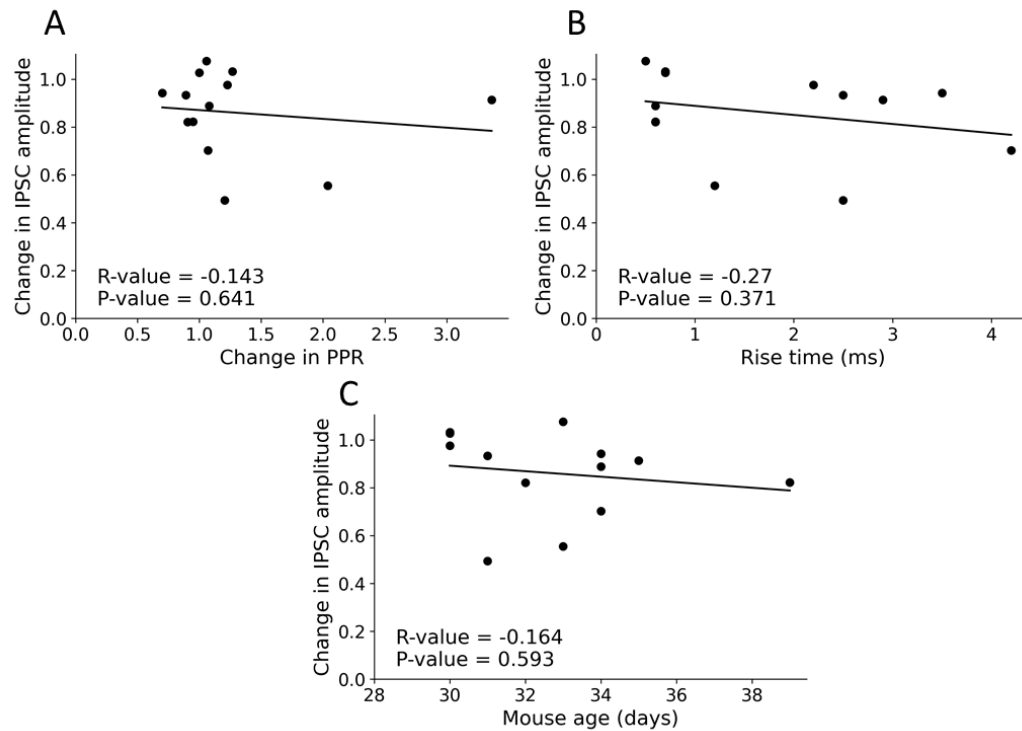


Figure 3-25: Impact of change in paired pulse ratio, rise time and mouse age on the change in IPSC amplitude with endogenous acetylcholine release. (A) Change in PPR. (B) Rise time. (C) Mouse age.

The effect of animal and gender on the change in IPSC amplitude was also analysed in Figure 3-26 to confirm there was no individual animal (Figure 3-26A) or gender (Figure 3-26B) responsible for the effects observed.

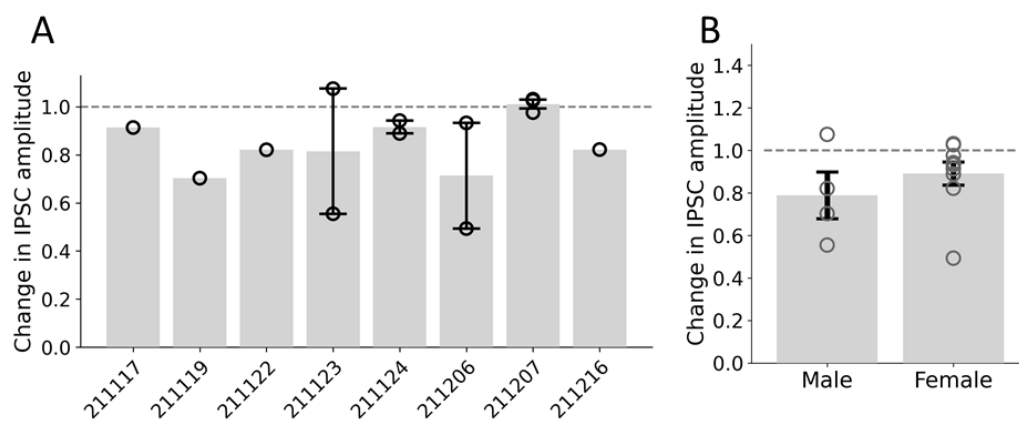


Figure 3-26: Effect of animal and gender on the change in IPSC amplitude. (A) Effect of animal on change on IPSC amplitude. X-axis = date of experiment as a reference to animal used. (B) Effect of mouse gender on change in IPSC amplitude. Males: n = 4 cells from 3 male mice, females: n = 9 cells from 5 female mice.

3.3.6 Preliminary experiments to study dendritic integration in CA3 neurons

To test the prediction from the modelling that acetylcholine could reduce the threshold for NMDA-mediated supra-linear integration, I performed preliminary experiments to try and assess dendritic integration properties of the recurrent and perforant path inputs in brain slices, with and without acetylcholine. I performed these experiments in current clamp, maintaining the membrane potential at approximately -70mV, to record excitatory post-synaptic potentials (EPSPs). The stimulating electrodes were positioned in the same location as the previous experiments to stimulate recurrent and perforant path axons alternately and triggered a single EPSP as well as a compound EPSP (see Methods). I then increased the stimulation intensity in each pathway throughout the duration of the experiment to test a range of input intensities. To analyse the relationship between input intensity and output at the soma, the rising slope of single EPSPs were calculated as a measure for the stimulation intensity and the area under the curve (AUC) of the decay phase of the compound EPSP was measured to detect plateau potentials and dendritic integration properties. Endogenous acetylcholine release was stimulated in the same way as the previous experiments, for 5 minutes at a frequency of 2 Hz.

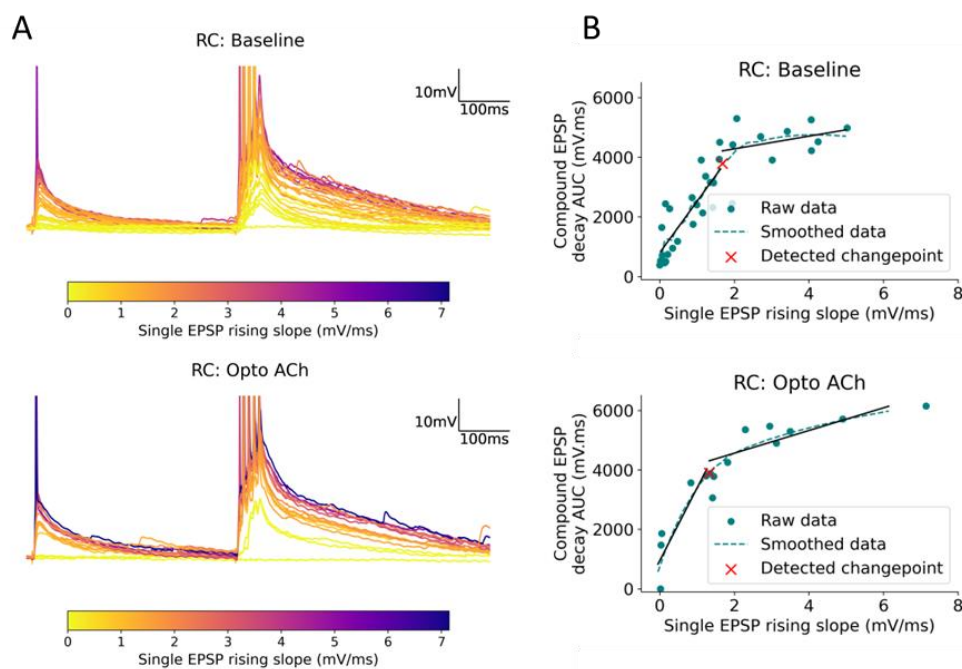


Figure 3-27: Example data from dendritic integration experiment stimulating recurrent inputs. (A) Raw traces from a single experiment (upper: baseline, lower: optogenetic stimulation). Traces are colour coded based on the rising slope of the single EPSP. (B) Relationship between rising slope of single EPSP with AUC of compound EPSP decay phase (upper: baseline, lower: optogenetic stimulation). Circles = raw data, dashed line = smoothed data, red cross = detected changepoint of smoothed data, black lines = linear regression of smoothed data before and after the changepoint.

Figure 3-27 and Figure 3-28 show raw data from an example experiment stimulating the recurrent inputs and the perforant path inputs, respectively. Figure 3-27A shows a slow decay phase after the compound

EPSP suggesting possible plateau potential-like representations from recurrent axon stimulation. To determine the nature of the input-output relationship, the AUC was calculated from 50 to 500 ms after the compound EPSP stimulation and plotted against the subthreshold rising slope of the single EPSP (Figure 3-27B) during a baseline period (upper) and during optogenetic acetylcholine stimulation (lower). The data was then smoothed (dashed line), a changepoint detected (red cross), and two linear regressions were fitted before and after the changepoint.

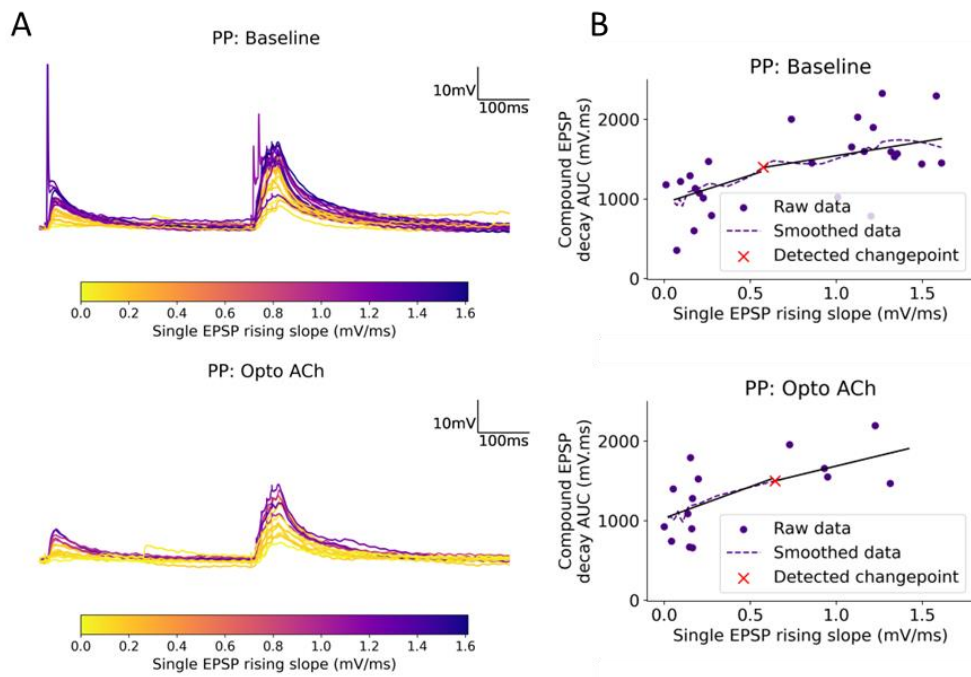


Figure 3-28: Example data from dendritic integration experiment stimulating perforant path inputs. (A) Raw traces from a single experiment (upper: baseline, lower: optogenetic stimulation). Traces are colour-coded based on the rising slope of the single EPSP. (B) Relationship between rising slope of single EPSP with AUC of compound EPSP decay phase (upper: baseline, lower: optogenetic stimulation). Circles = raw data, dashed line = smoothed data, red cross = detected changepoint of smoothed data, black lines = linear regression of smoothed data before and after the changepoint.

Comparing responses between recurrent and perforant path inputs, the rising slopes from perforant path stimulation were significantly smaller (0.47 ± 0.13 mV/ms) compared to recurrent evoked responses (1.44 ± 0.16 mV/ms), as would be expected, and overall, this was the general pattern seen in all 6 cells (Figure 3-29A). The maximum compound EPSP decay AUC was 2476.43 ± 824.95 mV.ms for recurrent-evoked responses and 2572.78 ± 542.88 mV.ms for perforant path-evoked responses (Figure 3-29B). However, when comparing the maximum AUC by normalising to its corresponding rising slope, the maximum AUC to slope ratio was larger in the perforant path responses (2862.94 ± 892.62 (perforant path) vs 1017.06 ± 175.59 (recurrent)) suggesting that smaller input intensities can produce greater outputs in the perforant path (Figure 3-29C). The relationship between the single EPSP rising slopes and the compound EPSP decay AUC was sublinear in the majority of cells, represented here as

a negative difference between the linear regression slopes after and before the changepoint slopes (RC slope difference = -1232.24 ± 503.65 ; PP slope difference = -2658.93 ± 1972.84) (Figure 3-29D).

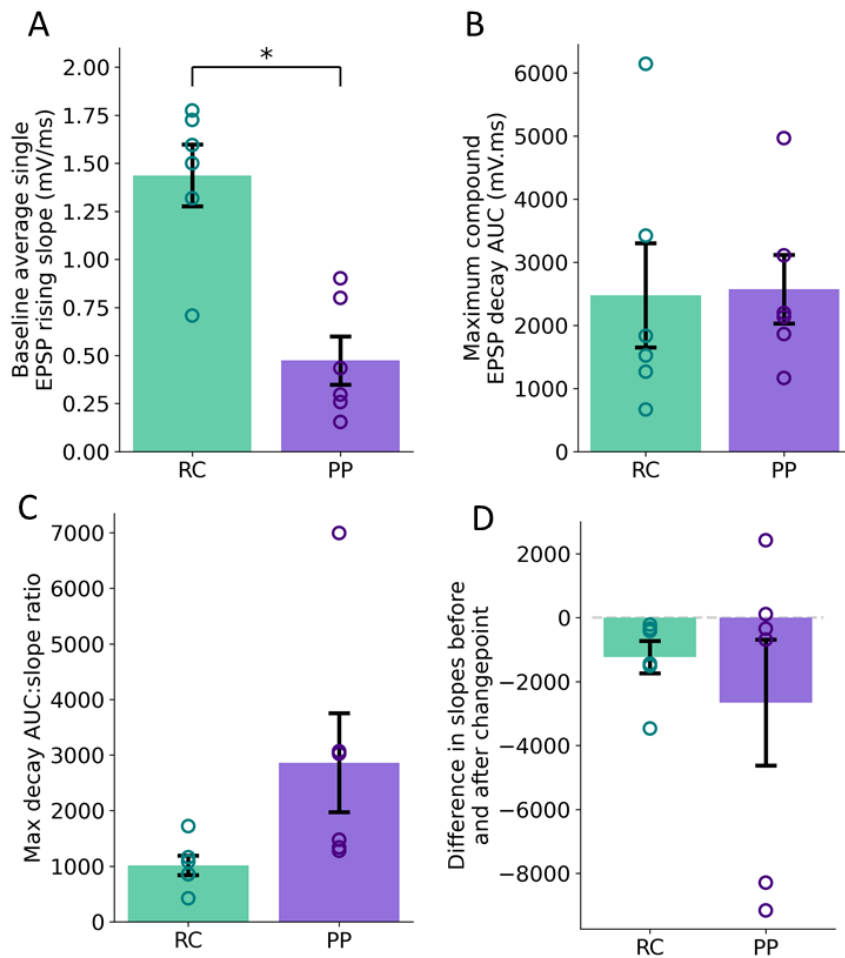


Figure 3-29: Comparison of baseline properties between recurrent- and perforant path-evoked responses. (A) Baseline average single EPSP rising slope. (B) Maximum compound EPSP decay AUC. (C) Maximum compound EPSP decay AUC to rising slope ratio. (D) Difference between linear regression slopes before and after the detected changepoint (slope after changepoint – slope before changepoint). (n = 6 cells, 4 mice). * = $p < 0.05$ (Wilcoxon rank-sum test).

Next, I analysed the impact of acetylcholine on the subthreshold rising slope and compound EPSP decay (Figure 3-30). Acetylcholine caused little change in the average subthreshold rising slope (Figure 3-30A) and average compound EPSP decay AUC (Figure 3-30B) in both pathways, but the change in the decay AUC was variable between cells. Acetylcholine also did not seem to cause a change in the maximum decay AUC to slope ratio in the perforant path but caused a small, but not significant, decrease in the recurrent path (RC = 0.69 ± 0.12 , PP = 1.01 ± 0.10) (Figure 3-30C).

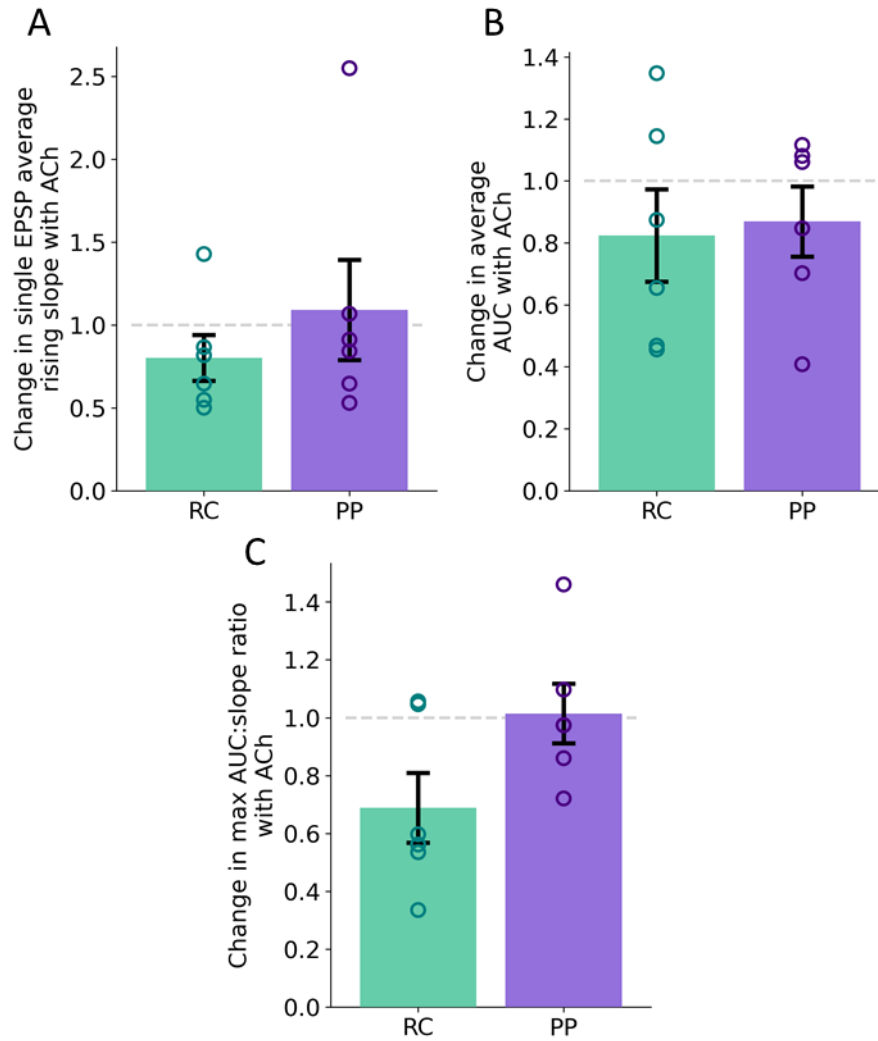


Figure 3-30: Effect of acetylcholine on subthreshold rising slope and compound EPSP decay. (A) Change in average rising slope. (B) Change in average compound EPSP decay AUC. (C) Change in maximum compound EPSP decay AUC to slope ratio. (n = 6 cells, 4 mice).

To compare the integration properties, I also measured the effect of acetylcholine on the linear regression slopes (Figure 3-31). There were variable changes in both linear regression slopes before and after the detected changepoint in both pathways, with no clear trend (Figure 3-31A, B). To further assess whether acetylcholine was affecting dendritic integration, I also analysed the change in the difference between the slopes with acetylcholine (Figure 3-31C). As quantified in Figure 3-29D, the relationships between the two linear regression slopes were on average sublinear. Therefore, here, a positive value means the relationship between the slopes shifted from sublinear to more linear, whereas a negative value represents a shift to a more sublinear relationship. Acetylcholine appeared to have little impact on these sublinear relationships (Figure 3-31C). On average, there was no change in the changepoint in the perforant path (1.01 ± 0.16) but in relation to the recurrent inputs, acetylcholine

slightly reduced the changepoint (0.80 ± 0.10) (Figure 3-31D). This means with acetylcholine, inputs from the recurrent collaterals reached the higher decay AUCs with a lower input intensity.

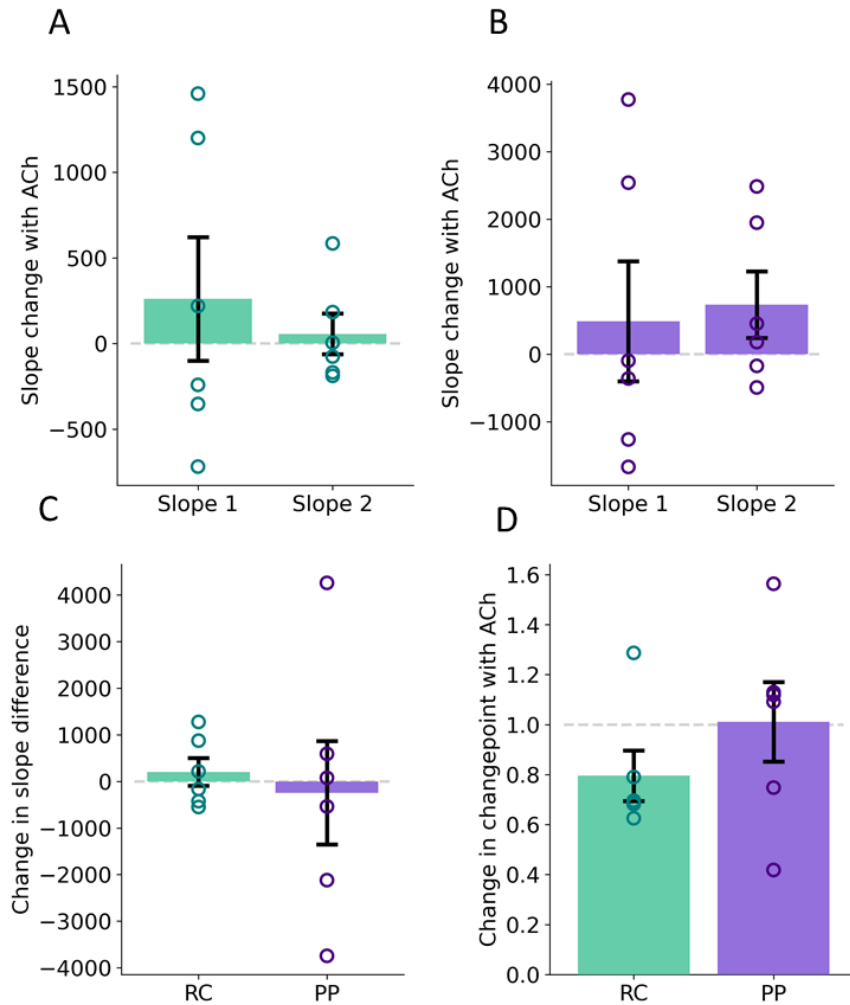


Figure 3-31: Effect of acetylcholine on dendritic integration properties in recurrent and perforant path-evoked responses. (A + B) Change in the linear regression slopes for recurrent (A) perforant path (B) inputs. Slope 1 = slope before the changepoint, slope 2 = slope after the changepoint. (C) Change in the difference between slopes with acetylcholine (D) Change in the changepoint. (n = 6 cells, 4 mice).

To summarise, the relationship between the input stimulation intensity and the compound EPSP decay AUC were sublinear in both the recurrent and perforant pathways (Figure 3-29D) and this relationship was minimally affected by acetylcholine (Figure 3-31C). There was a significant difference between the baseline subthreshold rising slopes in each pathway (Figure 3-29A) and the perforant path had a greater maximum AUC to slope ratio (Figure 3-29C). Acetylcholine also did not affect the average decay AUCs (Figure 3-30B) or the subthreshold rising slopes (Figure 3-30A) but slightly reduced the maximum AUC to slope ratio (Figure 3-30C) and the changepoint (Figure 3-31D) in the recurrent pathway.

3.4 Discussion

The experiments performed here have confirmed that carbachol reduces the CA3-CA3 excitatory synaptic transmission and increases CA3 cell excitability. Noradrenaline, on the other hand, did not affect this synaptic transmission or cell excitability. Additionally, using optogenetics to test the endogenous release of acetylcholine on CA3 synaptic transmission produced some surprising results. In terms of the perforant path and recurrent excitatory inputs, endogenous acetylcholine did not seem to have an effect on reducing this synaptic transmission, as would be expected from the experimental evidence using carbachol (Vogt and Regehr, 2001; Kremin and Hasselmo, 2007). On the other hand, endogenous acetylcholine did reduce inhibitory inputs to CA3 pyramidal neurons, but to a lesser extent than has previously been shown with carbachol application (Szabó et al., 2010). Additionally, increasing the stimulation intensity of the recurrent and perforant path inputs produced a sublinear increase in the compound EPSP decay AUC, which was minimally affected by endogenous acetylcholine.

There could be several explanations for the differences observed between bath applied carbachol and optogenetically-stimulated acetylcholine release and in fact there have been previous discrepancies between the impacts of endogenous vs exogenous neuromodulators in CA1 (Rosen et al., 2015; Bacon et al., 2020). As carbachol is bath applied to the slice at a reasonable concentration, it will reliably bind to and activate a high proportion of cholinergic receptors. On the other hand, the concentration of endogenously released acetylcholine in the CA3 region via optogenetic stimulation is unknown and therefore the physiological concentration of acetylcholine could be lower than the 5 μ M commonly used in *ex vivo* preparations. In fact, the endogenous release of noradrenaline in CA1 has been shown to exhibit effects most similar to 600 nM of bath-applied noradrenaline (Bacon et al., 2020), whereas the typical exogenous concentration used in experiments is \sim 20 μ M. In addition to the unknown concentration of endogenous acetylcholine in CA3, the precise location and release dynamics of acetylcholine in CA3 are also unknown. As explained in the Introduction chapter, there has been evidence for both volume and synaptically-targeted acetylcholine release in the hippocampus (Umbriaco et al., 1995; Takács et al., 2018; Disney and Higley, 2020), but the precise transmission dynamics in CA3 are unknown and therefore, the concentration of endogenous acetylcholine surrounding the particular synapses of interest could be lower than previously thought.

As acetylcholine has previously been shown to affect CA3 neurons differently (Hunt et al., 2018), the variability of acetylcholine's effect could reflect these distinct CA3 cell types. These cell types are positioned differentially along the proximodistal CA3 axis and so to help control for this, I recorded cells from approximately the same proximodistal CA3 location in each slice as well as from similar dorsoventral regions. When analysing the data, I also tested whether some factors such as the PSC rise

time, mouse age and gender could be influencing or correlated with the effect of acetylcholine on EPSC amplitude.

Acetylcholine produced little overall effect on the excitatory inputs to CA3 neurons here but there was a small, significant reduction in IPSC amplitude. This is line with previous carbachol studies showing reduced transmission from different types of interneurons in the CA3 region (Szabó et al., 2010). Here, I was recording IPSCs from stimulation of the CA3 pyramidal cell layer. As there are many types of interneurons in the CA3 region the exact subtype stimulated here was unknown but interneurons with axons in the pyramidal cell layer were most likely basket cells. The IPSC kinetics measured here also reflect PV-positive basket cell dynamics (Szabó et al., 2010; Udakis et al., 2020). In Szabó et al., (2010), they looked at the effect of carbachol on CA3 pyramidal neuron IPSCs from three different interneuron subtypes and showed that carbachol reduced IPSC amplitudes by between 70 and 95% in all interneuron types. Specifically, the PV-positive interneuron IPSCs were reduced by 70-75% (Szabó et al., 2010). This is to a greater extent than the results observed here but could be due to the fact that endogenous acetylcholine is released at a lower concentration or that it is localised to specific synapses. Overall, the reduction of inhibitory inputs, but not excitatory inputs, suggests that the main effect of acetylcholine could be to increase CA3 neuron excitability via disinhibition. In fact, within the DG-CA3 microcircuit, it was also found that acetylcholine modulated the inhibitory inputs, from mossy fibre activation, as opposed to the direct excitatory inputs (Prince et al., 2021).

Recently, the effect of endogenous acetylcholine, using this ChaT-cre:Ai32 mouse line, has been investigated on synaptic transmission in the CA1 region (Palacios-Filardo et al., 2021). It was found that acetylcholine reduced the excitatory Schaffer-collateral (SC) and entorhinal inputs by a similar amount but reduced the feedforward inhibition from the entorhinal cortex to a greater extent than from the SC input. This suggested that there was an overall enhancement of the excitatory-inhibitory balance from the entorhinal cortex. Compared to the CA1 region, the CA3 region should have a similar density of cholinergic fibres (Grybko et al., 2011); however, muscarinic receptor expression has been shown to vary between the regions (Levey et al., 1995). Acetylcholine modulates SC-CA1 transmission via pre-synaptic M4 activation (Dasari and Gullledge, 2011; Palacios-Filardo et al., 2021), which is densely expressed in the stratum radiatum in CA1 (Levey et al., 1995). However, there is much less M4 expression in the CA3 stratum radiatum and therefore suggests acetylcholine could have less impact on CA3-CA3 recurrent inputs, which is in line with these results. Additionally, the effect of endogenous acetylcholine on CA1 synaptic inputs was similar to the effect observed when bath applying 10 μ M carbachol (Palacios-Filardo et al., 2021). This could suggest that the concentration released from cholinergic fibres in the CA1 region is comparable to 10 μ M carbachol and in this instance, it is therefore possible that there is less endogenous release in the CA3 region, compared to CA1, or that there is less targeted modulation to specific synaptic contacts. Overall, acetylcholine seems to modulate

synaptic transmission in the CA1 and CA3 region differently, but the main effect in both regions, appears to be to increase the excitatory-inhibitory balance by reducing inhibitory synapses to a greater extent than excitatory.

The dendritic integration experiments performed here suggested that increasing the stimulation intensity of recurrent and perforant path axons produces a sublinear increase in the compound EPSP decay, as opposed to a supra-linear increase generated from the same stimulation protocol in CA1 neurons (Griesius et al., 2022). The aim of these experiments was to test the prediction from the modelling that acetylcholine could reduce the threshold required for NMDA-mediated supra-linear synaptic integration. The differences in the integration properties between the model and experiments were likely due to the fact that the inputs in the model were positioned in close proximity within a single dendritic branch whereas stimulation of pathway axons in brain slices activated a global response in the dendritic regions, that are unlikely to be focused within a single dendritic section. Therefore, the result from these experiments suggests that inputs between dendritic branches integrate sub-linearly and highlight a major difference in global integration properties between CA3 and CA1 neurons (Griesius et al., 2022). It has previously been shown that inputs activated within a single CA3 dendritic branch can produce NMDA-mediated supra-linear integration (Makara and Magee, 2013). Therefore, to generate this form of synaptic integration and test the effect of endogenous acetylcholine, inputs may need to be precisely stimulated within a dendritic branch using two-photon glutamate uncaging as in Makara and Magee, (2013). Additionally, distributing inputs across different dendritic branches in a reconstructed neuron model, to simulate stimulation of pathway axons in brain slice experiments, could test global synaptic integration properties between branches within a dendritic region. Indeed, this has been previously investigated in CA1 neuron models and experimentally in cortical neurons, in which clustered inputs on the same dendritic branch sum nonlinearly, whereas dispersed inputs on separate dendrite branches sum linearly or sub-linearly (Poirazi et al., 2003a, 2003b; Polsky et al., 2004).

When comparing recurrent and perforant path stimulation, the perforant path inputs had a higher maximum AUC to slope ratio suggesting that less input was needed to reach the maximum AUC compared to the recurrent inputs. This finding was comparable to the modelling result, in which less input was required in the SLM dendrites (perforant path inputs) to produce the maximal EPSP amplitude response. Endogenous acetylcholine also had a greater effect on the changepoint from the recurrent inputs, compared to the perforant path. This changepoint signified when the compound EPSP decay AUC had reached its maximum and started to plateau with increasing input intensity. In the model, the number of inputs required to reach the maximum slope of nonlinearity was measured, and acetylcholine had a greater impact on this threshold in the recurrent inputs compared to the perforant path inputs. Therefore, although the simulations and experiments were measuring different phenomena, in both

setups, acetylcholine had a greater influence on recurrent inputs to the SR dendrites compared to the perforant path inputs to the SLM dendrites.

3.4.1 Limitations / improvements

In these experiments, cholinergic fibres were stimulated at a frequency of 2 Hz, as was previously used in experiments assessing synaptic transmission in CA1 neurons (Palacios-Filardo et al., 2021). Cholinergic neurons in the medial septum have previously been shown to be slow firing (Simon et al., 2006) and therefore 2 Hz was used to represent a maximal firing rate that is typical during wakefulness and to represent a maximal physiological concentration of acetylcholine in the hippocampus. However, more recent experiments that measured the activity of medial septum cholinergic neurons detected peak firing rates between 7.5 and 15 Hz during active exploration in 6 out of the 7 neurons recorded (Ma et al., 2020). These neurons exhibited tonic firing during active exploration periods and REM sleep, whereas 1 out of the 7 maintained a slower firing rate as previously thought typical of these neurons (Simon et al., 2006). Therefore, the 2 Hz optogenetic stimulation used in these experiments may not reflect the *in vivo* firing patterns that correspond with high acetylcholine release in the hippocampus and higher stimulation frequencies could produce greater effects. To further understand and more accurately mimic *in vivo* acetylcholine release in brain slice experiments, it would be beneficial to measure acetylcholine release in the hippocampus using an acetylcholine sensor (Jing et al., 2020) during behaviours, such as exploration, and then to additionally monitor acetylcholine release *ex vivo* when optogenetically stimulating cholinergic neurons at different frequencies. This would help to indicate an appropriate stimulation frequency that releases a physiologically relevant amount of acetylcholine into the hippocampus.

In relation to the experiments measuring IPSC amplitudes, it could be beneficial to isolate specific inhibitory inputs from different interneurons to determine the extent to which acetylcholine affects different subtypes. Additionally, to validate the results shown here with the effect of endogenous acetylcholine on IPSC amplitude, additional experiments could have been performed with a cholinergic antagonist applied during optogenetic stimulation to confirm acetylcholine was causing the observed effect.

The sample size of the dendritic integration experiments could ideally be larger to verify the results shown here. These experiments suggested that it may be difficult to induce supra-linear dendritic integration in CA3 neurons with this particular experimental stimulation protocol. In addition, the duration of time spent measuring acetylcholine's effect on dendritic integration could increase to expand the quantity of datapoints collected. In Raus Balind et al. (2019) they categorized CA3 neurons based on their ability to generate complex spike bursts, similar to plateau potentials, at the soma and found that a group of CA3 neurons required combined proximal and distal inputs in order to generate

complex spike bursts. A protocol consisting of coincident perforant path and recurrent stimulation could therefore be beneficial for inducing supra-linear dendritic integration in CA3 neurons and for assessing acetylcholine's impact.

3.4.2 Functional implications

Endogenously released acetylcholine, as well as bath-applied noradrenaline, did not affect CA3 recurrent transmission. The impact of endogenous acetylcholine on CA3 neuron excitability was not tested here but carbachol increased membrane potential and input resistance, whereas noradrenaline did not. Taken in consideration with their effect on DG-CA3 circuitry (Prince et al., 2021), it is thought that both acetylcholine and noradrenaline facilitate the formation of memory ensembles by reducing the DG-CA3 feedforward inhibition, therefore increasing excitation and enhancing plasticity within CA3-CA3 connections. The results found here could therefore indicate that overall, similar to the DG-CA3 circuit, acetylcholine increases the excitability of CA3 neurons via reducing inhibitory inputs and that this could facilitate action potential output and backpropagating action potentials, potentially as a mechanism to facilitate plasticity induction. Further experiments to clarify the role of endogenous acetylcholine on CA3 neuron excitability and plasticity, as well as the impact of endogenous noradrenaline on CA3 synaptic inputs will be needed to validate these ideas.

3.4.3 Future studies

To further our understanding of how acetylcholine affects synaptic circuitry and integration within the CA3 region, future *ex vivo* experiments could include additional ways to test the effect of acetylcholine on CA3 dendritic integration, as explained in the previous chapter (Section 0).

As it is also important to understand how acetylcholine regulates memory processing, studying how acetylcholine modulates plasticity within the CA3 network would be highly beneficial. It has previously been shown that acetylcholine can facilitate synaptic plasticity in CA1 neurons (Fernández De Sevilla and Buño, 2010; Dennis et al., 2016) and it has been suggested that acetylcholine could facilitate plasticity between the recurrent connections within the CA3 network to facilitate memory storage (Hasselmo et al., 1995; Prince et al., 2021). Therefore, it will be important to understand the mechanisms by which acetylcholine could impact this plasticity.

To understand the impact of acetylcholine within the entire CA3 circuit, it would also be important to test its effect on other excitatory and inhibitory inputs to CA3 neurons, such as the mossy fibre (MF) input, as this particular pathway has important implications for learning and memory encoding. As carbachol has been found to modulate MF feedforward inhibition as opposed to direct MF excitatory transmission (Prince et al., 2021), it is predicted that endogenous acetylcholine would affect it in the

same way. To my knowledge, there have also been no studies looking at acetylcholine's effect on entorhinal-CA3 feedforward inhibition via the perforant path. In CA1 neurons, endogenous acetylcholine was shown to reduce the entorhinal excitatory input but reduce entorhinal feedforward inhibition to a greater extent, therefore overall enhancing the entorhinal excitatory-inhibitory balance (Palacios-Filardo et al., 2021).

Additionally, the use of optogenetics *in vivo* would be highly beneficial to assess the impact of acetylcholine on neuron activity during behaviour. The precise timing control with optogenetics could allow for manipulation of acetylcholine at precise time points during a memory task to understand its impact in encoding vs retrieval (Jarzebowski et al., 2021; Zhang et al., 2021). Taking advantage of developing technologies, such as acetylcholine sensors, could also be an important tool to use *in vivo* to further understand at which points acetylcholine is released in the CA3 region in relation to certain behaviours and tasks (Teles-Grilo Ruivo et al., 2017; Jing et al., 2020). Place cells are also present in the CA3 region, and therefore it would also be beneficial to assess the impact of acetylcholine on these place cell dynamics (Mamad et al., 2015).

In conclusion, acetylcholine release via optogenetics did not affect excitatory inputs to CA3 neurons but did reduce inhibitory inputs, potentially suggesting that acetylcholine increases CA3 pyramidal neuron excitability via disinhibition and that this could play a role in plasticity induction and the formation of memory ensembles within CA3 circuitry.

Chapter 4 General Discussion

The aim of this research was to further our understanding of how neuromodulators affect synaptic transmission and integration in CA3 pyramidal neurons, with the hope that it provides insight onto our understanding of how these neuromodulators affect this circuitry *in vivo*. Neuromodulators are released in response to external stimuli and in particular behavioural states. Combining this prior knowledge with the results of this research can suggest how these neuromodulators are affecting CA3 circuitry during particular behaviours and how this change in brain circuitry may be driving behaviour or learning and forming memories.

Chapter 2 investigated the impact of acetylcholine, via the inhibition of potassium channels, on dendritic NMDA-mediated nonlinearity in a biophysical computational model of a CA3 pyramidal neuron. The results from this modelling work predicted that acetylcholine's modulation of potassium channels can reduce the number of synaptic inputs required to initiate NMDA-mediated nonlinearity in dendrites. This effect was greater in the proximal stratum radiatum dendrites and was not fully explained by increased dendritic excitability or a particular potassium conductance. Additional findings were the modulation of the A-type (K_A) and calcium-activated (K_{Ca}) potassium conductances on the slope of nonlinearity and the NMDA spike half-width, respectively, which have been identified previously in CA1 neurons (Cai et al., 2004).

Chapter 3 investigated experimentally acetylcholine and noradrenaline's role in CA3 recurrent circuitry, as well as acetylcholine's impact on perforant path and inhibitory inputs to CA3 neurons. These experiments were performed in *ex vivo* brain slices using pharmacological and optogenetic techniques. The initial results showed that bath-applied noradrenaline had no impact on CA3 recurrent transmission, whereas bath-applied carbachol reduced CA3 recurrent transmission in line with previous studies (Vogt and Regehr, 2001; Kremin and Hasselmo, 2007). However, when testing the effect of endogenous acetylcholine release via blue light activation of channelrhodopsin-containing cholinergic fibres, no change in CA3 recurrent transmission was observed. Additionally, endogenous acetylcholine did not alter perforant path-CA3 inputs, as carbachol has previously been shown to (Kremin and Hasselmo, 2007). It did, however, reduce inhibitory inputs to CA3 neurons, in line with previous studies (Szabó et al., 2010). Furthermore, increasing stimulation intensity in both recurrent and perforant path evoked responses produced a sublinear increase in the compound EPSP decay, in contrast to findings in CA1 neurons which generated supra-linear increases (Griesius et al., 2022).

Taken together, these results offer new ideas about the impact of acetylcholine in the CA3 network. Acetylcholine has been previously thought to reduce the recurrent connections in the CA3 network, as

has been evidenced here and in previous studies when bath-applying carbachol (Vogt and Regehr, 2001; Kremin and Hasselmo, 2007). However, the results found here from using optogenetic techniques, suggest that endogenous acetylcholine has little impact on CA3 recurrent transmission and as mentioned in Chapter 3 suggests that the physiological maximal concentration of acetylcholine surrounding these synapses could be lower than previously thought and points towards specific synaptic targeting of acetylcholine in the CA3 region (Takács et al., 2018).

Cholinergic modulation of inhibitory transmission in CA3 had also been previously investigated via bath applying carbachol (Szabó et al., 2010) where it was found that carbachol reduced several types of interneuron-CA3 inputs. The findings from this study, testing the modulation by endogenous acetylcholine, are in agreement with results from Szabó et al., (2010) in which inhibitory inputs to CA3 neurons are reduced, however the extent of that reduction was different between the two studies. Carbachol reduced inhibitory transmission approximately 4-fold more (Szabó et al., 2010) compared to endogenous acetylcholine. As explained in Chapter 3, the concentration and spatiotemporal release properties of endogenous acetylcholine could explain the differences observed. To further compare the impact of endogenous acetylcholine shown here with studies using carbachol, it would be beneficial to measure the OLM nicotinic response with different concentrations of carbachol applied, to estimate the amount of acetylcholine released during optogenetic stimulation.

Although carbachol reduced recurrent synaptic inputs to CA3 neurons, it was also thought that acetylcholine facilitated plasticity between CA3-CA3 recurrent connections to encode new memory ensembles (Hasselmo et al., 1995; Rogers and Kesner, 2004; Prince et al., 2021), although this theory has not been confirmed experimentally. One of the mechanisms via which acetylcholine could facilitate this plasticity, is via post-synaptic mechanisms, such as dendritic spikes. Indeed, from the simulations performed in Chapter 2, it was proposed that acetylcholine could reduce the threshold number of inputs required to generate NMDA spikes, especially in the stratum radiatum dendrites that receive inputs from recurrent collaterals. Also, if acetylcholine does in fact not modulate CA3 recurrent transmission, as shown in Chapter 3, it could mean that the likelihood of inducing plasticity at these synapses is greater. It was recently shown in a network spiking model of CA3 (Prince et al., 2021) that increased CA3 excitability and reduction of CA3-CA3 transmission with acetylcholine, increased the speed of ensemble formation and enhanced the overlap between memory ensembles, respectively. However, taking into consideration the results here with endogenous acetylcholine, acetylcholine's main effect within CA3 may be to only increase CA3 neuron excitability and therefore may not additionally improve the overlap between memory ensembles. This however, provides the benefit of increasing the fidelity of memory retrieval in the model (Prince et al., 2021).

Taking all aspects into consideration, acetylcholine has more of an impact on reducing inhibitory transmission as opposed to excitatory transmission in CA3 (Figure 4-1) and within pyramidal neuron dendrites could be facilitating the generation of NMDA spikes. These key results suggest that acetylcholine's main mode of action in CA3 is reducing inhibitory inputs, and therefore increasing pyramidal neuron excitability, which could also facilitate dendritic spike generation.

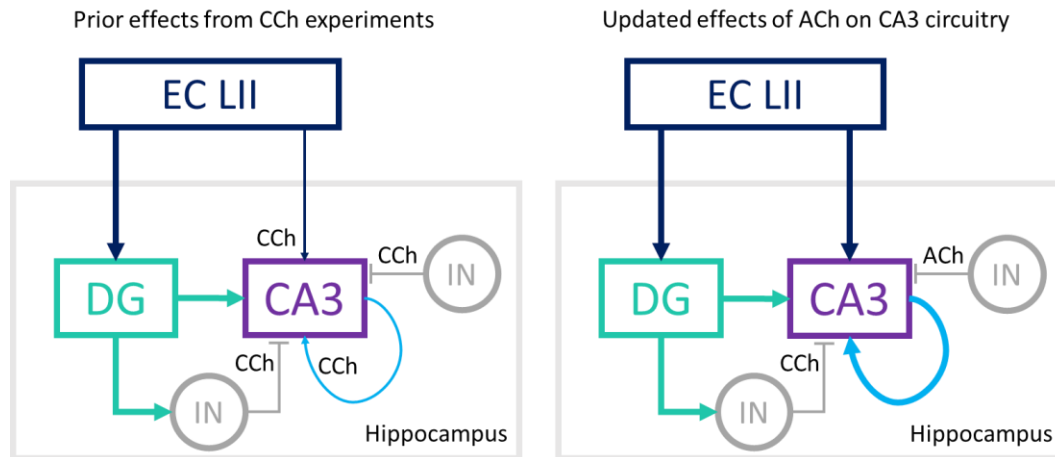


Figure 4-1: Prior and updated impact of acetylcholine on CA3 circuitry. The diagram on the left depicts results from previous literature whereby bath applied carbachol (CCh) reduces the inputs. The diagram on the right takes into account the effects found in this research from testing endogenous acetylcholine (ACh). Here, there was no effect found on the entorhinal (dark blue) and recurrent (light blue) inputs to CA3 neurons, but endogenous acetylcholine (ACh) did confirm the impact of CCh on inhibitory inputs. The impact of endogenous acetylcholine on mossy fibre excitatory and feedforward inhibition is currently not known.

In this thesis, experimental and computational modelling approaches were both used to explore the role of acetylcholine in CA3 synaptic transmission and integration. This was done as it broadened the scope of questions to investigate. Specifically, using computational models allowed exploration of questions that are technically very challenging to currently perform experimentally in brain slices. It also allowed for easy manipulation and control of all parameters, such as ion channel conductances, and helped gain insight into mechanistic explanations of phenomena. However, one of the key disadvantages to using biophysically detailed neuron models is the vast number of parameters that need to be set that we do not know the true values for. To tackle this here, a parameter optimisation algorithm was used to search the parameter space and identify the best set of parameters that most closely matched the experimental output. However, this approach still had weaknesses in that it was computationally expensive to run, and that there can be more than one optimal set of parameter values. Additionally, the data to match to was averaged data and therefore using a single neuron model did not capture this between-neuron variability. It could therefore be beneficial to run repeated simulations on different neuron morphologies and/or vary the ion channel densities.

Regarding the experimental approach, whole-cell patch clamp experiments were used to investigate the effect of endogenously released acetylcholine on CA3 synaptic inputs. This technique was used as it has previously been used to assess the same question using pharmacological, rather than optogenetic, intervention. Apart from the inherent disadvantages to voltage-clamp experiments, such as series resistance, space clamp issues and low-throughput, another downside was the lack of ability to directly assess dendritic activity as well as the uncertainty of the location and distribution of inputs to the dendritic tree. On the other hand, the modelling approach allowed precise positioning of inputs on different branches throughout the dendritic tree and to also measure the response at any location within the dendritic or somatic compartments. Using a model allowed investigation into NMDA nonlinear integration in every dendritic branch section within a single neuron, which is not possible to perform experimentally.

To integrate the experimental and modelling results presented here, the predictions from the modelling could be tested in experimental setups and further simulations could be performed to confirm and understand some of the experimental results. In particular, the prediction that acetylcholine facilitates NMDA spike generation could be investigated using two-photon glutamate uncaging with application of carbachol or optogenetic stimulation in different regions of the dendritic tree. The impact of blocking K_a and K_{ca} channels on NMDA spike properties could also be tested pharmacologically in slices. Furthermore, the sub-linear integration observed experimentally here could be tested in the reconstructed model by positioning synapses dispersed across the dendritic tree section and measuring the integration response at the soma.

In order to confirm acetylcholine's role in CA3 circuitry and memory encoding, some key questions still remain. It will be important to understand acetylcholine's impact on plasticity with the CA3 recurrent network as well as the mechanisms by which it may modulate this. It has previously been shown in CA3 neurons that NMDA spikes are necessary for inducing a particular type of synaptic plasticity in the recurrent inputs (Brandalise et al., 2016, 2021) that involves a combination of mossy fibre and recurrent input. Therefore, if acetylcholine enhances excitatory mossy fibre inputs, by reducing feedforward inhibition (Prince et al., 2021), reduces perisomatic inhibitory inputs (Chapter 3, Szabó et al., 2010), which in turn could additionally enhance mossy fibre inputs as well as increase excitability, and reduce the threshold required for NMDA spikes (Chapter 2), it is highly likely that it could facilitate this plasticity and therefore facilitate the formation of memory ensembles.

To conclude, this research has shown that endogenous acetylcholine reduced inhibitory, but not excitatory, inputs to CA3 pyramidal neurons, and that cholinergic modulation of potassium channels in a computational model facilitated the generation of dendritic NMDA spikes. These key findings could

both facilitate plasticity within the recurrent network and therefore provide a potential mechanism for memory formation.

Appendix A

This appendix describes the ion channel equations used for both the two-compartment and reconstructed neuron models. The model scripts, ion channel and synaptic mechanisms and neuron geometry for the reconstructed neuron model are also publicly available on ModelDB (accession number 267298). If different parameters were used for the two-compartment model, they have been highlighted below.

Voltage-dependent potassium channels

Equation A1: Potassium current equation

$$I_K = gmax * n * (V - V_k)$$

Where $gmax$ is the maximal channel conductance, n is the proportion of open channels, V is the membrane potential and V_k is the potassium equilibrium potential (-90 mV). n is dependent on the membrane potential and is calculated with the following equation representing the proportion of open channels:

Equation A2: Boltzmann activation function

$$n = \frac{1}{1 + \exp\left(\frac{V - V_{\frac{1}{2}} - sh}{k}\right)}$$

This equation reflects the channel conductance, as a function of the membrane potential (V). $V_{\frac{1}{2}}$ is the membrane potential at which the channel conductance is half maximal; k reflects the steepness of the sigmoidal activation curve and sh the shift in the curve. The parameters for each of the potassium channel mechanisms, excluding Ka , for the two-compartment (Table A2) and reconstructed models (Table A1) are shown below.

Table A1: Activation function parameters for potassium ion channels in the reconstructed neuron model. $V_{\frac{1}{2}}$ = half-maximal channel conductance voltage; k = slope of sigmoidal activation function; sh = shift in the curve. The reference column refers to the experimental data and/or the publication in which the channel equations and parameters were initially fitted. Km , Kir and Ih sh parameters displayed here were optimised for this model.

Channel type	$V_{\frac{1}{2}}$ (mV)	k	sh	References
Km	-40	-10	-30	Shah et al., (2008)
Kir	-98.92	10.89	30	Stegen et al., (2012); Yim et al., (2015)
Kdr	3.8	8.85	0	Klee et al., (1995); Hoffman et al., (1997)
Ih	-73	8	30	Magee, (1998)

Table A2: Activation function parameters for potassium ion channels in the two-compartment model. $V_{\frac{1}{2}}$ = half-maximal channel conductance voltage; k = slope of sigmoidal activation function; sh = shift in the curve. The reference column refers to the experimental data and/or the publication in which the channel equations and parameters were initially fitted. Km and Kir sh parameters displayed here were optimised for this model.

Channel type	$V_{\frac{1}{2}}(mV)$	k	sh	References
Km	-40	-10	11.40	Shah et al., (2008)
Kir	-98.92	10.89	5e-4	Stegen et al., (2012); Yim et al., (2015)
Kdr	3.8	8.85	0	Klee et al., (1995); Hoffman et al., (1997)
Ih	-73	8	0	Magee, (1998)

The decay time constants (τ) for the activation functions were described by the following equations for Km, Ih and Kdr channels:

$$\tau = b_0 + \frac{\beta(V)}{q\tau * a_0\tau * (1 + \alpha(V))}$$

Where $\alpha(V)$ and $\beta(V)$ represented the following rate constant functions:

$$\alpha(V) = \exp(0.001 * F/RT * z_{\text{etat}} * (V - V_{ht} - sh))$$

$$\beta(V) = \exp(0.001 * F/RT * z_{\text{etat}} * g_{mt} * (V - V_{ht} - sh))$$

Where F is the Faraday constant ($9.649 \times 10^4 \text{ C}\cdot\text{mol}^{-1}$), R is the gas constant ($8.315 \text{ J}\cdot\text{mol}^{-1}\cdot\text{K}^{-1}$), T is the temperature in Kelvin (308.16 K). The sh parameters are the same as in Table A1 and Table A2: Activation function parameters for potassium ion channels in the two-compartment model. above.

The decay time constant for Kir activation function was expressed as:

$$\tau = 5 * \frac{1}{q\tau * \left(a_0\tau * \exp\left(-\frac{V}{V_{ht}}\right) + b_0 * \exp\left(\frac{V}{V_{ht}}\right) \right)}$$

All parameter values for each of the conductances are displayed in Table A3 below.

Table A3: Parameters for time and rate constant function equations.

Channel	zetat	gmt	Vht	a0t	b0	qt
Km	7	0.4	-42	0.003	60	1
Kdr	-3	0.7	3.8	0.02	0	1
Ih	2.2	0.4	-75	0.011	0	1.35
Kir	-	-	67.08	0.0061	0.82	1

The Ka channel mechanism had a slightly more complicated set of equations as it included an inactivation gating variable, l , in addition to the activation gating variable, n . Moreover, the slope of activation was also dependent on the voltage and was therefore represented by an additional equation.

The activation (n), inactivation (l) and corresponding rate constant (α , β) and tau (τ_n , τ_l) equations for Ka from Klee et al., (1995) and Hoffman et al., (1997) are:

$$zeta = zetan + \frac{pw}{1 + \exp\left(\frac{v - tq - sh}{qq}\right)}$$

$$\alpha_N = \exp(0.001 * F/RT * zeta * (v - Vhn - sh))$$

$$\beta_N = \exp(0.001 * F/RT * zeta * gmn * (v - Vhn - sh))$$

$$\alpha_L = \exp(0.001 * F/RT * zetal * (v - Vhl - sh))$$

$$\beta_L = \exp(0.001 * F/RT * zetal * gml * (v - Vhl - sh))$$

$$n = \frac{1}{1 + \alpha_N(v)}$$

$$\tau_n = \frac{\beta_N(v)}{qt * a0n * (1 + \alpha_N(v))}$$

$$l = \frac{1}{1 + \alpha_L(v)}$$

$$\tau_l = 0.26 * \frac{v + 50 - sh}{qtl}$$

Where F is the Faraday constant ($9.649\text{e}4 \text{ C}\cdot\text{mol}^{-1}$), R is the gas constant ($8.315 \text{ J}\cdot\text{mol}^{-1}\cdot\text{K}^{-1}$), T is the temperature in Kelvin (308.16 K).

The parameters used for the Ka equations are in the table below.

Table A4: Parameters for Ka equations for the reconstructed and two-compartment models. Parameters here are from Klee et al., (1995), Hoffman et al., (1997) and Kim et al., (2012). Sh parameters were optimised during for these models.

	Reconstructed	Two-compartment
V_{hn}	-5	11
V_{hl}	-65	-56
sh	5.58	8.11
a_{0n}	0.05	0.05
z_{etan}	-1.8	-1.5
z_{etal}	3.7	3
g_{mn}	0.55	0.55
g_{ml}	1	1
pw	-1	-1
tq	-40	-40
qq	5	5
qt	5.87	5.87
qtl	1	1

The sh parameters for Ka, Km Ih and Kir were optimised for these models during the optimisation process. V_{hn} , V_{hl} , z_{etal} and z_{etan} for Ka were taken from Kim et al., (2012) for the reconstructed model.

Calcium-activated potassium channels

The first equation in this section describes the acetylcholine modulated small conductance calcium-activated potassium channel (Kca), from Combe et al., (2018).

Equation A3: Small conductance calcium-activated potassium channel activation function (SK/Kca)

$$o = \frac{1}{1 + \left(\frac{0.00019}{cai}\right)^4}$$

Where cai is the intracellular calcium concentration. The decay time constant (τ) for this activation function was 28 ms.

There were two additional calcium-dependent potassium channels present in the models. Firstly, the Kahp channel, involved in the slow after-hyperpolarisation (AHP). The following equations used were from Migliore et al., (1995):

Equation A4: Activation function for Kahp conductance.

$$o = \frac{10^8 * cai^4}{((10^8 * cai^4) + 0.005)}$$

Equation A5: Kahp time constant of the activation function.

$$\tau = \frac{1}{2.69 * ((10^8 * cai^4) + 0.005)}$$

Where cai was the intracellular calcium concentration.

The second additional calcium-dependent potassium channel was also dependent on the voltage with the equations as follows, also from Migliore et al., (1995):

Equation A6: Kc activation function.

$$o = \frac{\alpha(v, cai)}{\alpha(v, cai) + \beta(v, cai)}$$

Where v was the membrane potential, cai was the intracellular calcium concentration and $\alpha(v, cai)$ and $\beta(v, cai)$ were the following rate constant functions:

Equation A7: Kc rate constant equations.

$$\alpha(v, cai) = \frac{cai * 0.28}{cai + (0.00048 * \exp\left(\frac{-2 * 0.84 * F * v}{RT}\right))}$$

$$\beta(v, cai) = \frac{0.48}{cai / (1.3 * 10^{-7} * \exp\left(\frac{-2 * F * v}{RT}\right))}$$

Where F is the Faraday constant ($9.649 \times 10^4 \text{ C} \cdot \text{mol}^{-1}$), R is the gas constant ($8.315 \text{ J} \cdot \text{mol}^{-1} \cdot \text{K}^{-1}$), T is the temperature in Kelvin (308.16 K).

Equation A8: Time constant for Kc activation function.

$$\tau = \frac{1}{\alpha(v, cai) + \beta(v, cai)}$$

Voltage-dependent calcium channels

Kinetics for the following calcium channels were all from Migliore et al., (1995).

L-type calcium channel equations:

Equation A9: Calcium conductance (CaL)

$$g_{cal} = g_{calbar} * m * m * h2(cai)$$

$$h2(cai) = \frac{0.001}{0.001 + cai}$$

Equation A10: L-type calcium channel (CaL) activation function equations

$$m = \alpha(v) * \beta(v)$$

$$\alpha(v) = 15.69 * \frac{-1v + 81.5}{\left(\exp\left(\frac{-1v + 81.5}{10}\right) - 1\right)}$$

$$\beta(v) = \frac{1}{\alpha(v) + (0.29 * \exp(-\frac{v}{10.86}))}$$

Equation A11: L-type calcium channel (CaL) time constant equations for activation function.

$$\tau_{aum} = \frac{\beta_{amt}(v)}{5 * 0.1 * (1 + \alpha_{amt}(v))}$$

$$\alpha_{amt}(v) = \exp(0.001 * F/RT * 2 * (v - 4))$$

$$\beta_{amt}(v) = \exp(0.001 * F/RT * 2 * 0.1 * (v - 4))$$

N-type calcium channel equations:

Equation A12: Calcium conductance (N-type)

$$g_{can} = g_{canmax} * m * m * h * h2(cai)$$

Equation A13: N-type calcium conductance (CaN) activation function equations

$$m = \alpha_{ham}(v) * \beta_{ham}(v)$$

$$alphan(v) = 0.1967 * \frac{-1 * v + 19.88}{\exp\left(\frac{-1 * v + 19.88}{10}\right) - 1}$$

$$betam(v) = \frac{1}{alphan(v) + (0.046 * \exp\left(-\frac{v}{20.73}\right))}$$

$$h = alphan(v) * betam(v)$$

$$alphan(v) = 1.6e - 4 * \exp\left(-\frac{v}{48.4}\right)$$

$$betam(v) = \frac{1}{alphan(v) + \left(\frac{1}{\exp\left(\frac{-v + 39}{10}\right) + 1}\right)}$$

$$h2(cai) = 0.001 / (0.001 + cai)$$

$$tauh = 80$$

T-type calcium channel equations:

Equation A14: Calcium conductance (T-type)

$$gcat = gcatmax * m * m * h$$

Equation A15: T-type calcium channel (CaT) activation function equations

$$m = \frac{alphan(v)}{alphan(v) + betam(v)}$$

$$alphan(v) = 0.2 * \left(-1 * v + \frac{19.26}{\exp\left(\frac{-1 * v + 19.26}{10}\right)} - 1 \right)$$

$$betam(v) = 0.009 * \exp\left(-\frac{v}{22.03}\right)$$

$$h = \frac{a}{a + b}$$

$$a = 1.e - 6 * \exp\left(-\frac{v}{16.26}\right)$$

$$b = \frac{1}{\exp\left(\frac{-v + 29.79}{10}\right) + 1}$$

$$h\tau = \frac{betah(v)}{0.015 * (1 + alphah(v))}$$

$$alphah(v) = \exp(0.001 * F/RT * 3.5 * (v - (-75)))$$

$$betah(v) = \exp(0.001 * F/RT * 3.5 * 0.6 * (v - (-75)))$$

Appendix B

Appendix B: Properties of each stimulated dendrite section, ordered by distance from the soma. Section = the section reference number; Region = SR or SLM dendrite; Distance from soma = dendrite distance from soma in microns; Length = dendrite section length in microns; Diameter = dendrite diameter in microns; Resting R_{in} = dendrite resting input resistance; Tree position = whether the section was before (pre-) and/or after (post-) a branchpoint and/or a terminal dendrite; No. of branchpoints to soma = the number of branchpoints to the soma; No. of segments = the number of numerical segments for that section, related to the dendrite length; Ka peak conductance = the distance dependent Ka peak conductance for each section; Kir peak conductance = the distance dependent Kir peak conductance.

Section	Region	Distance from soma (μm)	Length (μm)	Diameter (μm)	Resting R_{in} ($\text{M}\Omega$)	Tree position	No. of branchpoints to soma	No. of segments	Ka peak conductance (S/cm^2)	Kir peak conductance (S/cm^2)
68	SR	151.82	20.73	1.27	162.11	pre- and post-branchpoint	4	1	5.60E-03	1.66E-05
3	SR	152.13	45.03	1.14	151.51	pre- and post-branchpoint	4	3	5.62E-03	1.66E-05
32	SR	170.82	63.65	0.80	250.22	pre- and post-branchpoint	5	5	6.64E-03	1.66E-05
25	SR	184.10	90.21	1.37	179.30	pre- and post-branchpoint	5	5	7.38E-03	1.66E-05
67	SR	186.34	89.77	0.77	262.87	terminal post-branchpoint	4	7	7.50E-03	1.66E-05
7	SR	186.85	54.90	0.94	188.40	pre- and post-branchpoint	5	3	7.53E-03	1.66E-05
72	SR	194.90	51.80	1.10	216.63	pre- and post-branchpoint	6	3	7.97E-03	1.66E-05
10	SR	196.09	73.38	1.32	176.46	pre- and post-branchpoint	5	5	8.04E-03	1.66E-05
44	SR	197.26	65.30	0.90	293.21	pre- and post-branchpoint	7	5	8.10E-03	1.66E-05
4	SR	201.84	54.39	0.66	302.64	terminal post-branchpoint	5	5	8.35E-03	1.66E-05
53	SR	202.39	165.01	0.95	272.53	pre- and post-branchpoint	4	9	8.38E-03	1.66E-05
5	SR	216.66	84.03	0.57	372.23	terminal post-branchpoint	5	7	9.17E-03	1.66E-05
71	SR	217.71	97.41	0.42	703.38	terminal post-branchpoint	6	9	9.22E-03	1.66E-05
49	SR	219.08	108.94	0.49	570.67	terminal post-branchpoint	7	9	9.30E-03	1.66E-05
69	SR	219.60	114.83	0.42	797.59	terminal post-branchpoint	5	11	9.33E-03	1.66E-05
74	SR	237.19	32.78	1.04	269.68	pre- and post-branchpoint	7	3	1.03E-02	1.66E-05
33	SR	239.44	73.60	0.43	695.04	terminal post-branchpoint	6	7	1.04E-02	1.66E-05
9	SR	243.39	58.19	0.61	413.65	terminal post-branchpoint	6	5	1.06E-02	1.66E-05
42	SR	245.24	235.46	0.63	663.14	post-branchpoint	6	17	1.07E-02	1.66E-05
37	SR	246.72	91.81	0.47	902.08	terminal post-branchpoint	6	7	1.08E-02	1.66E-05
73	SR	250.92	60.24	0.44	554.88	terminal post-branchpoint	7	5	1.11E-02	1.66E-05
8	SR	251.19	73.78	0.61	432.29	terminal post-branchpoint	6	5	1.11E-02	1.66E-05

34	SR	256.22	107.15	0.46	762.56	terminal post-branchpoint	6	9	1.13E-02	1.66E-05
48	SR	263.44	67.06	0.43	693.67	terminal post-branchpoint	8	7	1.17E-02	1.66E-05
11	SR	265.74	65.92	1.30	242.63	pre- and post-branchpoint	6	3	1.19E-02	1.66E-05
45	SR	281.20	102.58	0.78	454.55	post-branchpoint	8	7	1.27E-02	1.66E-05
31	SR	284.00	109.58	0.62	474.96	terminal post-branchpoint	6	9	1.29E-02	1.66E-05
22	SR	289.06	112.55	0.49	525.28	terminal post-branchpoint	6	9	1.31E-02	1.66E-05
26	SR	300.13	141.84	1.23	286.79	pre- and post-branchpoint	6	7	1.38E-02	1.66E-05
75	SR	301.89	96.64	0.43	701.88	pre- and post-branchpoint	8	9	1.39E-02	1.66E-05
61	SR	320.46	40.04	0.64	506.12	pre- and post-branchpoint	6	3	1.49E-02	1.66E-05
54	SR	324.97	80.16	0.45	772.70	terminal post-branchpoint	5	7	1.51E-02	1.66E-05
38	SR	325.08	248.52	0.60	1057.73	post-branchpoint	6	17	1.51E-02	1.66E-05
80	SR	331.42	155.70	0.52	655.43	post-branchpoint	8	13	1.55E-02	1.66E-05
21	SR	341.55	85.69	0.59	483.36	terminal post-branchpoint	7	7	1.60E-02	1.66E-05
12	SR	342.68	87.95	1.22	320.76	pre- and post-branchpoint	7	5	1.61E-02	1.66E-05
65	SR	371.58	62.19	0.42	914.14	terminal post-branchpoint	7	5	1.77E-02	1.66E-05
56	SR	375.70	150.52	0.61	726.55	pre- and post-branchpoint	6	11	1.79E-02	1.66E-05
76	SR	376.87	53.32	0.40	1395.49	terminal post-branchpoint	9	5	1.80E-02	1.66E-05
14	SR	398.60	23.90	0.93	393.90	pre- and post-branchpoint	8	3	1.92E-02	1.66E-05
62	SLM	405.64	130.31	0.41	1164.05	pre- and post-branchpoint	7	11	1.96E-02	1.82E-05
13	SLM	412.20	51.10	0.44	633.15	terminal post-branchpoint	8	5	1.99E-02	1.82E-05
20	SLM	429.74	38.37	0.60	512.52	terminal post-branchpoint	9	3	2.09E-02	1.82E-05
77	SLM	451.70	202.99	0.42	1699.23	pre- and post-branchpoint	9	17	2.21E-02	1.82E-05
83	SLM	458.50	252.03	0.60	1103.75	pre-branchpoint	8	17	2.25E-02	1.82E-05
15	SLM	458.63	96.15	0.76	545.51	pre- and post-branchpoint	9	7	2.25E-02	1.82E-05
57	SLM	463.81	25.70	0.34	1195.41	terminal post-branchpoint	7	3	2.28E-02	1.82E-05
58	SLM	475.82	49.73	0.51	1088.04	pre- and post-branchpoint	7	5	2.34E-02	1.82E-05
82	SLM	477.54	229.14	0.41	2178.65	terminal	6	19	2.35E-02	1.82E-05
28	SLM	483.75	225.40	0.59	828.56	pre- and post-branchpoint	7	17	2.39E-02	1.82E-05
64	SLM	502.20	62.81	0.40	2032.91	terminal post-branchpoint	8	7	2.49E-02	1.82E-05
27	SLM	517.41	292.72	0.58	908.51	terminal post-branchpoint	7	21	2.57E-02	1.82E-05
16	SLM	518.90	24.40	0.42	851.37	pre- and post-branchpoint	10	3	2.58E-02	1.82E-05
19	SLM	522.09	30.78	0.42	881.09	terminal post-branchpoint	10	3	2.60E-02	1.82E-05
81	SLM	522.60	146.53	0.42	2141.46	pre-branchpoint	6	13	2.60E-02	1.82E-05

84	SLM	537.13	255.71	0.40	2413.43	terminal	8	21	2.68E-02	1.82E-05
63	SLM	573.09	204.59	0.40	2575.84	terminal post-branchpoint	8	17	2.88E-02	1.82E-05
59	SLM	586.65	171.93	0.40	2102.38	terminal post-branchpoint	8	15	2.95E-02	1.82E-05
60	SLM	587.58	173.79	0.40	2109.01	terminal post-branchpoint	8	15	2.96E-02	1.82E-05
40	SLM	607.93	24.12	0.31	3083.06	terminal post-branchpoint	7	3	3.07E-02	1.82E-05
39	SLM	610.10	28.47	0.31	3122.53	terminal post-branchpoint	7	3	3.08E-02	1.82E-05
30	SLM	611.80	30.70	0.40	1823.73	terminal post-branchpoint	8	3	3.09E-02	1.82E-05
46	SLM	617.31	65.59	0.39	1912.94	terminal post-branchpoint	9	7	3.12E-02	1.82E-05
79	SLM	628.20	150.00	0.40	2899.72	terminal post-branchpoint	10	13	3.18E-02	1.82E-05
78	SLM	634.39	162.39	0.39	2939.43	terminal post-branchpoint	10	15	3.21E-02	1.82E-05
47	SLM	641.67	114.29	0.40	2139.26	terminal post-branchpoint	9	11	3.25E-02	1.82E-05

References

- Acquas E, Wilson C, Fibiger HC (1996) Conditioned and unconditioned stimuli increase frontal cortical and hippocampal acetylcholine release: effects of novelty, habituation, and fear. *J Neurosci* 16:3089–3096.
- Alonso LM, Marder E (2019) Visualization of currents in neural models with similar behavior and different conductance densities. *Elife* 8.
- Antic SD, Zhou WL, Moore AR, Short SM, Ikonomu KD (2010) The decade of the dendritic NMDA spike. *J Neurosci Res* 88:2991–3001.
- Aston-Jones G, Bloom FE (1981) Activity of norepinephrine-containing locus coeruleus neurons in behaving rats anticipates fluctuations in the sleep-waking cycle. *J Neurosci* 1:876–886.
- Astori S, Pawlak V, Köhr G (2010) Spike-timing-dependent plasticity in hippocampal CA3 neurons. *J Physiol* 588:4475.
- Auerbach JM, Segal M (1996) Muscarinic receptors mediating depression and long-term potentiation in rat hippocampus. *J Physiol* 492 (Pt 2):479–493.
- Aznavour N, Mechawar N, Descarries L (2002) Comparative Analysis of Cholinergic Innervation in the Dorsal Hippocampus of Adult Mouse and Rat: A Quantitative Immunocytochemical Study. *Hippocampus* 12:206–217.
- Bacon TJ, Pickering AE, Mellor JR (2020) Noradrenaline release from locus coeruleus terminals in the hippocampus enhances excitation-spike coupling in ca1 pyramidal neurons via β -adrenoceptors. *Cereb Cortex* 30:6135–6151.
- Baker JL, Perez-Rosello T, Migliore M, Barrionuevo G, Ascoli GA (2011) A computer model of unitary responses from associational/commissural and perforant path synapses in hippocampal CA3 pyramidal cells. *J Comput Neurosci* 31:137–158.
- Bazelot M, Teleńczuk MT, Miles R (2016) Single CA3 pyramidal cells trigger sharp waves in vitro by exciting interneurons. *J Physiol* 594:2565–2577.
- Berger-Sweeney J, Stearns NA, Murg SL, Floerke-Nashner LR, Lappi DA, Baxter MG (2001) Selective immunolesions of cholinergic neurons in mice: Effects on neuroanatomy, neurochemistry, and behavior. *J Neurosci* 21:8164–8173.
- Biscoe TJ, Straughan DW (1966) Micro-electrophoretic studies of neurones in the cat hippocampus. *J Physiol* 183:341–359.
- Bittner KC, Grienberger C, Vaidya SP, Milstein AD, Macklin JJ, Suh J, Tonegawa S, Magee JC (2015) Conjunctive input processing drives feature selectivity in hippocampal CA1 neurons. *Nat Neurosci* 18:1133–1142.
- Bittner KC, Milstein AD, Grienberger C, Romani S, Magee JC (2017) Behavioral time scale synaptic plasticity underlies CA1 place fields. *Science (80-)* 357:1033–1036.

- Bliss TVP, Lømo T (1973) Long-lasting potentiation of synaptic transmission in the dentate area of the anaesthetized rabbit following stimulation of the perforant path. *J Physiol* 232:331–356.
- Blokland A, Honig W, Raaijmakers WGM (1992) Effects of intra-hippocampal scopolamine injections in a repeated spatial acquisition task in the rat. *Psychopharmacology (Berl)* 109:373–376.
- Borhegyi Z, Varga V, Szilágyi N, Fabo D, Freund TF (2004) Phase segregation of medial septal GABAergic neurons during hippocampal theta activity. *J Neurosci* 24:8470–8479.
- Bramham CR, Bacher-Svendsen K, Sarvey JM (1997) LTP in the lateral perforant path is beta-adrenergic receptor-dependent. *Neuroreport* 8:719–724.
- Branco T, Häusser M (2011) Synaptic Integration Gradients in Single Cortical Pyramidal Cell Dendrites. *Neuron* 69:885–892.
- Brandalise F, Carta S, Helmchen F, Lisman J, Gerber U (2016) Dendritic NMDA spikes are necessary for timing-dependent associative LTP in CA3 pyramidal cells. *Nat Commun* 7:13480.
- Brandalise F, Carta S, Leone R, Helmchen F, Holtmaat A, Gerber U (2021) Dendritic Branch-constrained N-Methyl-d-Aspartate Receptor-mediated Spikes Drive Synaptic Plasticity in Hippocampal CA3 Pyramidal Cells. *Neuroscience* 489:57–68.
- Brandalise F, Gerber U (2014) Mossy fiber-evoked subthreshold responses induce timing-dependent plasticity at hippocampal CA3 recurrent synapses. *Proc Natl Acad Sci* 111:4303–4308.
- Brombas A, Kalita-De Croft S, Cooper-Williams EJ, Williams SR (2017) Dendro-dendritic cholinergic excitation controls dendritic spike initiation in retinal ganglion cells. *Nat Commun* 8.
- Brzosko Z, Zannone S, Schultz W, Clopath C, Paulsen O (2017) Sequential neuromodulation of hebbian plasticity offers mechanism for effective reward-based navigation. *Elife* 6.
- Buchanan KA, Petrovic MM, Chamberlain SEL, Marrion N V., Mellor JR (2010) Facilitation of Long-Term Potentiation by Muscarinic M1 Receptors Is Mediated by Inhibition of SK Channels. *Neuron* 68:948–963.
- Buzsáki G (1984) Feed-forward inhibition in the hippocampal formation. *Prog Neurobiol* 22:131–153.
- Cai L, Gibbs RB, Johnson DA (2012) Recognition of novel objects and their location in rats with selective cholinergic lesion of the medial septum. *Neurosci Lett* 506:261–265.
- Cai X, Liang CW, Muralidharan S, Kao JPY, Tang CM, Thompson SM (2004) Unique roles of SK and Kv4.2 potassium channels in dendritic integration. *Neuron* 44:351–364.
- Caldenhove S, Borghans LGJM, Blokland A, Sambeth A (2017) Role of acetylcholine and serotonin in novelty processing using an oddball paradigm. *Behav Brain Res* 331:199–204.
- Caporale N, Dan Y (2008) Spike Timing-Dependent Plasticity: A Hebbian Learning Rule. <http://dx.doi.org/10.1146/annurev.neuro.31.060407125639> 31:25–46.
- Carnevale NT, Hines ML (2006) The NEURON book. Cambridge University Press.
- Cheng Q, Yakel J (2014) Presynaptic $\alpha 7$ nicotinic acetylcholine receptors enhance hippocampal mossy fiber glutamatergic transmission via PKA activation. *J Neurosci* 34:124–133.
- Combe CL, Canavier CC, Gasparini S (2018) Intrinsic mechanisms of frequency selectivity in the

- proximal dendrites of CA1 pyramidal neurons. *J Neurosci* 38:8110–8127.
- Cox DJ, Racca C, LeBeau FEN (2008) Beta-adrenergic receptors are differentially expressed in distinct interneuron subtypes in the rat hippocampus. *J Comp Neurol* 509:551–565.
- Csicsvari J, Hirase H, Mamiya A, Buzsáki G (2000) Ensemble patterns of hippocampal CA3-CA1 neurons during sharp wave-associated population events. *Neuron* 28:585–594.
- Dasari S, Gullledge AT (2011) M1 and M4 receptors modulate hippocampal pyramidal neurons. *J Neurophysiol* 105:779–792.
- Davoudi H, Foster DJ (2019) Acute silencing of hippocampal CA3 reveals a dominant role in place field responses. *Nat Neurosci*:1.
- Debanne D, Gähwiler BH, Thompson SM (1998) Long-term synaptic plasticity between pairs of individual CA3 pyramidal cells in rat hippocampal slice cultures. *J Physiol* 507:237–247.
- Degro CE, Kulik A, Booker SA, Vida I (2015) Compartmental distribution of gabab receptor-mediated currents along the somatodendritic axis of hippocampal principal cells. *Front Synaptic Neurosci* 7.
- Dennis SH, Pasqui F, Colvin EM, Sanger H, Mogg AJ, Felder CC, Broad LM, Fitzjohn SM, Isaac JTR, Mellor JR (2016) Activation of Muscarinic M1 Acetylcholine Receptors Induces Long-Term Potentiation in the Hippocampus. *Cereb Cortex* 26:414–426.
- Diba K, Buzsáki G (2007) Forward and reverse hippocampal place-cell sequences during ripples. *Nat Neurosci* 10:1241–1242.
- Ding L, Chen H, Diamantaki M, Coletta S, Preston-Ferrer P, Burgalossi A (2020) Structural Correlates of CA2 and CA3 Pyramidal Cell Activity in Freely-Moving Mice. *J Neurosci* 40:5797–5806.
- Disney AA, Higley MJ (2020) Diverse Spatiotemporal Scales of Cholinergic Signaling in the Neocortex. *J Neurosci* 40:720–725.
- Do VH, Martinez CO, Martinez JL, Derrick BE (2002) Long-term potentiation in direct perforant path projections to the hippocampal CA3 region in vivo. *J Neurophysiol* 87:669–678.
- Dobrunz LE, Huang EP, Stevens CF (1997) Very short-term plasticity in hippocampal synapses. *Proc Natl Acad Sci U S A* 94:14843–14847.
- Dong C, Madar AD, Sheffield MEJ (2021) Distinct place cell dynamics in CA1 and CA3 encode experience in new environments. *Nat Commun* 12.
- Douchamps V, Jeewajee A, Blundell P, Burgess N, Lever C (2013) Evidence for Encoding versus Retrieval Scheduling in the Hippocampus by Theta Phase and Acetylcholine. *J Neurosci* 33:8689–8704.
- Doze VA, Cohen GA, Madison D V. (1991) Synaptic localization of adrenergic disinhibition in the rat hippocampus. *Neuron* 6:889–900.
- Dupret D, O'Neill J, Pleydell-Bouverie B, Csicsvari J (2010) The reorganization and reactivation of hippocampal maps predict spatial memory performance. *Nat Neurosci* 13:995–1002.
- Eglen RM (2006) Muscarinic receptor subtypes in neuronal and non-neuronal cholinergic function.

- Auton Autacoid Pharmacol 26:219–233.
- Ego-Stengel V, Wilson MA (2010) Disruption of ripple-associated hippocampal activity during rest impairs spatial learning in the rat. *Hippocampus* 20:1–10.
- Eichenbaum H (1999) The hippocampus and mechanisms of declarative memory. *Behav Brain Res* 103:123–133.
- Fernández De Sevilla D, Buño W (2010) The muscarinic long-term enhancement of NMDA and AMPA receptor-mediated transmission at Schaffer collateral synapses develop through different intracellular mechanisms. *J Neurosci* 30:11032–11042.
- Fernández de Sevilla D, Núñez A, Buño W (2020) Muscarinic Receptors, from Synaptic Plasticity to its Role in Network Activity. *Neuroscience*.
- Fortunato C, Debanne D, Scanziani M, Gähwiler BH, Thompson SM (1996) Functional characterization and modulation of feedback inhibitory circuits in area CA3 of rat hippocampal slice cultures. *Eur J Neurosci* 8:1758–1768.
- Foster DJ, Wilson MA (2006) Reverse replay of behavioural sequences in hippocampal place cells during the awake state. *Nature* 440:680–683.
- Fuhrmann F, Justus D, Sosulina L, Kaneko H, Beutel T, Friedrichs D, Schoch S, Schwarz MK, Fuhrmann M, Remy S (2015) Locomotion, Theta Oscillations, and the Speed-Related Firing of Hippocampal Neurons Are Controlled by a Medial Septal Glutamatergic Circuit. *Neuron* 86:1253–1264.
- Galloway CR, Ravipati K, Singh S, Lebois EP, Cohen RM, Levey AI, Manns JR (2018) Hippocampal place cell dysfunction and the effects of muscarinic M₁ receptor agonism in a rat model of Alzheimer's disease. *Hippocampus* 28:568–585.
- Gambino F, Pagès S, Kehayas V, Baptista D, Tatti R, Carleton A, Holtmaat A (2014) Sensory-evoked LTP driven by dendritic plateau potentials in vivo. *Nature* 515:116–119.
- Ghamari-Langroudi M, Bourque CW (2004) Muscarinic receptor modulation of slow afterhyperpolarization and phasic firing in rat supraoptic nucleus neurons. *J Neurosci* 24:7718–7726.
- Ghoneim MM, Mewaldt SP (1977) Studies on human memory: the interactions of diazepam, scopolamine, and physostigmine. *Psychopharmacology (Berl)* 52:1–6.
- Giacobini E (2000) Cholinesterase inhibitors stabilize Alzheimer's disease. *Ann N Y Acad Sci* 920:321–327.
- Giessel AJ, Sabatini BL (2010) M1 Muscarinic Receptors Boost Synaptic Potentials and Calcium Influx in Dendritic Spines by Inhibiting Postsynaptic SK Channels. *Neuron* 68:936–947.
- Gilbert P, Kesner RP (2003) Localization of function within the dorsal hippocampus: the role of the CA3 subregion in paired-associate learning. *Behav Neurosci* 117:1385–1394.
- Giocomo LM, Hasselmo ME (2005) Nicotinic modulation of glutamatergic synaptic transmission in region CA3 of the hippocampus. *Eur J Neurosci* 22:1349–1356.

- Giovannini MG, Rakovska A, Benton RS, Pazzagli M, Bianchi L, Pepeu G (2001) Effects of novelty and habituation on acetylcholine, GABA, and glutamate release from the frontal cortex and hippocampus of freely moving rats. *Neuroscience* 106:43–53.
- Girardeau G, Benchenane K, Wiener SI, Buzsáki G, Zugaro MB (2009) Selective suppression of hippocampal ripples impairs spatial memory. *Nat Neurosci* 12:1222–1223.
- Gold AE, Kesner RP (2005) The role of the CA3 subregion of the dorsal hippocampus in spatial pattern completion in the rat. *Hippocampus* 15:808–814.
- Golding NL, Staff NP, Spruston N (2002) Dendritic spikes as a mechanism for cooperative long-term potentiation. *Nature* 418:326–331.
- Griesius S, O'Donnell C, Waldron S, Thomas KL, Dwyer DM, Wilkinson LS, Hall J, Robinson ESJ, Mellor JR (2022) Reduced expression of the psychiatric risk gene *DLG2* (*PSD93*) impairs hippocampal synaptic integration and plasticity. *Neuropsychopharmacol* 2022:1–12.
- Grybko MJ, Hahm ET, Perrine W, Parnes JA, Chick WS, Sharma G, Finger TE, Vijayaraghavan S (2011) A transgenic mouse model reveals fast nicotinic transmission in hippocampal pyramidal neurons. *Eur J Neurosci* 33:1786–1798.
- Gu L, Kleiber S, Schmid L, Nebeling F, Chamoun M, Steffen J, Wagner J, Fuhrmann M (2014) Long-term in vivo imaging of dendritic spines in the hippocampus reveals structural plasticity. *J Neurosci* 34:13948–13953.
- Gulyás AI, Mlles R, Hájos N, Freund TF (1993) Precision and variability in postsynaptic target selection of inhibitory cells in the hippocampal CA3 region. *Eur J Neurosci* 5:1729–1751.
- Gulyás AI, Tóth K, Dános P, Freund TF (1991) Subpopulations of GABAergic neurons containing parvalbumin, calbindin D28k, and cholecystokinin in the rat hippocampus. *J Comp Neurol* 312:371–378.
- Guo NN, Li BM (2007) Cellular and subcellular distributions of $\beta 1$ - and $\beta 2$ -Adrenoceptors in the CA1 and CA3 regions of the rat hippocampus. *Neuroscience* 146:298–305.
- Guzman SJ, Schlögl A, Frotscher M, Jonas P (2016) Synaptic mechanisms of pattern completion in the hippocampal CA3 network. *Science* 353:1117–1123.
- Haas HL, Konnerth A (1983) Histamine and noradrenaline decrease calcium-activated potassium conductance in hippocampal pyramidal cells. *Nature* 302:432–434.
- Hagena H, Manahan-Vaughan D (2011) Learning-Facilitated Synaptic Plasticity at CA3 Mossy Fiber and Commissural-Associational Synapses Reveals Different Roles in Information Processing. *Cereb Cortex* 21:2442–2449.
- Hagger-Vaughan N, Storm JF (2019) Synergy of Glutamatergic and Cholinergic Modulation Induces Plateau Potentials in Hippocampal OLM Interneurons. *Front Cell Neurosci* 13.
- Hájos N, Pálhalini J, Mann EO, Németh B, Paulsen O, Freund TF (2004) Spike timing of distinct types of GABAergic interneuron during hippocampal gamma oscillations in vitro. *J Neurosci* 24:9127–9137.

- Hájos N, Papp EC, Acsády L, Levey AI, Freund TF (1998) Distinct interneuron types express m2 muscarinic receptor immunoreactivity on their dendrites or axon terminals in the hippocampus. *Neuroscience* 82:355–376.
- Hansen N (2016) The CMA Evolution Strategy: A Tutorial.
- Hansen N, Manahan-Vaughan D (2015) Hippocampal long-term potentiation that is elicited by perforant path stimulation or that occurs in conjunction with spatial learning is tightly controlled by beta-adrenoreceptors and the locus coeruleus. *Hippocampus* 25:1285–1298.
- Hasselmo ME (1999) Neuromodulation: acetylcholine and memory consolidation. *Trends Cogn Sci* 3:351–359.
- Hasselmo ME (2006) The role of acetylcholine in learning and memory. *Curr Opin Neurobiol* 16:710–715.
- Hasselmo ME, Schnell E, Barkai E (1995) Dynamics of learning and recall at excitatory recurrent synapses and cholinergic modulation in rat hippocampal region CA3. *J Neurosci* 15:5249–5262.
- Haugland KG, Olberg A, Lande A, Kjelstrup KB, Brun VH (2020) Hippocampal growth hormone modulates relational memory and the dendritic spine density in CA1. *Learn Mem* 27:33–44.
- Hebb DO (2005) *The Organization of Behavior : A Neuropsychological Theory*. Organ Behav.
- Hedrick T, Danskin B, Larsen RS, Ollerenshaw D, Groblewski P, Valley M, Olsen S, Waters J (2016) Characterization of Channelrhodopsin and Archaelrhodopsin in Cholinergic Neurons of Cre-Lox Transgenic Mice. *PLoS One* 11.
- Hemond P, Epstein D, Boley A, Migliore M, Ascoli GA, Jaffe DB (2008) Distinct classes of pyramidal cells exhibit mutually exclusive firing patterns in hippocampal area CA3b. *Hippocampus* 18:411–424.
- Henze DA, Cameron WE, Barrionuevo G (1996) Dendritic morphology and its effects on the amplitude and rise-time of synaptic signals in hippocampal CA3 pyramidal cells. *J Comp Neurol* 369:331–334.
- Hervé-Minvielle A, Sara S (1995) Rapid habituation of auditory responses of locus coeruleus cells in anaesthetized and awake rats. *Neuroreport* 6:1363–1368.
- Hoffman DA, Johnston D (1998) Downregulation of transient K⁺ channels in dendrites of hippocampal CA1 pyramidal neurons by activation of PKA and PKC. *J Neurosci* 18:3521–3528.
- Hoffman DA, Magee JC, Colbert CM, Johnston D (1997) K⁺ channel regulation of signal propagation in dendrites of hippocampal pyramidal neurons. *Nature* 387:869–875.
- Holthoff K, Kovalchuk Y, Konnerth A (2006) Dendritic spikes and activity-dependent synaptic plasticity. *Cell Tissue Res* 326:369–377.
- Hopfield JJ (1982) Neural networks and physical systems with emergent collective computational abilities. *Proc Natl Acad Sci U S A* 79:2554–2558.
- Hopkins WF, Johnston D (1984) Frequency-dependent noradrenergic modulation of long-term potentiation in the hippocampus. *Science* 226:350–352.

- Hopkins WF, Johnston D (1988) Noradrenergic enhancement of long-term potentiation at mossy fiber synapses in the hippocampus. *J Neurophysiol* 59:667–687.
- Huang YY, Kandel ER (1996) Modulation of both the early and the late phase of mossy fiber LTP by the activation of beta-adrenergic receptors. *Neuron* 16:611–617.
- Huerta PT, Lisman JE (1995) Bidirectional synaptic plasticity induced by a single burst during cholinergic theta oscillation in CA1 in vitro. *Neuron* 15:1053–1063.
- Hummos A, Franklin CC, Nair SS (2014) Intrinsic mechanisms stabilize encoding and retrieval circuits differentially in a hippocampal network model. *Hippocampus* 24:1430–1448.
- Hunt D, Puente N, Grandes P, Castillo P (2013) Bidirectional NMDA receptor plasticity controls CA3 output and heterosynaptic metaplasticity. *Nat Neurosci* 16:1049–1059.
- Hunt DL, Linaro D, Si B, Romani S, Spruston N (2018) A novel pyramidal cell type promotes sharp-wave synchronization in the hippocampus. *Nat Neurosci* 21:985–995.
- Hyun JH, Eom K, Lee K-H, Bae JY, Bae YC, Kim M-H, Kim S, Ho W-K, Lee S-H (2015) Kv1.2 mediates heterosynaptic modulation of direct cortical synaptic inputs in CA3 pyramidal cells. *J Physiol* 593:3617–3643.
- Ikonen S, McMahan R, Gallagher M, Eichenbaum H, Tanila H (2002) Cholinergic system regulation of spatial representation by the hippocampus. *Hippocampus* 12:386–397.
- Jadhav SP, Kemere C, German PW, Frank LM (2012) Awake hippocampal sharp-wave ripples support spatial memory. *Science* 336:1454–1458.
- Jarzebowski P, Tang CS, Paulsen O, Hay YA (2021) Impaired spatial learning and suppression of sharp wave ripples by cholinergic activation at the goal location. *Elife* 10.
- Jędrzejewski-Szmek Z, Abrahao KP, Jędrzejewska-Szmek J, Lovinger DM, Blackwell KT (2018) Parameter Optimization Using Covariance Matrix Adaptation—Evolutionary Strategy (CMA-ES), an Approach to Investigate Differences in Channel Properties Between Neuron Subtypes. *Front Neuroinform* 12:47.
- Ji JZ, Zhang XH, Li BM (2003) Deficient Spatial Memory Induced by Blockade of Beta-Adrenoceptors in the Hippocampal CA1 Region. *Behav Neurosci* 117:1378–1384.
- Jing M et al. (2018) A genetically encoded fluorescent acetylcholine indicator for in vitro and in vivo studies. *Nat Biotechnol* 36:726–737.
- Jing M et al. (2020) An optimized acetylcholine sensor for monitoring in vivo cholinergic activity. *Nat Methods* 17:1139.
- Jochems A, Yoshida M (2013) Persistent firing supported by an intrinsic cellular mechanism in hippocampal CA3 pyramidal cells. *Eur J Neurosci* 38:2250–2259.
- Joshi A, Salib M, Viney TJ, Dupret D, Somogyi P (2017) Behavior-Dependent Activity and Synaptic Organization of Septo-hippocampal GABAergic Neurons Selectively Targeting the Hippocampal CA3 Area. *Neuron* 96:1342.
- Jouvet M (1969) Biogenic amines and the states of sleep. *Science* (80-) 163:32–41.

- Jurgens CWD, Hammad HM, Lichter JA, Boese SJ, Nelson BW, Goldenstein BL, Davis KL, Xu K, Hillman KL, Porter JE, Doze VA (2007) Alpha2A adrenergic receptor activation inhibits epileptiform activity in the rat hippocampal CA3 region. *Mol Pharmacol* 71:1572–1581.
- Jurgens CWD, Rau KE, Knudson CA, King JD, Carr PA, Porter JE, Doze VA (2005) β 1 Adrenergic Receptor-Mediated Enhancement of Hippocampal CA3 Network Activity. *J Pharmacol Exp Ther* 314:552–560.
- Kaifosh P, Losonczy A (2016) Mnemonic Functions for Nonlinear Dendritic Integration in Hippocampal Pyramidal Circuits. *Neuron* 90:622–634.
- Kaifosh P, Lovett-Barron M, Turi GF, Reardon TR, Losonczy A (2013) Septo-hippocampal GABAergic signaling across multiple modalities in awake mice. *Nat Neurosci* 16:1182–1184.
- Kamondi A, Acsády L, Buzsáki G (1998) Dendritic spikes are enhanced by cooperative network activity in the intact hippocampus. *J Neurosci* 18:3919–3928.
- Karlsson MP, Frank LM (2009) Awake replay of remote experiences in the hippocampus. *Nat Neurosci* 12:913–918.
- Kaufman AM, Geiller T, Losonczy A (2020) A Role for the Locus Coeruleus in Hippocampal CA1 Place Cell Reorganization during Spatial Reward Learning. *Neuron* 105:1018-1026.e4.
- Kawasaki H, Palmieri C, Avoli M (1999) Muscarinic receptor activation induces depolarizing plateau potentials in bursting neurons of the rat subiculum. *J Neurophysiol* 82:2590–2601.
- Kim S, Guzman SJ, Hu H, Jonas P (2012) Active dendrites support efficient initiation of dendritic spikes in hippocampal CA3 pyramidal neurons. *Nat Neurosci* 15:600–606.
- Klee R, Ficker E, Heinemann U (1995) Comparison of voltage-dependent potassium currents in rat pyramidal neurons acutely isolated from hippocampal regions CA1 and CA3. *J Neurophysiol* 74:1982–1995.
- Knierim JJ, Neunuebel JP (2016) Tracking the flow of hippocampal computation: Pattern separation, pattern completion, and attractor dynamics. *Neurobiol Learn Mem* 129:38–49.
- Knierim JJ, Neunuebel JP, Deshmukh SS (2013) Functional correlates of the lateral and medial entorhinal cortex: objects, path integration and local-global reference frames. *Philos Trans R Soc Lond B Biol Sci* 369.
- Kobayashi K, Poo M (2004) Spike train timing-dependent associative modification of hippocampal CA3 recurrent synapses by mossy fibers. *Neuron* 41:445–454.
- Kohus Z, Káli S, Rovira-Esteban L, Schlingloff D, Papp O, Freund TF, Hájos N, Gulyás AI (2016) Properties and dynamics of inhibitory synaptic communication within the CA3 microcircuits of pyramidal cells and interneurons expressing parvalbumin or cholecystokinin. *J Physiol* 594:3745–3774.
- Kosaka T, Katsumaru H, Hama K, Wu JY, Heizmann CW (1987) GABAergic neurons containing the Ca²⁺-binding protein parvalbumin in the rat hippocampus and dentate gyrus. *Brain Res* 419:119–130.

- Kosaka T, Kosaka K, Tateishi K, Hamaoka Y, Yanaihara N, Wu J -Y, Hama K (1985) GABAergic neurons containing CCK-8-like and/or VIP-like immunoreactivities in the rat hippocampus and dentate gyrus. *J Comp Neurol* 239:420–430.
- Kosaka T, Wu JY, Benoit R (1988) GABAergic neurons containing somatostatin-like immunoreactivity in the rat hippocampus and dentate gyrus. *Exp Brain Res* 71:388–398.
- Kremin T, Hasselmo ME (2007) Cholinergic suppression of glutamatergic synaptic transmission in hippocampal region CA3 exhibits laminar selectivity: Implication for hippocampal network dynamics. *Neuroscience* 149:760–767.
- Kuruvilla M V., Ainge JA (2017) Lateral Entorhinal Cortex Lesions Impair Local Spatial Frameworks. *Front Syst Neurosci* 11:30.
- Larkin MC, Lykken C, Tye LD, Wickelgren JG, Frank LM (2014) Hippocampal output area CA1 broadcasts a generalized novelty signal during an object-place recognition task. *Hippocampus* 24:773–783.
- Larkum ME, Nevian T, Sandier M, Polsky A, Schiller J (2009) Synaptic integration in tuft dendrites of layer 5 pyramidal neurons: A new unifying principle. *Science* (80-) 325:756–760.
- Larkum ME, Zhu JJ (2002) Signaling of layer 1 and whisker-evoked Ca²⁺ and Na⁺ action potentials in distal and terminal dendrites of rat neocortical pyramidal neurons in vitro and in vivo. *J Neurosci* 22:6991–7005.
- Lasztóczy B, Tukker JJ, Somogyi P, Klausberger T (2011) Terminal Field and Firing Selectivity of Cholecystokinin-Expressing Interneurons in the Hippocampal CA3 Area. *J Neurosci* 31:18073.
- Lawrence JJ, Statland JM, Grinspan ZM, McBain CJ (2006) Cell type-specific dependence of muscarinic signalling in mouse hippocampal stratum oriens interneurons. *J Physiol* 570:595–610.
- Leão RN, Mikulovic S, Leão KE, Munguba H, Gezelius H, Enjin A, Patra K, Eriksson A, Loew LM, Tort ABL, Kullander K (2012) OLM interneurons differentially modulate CA3 and entorhinal inputs to hippocampal CA1 neurons. *Nat Neurosci* 15:1524–1530.
- Lee AK, Wilson MA (2002) Memory of sequential experience in the hippocampus during slow wave sleep. *Neuron* 36:1183–1194.
- Lee H, GoodSmith D, Knierim JJ (2020) Parallel processing streams in the hippocampus. *Curr Opin Neurobiol* 64:127–134.
- Lee H, Wang C, Deshmukh SS, Knierim JJ (2015) Neural Population Evidence of Functional Heterogeneity along the CA3 Transverse Axis: Pattern Completion versus Pattern Separation. *Neuron* 87:1093–1105.
- Lee I, Kesner RP (2004a) Differential contributions of dorsal hippocampal subregions to memory acquisition and retrieval in contextual fear-conditioning. *Hippocampus* 14:301–310.
- Lee I, Kesner RP (2004b) Encoding versus retrieval of spatial memory: double dissociation between the dentate gyrus and the perforant path inputs into CA3 in the dorsal hippocampus. *Hippocampus*

14:66–76.

- Lee I, Yoganarasimha D, Rao G, Knierim JJ (2004) Comparison of population coherence of place cells in hippocampal subfields CA1 and CA3. *Nature* 430:456–459.
- Lemon N, Aydin-Abidin S, Funke K, Manahan-Vaughan D (2009) Locus coeruleus activation facilitates memory encoding and induces hippocampal LTD that depends on β -Adrenergic receptor activation. *Cereb Cortex* 19:2827–2837.
- Letzkus JJ, Wolff SBE, Meyer EMM, Tovote P, Courtin J, Herry C, Lüthi A (2011) A disinhibitory microcircuit for associative fear learning in the auditory cortex. *Nature* 480:331–335.
- Levey AI, Edmunds SM, Koliatsos V, Wiley RG, Heilman CJ (1995) Expression of m1-m4 Muscarinic Acetylcholine Receptor Proteins in Rat Hippocampus and Regulation by Cholinergic Innervation. *J Neurosci* 15:4077–4092.
- Lewis PR, Shute CCD, Silver A (1967) Confirmation from choline acetylase analyses of a massive cholinergic innervation to the rat hippocampus. *J Physiol* 191:215–224.
- Liu Y, Cui L, Schwarz MK, Dong Y, Schlüter OM (2017) Adrenergic Gate Release for Spike Timing-Dependent Synaptic Potentiation. *Neuron* 93:394–408.
- Losonczy A, Makara JK, Magee JC (2008) Compartmentalized dendritic plasticity and input feature storage in neurons. *Nature* 452:436–441.
- Lu L, Igarashi KM, Witter MP, Moser EI, Moser M-B (2015) Topography of Place Maps along the CA3-to-CA2 Axis of the Hippocampus. *Neuron* 87:1078–1092.
- Lynch MA, Bliss TVP (1986) Noradrenaline modulates the release of [14 C]glutamate from dentate but not from CA1/CA3 slices of rat hippocampus. *Neuropharmacology* 25:493–498.
- Ma X, Zhang Y, Wang L, Li N, Barkai E, Zhang X, Lin L, Xu J (2020) The Firing of Theta State-Related Septal Cholinergic Neurons Disrupt Hippocampal Ripple Oscillations via Muscarinic Receptors. *J Neurosci* 40:3591–3603.
- Magee JC (1998) Dendritic hyperpolarization-activated currents modify the integrative properties of hippocampal CA1 pyramidal neurons. *J Neurosci* 18:7613–7624.
- Magee JC (2000) Dendritic integration of excitatory synaptic input. *Nat Rev Neurosci* 2000 13 1:181.
- Magee JC, Cook EP (2000) Somatic EPSP amplitude is independent of synapse location in hippocampal pyramidal neurons. *Nat Neurosci* 2000 3 3:895–903.
- Magó Á, Kis N, Lükő B, Makara JK (2021) Distinct dendritic Ca²⁺ spike forms produce opposing input-output transformations in rat CA3 pyramidal cells. *Elife* 10.
- Major G, Larkum ME, Schiller J (2013) Active properties of neocortical pyramidal neuron dendrites. *Annu Rev Neurosci* 36:1–24.
- Major G, Polsky A, Denk W, Schiller J, Tank DW (2008) Spatiotemporally graded NMDA spike/plateau potentials in basal dendrites of neocortical pyramidal neurons. *J Neurophysiol* 99:2584–2601.
- Makara JK, Magee JC (2013) Variable dendritic integration in hippocampal CA3 pyramidal neurons.

- Neuron 80:1438–1450.
- Malik R, Johnston D (2017) Dendritic GIRK channels gate the integration window, plateau potentials, and induction of synaptic plasticity in dorsal but not ventral CA1 neurons. *J Neurosci* 37:3940–3955.
- Mamad O, McNamara HM, Reilly RB, Tsanov M (2015) Medial septum regulates the hippocampal spatial representation. *Front Behav Neurosci* 9:166.
- Marder E, Taylor AL (2011) Multiple models to capture the variability in biological neurons and networks. In: *Nature Neuroscience*, pp 133–138. Nature Publishing Group.
- Markram H, Segal M (1990) Electrophysiological characteristics of cholinergic and non-cholinergic neurons in the rat medial septum-diagonal band complex. *Brain Res* 513:171–174.
- Marrone DF, Satvat E, Odintsova I V., Gheidi A (2014) Dissociation of spatial representations within hippocampal region CA3. *Hippocampus* 24:1417–1420.
- Martinello K, Huang Z, Lujan R, Tran B, Watanabe M, Cooper EC, Brown DA, Shah MM (2015) Cholinergic afferent stimulation induces axonal function plasticity in adult hippocampal granule cells. *Neuron* 85:346–363.
- McHugh TJ, Jones MW, Quinn JJ, Balthasar N, Coppari R, Elmquist JK, Lowell BB, Fanselow MS, Wilson MA, Tonegawa S (2007) Dentate gyrus NMDA receptors mediate rapid pattern separation in the hippocampal network. *Science* 317:94–99.
- McMahon DBT, Barrionuevo G (2002) Short- and Long-Term Plasticity of the Perforant Path Synapse in Hippocampal Area CA3. *J Neurophysiol* 88:528–533.
- Meeter M, Murre JMJ, Talamini LM (2004) Mode shifting between storage and recall based on novelty detection in oscillating hippocampal circuits. *Hippocampus* 14:722–741.
- Mendell AL, Atwi S, Bailey CDC, McCloskey D, Scharfman HE, MacLusky NJ (2017) Expansion of mossy fibers and CA3 apical dendritic length accompanies the fall in dendritic spine density after gonadectomy in male, but not female, rats. *Brain Struct Funct* 222:587.
- Migliore M, Cook EP, Jaffe DB, Turner DA, Johnston D (1995) Computer simulations of morphologically reconstructed CA3 hippocampal neurons. *J Neurophysiol* 73:1157–1168.
- Miles R, Tóth K, Gulyás AI, Hájos N, Freund TF (1996) Differences between somatic and dendritic inhibition in the hippocampus. *Neuron* 16:815–823.
- Miles R, Wong RK (1987) Inhibitory control of local excitatory circuits in the guinea-pig hippocampus. *J Physiol* 388:611–629.
- Milner TA, Lee A, Aicher SA, Rosin DL (1998) Hippocampal 2A-Adrenergic Receptors Are Located Predominantly Presynaptically but Are Also Found Postsynaptically and in Selective Astrocytes. *J Comp Neurol*.
- Milner TA, Shah P, Pierce JP (2000) Adrenergic Receptors Primarily Are Located on the Dendrites of Granule Cells and Interneurons but Also Are Found on Astrocytes and a Few Presynaptic Profiles in the Rat Dentate Gyrus.

- Miranda MI, Ramírez-Lugo L, Bermúdez-Rattoni F (2000) Cortical cholinergic activity is related to the novelty of the stimulus. *Brain Res* 882:230–235.
- Mishra RK, Kim S, Guzman SJ, Jonas P (2016) Symmetric spike timing-dependent plasticity at CA3–CA3 synapses optimizes storage and recall in autoassociative networks. *Nat Commun* 7:11552.
- Mitsushima D, Sano A, Takahashi T (2013) A cholinergic trigger drives learning-induced plasticity at hippocampal synapses. *Nat Commun* 4.
- Mizuseki K, Royer S, Diba K, Buzsáki G (2012) Activity dynamics and behavioral correlates of CA3 and CA1 hippocampal pyramidal neurons. *Hippocampus* 22:1659–1680.
- Murchison CF, Zhang XY, Zhang WP, Ouyang M, Lee A, Thomas SA (2004) A distinct role for norepinephrine in memory retrieval. *Cell* 117:131–143.
- Nadler JV, Vaca KW, White WF, Lynch GS, Cotman CW (1976) Aspartate and glutamate as possible transmitters of excitatory hippocampal afferents. *Nat* 1976 2605551 260:538–540.
- Nakamura N, Flasbeck V, Maingret N, Kitsukawa T, Sauvage M (2013) Proximodistal segregation of nonspatial information in CA3: preferential recruitment of a proximal CA3-distal CA1 network in nonspatial recognition memory. *J Neurosci* 33:11506–11514.
- Nakamura T, Nakamura K, Lasser-Ross N, Barbara JG, Sandler VM, Ross WN (2000) Inositol 1,4,5-Trisphosphate (IP3)-Mediated Ca^{2+} Release Evoked by Metabotropic Agonists and Backpropagating Action Potentials in Hippocampal CA1 Pyramidal Neurons. *J Neurosci* 20:8365–8376.
- Nakashiba T, Young JZ, McHugh TJ, Buhl DL, Tonegawa S (2008) Transgenic Inhibition of Synaptic Transmission Reveals Role of CA3 Output in Hippocampal Learning. *Science* (80-) 319:1260–1264.
- Nakazawa K, Quirk MC, Chitwood RA, Watanabe M, Yeckel MF, Sun LD, Kato A, Carr CA, Johnston D, Wilson MA, Tonegawa S (2002) Requirement for hippocampal CA3 NMDA receptors in associative memory recall. *Science* (80-) 297:211–218.
- Nakazawa K, Sun LD, Quirk MC, Rondi-Reig L, Wilson MA, Tonegawa S (2003) Hippocampal CA3 NMDA receptors are crucial for memory acquisition of one-time experience. *Neuron* 38:305–315.
- Nash MS, Willets JM, Billups B, Challiss RAJ, Nahorski SR (2004) Synaptic activity augments muscarinic acetylcholine receptor-stimulated inositol 1,4,5-trisphosphate production to facilitate Ca^{2+} release in hippocampal neurons. *J Biol Chem* 279:49036–49044.
- Neki A, Ohishi H, Kaneko T, Shigemoto R, Nakanishi S, Mizuno N (1996) Pre- and postsynaptic localization of a metabotropic glutamate receptor, mGluR2, in the rat brain: an immunohistochemical study with a monoclonal antibody. *Neurosci Lett* 202:197–200.
- Neunuebel JP, Knierim JJ (2014) CA3 Retrieves Coherent Representations from Degraded Input: Direct Evidence for CA3 Pattern Completion and Dentate Gyrus Pattern Separation. *Neuron* 81:416–427.
- Neunuebel JP, Yoganarasimha D, Rao G, Knierim JJ (2013) Conflicts between Local and Global Spatial

- Frameworks Dissociate Neural Representations of the Lateral and Medial Entorhinal Cortex. *J Neurosci* 33:9246–9258.
- Noguchi A, Huszár R, Morikawa S, Buzsáki G, Ikegaya Y (2022) Inhibition allocates spikes during hippocampal ripples. *Nat Commun* 13:1280.
- Norris D (2017) Short-term memory and long-term memory are still different. *Psychol Bull* 143:992–1009.
- Nowak L, Bregestovski P, Ascher P, Herbet A, Prochiantz A (1984) Magnesium gates glutamate-activated channels in mouse central neurones. *Nature* 307:462–465.
- Núñez A, Domínguez S, Buño W, de Sevilla DF (2012) Cholinergic-mediated response enhancement in barrel cortex layer V pyramidal neurons. *J Neurophysiol* 108:1656–1668.
- O’Keefe J, Dostrovsky J (1971) The hippocampus as a spatial map. Preliminary evidence from unit activity in the freely-moving rat. *Brain Res* 34:171–175.
- O’Reilly RC, McClelland JL (1994) Hippocampal conjunctive encoding, storage, and recall: avoiding a trade-off. *Hippocampus* 4:661–682.
- Palacios-Filardo J, Udakis M, Brown GA, Tehan BG, Congreve MS, Nathan PJ, Brown AJH, Mellor JR (2021) Acetylcholine prioritises direct synaptic inputs from entorhinal cortex to CA1 by differential modulation of feedforward inhibitory circuits. *Nat Commun* 2021 12:1–16.
- Poirazi P, Brannon T, Mel BW (2003a) Arithmetic of subthreshold synaptic summation in a model CA1 pyramidal cell. *Neuron* 37:977–987.
- Poirazi P, Brannon T, Mel BW (2003b) Pyramidal neuron as a two-layer neural network. *Neuron* 37:989–999.
- Polsky A, Mel BW, Schiller J (2004) Computational subunits in thin dendrites of pyramidal cells. *Nat Neurosci* 7:621–627.
- Posani L, Cocco S, Monasson R (2018) Integration and multiplexing of positional and contextual information by the hippocampal network Bush D, ed. *PLOS Comput Biol* 14:e1006320.
- Prince LY, Bacon T, Humphries R, Tsaneva-Atanasova K, Clopath C, Mellor JR (2021) Separable actions of acetylcholine and noradrenaline on neuronal ensemble formation in hippocampal CA3 circuits Bush D, ed. *PLOS Comput Biol* 17:e1009435.
- Prince LY, Bacon TJ, Humphries R, Tsaneva-Atanasova K, Clopath C, Mellor JR (n.d.) Separable actions of acetylcholine and noradrenaline on memory ensemble formation in hippocampal CA3 circuits.
- Rall W (1962a) Theory of Physiological Properties of Dendrites. *Ann N Y Acad Sci* 96:1071–1092.
- Rall W (1962b) Electrophysiology of a Dendritic Neuron Model. *Biophys J* 2:145.
- Rall W (1967) Distinguishing theoretical synaptic potentials computed for different soma-dendritic distributions of synaptic input. *J Neurophysiol* 30:1138–1168.
- Rall W, Burke RE, Smith TG, Nelson PG, Frank K (1967) Dendritic location of synapses and possible mechanisms for the monosynaptic EPSP in motoneurons. *J Neurophysiol* 30:1169–1193.

- Raus Balind S, Magó Á, Ahmadi M, Kis N, Varga-Németh Z, Lőrincz A, Makara JK (2019) Diverse synaptic and dendritic mechanisms of complex spike burst generation in hippocampal CA3 pyramidal cells. *Nat Commun* 10:1–15.
- Robinson NTM, Descamps LAL, Russell LE, Buchholz MO, Bicknell BA, Antonov GK, Lau JYN, Nutbrown R, Schmidt-Hieber C, Häusser M (2020) Targeted Activation of Hippocampal Place Cells Drives Memory-Guided Spatial Behavior. *Cell* 183:1586-1599.e10.
- Rogers JL, Kesner RP (2003) Cholinergic modulation of the hippocampus during encoding and retrieval. In: *Neurobiology of Learning and Memory*, pp 332–342. Academic Press Inc.
- Rogers JL, Kesner RP (2004) Cholinergic modulation of the hippocampus during encoding and retrieval of tone/shock-induced fear conditioning. *Learn Mem* 11:102–107.
- Rogers S, Rozman PA, Valero M, Doyle WK, Buzsáki G (2021) Mechanisms and plasticity of chemogenically induced interneuronal suppression of principal cells. *Proc Natl Acad Sci U S A* 118.
- Rogers SL, Friedhoff LT (1996) The efficacy and safety of donepezil in patients with Alzheimer's disease: results of a US Multicentre, Randomized, Double-Blind, Placebo-Controlled Trial. The Donepezil Study Group. *Dementia* 7:293–303.
- Rolls ET (1996) A theory of hippocampal function in memory. *Hippocampus* 6:601–620.
- Rolls ET (2016) Pattern separation, completion, and categorisation in the hippocampus and neocortex. *Neurobiol Learn Mem* 129:4–28.
- Rolls ET (2018) The storage and recall of memories in the hippocampo-cortical system. *Cell Tissue Res* 373:577–604.
- Rosen ZB, Cheung S, Siegelbaum SA (2015) Midbrain dopamine neurons bidirectionally regulate CA3-CA1 synaptic drive. *Nat Neurosci* 18:1763–1771.
- Sah P, McLachlan EM (1991) Ca(2+)-activated K⁺ currents underlying the afterhyperpolarization in guinea pig vagal neurons: a role for Ca(2+)-activated Ca²⁺ release. *Neuron* 7:257–264.
- Sah P, McLachlan EM (1992) Potassium currents contributing to action potential repolarization and the afterhyperpolarization in rat vagal motoneurons. *J Neurophysiol* 68:1834–1841.
- Sara SJ, Vankov A, Hervé A (1994) Locus coeruleus-evoked responses in behaving rats: A clue to the role of noradrenaline in memory. *Brain Res Bull* 35:457–465.
- Sasaki T, Piatti VC, Hwaun E, Ahmadi S, Lisman JE, Leutgeb S, Leutgeb JK (2018) Dentate network activity is necessary for spatial working memory by supporting CA3 sharp-wave ripple generation and prospective firing of CA3 neurons. *Nat Neurosci* 21:258–269.
- Save E, Sargolini F (2017) Disentangling the Role of the MEC and LEC in the Processing of Spatial and Non-Spatial Information: Contribution of Lesion Studies. *Front Syst Neurosci* 11.
- Schacter DL (1987) Implicit Memory: History and Current Status. *J Exp Psychol Learn Mem Cogn* 13:501–518.
- Schlingloff D, Káli S, Freund TF, Hájos N, Gulyás AI (2014) Mechanisms of sharp wave initiation and

- ripple generation. *J Neurosci* 34:11385–11398.
- Schoenfeld G, Carta S, Rupprecht P, Ayaz A, Helmchen F (2021) In Vivo Calcium Imaging of CA3 Pyramidal Neuron Populations in Adult Mouse Hippocampus. *eNeuro* 8.
- Scoville WB, Milner B (1957) LOSS OF RECENT MEMORY AFTER BILATERAL HIPPOCAMPAL LESIONS. *J Neurol Neurosurg Psychiatr* 20.
- Segev I, Rinzel J, Shepherd GM, Borst A (1995) The theoretical foundation of dendritic function. *Trends Neurosci* 18:512–512.
- Shah MM, Migliore M, Valencia I, Cooper EC, Brown DA (2008) Functional significance of axonal Kv7 channels in hippocampal pyramidal neurons. *Proc Natl Acad Sci U S A* 105:7869.
- Sharma G, Grybko M, Vijayaraghavan S (2008) Action Potential-Independent and Nicotinic Receptor-Mediated Concerted Release of Multiple Quanta at Hippocampal CA3–Mossy Fiber Synapses. *J Neurosci* 28:2563–2575.
- Sharma G, Vijayaraghavan S (2003) Modulation of presynaptic store calcium induces release of glutamate and postsynaptic firing. *Neuron* 38:929–939.
- Sheffield MEJ, Adoff MD, Dombeck DA (2017) Increased Prevalence of Calcium Transients across the Dendritic Arbor during Place Field Formation. *Neuron* 96:490-504.e5.
- Sheffield MEJ, Dombeck DA (2015) Calcium transient prevalence across the dendritic arbour predicts place field properties. *Nature* 517:200–204.
- Shi YF, Han Y, Su YT, Yang JH, Yu YQ (2015) Silencing of Cholinergic Basal Forebrain Neurons Using Archærhodopsin Prolongs Slow-Wave Sleep in Mice. *PLoS One* 10.
- Shigemoto R, Kinoshita A, Wada E, Nomura S, Ohishi H, Takada M, Flor PJ, Neki A, Abe T, Nakanishi S, Mizuno N (1997) Differential presynaptic localization of metabotropic glutamate receptor subtypes in the rat hippocampus. *J Neurosci* 17:7503–7522.
- Sigel E, Steinmann ME (2012) Structure, function, and modulation of GABA(A) receptors. *J Biol Chem* 287:40224–40231.
- Simon AP, Poindessous-Jazat F, Dutar P, Epelbaum J, Bassant MH (2006) Firing Properties of Anatomically Identified Neurons in the Medial Septum of Anesthetized and Unanesthetized Restrained Rats. *J Neurosci* 26:9038.
- Sohn JW, Lee D, Cho H, Lim W, Shin HS, Lee SH, Ho WK (2007) Receptor-specific inhibition of GABAB-activated K⁺ currents by muscarinic and metabotropic glutamate receptors in immature rat hippocampus. *J Physiol* 580:411–422.
- Soldado-Magraner S, Brandalise F, Honnuraiah S, Pfeiffer M, Moulinier M, Gerber U, Douglas R (2020) Conditioning by subthreshold synaptic input changes the intrinsic firing pattern of CA3 hippocampal neurons. *J Neurophysiol* 123:90–106.
- Son JH, Winzer-Serhan UH (2008) Expression of neuronal nicotinic acetylcholine receptor subunit mRNAs in rat hippocampal GABAergic interneurons. *J Comp Neurol* 511:286–299.
- Song D, Yang Q, Lang Y, Wen Z, Xie Z, Zheng D, Yan T, Deng Y, Nakanishi H, Quan Z, Qing H

- (2018) Manipulation of hippocampal CA3 firing via luminopsins modulates spatial and episodic short-term memory, especially working memory, but not long-term memory. *Neurobiol Learn Mem* 155:435–445.
- Sorra KE, Harris KM (1993) Occurrence and three-dimensional structure of multiple synapses between individual radiatum axons and their target pyramidal cells in hippocampal area CA1. *J Neurosci* 13:3736–3748.
- Sotty F, Danik M, Manseau F, Laplante F, Quirion R, Williams S (2003) Distinct electrophysiological properties of glutamatergic, cholinergic and GABAergic rat septohippocampal neurons: novel implications for hippocampal rhythmicity. *J Physiol* 551:927.
- Squire LR, Zola-Morgan M (1991) *Conscious and Unconscious Memory Systems*. Cold Spring Harb Perspect Biol 7:21667–21668.
- Stegen M, Kirchheim F, Hanuschkin A, Staszewski O, Veh RW, Wolfart J (2012) Adaptive Intrinsic Plasticity in Human Dentate Gyrus Granule Cells during Temporal Lobe Epilepsy. *Cereb Cortex* 22:2087–2101.
- Sun J, Kapur J (2012) M-type potassium channels modulate Schaffer collateral-CA1 glutamatergic synaptic transmission. *J Physiol* 590:3953–3964.
- Sun Q, Sotayo A, Cazzulino AS, Snyder AM, Denny CA, Siegelbaum SA (2017) Proximodistal Heterogeneity of Hippocampal CA3 Pyramidal Neuron Intrinsic Properties, Connectivity, and Reactivation during Memory Recall. *Neuron* 95:656–672.e3.
- Szabadics J, Soltesz I (2009) Functional specificity of mossy fiber innervation of GABAergic cells in the hippocampus. *J Neurosci* 29:4239–4251.
- Szabó GG, Holderith N, Gulyás AI, Freund TF, Hájos N (2010) Distinct synaptic properties of perisomatic inhibitory cell types and their different modulation by cholinergic receptor activation in the CA3 region of the mouse hippocampus. *Eur J Neurosci* 31:2234–2246.
- Takács VT, Cserép C, Schlingloff D, Pósfai B, Szőnyi A, Sos KE, Környei Z, Dénes Á, Gulyás AI, Freund TF, Nyiri G (2018) Co-transmission of acetylcholine and GABA regulates hippocampal states. *Nat Commun* 2018 91 9:1–15.
- Takahashi H, Magee JC (2009) Pathway Interactions and Synaptic Plasticity in the Dendritic Tuft Regions of CA1 Pyramidal Neurons. *Neuron* 62:102–111.
- Takahashi K, Kayama Y, Lin JS, Sakai K (2010) Locus coeruleus neuronal activity during the sleep-waking cycle in mice. *Neuroscience* 169:1115–1126.
- Teles-Grilo Ruivo LM, Baker KL, Conway MW, Kinsley PJ, Gilmour G, Phillips KG, Isaac JTR, Lowry JP, Mellor JR (2017) Coordinated Acetylcholine Release in Prefrontal Cortex and Hippocampus Is Associated with Arousal and Reward on Distinct Timescales. *Cell Rep* 18:905–917.
- Tennant SA, Fischer L, Garden DLF, Gerlei KZ, Martinez-Gonzalez C, McClure C, Wood ER, Nolan MF (2018) Stellate Cells in the Medial Entorhinal Cortex Are Required for Spatial Learning. *Cell*

Rep 22:1313–1324.

- Tigaret CM, Chamberlain SEL, Sadowski JHLP, Hall J, Ashby MC, Mellor JR (2018) Convergent metabotropic signaling pathways inhibit SK channels to promote synaptic plasticity in the hippocampus. *J Neurosci* 38:9252–9262.
- Tigaret CM, Olivo V, Sadowski JHLP, Ashby MC, Mellor JR (2016) Coordinated activation of distinct Ca(2+) sources and metabotropic glutamate receptors encodes Hebbian synaptic plasticity. *Nat Commun* 7.
- Traynelis SF, Wollmuth LP, McBain CJ, Menniti FS, Vance KM, Ogden KK, Hansen KB, Yuan H, Myers SJ, Dingledine R (2010) Glutamate receptor ion channels: structure, regulation, and function. *Pharmacol Rev* 62:405–496.
- Treves A, Rolls ET (1992) Computational constraints suggest the need for two distinct input systems to the hippocampal CA3 network. *Hippocampus* 2:189–199.
- Treves A, Rolls ET (1994) Computational Analysis of the Role of the Hippocampus in Memory.
- Truong C, Oudre L, Vayatis N (2020) Selective review of offline change point detection methods. *Signal Processing* 167:107299.
- Tsubokawa H, Ross WN (1997) Muscarinic Modulation of Spike Backpropagation in the Apical Dendrites of Hippocampal CA1 Pyramidal Neurons. *J Neurosci* 17:5782–5791.
- Tsukamoto M, Yasui T, Yamada MK, Nishiyama N, Matsuki N, Ikegaya Y (2003) Mossy fibre synaptic NMDA receptors trigger non-hebbian long-term potentiation at entorhino-CA3 synapses in the rat. *J Physiol* 546:665–675.
- Tukker JJ, Lasztóczy B, Katona L, Roberts JDB, Pissadaki EK, Dalezios Y, Márton L, Zhang L, Klausberger T, Somogyi P (2013) Distinct Dendritic Arborization and In Vivo Firing Patterns of Parvalbumin-Expressing Basket Cells in the Hippocampal Area CA3. *J Neurosci* 33:6809.
- Tulving E (1972) Episodic and semantic memory. In: *Organization of memory*.
- Udakis M, Pedrosa V, Chamberlain SEL, Clopath C, Mellor JR (2020) Interneuron-specific plasticity at parvalbumin and somatostatin inhibitory synapses onto CA1 pyramidal neurons shapes hippocampal output. *Nat Commun* 2020 111 11:1–17.
- Ul Haq R, Liotta A, Kovacs R, Rösler A, Jarosch MJ, Heinemann U, Behrens CJ (2012) Adrenergic modulation of sharp wave-ripple activity in rat hippocampal slices. *Hippocampus* 22:516–533.
- Umbriaco D, Garcia S, Beaulieu C, Descarries L (1995) Relational features of acetylcholine, noradrenaline, serotonin and GABA axon terminals in the stratum radiatum of adult rat hippocampus (CA1). *Hippocampus* 5:605–620.
- Van Cauter T, Camon J, Alvernhe A, Elduayen C, Sargolini F, Save E (2013) Distinct Roles of Medial and Lateral Entorhinal Cortex in Spatial Cognition. *Cereb Cortex* 23:451–459.
- Vandecasteele M, Varga V, Berényi A, Papp E, Barthó P, Venance L, Freund TF, Buzsáki G (2014) Optogenetic activation of septal cholinergic neurons suppresses sharp wave ripples and enhances theta oscillations in the hippocampus. *Proc Natl Acad Sci U S A* 111:13535–13540.

- Vanderwolf CH (1969) Hippocampal electrical activity and voluntary movement in the rat. *Electroencephalogr Clin Neurophysiol* 26:407–418.
- Vankov A, Hervé-Minvielle A, Sara SJ (1995) Response to Novelty and its Rapid Habituation in Locus Coeruleus Neurons of the Freely Exploring Rat. *Eur J Neurosci* 7:1180–1187.
- Viney TJ, Lasztoczi B, Katona L, Crump MG, Tukker JJ, Klausberger T, Somogyi P (2013) Network state-dependent inhibition of identified hippocampal CA3 axo-axonic cells in vivo. *Nat Neurosci* 16:1802–1811.
- Vogt KE, Regehr WG (2001) Cholinergic modulation of excitatory synaptic transmission in the CA3 area of the hippocampus. *J Neurosci* 21:75–83.
- Wagatsuma A, Okuyama T, Sun C, Smith LM, Abe K, Tonegawa S (2017) Locus coeruleus input to hippocampal CA3 drives single-trial learning of a novel context. *Proc Natl Acad Sci U S A* 115:E310–E316.
- Walling SG, Brown RA, Miyasaka N, Yoshihara Y, Harley CW (2012) Selective wheat germ agglutinin (WGA) uptake in the hippocampus from the locus coeruleus of dopamine- β -hydroxylase-WGA transgenic mice. *Front Behav Neurosci* 6.
- Walling SG, Harley CW (2004) Locus ceruleus activation initiates delayed synaptic potentiation of perforant path input to the dentate gyrus in awake rats: a novel beta-adrenergic- and protein synthesis-dependent mammalian plasticity mechanism. *J Neurosci* 24:598–604.
- Weber JP, Andrásfalvy BK, Polito M, Magó Á, Ujfalussy BB, Makara JK (2016) Location-dependent synaptic plasticity rules by dendritic spine cooperativity. *Nat Commun* 7.
- Williams SR, Fletcher LN (2019) A Dendritic Substrate for the Cholinergic Control of Neocortical Output Neurons.
- Wilson IA, Ikonen S, Gallagher M, Eichenbaum H, Tanila H (2005) Age-Associated Alterations of Hippocampal Place Cells Are Subregion Specific. *J Neurosci* 25:6877–6886.
- Witter MP (2007) Intrinsic and extrinsic wiring of CA3: indications for connectional heterogeneity. *Learn Mem* 14:705–713.
- Wong RKS, Prince DA, Basbaum AI (1979) Intradendritic recordings from hippocampal neurons. *Proc Natl Acad Sci* 76:986–990.
- Yang Q, Song D, Xie Z, He G, Zhao J, Wang Z, Dong Z, Zhang H, Yang L, Jiang M, Wu Y, Shi Q, Li J, Yang J, Bai Z, Quan Z, Qing H (2021) Optogenetic stimulation of CA3 pyramidal neurons restores synaptic deficits to improve spatial short-term memory in APP/PS1 mice. *Prog Neurobiol* 209:102209.
- Yi F, Ball J, Stoll KE, Satpute VC, Mitchell SM, Pauli JL, Holloway BB, Johnston AD, Nathanson NM, Deisseroth K, Gerber DJ, Tonegawa S, Lawrence JJ (2014) Direct excitation of parvalbumin-positive interneurons by M1 muscarinic acetylcholine receptors: roles in cellular excitability, inhibitory transmission and cognition. *J Physiol* 592:3463–3494.
- Yim MY, Hanuschkin A, Wolfart J (2015) Intrinsic rescaling of granule cells restores pattern separation

- ability of a dentate gyrus network model during epileptic hyperexcitability. *Hippocampus* 25:297–308.
- Yu AJ, Dayan P (2005) Uncertainty, Neuromodulation, and Attention. *Neuron* 46:681–692.
- Yun SH, Cheong MY, Mook-Jung I, Huh K, Lee CJ, Jung MW (2000) Cholinergic modulation of synaptic transmission and plasticity in entorhinal cortex and hippocampus of the rat. *Neuroscience* 97:671–676.
- Zalutsky RA, Nicoll RA (1990) Comparison of two forms of long-term potentiation in single hippocampal neurons. *Science* 248:1619–1624.
- Zhang H, Lin SC, Nicolelis MAL (2010) Spatiotemporal coupling between hippocampal acetylcholine release and theta oscillations in vivo. *J Neurosci* 30:13431–13440.
- Zhang Y, Cao L, Varga V, Jing M, Karadas M, Li Y, Buzsáki G (2021) Cholinergic suppression of hippocampal sharp-wave ripples impairs working memory. *Proc Natl Acad Sci U S A* 118.
- Zheng F, Wess J, Alzheimer C (2012) M 2 muscarinic acetylcholine receptors regulate long-term potentiation at hippocampal CA3 pyramidal cell synapses in an input-specific fashion. *J Neurophysiol* 108:91–100.